THÈSE

Pour l'obtention du titre de :

DOCTEUR de L'UNIVERSITÉ DE LORRAINE

Spécialité: Sciences des Matériaux

Présentée par :
Youssef Samih

Thermomechanical surface treatments of austenitic stainless steels and their effects on subsequent nitriding during "Duplex" treatments

---

Thèse soutenue publiquement le 04 Juillet 2014 à 14h, à la salle Ferrari (Université de Lorraine-Metz) devant le jury composé de :

Cécile Langlade	Professeure à l'Université de Technologie de Belfort Montbéliard	Rapporteur
Guillaume Kermouche	Professeur à l'Ecole Nationale Supérieure des Mines de Saint-Etienne	Rapporteur
JianXin Zou	Professeur à l'Université Shanghai Jiao Tong, Chine	Rapporteur
Vincent Robin	Responsable de recherche chez AREVA-France	Examinateur
Nathalie Allain	Maitre de conférence - HDR à l'Université de Lorraine	Examinateur
Frédéric Chateau	Responsable Etude/Procédés chez SONATS-Europtechnologies	Invité
Thierry Czerwiec	Professeur à l'Université de Lorraine	Invité
Bernard Bolle	Maitre de conférences à l'ENIM	Co-directeur de thèse
Chuang Dong	Professeur à l'Université de Technologie de Dalian, Chine	Directeur de thèse
Thierry Grosdidier	Professeur à l'Université de Lorraine	Directeur de thèse

Acknowledgement

First of all, I would like to pay tribute to my PhD co-director, Doctor Bernard Bolle, dieddramatically on May 5th 2014. His remarks and relevant advices were extremely important and primordial to achieve the present work. It was ahonour for me to be trained by him on the use of the X-Ray Diffraction technique and learn the metallurgy notions in general. His encouragement and every-day assistance were crucial during my PhD Thesis. Beside his scientific skills, Bernard was a very kind person, encouraging all the PhD students.

I would like also to thank Professor Thierry Grosdidier, my PhD advisor, for his help, guidance and patience. His wide knowledge and scientific experience allowed me to better understand and expalin the obtained experimentalresults. He helped me a lot to develop my background in metallurgy and surface treatments of materials.

I am also very grateful to Professor Dong Chuang, my advisor in Dalian University of Technology. My residence periods in Dalian were successful because of the different discussions we had, to better understand the obtained results. I would like to thank him also for his help and assistance to make my living periods in Dalian very pleasant.

I take also the opportunity to thank Dr. Benoit Beausir for all the interesting discussions we had, and also for his help in achieving a main part of my thesis, by giving me the access to his EBSD post-treatment software.

I also thank Professor Thierry Czerwiec and Dr. Grégory Marcos, from Jean Lamour Institute (Nancy), for their help in carrying out the nitriding treatments and the chemical composition measurements.

I am indebted to all my colleagues and friends who have supported me over the last few years: Cécile, Alban, Julien, Heitham and all the other PhD students for the nice moments we had in LEM3.

Last but not the least, I am very thankful to my parents Mohamed Larbi et Habiba, my sisters Loubna and Meriem, for their support and encouragement during my PhD period. Thank you a lot.

Summary

Chapter III: Investigation of the Surface Mechanical Attrition Treatment (SMAT) effects on the microstructure and contamination of the AISI 316L and AISI 660 stainless steels surfaces

Chapter IV: Effect of the surface activation by mechanical and thermomechanical treatments on the nitrogen diffusion in the surface of the AISI 316L

Introduction

Surface properties have a significant effect on the reliability and lifetime of engineering components operating under various conditions in different environments. The surface engineering deals with methods for achieving the desired surface requirements and their behavior in service for engineering components. While the surface of any component may be selected on the basis of texture and color, engineering components generally demand a lot more than this. Thus the surface optimization cannot be neglected in the mechanical design and an appropriate surface treatment can often be used to obtain enhanced and optimized surface properties.

The austenitic stainless steels contain a minimum of 16 wt.% of chromium and a sufficient Nickel and/or Manganese to keep the face-centred cubic (fcc) structure. The most used stainless steels belong to the 300 series. These alloys have a good corrosion resistance and maintain their strength at high temperatures. They are used predominantly in the automotive, aerospace and construction industries. For the fabrication of the control rods of pressured water nuclear reactors, plasma nitriding can be used to enhance the hardness and wear resistances of the AISI 316L stainless steel.

Nitriding stainless steels at temperatures of about 500 °C was widely used to enhance surface properties. However, this leads to the deterioration of the corrosion resistance. Actually, at these nitriding temperatures, the precipitation of chromium nitrides near the top surface occurs. Less chromium is then available to form the protective passive film of chromium oxide (Cr_2O_3). At nitriding temperatures below 420 °C, it is possible to form a single-phase diffusion layer, which presents higher hardness, good wear and fatigue resistances, an also maintain the stainless aspect of the alloy. The phase that is formed under these conditions is commonly called expanded austenite, S-phase, m-phase or γ_N. This phase is a saturated solid solution in nitrogen with a deformed FCC lattice. Although the low temperatures nitriding of the stainless steels enhances the hardness and wear resistance, it is not sufficient for some industrial application due to the low thickness of the nitride layer and its low nitrogen content.

Recent works have shown that the activation of the materials surface by means of mechanical treatments could enhance the diffusion of nitrogen. The mechanical surface treatments are used to enhance the materials properties by combining the effects of the hardening, microstructure modification and induced residual stresses. These treatments lead to severe significant plastic deformation and are, for example, the shot peening, roller burnishing, pounding or the mechanical attrition treatments.

The Surface Mechanical Attrition Treatment (SMAT) is a fairly recently developed technique, which could be of great interest industrially. In this technique, a large number of balls are placed in a chamber and vibrated at high frequency by a generator. The material surface is then impacted repeatedly by the flying balls, leading to the formation of a surface heavily plastically deformed and the formation of nanostructured structure (grain size < 100 nm) and high density of defects. This leads to an enhancement physico-chemical and mechanical properties, and also may enhance the diffusion of nitrogen in the surface of stainless steels.

The aim of the present thesis is to study, on stainless steels, the effects of "duplex" treatments involving a first step of surface activation by means of thermo-mechanical treatments followed by an additional step of low temperature nitriding. The steels investigated here are (i) the AISI 316L austenitic stainless steel, that was already the subject of a few studies in the literature on surface improvement by nitriding and duplex treatments, and (ii) the AISI 660 austenitic stainless steel, investigated for industrial requirement for the first time after this kind of treatments.

This manuscript is divided into four different chapters. The first one is an overview of the state of the art concerning the enhancements observed after only the nitriding process, and also after the SMAT as well as different mechanical-nitriding duplex treatments.

The second chapter recalls, in a first part, the properties and initial microstructure of the investigated alloys. The second part contains the basis of the theory used after in the different calculations, as well as a brief description of the characterization techniques (Electron BackScattered Diffraction technique, chemical analysis, hardness …etc.).

In the third chapter, the surface microstructures of the AISI 316L and AISI 660 alloys modified by the SMAT process -under different conditions- are analyzed. In a first part, a new method of quantification of the effectiveness of the SMAT process is developed based on the analysis of Geometrically Necessary Dislocations, in order to investigate more quantitatively the individual effect of the different SMAT parameters. The second part deals with the analysis and quantification of the induced surface chemical contamination.

The fourth chapter deals with a comparative analysis of various duplex treatments where the nitriding is done on different types of severely deformed surfaces. This chapter is divided into two parts. The first part concentrates on the nitriding of the AISI 316L alloy deformed by the SMAT. The evolution of the nitride layers and the surface hardness were investigated. In the second part, cold rolling and High Current Pulsed Electron Beam (HCPEB) are used as the surface activator techniques prior to nitriding. The characterization of the formed nitrided layers and the surface

hardness allows comparing the effectiveness of the different surface activation to enhance the nitrogen diffusion and improve the surface properties.

Finally, a general conclusion and some proposal for future prospective work are given.

Chapter I

State of the art: the mechanical and thermo-mechanical surface treatments of stainless steels and their influence on the microstructure and the associated properties

In this first chapter, an overview of the effects of the studied surface treatments is given. The induced microstructure modifications as well as the associated mechanical properties (essentially the surface hardness) are given after surface treatment of different steels.

In a first section, the different types of mechanisms responsible of the microstructure strengthening are detailed. This will help to understand the occurring modifications by the studied surface treatments.

In the following three sections, the principal surface treatments principles and their effects on the microstructure are given. The Surface Mechanical Attrition Treatment (SMAT), the High Current Pulsed Electron Beam (HCPEB) and the plasma nitriding techniques are described in term of technical principles and the effects on the microstructures and hardness evolutions. The given information concerning each treatment will be important to understand the evolution of nitrogen diffusion on different treated surfaces.

A last section will focuses then on the effect of these surface treatments on the nitrogen transport on surface of steels, and more particularly stainless steels, as they are the studied materials in the present work. Results concerning the evolution of the nitrogen diffusion on SMAT-ed surfaces are given firstly. Then, the obtained results on materials treated by other severe plastic deformation techniques (such as cold rolling, high pressure torsion) prior to nitriding are grouped. The probably mechanisms responsible of increasing the nitrogen diffusion are then synthetized at the end of this chapter.

Summary

I. The strengthening mechanisms of materials

Before describing the different surface treatments used in the present work and their effects on the microstructure, a general overview of the different strengthening (hardening) mechanisms in metals will be given in this first section.

In a given environment, the strength and ductility of steel are determined by its composition and microstructure. The latter can be changed through three measures: changing composition, heat treatment and plastic working. Yield strength gauges the capability of a material against plastic deformation. In crystalline materials, plastic deformation is carried out, in most cases, by dislocation multiplication and motion.

One of the objectives of the surface treatment is the hardening of the surface in order to activate mechanisms that prohibit the mobility of the dislocations. There are five main strengthening mechanisms for metals. They are described in the following sub-sections.

I. 1   The solid solution strengthening

The strengthening effect of solutes is well known and has been investigated by a number of researchers over the years. Different interactions exist between solutes and the solvent lattice, but only elastic type interactions are considered, which are essentially of two kinds: size effects and modulus effects. The reader is referred to the different works proposed in the literature for more details about these effects (as example (Fleischer, 1967)). Here, only the different solid solution types are described.

The solid solution strengthening technique consists on adding atoms of one element (the alloying element) to the crystalline lattice of another element (the base metal). The alloying element diffuses into the matrix, forming a solid solution. There are two types of solid solution in the crystal lattice:

- o The substitutional solid solution (Fig. I. 1a and b): the solute atoms are large enough that they can replace solvent atoms in their lattice positions. Two configurations exist: random (Fig. I. 1a) and orderly (Fig. I. 1b) substitutional solid solution.
- o The interstitial solid solution (Fig. I. 1c): The atoms crowd into the interstitial sites, causing the bonds of the solvent atoms to compress and thus deform the material.

| (a) Random substitutional solid solution | (b) Orderly substitutional solid solution | (c) Interstitial solid solution |
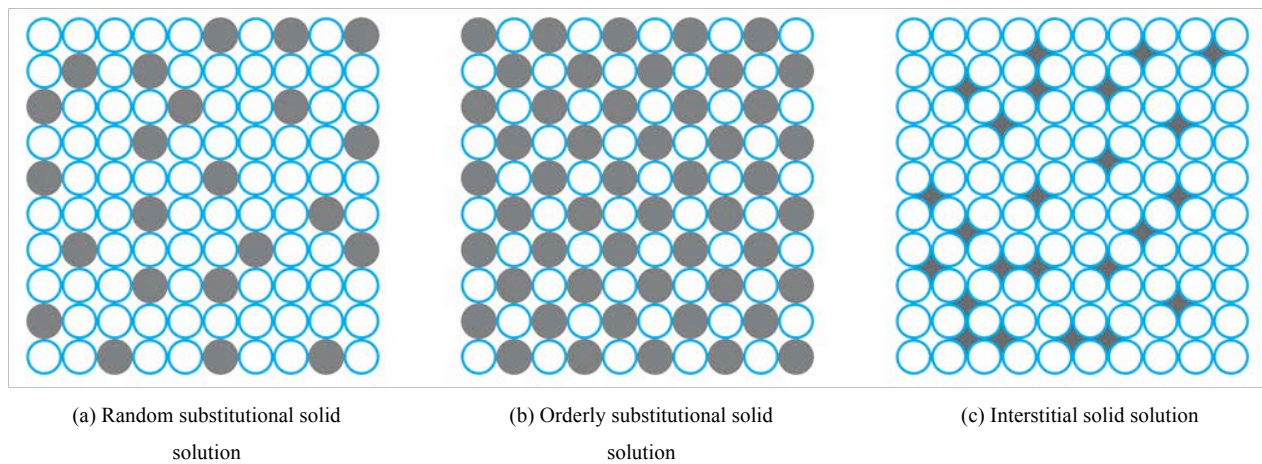
Fig. I. 1: Atoms location in the metallic solid solution (Thomas and Schmitt, 2002).

In the case of steels, the elements Mn, Si, Cr, Mo and Ni are for example substitutional solutes, while the C and N are interstitial ones.

I. 2   **Work hardening (or strain hardening) in the case of the fcc materials**

Work hardening (also called strain-hardening or cold-working) is the process of making a metal harder and stronger through plastic deformation. When a metal is plastically deformed, dislocations move and additional dislocations are generated. The more dislocations within a material, the more they will interact and become pinned or tangled. This will result in a decrease in the mobility of the dislocations and a strengthening of the material. This type of strengthening is commonly called cold working.

In the case of face centered cubic (fcc) materials, two hardening mechanisms can undertake:

o Partial dislocations gliding: the perfect dislocations dissociate under the high stress when the stacking fault energy is very low, the plastic deformation occurs then by the spacing of the partial dislocations in the sliding plan, which leads to the formation of large strips of stacking faults (Fig. I. 2).

o Mechanical twinning: the plastic deformation involves shear of a part of the crystal between two planes. These planes will form the interface with noun-deformed part, as shown in Fig. I. 3.
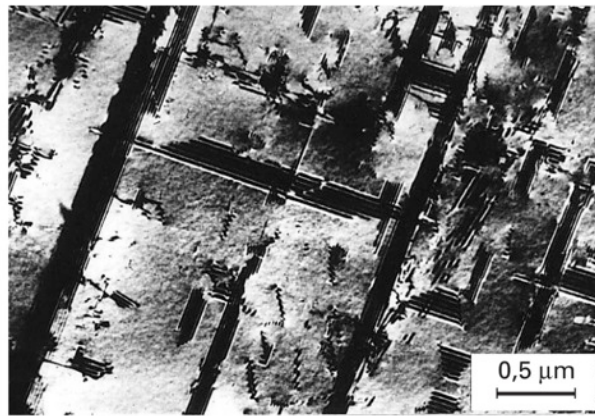
Fig. I. 2: Stacking faults formed by the propagation of partial dislocations in an austenitic stainless steel (with low SFE) (Thomas and Schmitt, 2002).
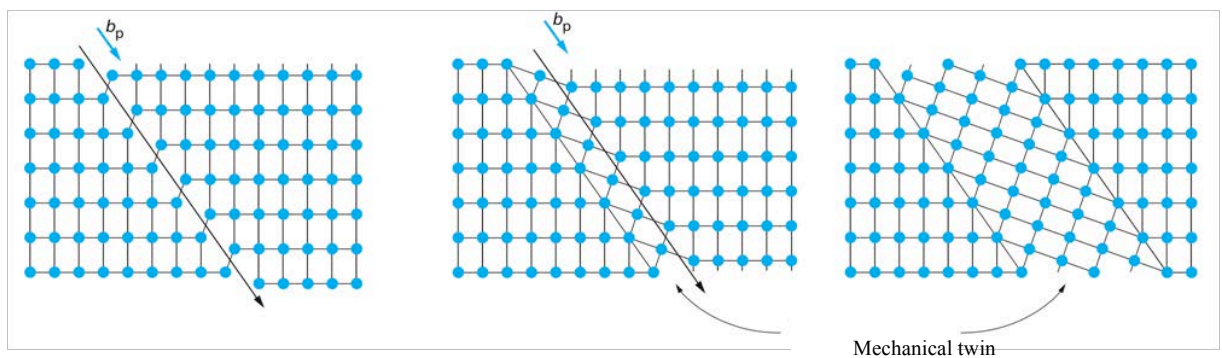
Fig. I. 3: Schematic formation steps of a mechanical twin in a fcc material by the sliding of the partial dislocations (Thomas and Schmitt, 2002).

I. 3   **The grain boundary strengthening (or the Hall-Petch strengthening)**

The grain boundaries have a profound effect on the mechanical properties of materials leading to the well-known Hall–Petch relationship, which describes the yield stress in terms of the grain size:

$$\sigma_e = \sigma_0 + k.d^{-\frac{1}{2}} \qquad Eq.\ I.\ 1$$

Where σ_e is the yield stress, σ_o is a material constant characterizing the starting stress for dislocation movement (or the resistance of the lattice to dislocation motion), 'k' is the strengthening coefficient (a constant unique to each material), and d is the average grain diameter.

It is based on the principle that grain boundaries block dislocation movement and that the density of dislocations have an effect on how easily dislocations can traverse grain boundaries and travel from grain to grain. So, by changing grain size, the dislocation movement and yield strength are influenced.

In addition, as far as twin boundaries are considered as interfaces, their presence suggests a contribution in the enhanced strengthening.

I. 4   **Precipitation hardening**

This method of strengthening consists on hardening the material by precipitating finely dispersed precipitates of the solute in a supersaturated matrix. These fine precipitates impede the movement of dislocations, or defects in a crystal's lattice. This process involves the following three basic steps:

1. Solution treatment: the alloy is heated to a relatively high temperature that allows any precipitates or alloying elements to go into a solid solution.

2. Quenching: in which the solution treated alloy is cooled to create a supersaturated solid solution. The cooling can be achieved using air, water or oil. Regardless the cooling method, the cooling rate must be sufficiently rapid to create a supersaturated solution.

3. Precipitation or age hardening: the quenched alloy is heated to an intermediate temperature and held for a period of time. At these intermediate temperatures, the supersaturated solid solution decomposes and the alloying elements form small precipitates clusters inside grains. These precipitates block the movement of dislocations and consequently the alloy becomes harder and resists to deformation.

I. 5   **The phase transformation and hardening**

During the plastic deformation, two different types of martensite can be formed: a hexagonal close packed (hcp) martensite, called ε-martensite, then a bcc martensite, called α'-martensite. The α' martensite is present in the fcc lattice in form of small aggregates in the intersection of the ε-martensite bands. The number as well as the size of these aggregates increases as function of the total deformation imparted to the material.

The hardening of material due to the phase transformation appears clearly in the tensile strength test for example. The necking is delayed and the elongation at rupture is increased. This phenomenon of plasticity induced by phase transformation is currently designed as TRIP (TRansformation Induced Plasticity).

The description of these different hardening mechanisms will be important in the understanding of the effects of the plastic deformation techniques studied in the present work. These techniques are described in the next sections.

II. Surface modification of steels by Surface Mechanical Attrition treatment (SMAT): the microstructure and mechanical properties evolutions

II. 1   The SMAT treatment principle

The Surface Mechanical Attrition Treatment (SMAT) (Liu et al., 2000; Lu and Lu, 2004) is a fairly recent technique for mechanical surface treatment. In this technique, a large number of balls are placed in a chamber and vibrated at high frequency by a generator, as shown in Fig. I. 4(Lu and Lu, 2004). The sample to be treated, fixed at the upper side of the chamber, is impacted repeatedly by the flying balls so that its surface becomes heavily plastically deformed.
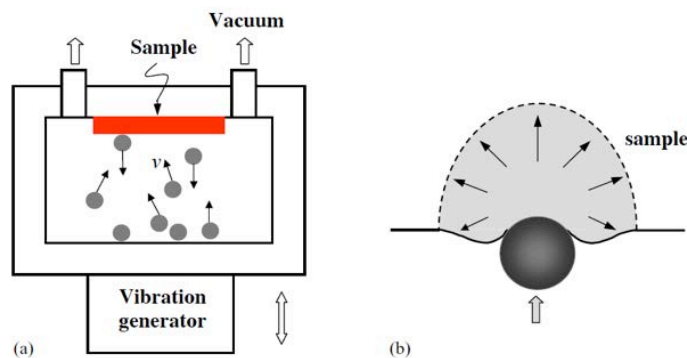
Fig. I. 4: (a) Schematic illustration of the SMAT principle, (b) typical multidirectional plastic deformation in the sample surface layer induced by the impact of the balls (Lu and Lu, 2004).

Ball size varies between 1 to 10 mm in diameter and can be in different materials nature. In addition, the vibration frequency of the generator is in the range from 50 Hz to 20 kHz, and vibration amplitude in the range of 20 μm to 150 μm. All the SMAT modifiable parameters are summarized in Table I. 1. The parameters used in the present study are given in the beginning of Chapter III and IV.

When the balls are resonated in the SMAT chamber, the 'flying' balls impact the sample surface. The velocity of the balls was estimated to be in the range of 1-20 m/s. It is important to note that the impacts of the balls with the sample surface are random because of the random directions of the balls inside the chamber and also because of the balls collisions.

Balls	Diameter	1 mm to 10 mm
	Nature	Steel or ceramic
	Weight	Few grams to tens of grams
Generator	Amplitude	20 to 150 μm
	Frequency	50 Hz to 20 kHz
Distance sample - Sonotrode	10 to 100 mm	
Duration	Few seconds to hours	

Table I. 1: The adjustable SMAT parameter used for the SMAT.

As consequence, the balls impact the surface at high strain rates and induce severe plastic deformation. A graded microstructure is then obtained as shown in Fig. I. 5. At the extreme surface where the strain and strain rate are maximum, a nanostructured layer is formed. Below this layer, refined microstructure and deformed coarse-grained layers are observed, respectively.
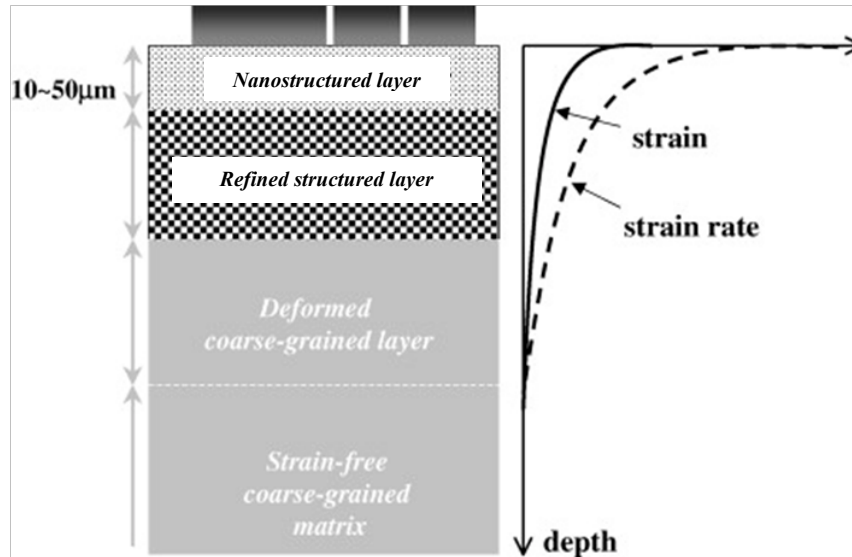
Fig. I. 5: Illustration of the microstructure characteristics and distributions of strain and strain rate from the top surface along depth after SMAT.

Beside its conventional use to harden the surface and improve its wear and fatigue properties (Roland et al., 2006; Wang et al., 2006b), SMAT has also been used, for example, to activate the surface before nitriding (Lin et al., 2006; Panicaud et al., 2012; Tong et al., 2003, 2007)or to create multilayered laminate composites by subsequent roll bonding (Waltz et al., 2009). For all these potential applications, the metallurgical and microstructural states of the deformed surface have to be tailored in different ways and in a reproducible manner to form nanostructures and/or deep hardened zones. As for severe plastic deformation processes, the grain refinement and nanocrystalline formation mechanisms involves dislocations activities, mechanical twinning and interaction of dislocations with mechanical twins.

Therefore, as the SMAT will be used in the current work to activate the surface of austenitic stainless steel prior to the Plasma Nitriding treatment, it is important to overview firstly how the SMAT modify the microstructure (refinement mechanisms) and properties of stainless steels.

II. 2 The microstructure refinement mechanisms occurring during the SMAT

During the SMAT, the plastic deformation occurred introduce a high density of defects in the material surface and subsurface. Hughes et al.(Hughes, 2001; Hughes and Hansen, 1995, 1997) showed that at large strain, this leads to structures composed of dislocation boundaries with high

misorientations forming a typical cell block-structure. It was also observed that when the strain is increased, this block-structure is reoriented to a lamellar structure (see Fig. I. 6 for illustration). The cell block structure contains microbands (MBs) and single dense dislocation walls (DDWs), which around blocks of equiaxed cells. On the other side, in a typical lamellar structure at large strain, the lamellar boundaries (LBs) sandwich thin layers of cells and subgrains oriented along the material flow direction.
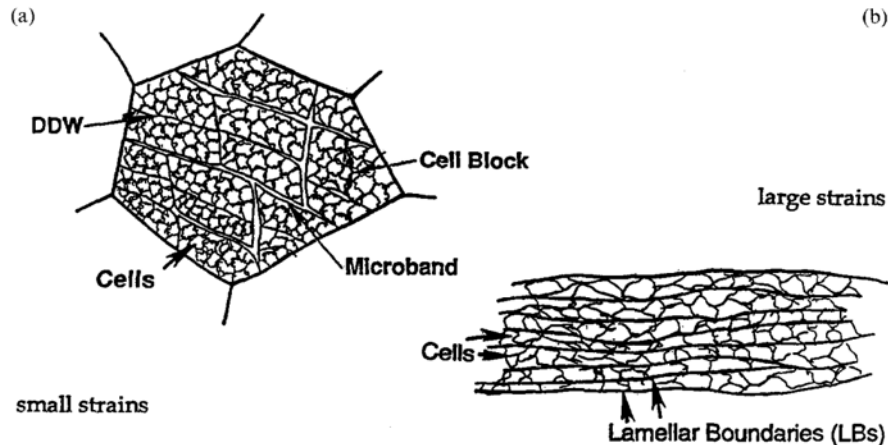
Fig. I. 6: Schematic drawing of deformation microstructures and grain subdivision. (a) Small to medium strain (Von-Mises strain,ε_{VM}= 0.06 - 0.80 with long microbands and dense dislocation walls (DDW) surrounding groups of cells in cell blocks; (b) large strain, ε_{VM}> 1 with lamellar boundaries (LBs) parallel to the deformation direction, sandwiching in narrow slabs of cells or equiaxed subgrains.

The nanostructuration mechanisms of materials depend on their Stacking Fault Energy (SFE). For **materials of low SFEs** such as stainless steels and Inconel 600 (Tao et al., 2003), the deformation mechanisms are governed by the mechanical twinning. The refinement mechanisms were schematized in 4 essential steps (as shown in Fig. I. 7):

- Step 1: Formation of a high density of twin boundaries which subdivide the original coarse grains, which are subdivided into Lamellar Twin-Matrix Alternated Blocks (LTMABs) (step 1 in Fig. I. 7),

- Steps 2 and 3: Two possibilities exist for step 2:

  2A :It was found for Inconel 600 (SFE of 28 mJ/m²) that the driving force for growth of microtwins is not high enough to overcome the barriers of the encountered twin boundaries. Dislocation activities become then functional inside the LTMABs when the strain increases. For minimizing the strain energy, these dislocations arrange themselves into dislocations walls (Step 2A), leading to the subdivision of the LTMABs into equiaxed nanometer-sized blocks (Step 3).

  2B : For materials of lower SFEs (the case the AISI 304) with even smaller SFEs (16.8 mJ/m²), the driving force for growth of mechanical twins is sufficiently high to

overcome the twin boundaries (Step 2B in Fig. I. 7), and thereby the twin-twin interaction occurs forming equiaxed nanometer-sized blocks with misorientation (Step 3).

- Step 4: When the grain size is reduced down to the nanometer range, the grain rotation and grain boundary sliding will be much easier in comparison with coarse grains ones(Van Swygenhoven et al., 2000). This leads to the formation of randomly orientated nanocrystalline (Step 4).

On the other hand, for **materials of high SFEs** as iron and aluminum, the refinement mechanism of the structure depends essentially on the dislocation gliding. The nanocrystallization process is carried out here also in four essential steps:

1. Multiplication of the dislocation grids (Fig. I. 8a).
2. Formation of cells or dense dislocations walls subdividing the grains in different parts (Fig. I. 8b).
3. Transformation of the cells and dense dislocations walls into sub-boundaries inside the grain.
4. Evolution of these sub-boundaries to "conventional" grain boundaries with higher misorientation.
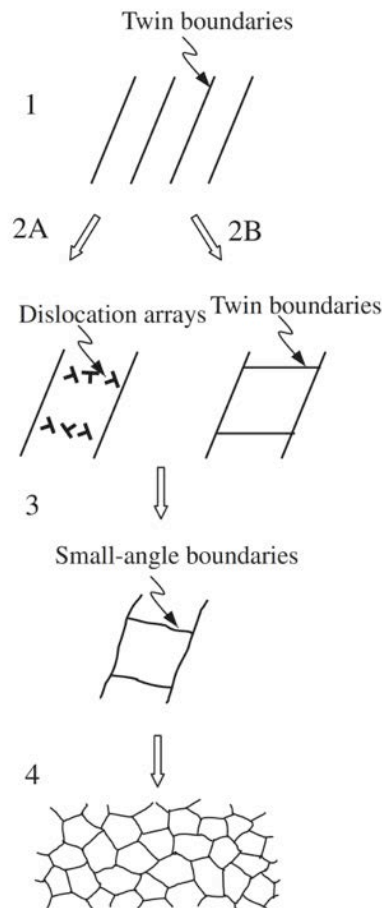
Fig. I. 7: A schematic illustration of grain refinement during SMAT for the two samples with low stacking fault energies(Tao et al., 2003).

(a)   (b)
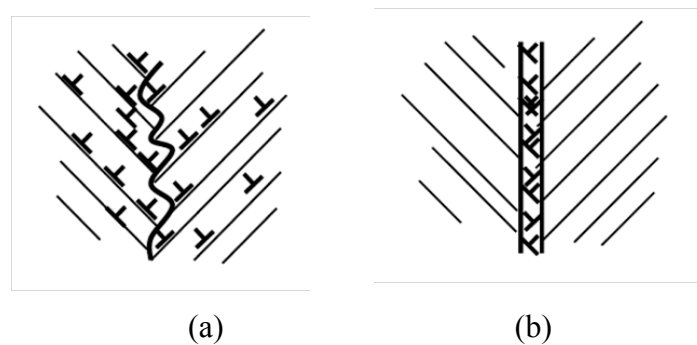
Fig. I. 8: New grain boundaries arrangement in the nanostructured layers. (a) Apparition of dislocations during the plastic deformation and (b) grouping of these dislocations to form a dense dislocation wall (Bagheri and Guagliano, 2009).

In the present work, and as it will be presented later, two materials with different SFEs will be treated by SMAT. These results issued from the literature (presented above) show how the SFE of

the materials can modify the material behavior in term of accommodation of the plastic deformation, and it will be useful in the understanding of the obtained results in the present work.

II. 3   Typical effects of the SMAT on the microstructure of austenitic stainless steels

As described before, the plastic deformation mechanisms are essentially function of the SFEs of the treated material. Therefore, in this section, the literature review of the SMAT effects on microstructure and associated properties will be focused on materials in the same SFEs range (AISI 316L and AISI 304). Nevertheless, the AISI 660 was not previously treated by severe plastic deformation techniques.

Surface nanocrystallization was carried out on the AISI 316L surface by means of Ultrasonic Shot Peening (USP) -other designation used for the SMAT- using a vibration frequency of 20 kHz, balls of 3 mm diameter and during from 30 to 810 s(Liu et al., 2000). As shown in Fig. I. 9a, a graded microstructure is observed. Microbands of about 100 nm widths can be observed at extreme top layer (Fig. I. 9b). In the region of about 5 to 30 µm depth, multiple-slip is observed, as it is identified in Fig. I. 9c.
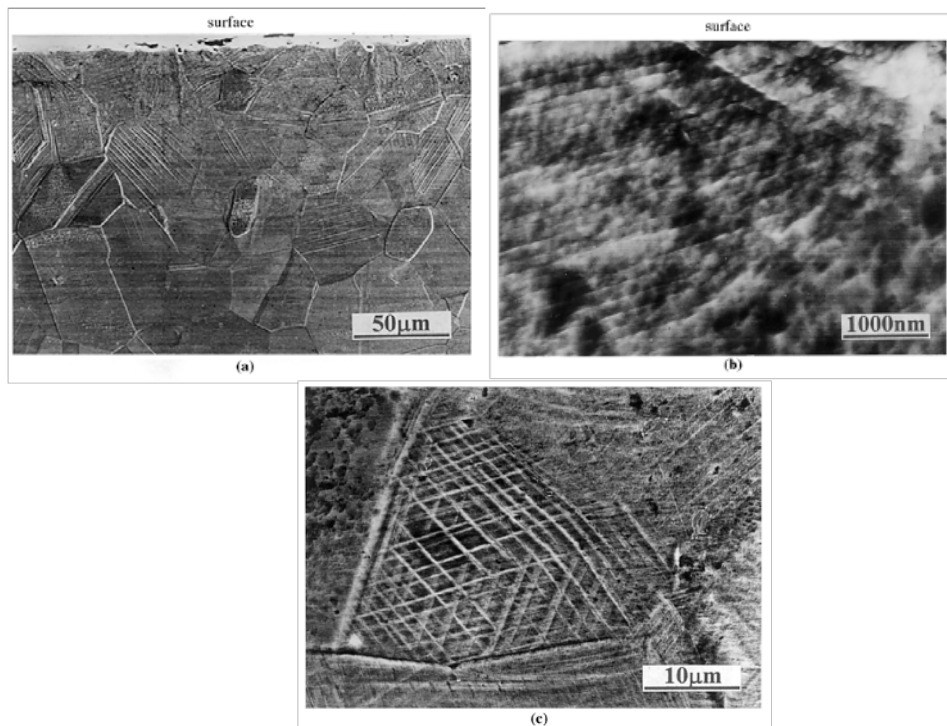
Fig. I. 9: (a) SEM cross-section observation of the 316L sample after 810sUltrasonic Shot Peening (UPS) treatment. (b) A close observation of the microbands in the top surface layer; (c) and the multiple-slip in the subsurface layer (Liu et al., 2000).

In another study(Lu et al., 2006), where the AISI 316L was treated for 60 min by SMAT with balls of 8 mm diameter and a frequency of 50Hz, the deformed layer of more than 100 µm was

revealed by optical microscopy, as observed in Fig. I. 10. Complementary Transmission Electron Microscopy (TEM) observations carried out at a distance of 50 μm below the treated surface showed the presence of parallel (Fig. I. 11a) and intercrossed twins (Fig. I. 11b).
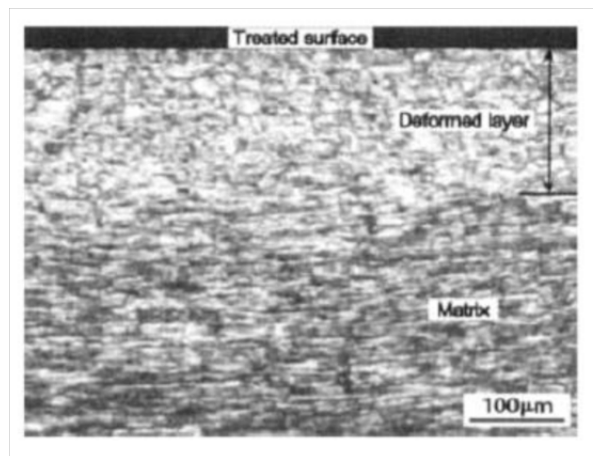
Fig. I. 10: Cross section Optical micrograph of a sample treated for 60 min, showing the deformed layer and the initial material (matrix)(Lu et al., 2006).
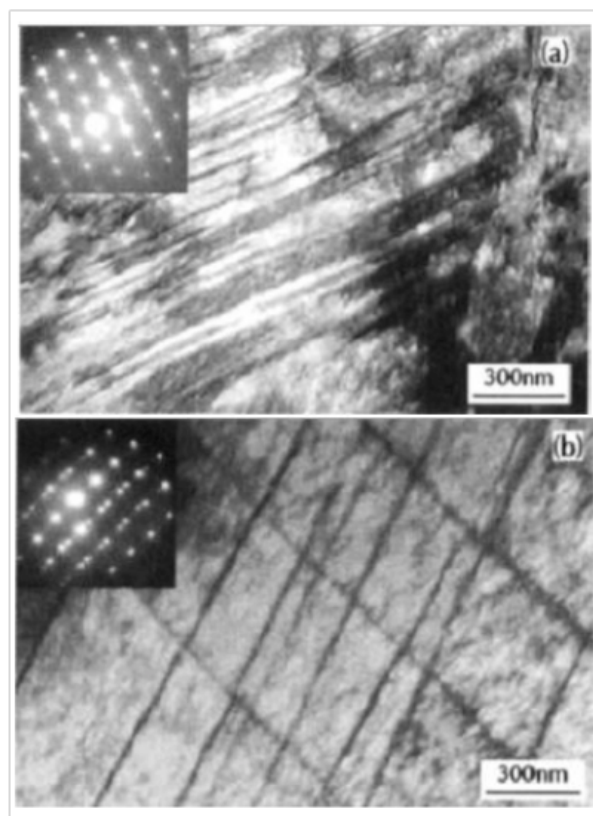
Fig. I. 11: TEM micrograph and diffraction patterns done at about 50 μm from the top treated surface. (a) Parallel twins, (b) multi-directional twins(Lu et al., 2006).

Similar deformation mechanisms were observed at different depths from the top treated surface by Roland et al (Roland et al., 2007). The SMAT was done with 3 mm balls (in hardened steel) and an amplitude of vibration of 25 μm for durations ranged from 5 to 30 minutes. At a depth of 50 μm

from the top surface, typical intersection of twins is observed (Fig. I. 12a). In this figure, it can be seen that after the multidirectional repetitive loading during the SMAT, different twin systems are activated. This phenomenon was supposed to be in the origin of generation of nano-grains. At 200 μm below the surface, unidirectional parallel mechanical twins are observed (as shown in Fig. I. 12b) leading to the formation of a twin-matrix alternative lamellar structure.

(a   (b
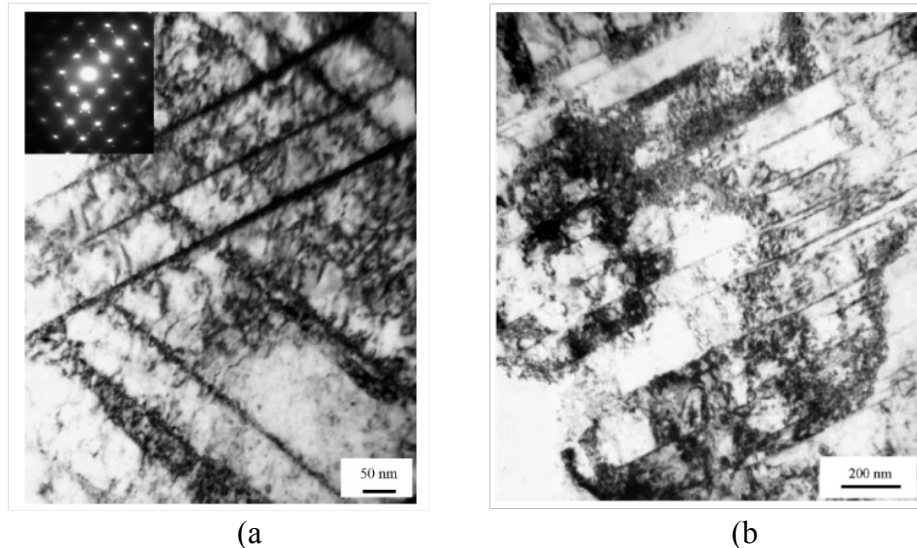
Fig. I. 12: TEM image of the microstructure at the depth of (a) 50 μm and (b) 200 μm in the sample subjected to SMAT, illustrating twin–twin intersections(Roland et al., 2007).

II. 4   Effect of the different SMAT processing parameters on the microstructure and mechanical properties of stainless steels

The introduction of such defects density within the material by SMAT leads to a significant enhancement of the mechanical properties. In this section, the effect of the SMAT parameters (SMAT duration, balls diameter, amplitude of vibration ...etc.) on the mechanical properties will be described.

II. 4. 1   Effects of the SMAT duration

It has been shown in previous work that the surface hardness of stainless steels is time-dependent. Among these works, after SMAT of an AISI 304 with durations in the range of 20 to 300 min, Sun et al. observed an increase of the hardness in the deformed layer, as shown in Fig. I. 13(Sun, 2013). The top surface hardness reaches about 350 HV with the lowest duration (20 min)- and about 500 HV with the maximum SMAT duration (300 min). It was also seen that the surface hardness near the top surface (within ~ 100 μm) saturated from a SMAT duration of 180 min. However, deeper hardened depths were obtained by increasing the duration. This hardness enhancement was attributed to the combination results of strain hardening, structural

nanocrystallization and also martensite formation, which is a well-known phenomenon in severely deformed austenitic stainless steels with low Ni content(Zhang et al., 2003).
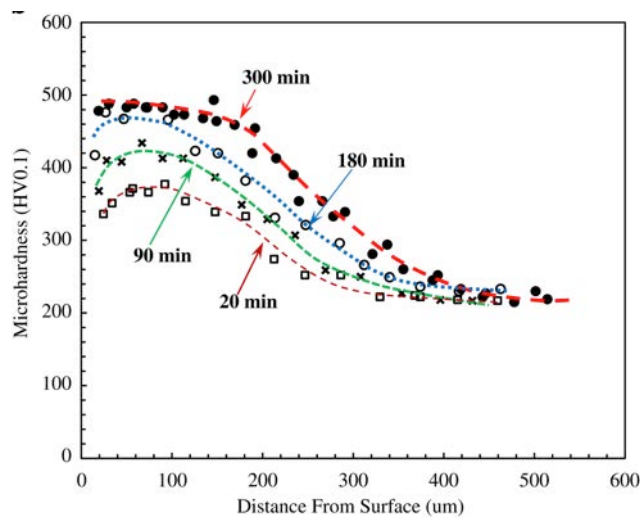
Fig. I. 13: The microhardness profiles measured across the SMAT layers of AISI 304 treated for various times (balls of 6 mm diameter were used to treat the surface)(Sun, 2013).

The same tendency was depicted after SMAT of an AISI 316L (Arifvianto et al., 2011), where the hardness was increased by approximately two times at a distance of 0.1 mm from the treated surface, as shown below in Fig. I. 14. In addition, similar saturation effect -observed in the case of the AISI 304 by Sun et al.(Sun, 2013)- was depicted, where further surface hardness increase does not occur after 10 min of treatment.
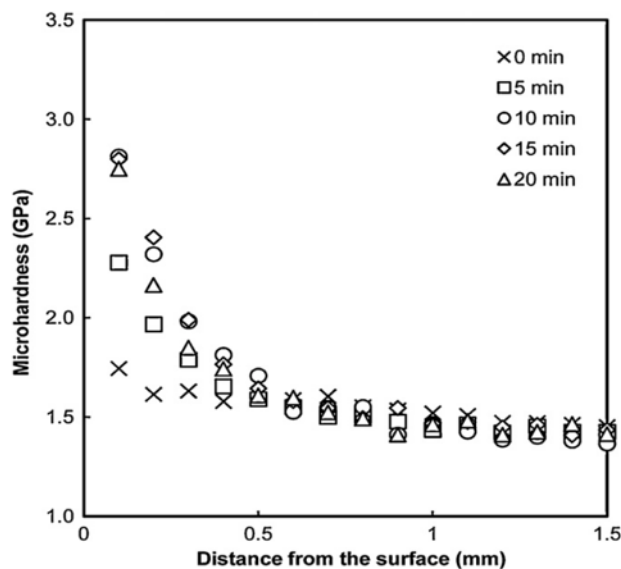
Fig. I. 14: Microhardness evolution as function of the distance from the treated surface by SMAT of an AISI 316L with balls of 4,76 mm diameter (Arifvianto et al., 2011).

In addition to the hardness evolution, the wear resistance is significantly improved. It was found in the work of Sun et al.(Sun, 2013)that the SMAT can produce a wear resistant layer of hundred of

microns thick on the surface of AISI 304.As shown in Fig. I. 15a, under lubrication condition, the SMAT-ed sample exhibits much better wear resistance than the untreated one, particularly at high loads, where the wear volume was reduced by about 3 times. In addition, analysis of the surface profiles in the wear tracks-given in Fig. 15billustrates the pileup height formed in the untreated and SMAT-ed samples. In both cases, material pileup at the two edges of the track are revealed but was larger and deeper in the case of the untreated material. It was concluded that the formed SMAT layer, due to its higher hardness, provides more resistance to plastic deformation and thus better wear resistance of the AISI 304 under lubricated sliding(Sun, 2013).
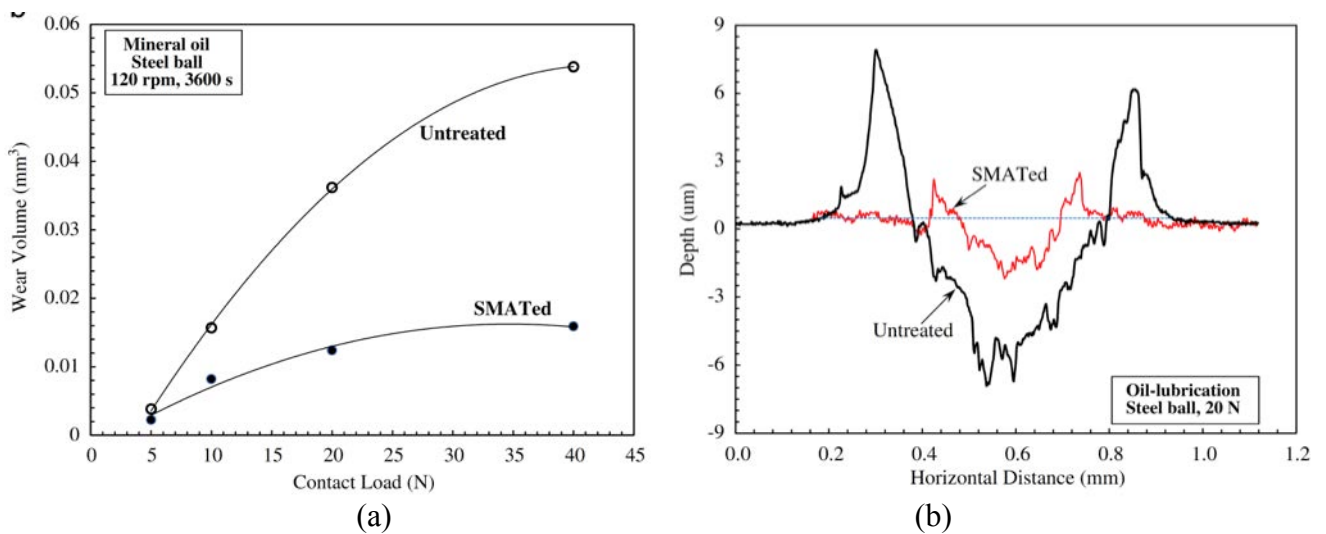
Fig. I. 15: (a) WearvolumeasafunctionofappliednormalloadunderoillubricatedconditionfortheuntreatedandSMAT-ed specimens against a steel ball slider. (b) Typical surface profiles across the wear tracks on the untreated and SMAT-ed specimens resulted from oil-lubricated wear testing under 20N load.

The effect of SMAT duration can also be revealed in the evolution of the tensile and bending properties of a SMAT-ed AISI 316L(Roland et al., 2007). Tensile tests were carried out on an untreated sample and three samples SMAT-ed for different durations. The results are given in Fig. I. 16. Compared with the untreated sample, the SMAT-ed samples are characterized by a significant increase of the yield stress and the mechanical strength. This was explained by the high performance of the formed nanocrystalline layer, which sustains an important part of the loading during the deformation, and thereby contributes to the overall enhancement of these mechanical properties.
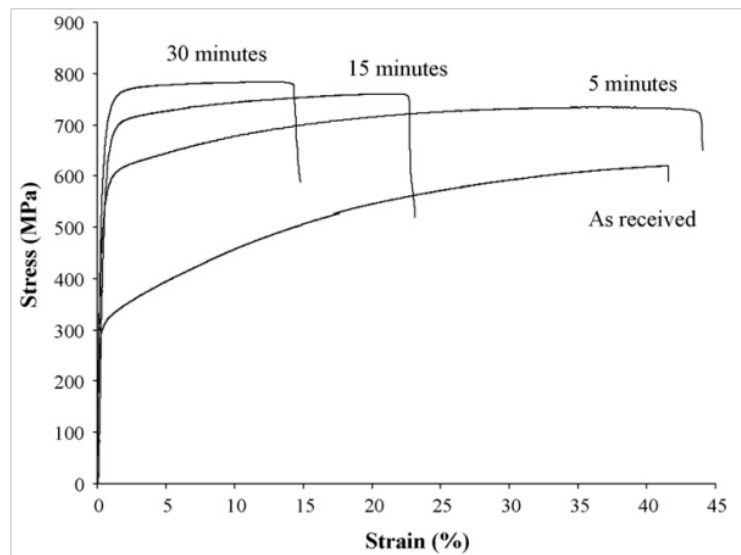
Fig. I. 16: Tensile stress–strain curves obtained for different SMAT times(Roland et al., 2007).

II. 4. 2   Effects of the amplitude of vibration

Another important parameter in the SMAT process is the amplitude of vibration. It impacts directly the balls speed and thereby the energy imparted to the surface. Roland et al. (Roland et al., 2007)analyzed the evolution of a AISI 316L microhardness from the top surface towards the material core treated under two amplitudes of vibrations : 25 and 50 µm (Fig. I. 17). This result indicates firstly that there is no notable difference in hardness between the two conditions at the extreme treated surface, caused probably by a saturation effect (grain size stabilization). However, when the treatment is more severe (50 µm of amplitude), the hardened layer is thicker. This is explained by a higher strain rate supported by the material in the last case.
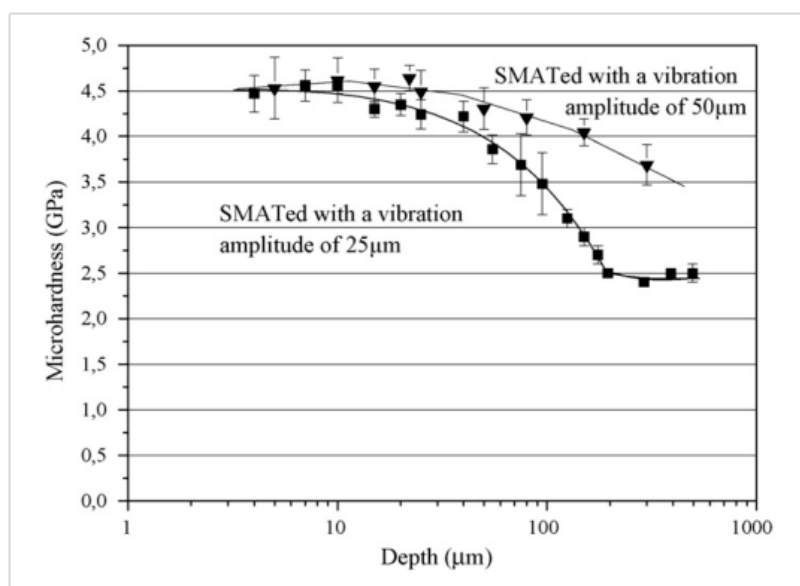
Fig. I. 17: Variations of the microhardness with the distance from the treated surface determined for the AISI 316L (Roland et al., 2007).

II. 4. 3   Influence of the balls number and diameter

The number of the balls present in the chamber and their diameter are also two important factors impacting the materials properties. Fig. I. 18gives (a) the effect of the number of balls and (b) the effect of the balls diameter on the microhardness distribution for a treated AISI 316L (Arifvianto et al., 2011). With a higher number of balls in the chamber (Fig. I. 18a), the microhardness with 375 balls is slightly higher than that using 250 balls at a distance of 0.1 mm from the surface. This indicates that increasing the number of balls accelerates the formation of nanocrystallites, martensite and residual stress on the surface, responsible of the hardness enhancement.

Furthermore, the use of larger balls in the SMAT leads to a significant hardness increase, as shown in Fig. I. 18b, and more especially with balls of 6.35 mm diameter, where the hardness was increased in both the extreme top surface and also the subsurface within about more than 1.5 mm.
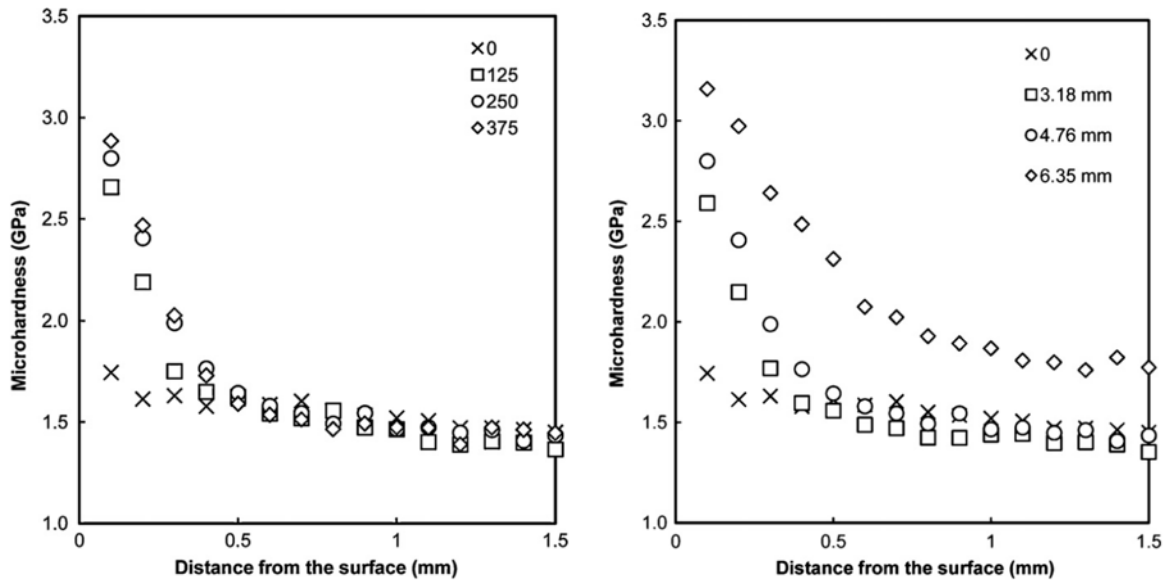
Fig. I. 18: Effect of (a) the balls number and (b) the balls diameter on the near microhardness evolution of a SMAT-ed AISI 316L (Arifvianto et al., 2011).

From the results issued from these different works, it is clear that the different SMAT processing parameters have an important effect on the treated material microstructure evolution as well as the associated mechanical properties. However, the effect of each parameter on the modification of the microstructure is still missing. In the present work, in Chapter III, a new technique based on the microstructure analysis by Electron BackScatterd Diffraction (EBSD) is given and details how the graded microstructure formed after SMAT will evolve as function of some processing parameters, such as the SMAT duration, the balls diameter and nature as well as the amplitude of vibration.

III. The surface modification by High Current Pulsed Electron Beam (HCPEB) technique

Among the surface treatments techniques, the High Current Pulsed Electron Beam (HCPEB) technique is a very recent one (Proskurovsky et al., 1997, 1998, 2000; Rotshtein et al., 2006). It was developed in Russian Institute of High Current Electronics in Tomsk. In the 1990s, the research group led by Proskurovsky et al. has achieved considerable success in the creation of a high current pulsed electron beam source that contains an electron gun with an emission cathode and a plasma anode placed in a guide magnetic field (Proskurovsky et al., 1998). The HCPEB source has the following operating parameters: electron energy 0.5-40 keV; and pulse duration 0.5-5 µs; energy density 0.5-40 J/cm^2; beam cross section area 10-50 cm^2; and pulse repetition rate 0.2 Hz. Proskurovsky et al. have investigated the implications of HCPEB for treating industrial alloys and suggested its potential applications as an efficient method for thermal protection, rapid annealing, surface cleaning and surface alloying. For the moment, the HCPEB is only available in Russia (Proskurovsky et al., 1998) and China (Hao et al., 2001).

III. 1 Principle of the HCPEB technique

The high-density electron pulses of short durations induce dynamic temperature fields in the surface layers giving rise to superfast heating and/or melting. This is followed by a rapid solidification and cooling of the material surface. In addition, a dynamic stress field is formed that causes intense deformation in the material sub-layer or even deeper in the substrate. The principle of the generation of the HCPEB in plasma filled system is illustrated in Fig. I. 19(Proskurovsky et al., 1997).
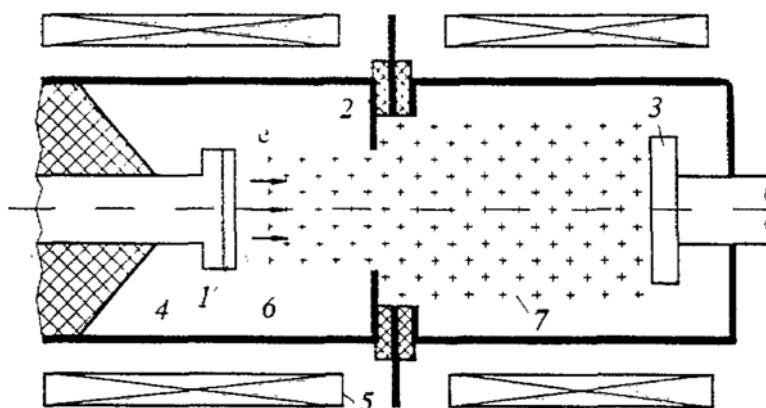
Fig. I. 19: Schema of the principle of the production of low-energy intense electron beams in a plasma-field diode. 1: explosive-emission cathode, 2: anode unit with spark plasma sources, 3: Collector, 4: Vacuum chamber, 5: Solenoid, 6: cathode plasma, 7:anode plasma (Proskurovsky et al., 1997).

The explosive emission cathode is made of graphite. The anode is made of stainless steel and has a hole in its center through which the beam passes. Graphite-cathode spark plasma sources are placed evenly in a circle behind the anode. The electron beam is transported through the anode plasma to the collector. To prevent the beam from pinching, an external magnetic field is used.

The electron source operates as follows: as the magnetic field reaches its maximum, the spark sources are switched on and the anode plasma fills the acceleration gap and the beam drift space. After 2-3 µs, an accelerating voltage produced by a voltage pulse generator is applied to the cathode. The anode plasma, owing to its good conductivity, acquires the potential of the anode and the effective gap spacing in the diode shortens abruptly. This results in the initiation of explosive electron emission at the cathode. The voltage applied tithe diode is localized across the double layer between the cathode and anode plasmas where the electron beam is generated.

The HCPEB irradiation leads to a gradient structure usually contained three different defined zones (melted zone, Heat-Affected Zone (HAZ) and stress propagation zone), as is shown in Fig. Three successive regions can be formed at the surface after the LEHCPEB irradiation: (i) a melted and rapidly solidified zone (10^7 to 10^8 K/s) on the top treated surface (~ 1 µm)(Rotshtein et al., 2004a; Zou et al., 2006), (ii) a heat affected zone where solid state phase transformations and recrystallization can occur (~10 µm) (Zou et al., 2007)and (iii) a stress-wave affected layer by the dynamic stress field induced (~100 µm), where the material hardness can be modified due to the stress wave propagation (Qin et al., 2009).
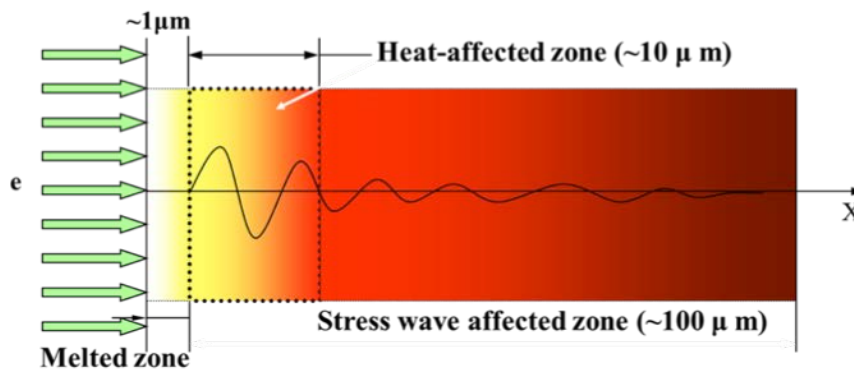
Fig. I. 20: Schematic diagram of three zones generated by HCPEB treatment.

Many studies with intention of understanding the modification effects not only on the treated surface and near-surface but also at greater depths of hundreds of micrometers have been carried out and a lot of meaningful results have been reported in literature (Proskurovsky et al., 1997, 2000; Zou et al., 2008).

III. 2 **Surface modification effects**

Modification effects through the HCPEB treatment on surface and near-surface of steels and intermetallic alloys including metastable phase and nanostructure formation (Guan et al., 2005; Proskurovsky et al., 1997; Zou et al., 2006a), surface homogenizing and crater formation (Gao et al., 2007; Grosdidier et al., 2007; Proskurovsky et al., 1998, 2000; Rotshtein et al., 2004b; Zou et al., 2006) as well as the texture modification (Grosdidier et al., 2008; Zhang et al., 2007)have already received extensive attention.

The HCPEB acting on sample surface can generate melting and the presence of craters on the top surface, as shown in Fig. I. 21. It is well established that the formation of craters is correlated with local uneven distribution of chemical elements or second phases (Proskurovsky et al., 2000; Zou et al., 2006). Studies on various steels also reveal that with increasing number of HCPEB pulses, the crater density decreases sharply. This sharp decrease of crater density is believed to be due to the eruption of local micro-irregularities. In fact, statistics on the number density of second phase particles or inclusions as a function of HPCEB pulses in previous studies show the same trend with the crater density(Zou et al., 2006).The eruption of local micro-irregularities makes it possible to clean the surfaces and improve the corrosion resistance of the treated materials.

The rapid solidification with a solid front velocity of about 2-10 m s^{-1} (Proskurovsky et al., 1998; Zou et al., 2004) and fast cooling (estimated to be about 10^7-10^8 K s^{-1}) processes make it possible to maintain the non-equilibrium microstructures to the room temperature and refine the grains to sub-micron (Proskurovsky et al., 1997; Zou et al., 2006). This leads to the formation of a surface layer with improved physical, chemical and strength properties (Hao et al., 2005; Ivanov et al., 2002, 2002; Zou et al., 2004).
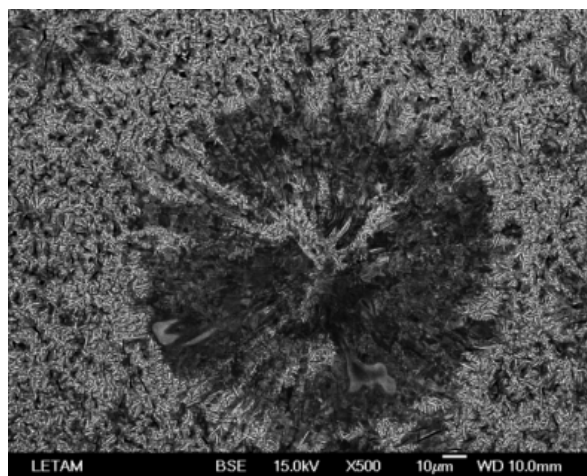
Fig. I. 21: An image showing a typical crater on the surface of the HCPEB treated D2 steel.

As described previously, the HCPEB treatment is a process coupled with thermal effect and stress. It always causes intense heating, rapid cooling and solidification. This process has potential to change the grain orientations in the treated layers. Zou et al. have firstly reported the evolution of texture in the HCPEB treated samples of NiTi shape memory alloy(Zhang et al., 2007), and AISI D2 cold working die steel (Zou et al., 2007).An example showing the presence of the mixed<100>+ <110> fiber texture in the rapid solidified treated layer of the HCPEB treated NiTi shape memory alloy is shown in Fig. I. 22, where the Normal direction (Z1) is parallel to the HCPEB direction.
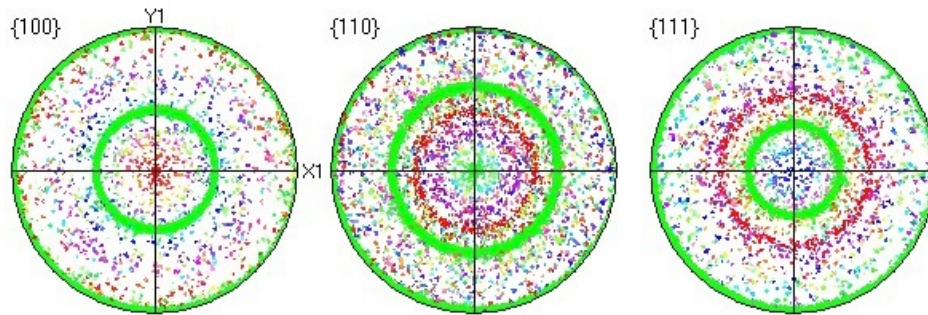
Fig. I. 22: Pole figures showing fiber texture containing components of <100> and <110> for NiTi shape memory alloy generated by HCPEB treatment(Zou et al., 2006).

An interesting phenomenon also observed in a 316L stainless steel surface after HCPEB, it is the deformation twinning occurring only in <111> orientated grains, while grains with other orientations show few signs of deformation twinning (Zou et al., 2008), as can be observed in Fig. I. 23 (where the (001) direction is parallel to the beam direction). This indicates that deformation was triggered and it was orientation dependent.
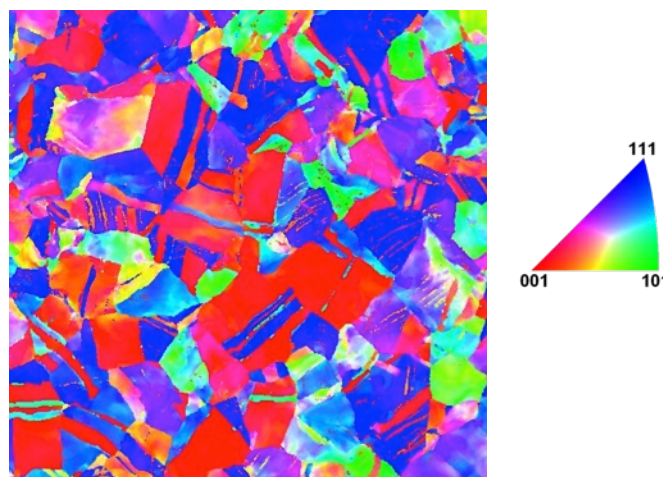
Fig. I. 23: EBSD orientation map of the HCPEB treated 316L sample showing twins within the <111> grains (Zou et al., 2008).

III. 3 **Deep induced-modification effects**

It has been proposed in a simulation work (Qin et al., 2003)that the generation of a stress wave was due to a special sub-layer heating mode. Thus, the HCPEB deep modification effects should be the consequence of stress wave propagation in the sub-layer, because the heat-affected zone is a few tens of micrometers in depth according to the simulations.

The stress affected zone, is usually hardened over depth exceeding several hundred micron (Hao et al., 2005; Proskurovsky et al., 1997; Qin et al., 2004, 2009). For instance, Proskurovsky et al. (Proskurovsky et al., 2000) have examined the in-depth distribution of microhardness for prequenched steel irradiated by HCPEB, as shown in Fig. I. 24. The microhardness pattern shows a clearly wave-like distribution (until about 300 μm), far beyond the depth of melted layer.
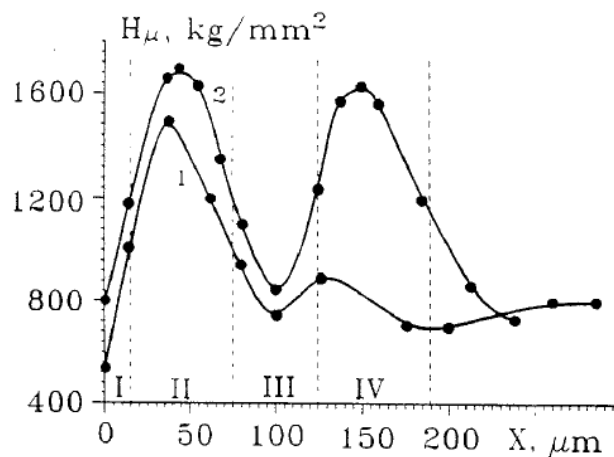
Fig. I. 24: In-depth distribution of microhardness for a prequenched carbon steel 45. (1) 1 pulse (2) 300 pulses (Proskurovsky et al., 2000).

This deep modification effect was also studied by Qin et al.(Qin et al., 2009)in the case of a pure Al (simple metal without any solid-state transition to study the basic material modifications processes). Combining simulation work, they pointed out that the deep modification effect is caused by an intense stress wave originated from sub-layer transmittance of an intense radial stress. Fig. I. 25 shows the harness evolution from the top surface for a pure Al alloy treated with 15 pulses for 20 min and the simulated results of the stress wave propagation. The characteristic wave-like distribution of the hardness within about 1 mm is found (Fig. I. 25a). The simulations results that the stress wave propagated and reversed its polarity during the HCPEB treatment (Fig. I. 25b). The authors reported that this was responsible of the plastic deformation of pure Al, both in twinning and in dislocation modes, giving rise to the surface and sub-surface hardening.
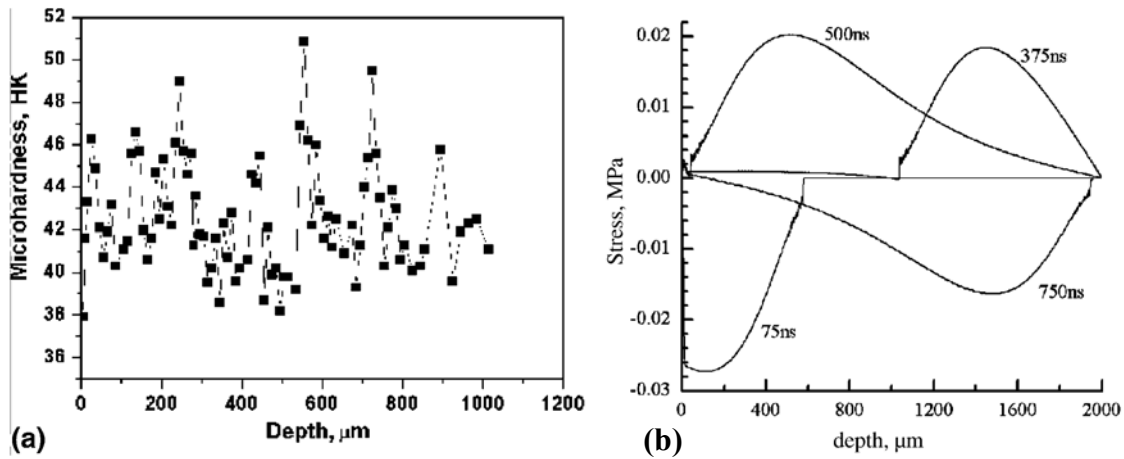
Fig. I. 25: (a) Depth distribution of microhardness on the cross-sections of the Al sample bombarded by HCPEB with 15 pulses for 20 mm. (b) Simulation of the transmission and reflection of the generated thermoelastic stress wave.

Under the melting mode, the microstructure at the sub-surface that did not melt but can be affected over a depth of about 100 μm by the combination of a quasi-static thermal stress and the propagation of a shock wave(Grosdidier et al., 2011; Zou et al., 2009).Fig. I. 26shows cross section information illustrating these effects, which is the cross section micrograph of a D2 steel treated for 20 pulses under 27 keV. It reveals a significant reduction in grain size (zone II) below the melted layer (zone I). The formation of ultra fine equiaxed grains in this zone is the result of combined heavy deformation and recrystallization induced by the drastic thermal stresses.
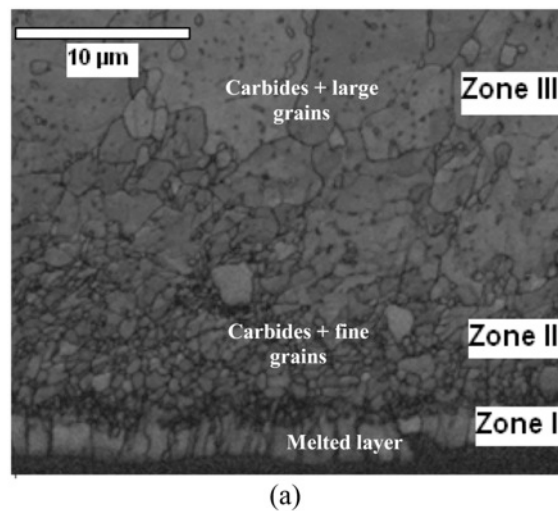
Fig. I. 26: cross section image showing the evolution of microstructure of a D2 steel after 20 pulses(Grosdidier et al., 2011).

IV.   Low Temperature Plasma Nitriding of steels

The surface treatments (SMAT and HCPEB) presented in the previous sections are used as surface activators prior to Plasma Nitriding. Before analyzing the effects of these surface treatments on the diffusion of nitrogen, it is important to describe the mechanisms of the only nitriding process. This part of this chapter contains then general information about the Plasma Nitriding treatment as well as the effects of nitrogen insertion on the microstructure modification and the associated properties of austenitic stainless steels.

IV. 1 The Low Temperature Plasma Nitriding (LTPN) treatment

Austenitic stainless steels are widely used in the chemical and food-processing industries due to its high corrosion resistance, which is based on the presence of a very stable surface oxide layer. However, despite their high resistance corrosion, the application rage of stainless steels is limited, owing to the poor tribological properties. Traditional processes such as gas-nitriding and gas-carburizing can improve hardness and wear properties of stainless steels, but generally, lead to a deterioration of the corrosion resistance, as such processes are typically take part at temperatures above 500 °C (formation of chromium nitrides/carbides).

Nitriding is a thermo-chemical treatment used to enhance the wear, fatigue or the corrosion properties of materials. In comparison with other thermo-chemical treatment, nitriding presents the advantage to modify fairly lightly the shapes and surface state of materials. In addition, it was discovered in the mid-80'es that hard and wear resistant surface layer could be obtained without observing a loss of corrosion resistance when nitriding stainless steel at temperatures below 450° - 550 °C (Zhang and Bell, 1985).The new phase responsible for the favorable properties associated with low-temperature nitriding was designed by several names in the literature: S phase(Ichii et al., 1986), M phase (Marchev et al., 1999), γ_N phase or expanded austenite(Collins et al., 1995). It will be called γ_N in this work. This phase is obtained when high quantities of nitrogen atoms and/or carbon are dissolved in the stainless steel matrix (in solid solution) at temperatures below 450 ° - 550 °C. This causes an expansion of the fcc lattice structure, where the nitrogen atoms reside in the octahedral interstices of the fcc lattice, as shown in Fig. I. 27.
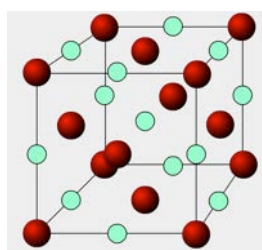
Fig. I. 27: Schematic illustration of an austenitic unit cell showing (in light green) the octahedral interstices.

The formation of this new phase is depicted by experimental technique and essentially and easily by the X-Ray Diffraction (XRD) technique. In the XRD pattern, in addition to γ-phase, a new broadened peak corresponding to the $γ_N$-phase appears at lower angles. This was regularly reported in the literature after low temperature plasma nitriding of an AISI 316L(Mingolo et al., 2006; Stinville et al., 2010; Templier et al., 2010). In the work of Stinville et al for example, after nitriding an AISI 316Lduring 20 min to 160 hours, the XRD patterns shown in Fig. I. 28show that $γ_N$ peaks appear after all the treatment durations. A shift towards low angles and broadening of the peaks appears clearly. In addition as the nitriding duration increases, the shift to lower angles increases too.
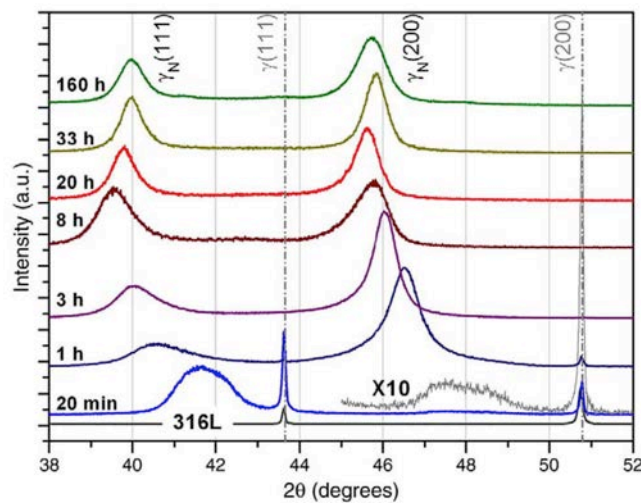
Fig. I. 28: XRD patterns for different nitriding durations. The peaks 316L (γ) and expanded austenite (γN) are indicated for the 111 and the 200 reflections (The low intensity 200$γ_N$ peak for 20 min of nitriding has been multiplied by 10) (Stinville et al., 2010).

The high nitrogen content dissolved in the matrix leads to a noticeable expansion of the lattice, which increases the lattice parameter and gives rise to high compressive residual stresses. In the same work (Stinville et al., 2010), from the position of the $γ_N(111)$ and $γ_N(220)$ positions, the lattice parameter can be determined. The evolution as function of the nitriding duration is presented in Fig. I. 29. Both lattice parameters increase as function of the nitriding durations to reach about 0.39 nm after 8h hours of nitriding, and then remain quite constant up to 160 hours. As there is no possibility for the nitride layer to expand in the direction of the surface, this leads to the formation of high compressive stresses within the nitride layer. This stress effect is traduced in the XRD patterns in form of shift to lower angles of diffraction.
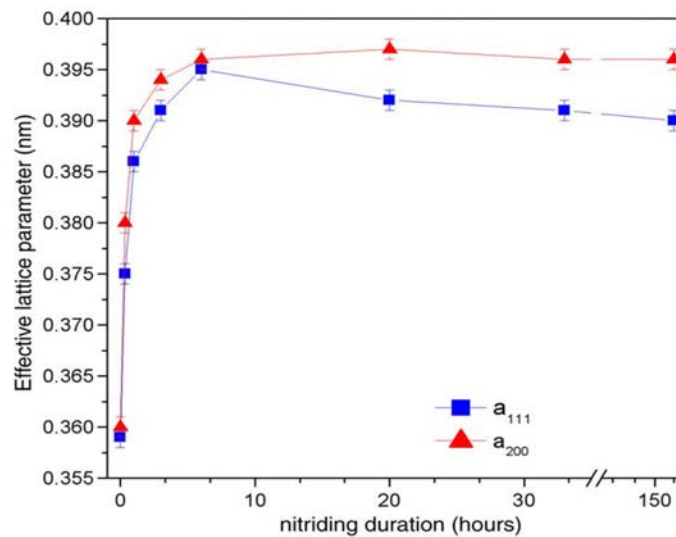
Fig. I. 29: Effective lattice parameter obtained from the 200 and 111 reflections for different nitriding durations (Stinville et al., 2010).

Concerning the peak broadening, it was reported in previous works that the observed asymmetric broadening is an immediate consequence of the range of compositions within the nitrided layer (Christiansen et al., 2010). An example of nitrogen profiles is given in Fig. I. 30a, where it is clearly observed that the N concentration decreases from the top surface towards the material core. Indeed, it was shown that this variation in the chemical composition affects directly the lattice parameter. Christiansen et al. analyzed the evolution of the lattice parameter as function of the contents of interstitial atoms y_N and y_C respectively, which express the number of interstitial atoms N or C per metal atom in the AISI 316Lstainless steel. This evolution is given in Fig. I. 30b. The lattice of expanded austenite expands linearly proportionally with the number of interstitial atoms dissolved. This explains clearly the γ_N-peak broadening.
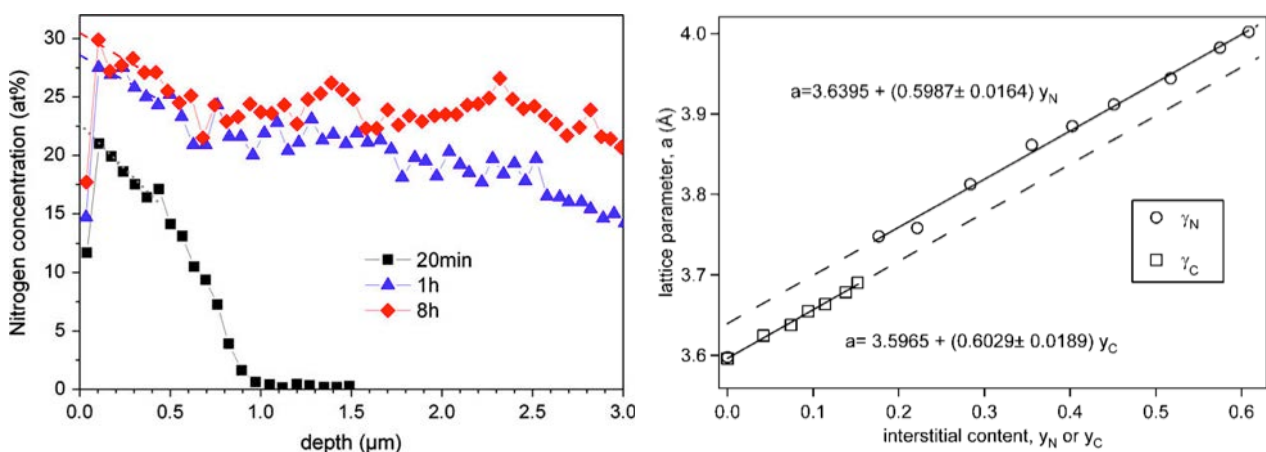
Fig. I. 30: (a) Nitrogen distribution profiles of specimen nitrided at 400 °C for 20 min, 1 h and 8 h (Stinville et al., 2010).
(b) Lattice parameter a of nitrogen stabilized and carbon stabilized expanded austenite (c_N and c_C respectively) as a function of number of interstitial atoms N or C per metal atom (y_N or y_C) (Christiansen et al., 2010).

IV. 2 **The modifications of the stainless steels microstructure induced by the Low Temperature Plasma Nitriding (LTPN) process**

IV. 2. 1 The surface morphology modifications

The signature of the plastic deformation induced by the plasma nitriding can be observed directly on the treated surface morphology. This typical morphology was observed after nitriding for 33h of an AISI 316L(Stinville et al., 2010). As shown in Fig. I. 31, different slip bands corresponding to {111} planes sliding have been observed
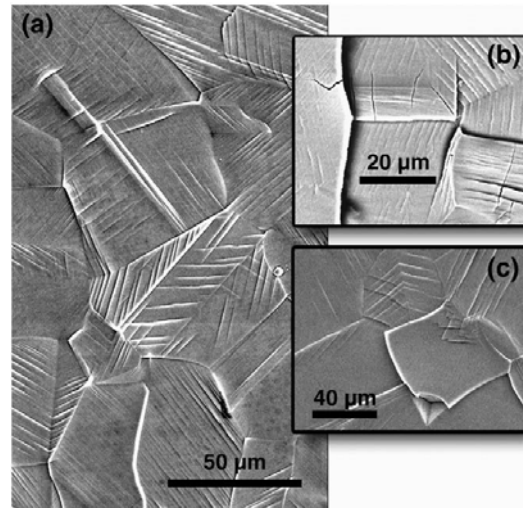
Fig. I. 31:Scanning Electron Microscopy images of the surface after 33 h of nitriding: (a) slip bands are observed in each grain, also (b) some cracks and (c) the beginning of delamination (Stinville et al., 2010).

Fig. I. 31a shows the topography of the surface where one system of slip bands is observed to be predominant for most of the grains with few traces probably corresponding to another system. In addition, some damage in form of very small cracks appears preferentially near the grain boundaries (Fig. I. 31b). This surface damage can be sufficient to favor the loss of some grains by delamination as shown in Fig. I. 31c. This morphology was related to the compressive stress induced by the lattice expansion after nitrogen insertion(Stinville et al., 2010).

In addition to this characteristic surface morphology, the nitriding process induced re-texturing of the surface microstructure, which depends on the initial orientation of grains. This is illustrated in Fig. I. 32, which shows the EBSD mapping of the same zone before and after nitriding for 8h(Stinville et al., 2010). The given orientation is corresponding to the colors triangle where <001> is parallel to the normal direction to the surface. It is observed that the grains morphology remains identical while the crystallographic texture is changed. It is clearly observed that the after nitriding, the initial <101> texture is softened, and <111>and <001> are strengthened (Fig. I. 32b and d).
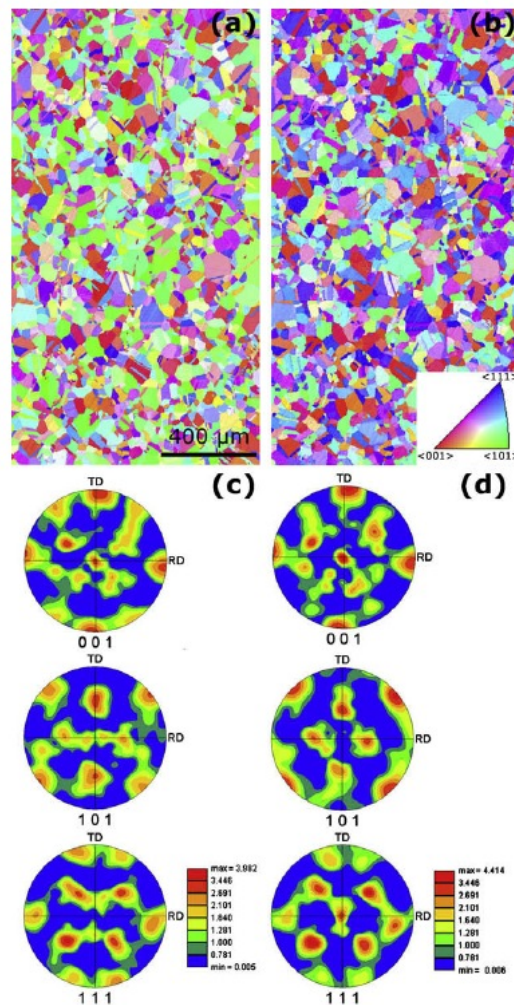
Fig. I. 32: EBSD maps showing the orientation according to the surface normal before nitriding (a) and after nitriding for 8 h at 400 C (b). The colour code is presented by the associated standard inverse pole figure. Corresponding {0 0 1}, {1 0 1} and {1 11} pole figures illustrating the texture before (c) and after (d) 8 h of nitriding. In these figures the red and blue colours correspond to maximum and minimum ODF values, respectively (Stinville et al., 2010b).

To better illustrate this surface texturing after nitriding, the Inverse Pole Figure (IPF) was used (Stinville et al., 2010), as shown in Fig. I. 33. It presents the evolution of the orientation for the different grains presented in the EBSD map. The black dot represents the orientation before nitriding and the black line indicates its orientation evolution after the treatment. From this figure, considering the subdivision of the IPF into several regions, three types of the lattice re-orientation can be depicted:

1. Grains oriented initially within the domain <111> - <101> are re-oriented towards the <111> direction (region 1).

2. Initial grains "half-way" between the <001> and the <111> orientations present a re-orientation towards the <001> - <111> line (region 2).

3. Initial grains oriented close to the <001> direction are re-oriented quite towards the same direction (region 3).
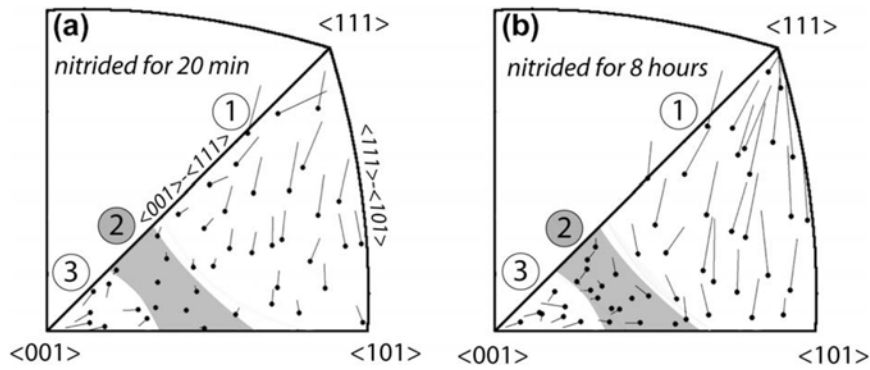
Fig. I. 33: ND inverse pole figure showing the evolution of the orientation of some grains before and after 8 h of nitriding. The ND inverse pole figure is subdivided into 3 regions with different main trends. Initial orientations are marked as black dots and the end of a line gives the re-orientation after nitriding(Stinville et al., 2010).

The authors explained this re-orientation of the nitrided regions of the grains by the huge compressive stresses that are induced when the incorporated nitrogen atoms distend the lattice of the initial austenitic grains.

IV. 2. 2 The-cross section microstructure evolution

In addition to the changes occurred on the top treated surface, the in-depth microstructure is also modified. As described in the beginning of this section, the plasma nitriding leads to the formation of the new phase γ_N. This phase is formed on the surface of stainless steels in form of a layer, where the thickness changes as function of the nitriding conditions. Several previous works studied the evolution of this layer as function of the treatment duration and temperatures. After nitriding of an AISI 316Lunder 430 °C for different durations, cross-sections of the nitrided samples were observed (Fossati et al., 2006), as shown in Fig. I. 34. The nitrided layers appear clearly in the case of both nitrided samples. The white line separating the nitrided layer and the matrix was due to the etching. It is also observed that increasing the nitriding duration results clearly in an increase of the nitride depths.
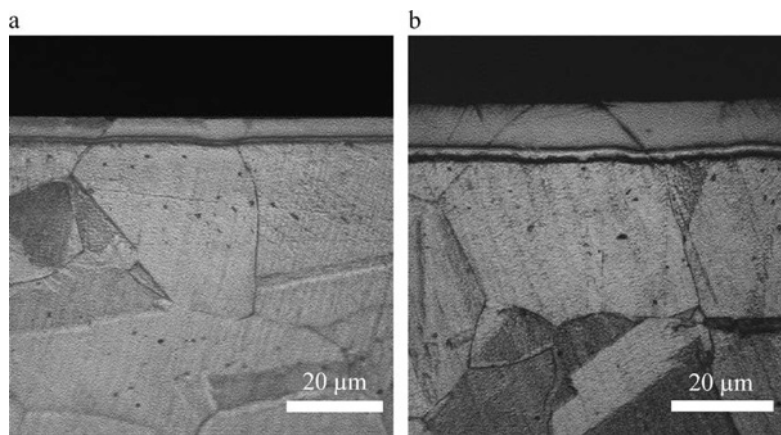
Fig. I. 34: Microstructure of the modified layers formed on the AISI 316L austenitic stainless steel samples by glow-discharge nitriding treatment at 430 °C for (a) 2 hand (b) 5 hours(Fossati et al., 2006).

The influence of the nitriding temperature was also investigated. In the work of Borgioli et al. (Borgioli et al., 2005), the evolution of the nitrided layer thickness as function of the treatment temperature was studied. As shown in Fig. I. 35, the nitrided layer thickness consists of the γ_N-phase, and increases as the temperature of nitriding increases from 400 to 470 °C. However, as the nitriding temperature increases, chromium and iron nitrides are detected in the layer, which may deteriorate the corrosion resistance of the stainless alloy. In the present work, our treatments are carried out at low temperature (350 °C) to avoid this phenomenon.
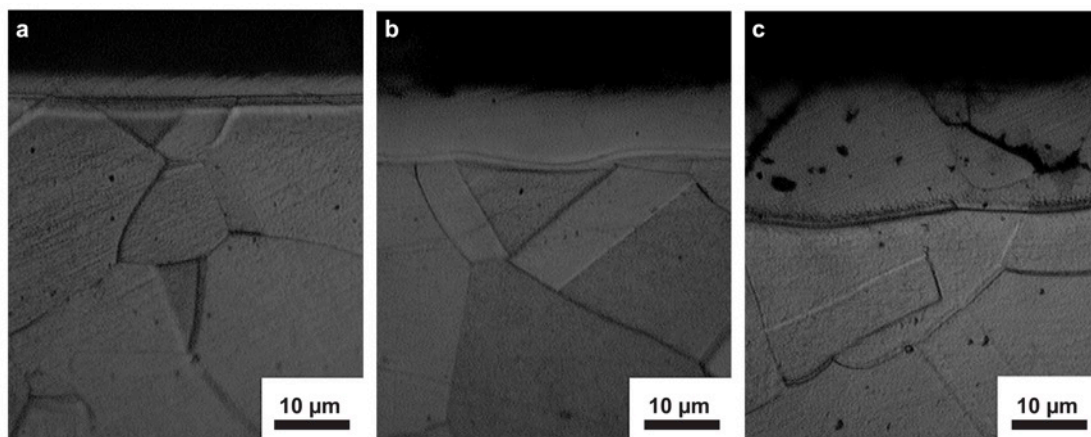
Fig. I. 35: Micrographs of the modified layer of the AISI 316L samples nitrided at (a) 400, (b) 430, and (c) 470°C(Borgioli et al., 2005).

In addition in to the increase of the nitrided layer thickness with the treatment duration and temperature, the crystallographic structure and misorientation inside the γ_N-layer was modified. It has been demonstrated by EBSD measurement that, in addition to the lattice expansion, the nitrogen incorporation into the AISI 316L matrix induces significant lattice rotations inside the nitrided layer(Templier et al., 2010). In Fig. I. 36, a quite linear depth-dependent lattice rotation is observed.

This misorientation reaches a maximum close to the treated surface where the nitrogen content is maximum, then decreases close to the interface with the matrix (γ-phase).
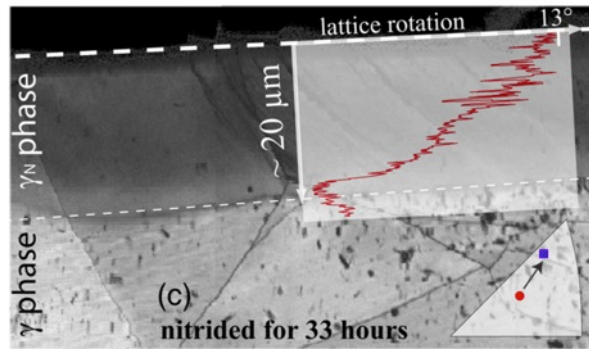
Fig. I. 36: The gradient of the misorientation across then nitrided zone of an AISI 316L after 33 h of nitriding, where the bold white dashed line indicates the surface (the red circle and the blue square in the insert ND inverse pole figure indicate the orientation of the non-nitrided and nitrided region of the grain, respectively)(Templier et al., 2010).

Asgari et al also observed this phenomenon after Pulsed Plasma Nitriding (PPN) of an ASIS 316L (Asgari et al., 2011). EBSD examination of the nitrided layer showed a high amount of plasticity induced in the layer during its formation. The evolution of the maximum of misorientation angle and the nitrogen content as function of the distance from the surface is presented in Fig. I. 37. It is observed in this figure that the misorientation reaches a maximum of about 11 ° at the top nitrided layer and decreases to almost nullify in the un-nitrided zone.
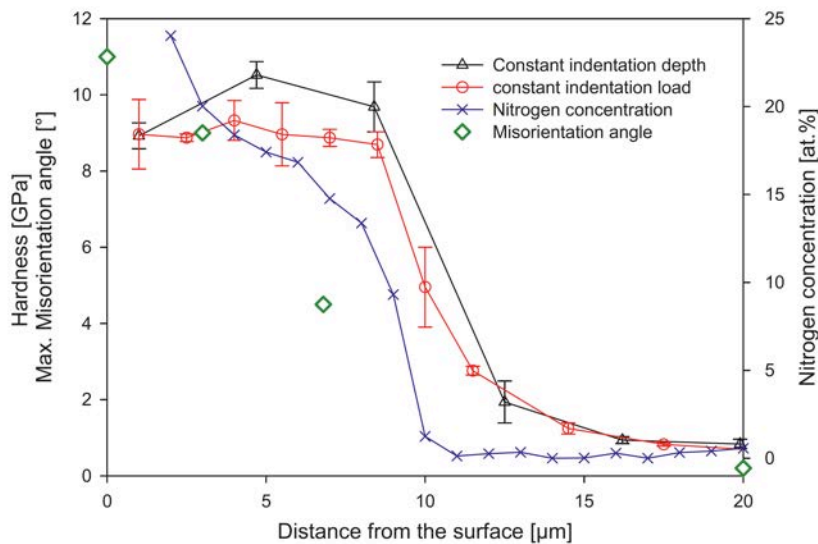
Fig. I. 37: Nitrogen atomic concentration, hardness and change in misorientation angle of the S-phase layer across the depth of the layer after PPN treatment (Asgari et al., 2011).

To understand the effect of grain rotation on nitrogen transport, Martinavičius et al. also have investigated nitriding of a single crystalline AISI 316L with three different crystalline orientations

(Martinavičius et al., 2009).After nitriding at 400 °C, the nitrogen penetration depth depends significantly on the crystalline orientation, with the highest penetration depth for (001) orientation.

These cited results show then that the steel crystallographic orientation can affects directly the nitrogen diffusion, and thereby the thickness of the nitrided layer. In addition, a correlation was found between the nitrogen content and the induced misorientation.

IV. 3   Hardness evolution after plasma nitriding of austenitic stainless steels

Plasma nitriding is commonly used to increase the materials hardness and wear resistance without reducing the good corrosion resistance of stainless steels. The microstructure modifications and induced-defects shown in the previous section are responsible of these enhancements. Several works carried out investigations on the evolution of the mechanical properties of stainless steels after plasma nitriding.

Typical profile of the hardness profile after plasma nitriding of an AISI F51 duplex stainless steel is given in Fig. I. 38(Pinedo et al., 2013).The material was nitrided at 400°C for 20 hours in in a 75% N_2 + 25% H_2 atmosphere. The hardness reaches about 1000 HV near the top nitrided surface, almost 5 times more than the initial hardness (200 HV). This enhancement was attributed to nitrogen super-saturation built-up in the expanded phases.
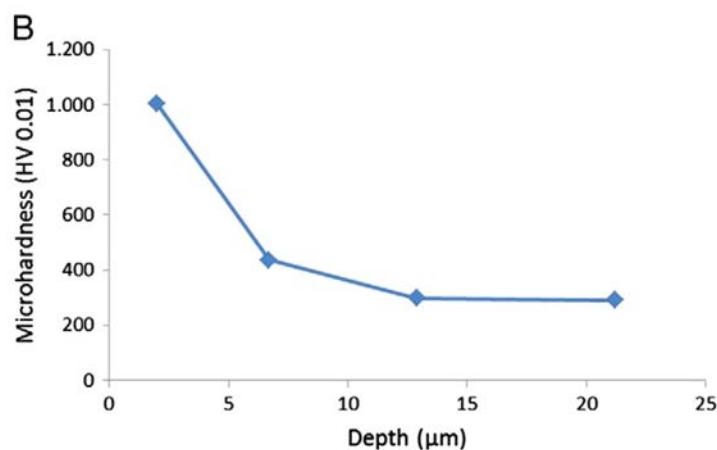
Fig. I. 38: Variation of microhardness of a plasma nitrided AISI F51 duplex as a function of the depth from the surface(Pinedo et al., 2013).

It was also found that surface hardness of nitrided samples is time and temperature dependent(Wang et al., 2006). After nitriding an AISI 304 under 420 °C for different duration, it was shown that the Microhardness increases with the increase of the nitriding time (Fig. I. 39). The increase in hardness is due to the increase of the nitrided layer thickness and the high nitrogen content in the layer.
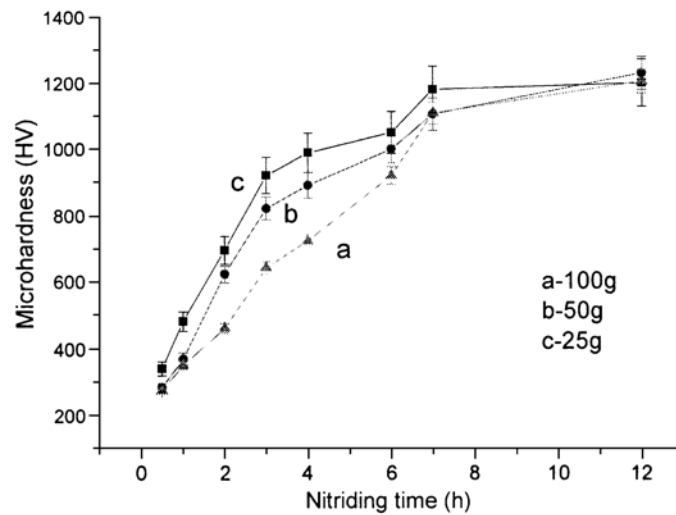
Fig. I. 39: Surface Microhardness of nitrided AISI 304 surfaces vs. processing time(Wang et al., 2006a).

In the work of Jeong et al., as shown in Fig. I. 40, after plasma nitriding of an AISI 316L at the temperatures of 400 and 500 °C for 5 hours, the hardness reaches about 1120 and 1300 HV, respectively(Jeong and Kim, 2001). The variations with pulse frequency showed only small differences. The difference in hardness between the two nitriding temperatures was considered to be related with the kind of the formed layers, where hard iron and chromium nitrides are formed at 500°C.
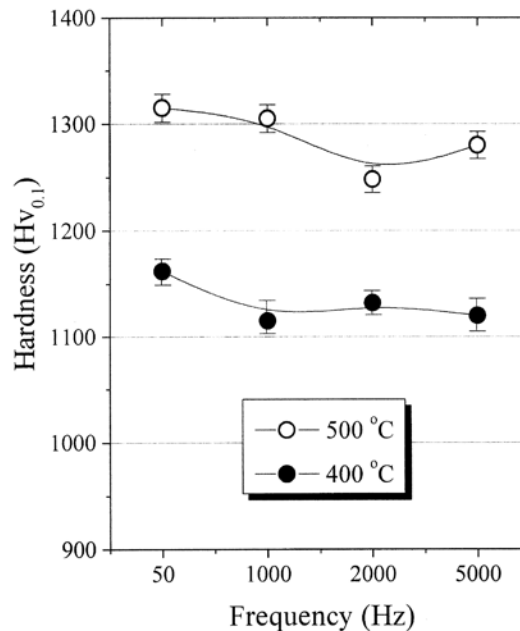
Fig. I. 40: Variation of hardness of plasma nitrided AIS 316 with frequency and temperature(Jeong and Kim, 2001).

V. The use of Severe plastic Deformation techniques as surface activators for improved "Duplex" thermo-mechanical treatments

As mentioned in the introduction of this thesis, the aim of the severe plastic deformation used is to enhance the nitrogen diffusion within the surface of stainless steels. This section contains an overview of the results obtained after nitriding of deformed surfaces by different plastic deformation processes. Firstly, some important results concerning the effects of the Surface Mechanical Attrition Treatment (SMAT) on the nitrogen diffusion will be given. Secondly, the surface activation by shot peening before nitriding is outlined. Finally, treatments such as cold rolling, High-pressure torsion and plastic deformation techniques were also used to activate the surface prior the thermo-chemical treatment and the results are grouped in the last sub-section.

V. 1 The SMAT+nitriding duplex treatment

The Surface Mechanical Attrition Treatment was used in several works in the purpose of accelerating the nitrogen diffusion and also to increase to the surface hardness and wear resistance of materials. Some examples of results obtained in recent works will be given here.

After nanocrystallization of a low-carbon steel by SMAT, Gu et al. showed that the nitriding efficiency of SMAT-ed samples had been significantly improved (Gu et al., 2002).The SMAT was carried out using balls of 2 mm diameter and for 450 s. In this work, as the nitriding temperatures were in the range of 460 to 560 °C, the nitrided layers were composed of γ'-Fe_4N and when under the highest nitriding condition (560 °C for 18 hours), particles of ε-$Fe_{2-3}N$ were also observed. Fig. I. 41 shows the evolution of the thickness of the γ'-layer as function of the nitriding duration, under the three nitriding temperatures(Gu et al., 2002).

(a) (b) (c)
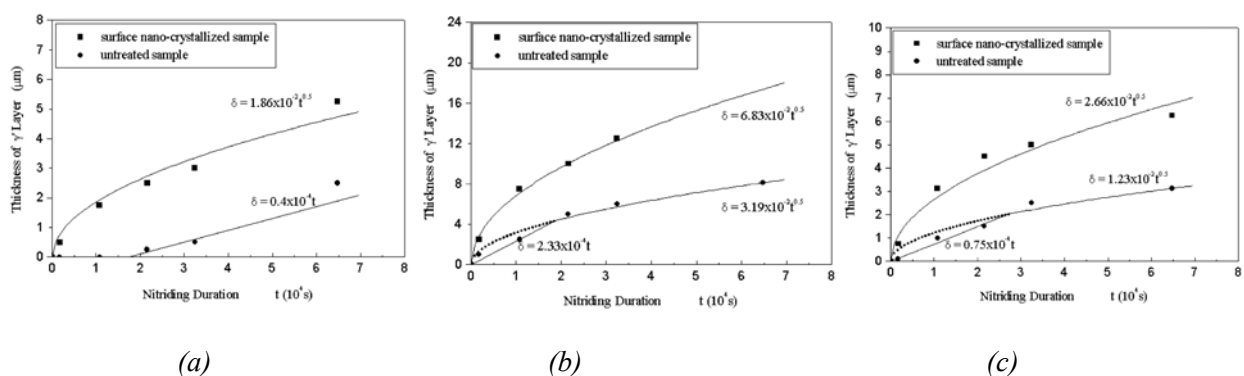
Fig. I. 41: Thickness of the γ' layer as function of the nitriding duration at (a) 460 °C, (b) 500 °C and (c) 560 °C of a low-carbon steel(Gu et al., 2002).

It is clearly observed that undependably of the nitriding temperature, the SMAT process increases significantly the diffusion. The γ'-layer thickness is increased by more than two time when the nitriding is carried out on nanocrystalized surfaces.

Similar effect was found after nitriding of SMAT-ed pure iron (Tong et al., 2007). The samples were treated by SMAT using balls of 8 mm diameter vibrated by a generator with a frequency of 3 kHz and nitrided at 500 °C for 2 hours. Fig. I. 43gives micrographs of the cross section morphologies of the nitrided samples as well as the evolution of the hardness. It is observed that the nitrided layer (arrowed compound layer) is twice thicker in the case of the SMAT+ nitrided sample (Fig. I. 43a) than in the coarse grained one (Fig. I. 43a). In addition, in the zone marked II in Fig. I. 43b, there exists small island-like structures, which was through to be the γ'-Fe_4N precipitates or other nitrides.
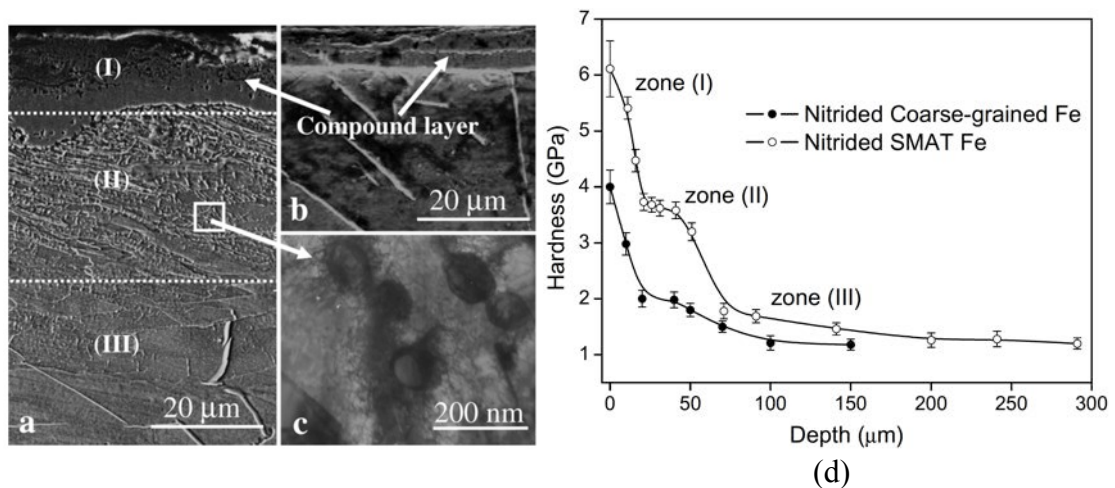
Fig. I. 43: A cross-sectional SEM observation of (a) the SMAT nitrided sample and (b) nitrided coarse-grained sample. (c) A bright-field TEM image of the layer at about 30 μm from the top surface in the nitrided SMAT sample. (d)Hardness variations with depth in the nitrided coarse-grained and SMAT samples(Tong et al., 2007).

This increase of the nitrided layer thickness is accompanied with a significant increase of the surface hardness, as shown in Fig. I. 43c. It can be seen that the hardness of the SMAT-nitrided sample reaches about 6,1 GPa (~ 610 HV), which is higher than that for the only nitrided sample (about 4 GPa - ~ 408 HV). These profiles show also that the hardened layers were about 100μm and 200 μm for the nitrided and SMAT+nitrided samples, respectively. The increase of the extreme surface hardness was attributed to the abundance of very small nitride precipitates, and the subsurface hardness enhancement to the presence of a high density of defects induced by SMAT.

More recently, the combined effect of superficial nanocrystallization by SMAT followed by plasma nitriding on the nitrogen diffusion and surface hardness of an AISI 316L was studied(Chemkhi et al., 2013). The samples were treated by SMAT using 3 mm balls diameter for

30 min, then nitrided at 425 °C for 20 hours. As can be observed in Fig. I. 44a, with respect to the sample only nitrided (marked N425), the preliminary SMAT process decreased the thickness and homogeneity of the nitrided layer (sample SN425). This diminishment was believed to be due to surface oxides, formed during SMAT, that block the nitrogen diffusion. An additional polishing step was then carried out between the SMAT and the nitriding in order to remove this barrier oxide. In the latter condition, thicker and continuous nitrided layer was formed (SPN425), reaching about 40 μm, instead of 26 μm (for the N425).

In addition to the increase of the nitrogen diffusion, the combination of the SMAT and nitriding leads to improved surface hardness(Chemkhi et al., 2013). The evolution of hardness as function of the distance from the top surface is given Fig. I. 44b for the different treated samples. It is observed near the top surface that the hardness of the SMAT+nitrided sample (SN425) is much lower than the only nitrided one. However, when a step of polishing is used between the SMAT and nitriding, the hardness of the SPN425 sample reaches almost the same hardness as the only nitrided one (~1100 HV). In addition the hardened layer in the case of the SPN425 sample is thicker than the SN425 one, which indicated that the nitrided layer of the SPN425 is thicker.

(a)   (b)
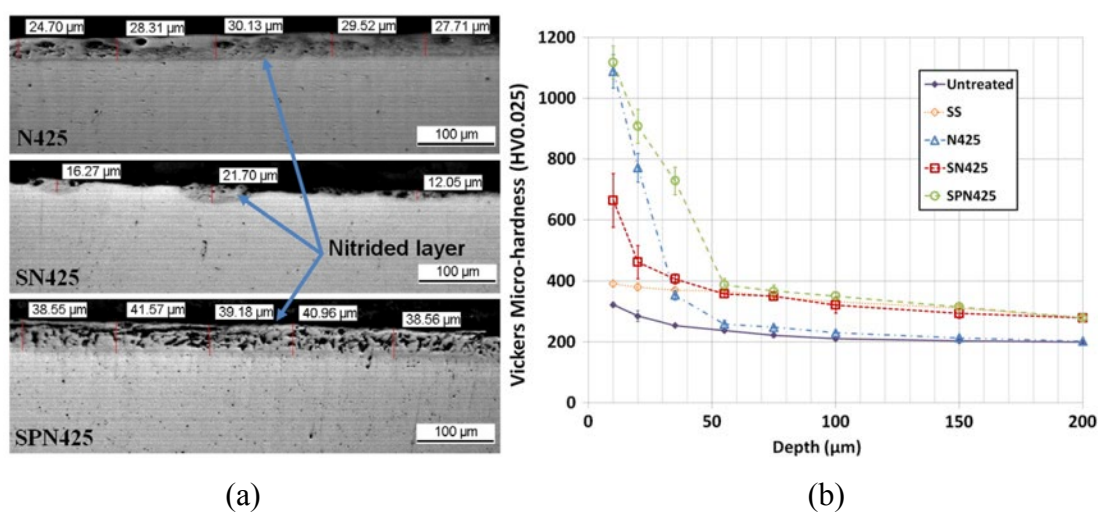
Fig. I. 44: (a) Cross-sectional optical micrographs of an AISI 316Lnitrided (N425), SMAT+ nitrided (SN425) and SMAT+Polished+Nitrided (SPN425) samples. (b) Average cross-sectional Vickers micro-hardness (Chemkhi et al., 2013).

These results illustrate the effect of the SMAT on nitriding of stainless steels. More particularly, despite the formation of small quantities of CrN, the use of SMAT as surface activator, followed by a polishing step, leads to the increase of the nitrided depth.

V. 2   **Other severe plastic deformation techniques used as surface activators**

Beside the SMAT, other plastic deformation techniques were used to activate the surface prior to thermo-chemical treatments. The effect of severe plastic deformation by cold High Pressure Torsion (HPT) on plasma nitriding of different alloys was investigated (Ferkel et al., 2002). Samples in AISI 304 were nitrided for 3 hours at 350 °C after the HPT process. From the SEM observations of the cross section, shown in Fig. I. 45, the HPT (upper right) transforms the initial coarse-grained structure into very fine grained-one. Shear banding is also seen. After nitriding, compared to the initially coarse-grained sample (lower right), the HPT then nitrided sample (lower right) presents thicker nitrided layer. A layer of 2 to 3 μm thickness, two times thicker than the initial nitrided sample, cans be seen. These experimental observations demonstrate that the microstructure of the HPT material does have a significant influence on nitrogen diffusion.
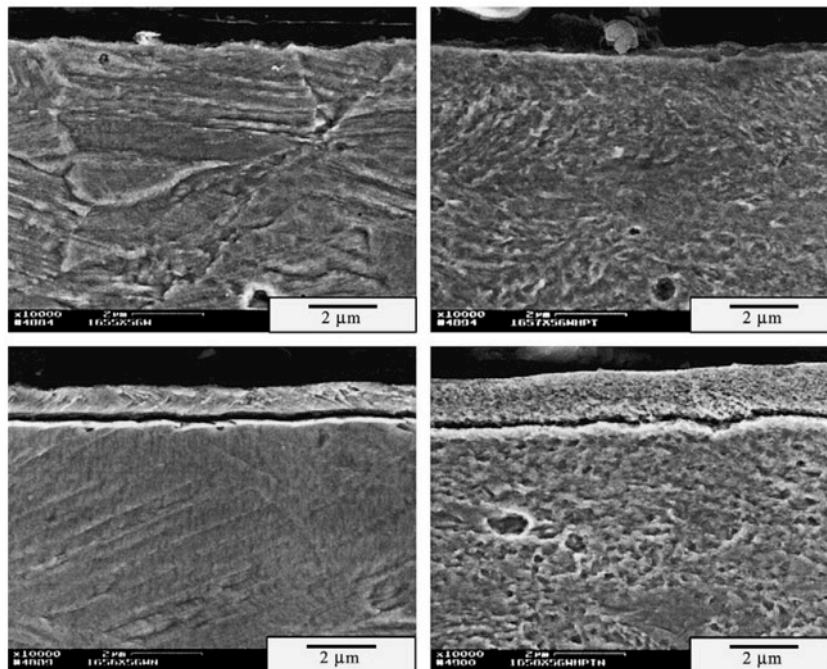
Fig. I. 45: SEM pictures of a section across near surface layer of the AISI 304. Upper part: unprocessed reference material (upper left) and the same material after HPT (upper right). Lower part: material after nitriding only (lower left) and after HPT followed by nitriding (lower right)(Ferkel et al., 2002).

This increase of the nitrided depth on HPT-treated surfaces is associated with a significant increase of the surface hardness(Ferkel et al., 2002). The results are given in Fig. I. 46. These microhardness measurements show that the largest increase is achieved by combining HPT and nitriding, where the hardness reaches about 1400 HV near the top surface then decreases to about 1000 HV with the highest indentation load. The hardness in this one remains higher than the one of the only HPT-treated sample, which is due to the formed nitrided layer.
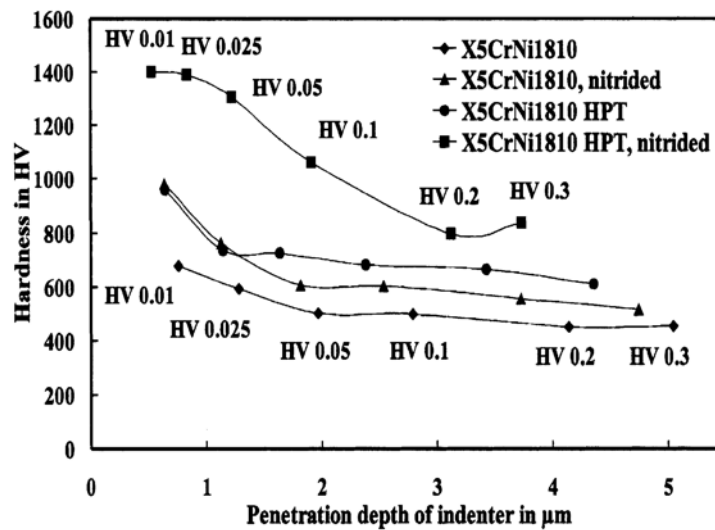
Fig. I. 46: Microhardness of the stainless steel as a function of the residual penetration depth of the indenter. The load used in hardness measurement was increased stepwise starting with the lowest value (HV 0.01) (left symbol on each curve) and going up to the largest one (HV 0.3) (right symbol on each curve)(Ferkel et al., 2002).

Another plastic deformation used as surface activator prior to nitriding is the cold rolling. Egawa et al. have studied the effect of cold forming on low temperature plasma nitriding of austenitic stainless steels(Egawa et al., 2009). AISI 316 and AISI 304 samples were cold-rolled under two different reduction ratios (31 and 62 %) then nitrided at 400 °C (duration not mentioned). The evolution of the nitrided layers morphology is given in Fig. I. 47and the nitrided depth are also indicated in the figure. It is observed that the nitrided layer thickness increases with an increase of the rolling reduction for both alloys. These results are comforted with chemical analysis carried out on the samples surface (as shown in Fig. I. 48). Higher increase of the nitrided layer formed on the surface of the 62% cold-rolled AISI 304 is observed, because of the deformation-induced martensite (bcc structure), characterized by higher diffusion of nitrogen.
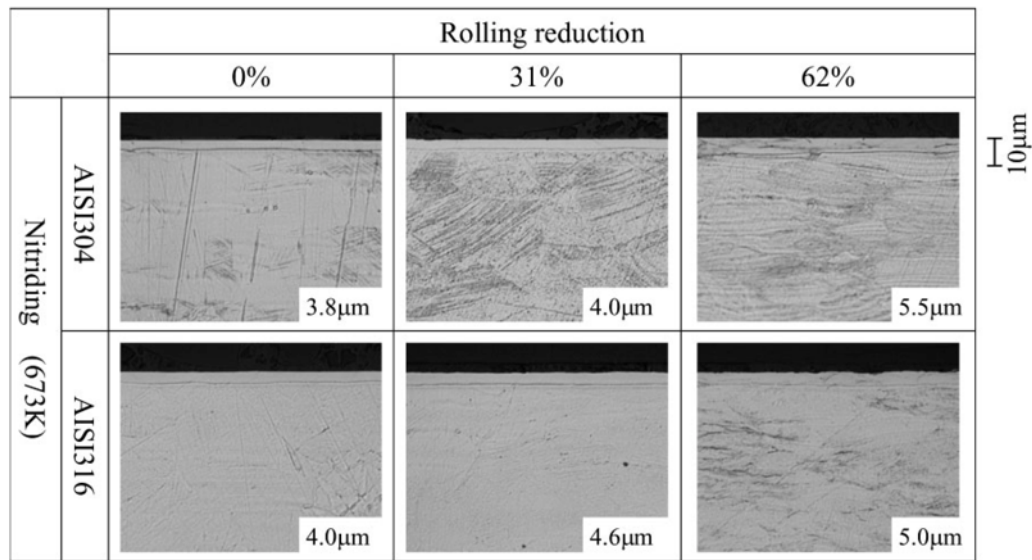
Fig. I. 47: Microstructure of surface layers formed on the AISI 304and AISI 316L and the corresponding nitrided depths as function of the rolling reduction(Egawa et al., 2009).
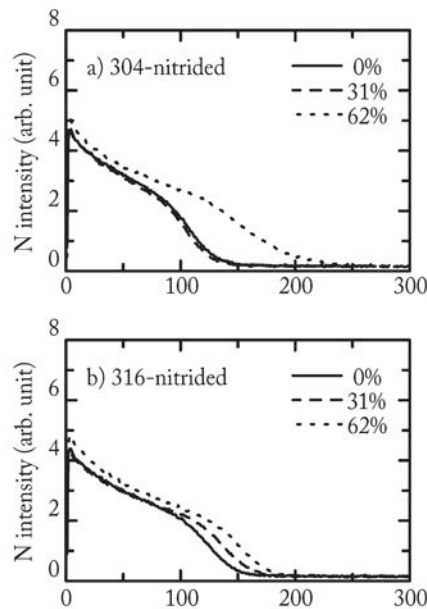
Fig. I. 48: Nitrogen profiles obtained after nitriding the AISI 304 and AISI 316L(Egawa et al., 2009).<

V. 3 Assumptions concerning the enhancement of the thermo-chemical treatment by mechanical treatment activation

The nanostructuration of the treated surfaces by the different presented techniques was generally given as the reason of the nitrogen diffusion enhancement. Indeed, for a nanostructured material of a grain size of about 10 nm, the grain boundaries density is increased by about 30 %(Ji et al., 2005; Suryanarayana and Koch, 2000). These grain boundaries can accelerate the diffusion of chromium for example(Wang et al., 2005) and nitrogen(Tong et al., 2003, 2006). In addition, the

density of triple junctions strongly increases with a decreasing grain size, as they are larger, chromium diffuses more easily (Wang et al., 2003).

In the case of pure iron, the activation energy is two times smaller in the grains boundaries than in the grains, and the nitrogen diffusivity along grain boundaries ($5,4 \cdot 10^{-7}$ cm^{-2}.s^{-1}) is two times more than inside grains ($3,3 \cdot 10^{-7}$ cm^{-2}.s^{-1}) at 300 °C (Tong et al., 2003). These properties can explain the increase of nitrogen diffusion

Further more, the highly deformed microstructure, associated with the introduction of defects and phase transformations, can affect the nitrogen diffusion. In the case of austenitic stainless steels, the plastic deformation may induces phase transformation of the austenite into martensite(Ji et al., 2005; Lin et al., 2006; Lu and Lu, 2004; Zhang et al., 2003). It is also well know that the diffusion coefficient of nitrogen is more important in the martensite than in the austenite(Ji et al., 2005), even if the solubility of the nitrogen is less in theα-phase than in the γ one. The formed martensite can then lead to an enhancement of the nitrogen transport.

References

Arifvianto, B., Suyitno, Mahardika, M., Dewo, P., Iswanto, P.T., and Salim, U.A. (2011). Effect of surface mechanical attrition treatment (SMAT) on microhardness, surface roughness and wettability of AISI 316L. Mater. Chem. Phys. *125*, 418–426.

Asgari, M., Barnoush, A., Johnsen, R., and Hoel, R. (2011). Microstructural characterization of pulsed plasma nitrided 316L stainless steel. Mater. Sci. Eng. -Struct. Mater. Prop. Microstruct. Process. *529*, 425–434.

Bagheri, S., and Guagliano, M. (2009). Review of shot peening processes to obtain nanocrystalline surfaces in metal alloys. Surf. Eng. *25*, 3–14.

Borgioli, F., Fossati, A., Galvanetto, E., and Bacci, T. (2005). Glow-discharge nitriding of AISI 316L austenitic stainless steel: influence of treatment temperature. Surf. Coat. Technol. *200*, 2474–2480.

Chemkhi, M., Retraint, D., Roos, A., Garnier, C., Waltz, L., Demangel, C., and Proust, G. (2013). The effect of surface mechanical attrition treatment on low temperature plasma nitriding of an austenitic stainless steel. Surf. Coat. Technol. *221*, 191–195.

Christiansen, T.L., Hummelshoj, T.S., and Somers, M. a. J. (2010). Expanded austenite, crystallography and residual stress. Surf. Eng. *26*, 242–247.

Collins, G., Hutchings, R., Short, K., Tendys, J., Li, X., and Samandi, M. (1995). Nitriding of Austenitic Stainless-Steel by Plasma Immersion Ion-Implantation. Surf. Coat. Technol. *74-5*, 417–424.

Egawa, M., Matsuda, Y., Ueda, N., Sone, T., Tsujikawa, M., and Nakata, K. (2009). Effect of Cold Forming on Low-Temperature Plasma Nitriding and Carburizing Characteristics of Austenitic Stainless Steel. Plasma Process. Polym. *6*, S893–S896.

Ferkel, H., Glatzer, M., Estrin, Y., and Valiev, R.Z. (2002). RF plasma nitriding of a severely deformed high alloyed steel. Scr. Mater. *46*, 623–628.

Fleischer, R.L. (1967). The flow stress of body-centered cubic metals: inherent lattice hardening or solution hardening? Acta Metall. *15*, 1513–1519.

Fossati, A., Borgioli, F., Galvanetto, E., and Bacci, T. (2006). Glow-discharge nitriding of AISI 316L austenitic stainless steel: influence of treatment time. Surf. Coat. Technol. *200*, 3511–3517.

Gao, B., Hao, S., Zou, J., Wu, W., Tu, G., and Dong, C. (2007). Effect of high current pulsed electron beam treatment on surface microstructure and wear and corrosion resistance of an AZ91HP magnesium alloy. Surf. Coat. Technol. *201*, 6297–6303.

Grosdidier, T., Zou, J., Ji, G., Zhang, K., Zhang, X., Hao, S., and Dong, C. (2007). Modifications of surface microstructure and properties induced by high current pulsed electron beam (HCPEB) treatments of intermetallics. In Advanced Intermetallic-Based Alloys, J. Wiezorek, C.L. Fu, M. Takeyama, D. Morris, and H. Clemens, eds. (Warrendale: Materials Research Society), pp. 51–56.

Grosdidier, T., Zou, J.X., Stein, N., Boulanger, C., Hao, S.Z., and Dong, C. (2008). Texture modification, grain refinement and improved hardness/corrosion balance of a FeAl alloy by pulsed electron beam surface treatment in the "heating mode."Scr. Mater. *58*, 1058–1061.

Grosdidier, T., Samih, Y., Allain-Bonasso, N., Bolle, B., Zou, Z.X., Quin, Y., Hao, S.Z., and Dong, C. (2011). Grain Refinement and Hardening Induced by Heavy Deformation using Low Energy High Current Pulsed Electron Beam Surface Treatment. In Nanomaterials by Severe Plastic Deformation: Nanospd5, Pts 1 and 2, J.T. Wang, R.B. Figueiredo, and T.G. Langdon, eds. (Stafa-Zurich: Trans Tech Publications Ltd), pp. 499–504.

Gu, J.F., Bei, D.H., Pan, J.S., Lu, J., and Lu, K. (2002). Improved nitrogen transport in surface nanocrystallized low-carbon steels during gaseous nitridation. Mater. Lett. *55*, 340–343.

Guan, Q.F., Zou, H., Zou, G.T., Wu, A.M., Hao, S.Z., Zou, J.X., Qin, Y., Dong, C., and Zhang, Q.Y. (2005). Surface nanostructure and amorphous state of a low carbon steel induced by high-current pulsed electron beam. Surf. Coat. Technol. *196*, 145–149.

Hao, S., Yao, S., Guan, J., Wu, A., Zhong, P., and Dong, C. (2001). Surface treatment of aluminum by high current pulsed electron beam. Curr. Appl. Phys. *1*, 203–208.

Hao, S.Z., Gao, B., Wu, A.M., Zou, J.X., Qin, Y., Dong, C., and Guan, Q.F. (2005). Surface modification of steels and magnesium alloy by high current pulsed electron beam. Nucl. Instrum. Methods Phys. Res. Sect. B-Beam Interact. Mater. At. *240*, 646–652.

Hughes, D.. (2001). Microstructure evolution, slip patterns and flow stress. Mater. Sci. Eng. A *319–321*, 46–54.

Hughes, D.A., and Hansen, N. (1995). High angle boundaries and orientation distributions at large strains. Scr. Metall. Mater. *33*, 315–321.

Hughes, D.A., and Hansen, N. (1997). High angle boundaries formed by grain subdivision mechanisms. Acta Mater. *45*, 3871–3886.

Ichii, K., Fujimura, K., and Takase, T. (1986). Structure of the ion-nitrided layer of 18-8 stainless steel. Technol Rep Kansai Univ 135–144.

Ivanov, Y., Matz, W., Rotshtein, V., Gunzel, R., and Shevchenko, N. (2002a). Pulsed electron-beam melting of high-speed steel: structural phase transformations and wear resistance. Surf. Coat. Technol. *150*, 188–198.

Ivanov, Y., Matz, W., Rotshtein, V., Guenzel, R., and Shevchenko, N. (2002b). Enhanced wear resistance of high-speed steel by pulsed electron-beam melting (Chengdu: Southwest Jiaotong Univ Press).

Jeong, B.-Y., and Kim, M.-H. (2001). Effects of pulse frequency and temperature on the nitride layer and surface characteristics of plasma nitrided stainless steel. Surf. Coat. Technol. *137*, 249–254.

Ji, S.J., Wang, L., Sun, J.C., and Hei, Z.K. (2005). The effects of severe surface deformation on plasma nitriding of austenitic stainless steel. Surf. Coat. Technol. *195*, 81–84.

Lin, Y., Lu, J., Wang, L., Xu, T., and Xue, Q. (2006). Surface nanocrystallization by surface mechanical attrition treatment and its effect on structure and properties of plasma nitrided AISI 321 stainless steel. Acta Mater. *54*, 5599–5605.

Liu, G., Lu, J., and Lu, K. (2000). Surface nanocrystallization of 316L stainless steel induced by ultrasonic shot peening. Mater. Sci. Eng. A *286*, 91–95.

Lu, K., and Lu, J. (2004). Nanostructured surface layer on metallic materials induced by surface mechanical attrition treatment. Mater. Sci. Eng. -Struct. Mater. Prop. Microstruct. Process. *375*, 38–45.

Lu, A., Zhang, Y., Li, Y., and Liu, G. (2006). Effect of nanocrystalline and twin boundaries on corrosion behavior of 316l stainless steel using smat. Acta Metall. Sin. Engl. Lett. *19*, 183–189.

Marchev, K., Landis, M., Vallerio, R., Cooper, C.V., and Giessen, B.C. (1999). The m phase layer on ion nitrided austenitic stainless steel (III): an epitaxial relationship between the m phase and the γ parent phase and a review of structural identifications of this phase. Surf. Coat. Technol. *116–119*, 184–188.

Martinavičius, A., Abrasonis, G., Möller, W., Templier, C., Rivière, J.P., Declémy, A., and Chumlyakov, Y. (2009). Anisotropic ion-enhanced diffusion during ion nitriding of single crystalline austenitic stainless steel. J. Appl. Phys. *105*, 093502.

Mingolo, N., Tschiptschin, A.P., and Pinedo, C.E. (2006). On the formation of expanded austenite during plasma nitriding of an AISI 316L austenitic stainless steel. Surf. Coat. Technol. *201*, 4215–4218.

Panicaud, B., Retraint, D., Grosseau-Poussard, J.-L., Li, L., Guérain, M., Goudeau, P., Tamura, N., and Kunz, M. (2012). Experimental and numerical study of the effects of a nanocrystallisation treatment on high-temperature oxidation of a zirconium alloy. Corros. Sci. *60*, 224–230.

Pinedo, C.E., Varela, L.B., and Tschiptschin, A.P. (2013). Low-temperature plasma nitriding of AISI F51 duplex stainless steel. Surf. Coat. Technol. *232*, 839–843.

Proskurovsky, D.I., Rotshtein, V.P., and Ozur, G.E. (1997). Use of low-energy, high-current electron beams for surface treatment of materials. Surf. Coat. Technol. *96*, 117–122.

Proskurovsky, D.I., Rotshtein, V.P., Ozur, G.E., Markov, A.B., Nazarov, D.S., Shulov, V.A., Ivanov, Y.F., and Buchheit, R.G. (1998). Pulsed electron-beam technology for surface modification of metallic materials. J. Vac. Sci. Technol. -Vac. Surf. Films *16*, 2480–2488.

Proskurovsky, D.I., Rotshtein, V.P., Ozur, G.E., Ivanov, Y.F., and Markov, A.B. (2000). Physical foundations for surface treatment of materials with low energy, high current electron beams. Surf. Coat. Technol. *125*, 49–56.

Qin, Y., Dong, C., Wang, X.G., Hao, S.Z., Wu, A.M., Zou, J.X., and Liu, Y. (2003). Temperature profile and crater formation induced in high-current pulsed electron beam processing. J. Vac. Sci. Technol. A *21*, 1934–1938.

Qin, Y., Zou, J.X., Dong, C., Wang, X.G., Wu, A.M., Liu, Y., Hao, S.Z., and Guan, Q.F. (2004). Temperature-stress fields and related phenomena induced by a high current pulsed electron beam. Nucl. Instrum. Methods Phys. Res. Sect. B-Beam Interact. Mater. At. *225*, 544–554.

Qin, Y., Dong, C., Song, Z., Hao, S., Me, X., Li, J., Wang, X., Zou, J., and Grosdidier, T. (2009). Deep Modification of materials by thermal stress wave generated by irradiation of high-current pulsed electron beams. J. Vac. Sci. Technol. A *27*, 430–435.

Roland, T., Retraint, D., Lu, K., and Lu, J. (2006). Fatigue life improvement through surface nanostructuring of stainless steel by means of surface mechanical attrition treatment. Scr. Mater. *54*, 1949–1954.

Roland, T., Retraint, D., Lu, K., and Lu, J. (2007). Enhanced mechanical behavior of a nanocrystallised stainless steel and its thermal stability. Mater. Sci. Eng. A *445–446*, 281–288.

Rotshtein, V.P., Proskurovsky, D.I., Ozur, G.E., Ivanov, Y.F., and Markov, A.B. (2004a). Surface modification and alloying of metallic materials with low-energy high-current electron beams. Surf. Coat. Technol. *180*, 377–381.

Rotshtein, V.P., Ivanov, Y.F., Proskurovsky, D.I., Karlik, K.V., Shulepov, I.A., and Markov, A.B. (2004b). Microstructure of the near-surface layers of austenitic stainless steels irradiated with a low-energy, high-current electron beam. Surf. Coat. Technol. *180*, 382–386.

Rotshtein, V.P., Ivanov, Y.F., Markov, A.B., Proskurovsky, D.I., Karlik, K.V., Oskomov, K.V., Uglov, B.V., Kuleshov, A.K., Novitskaya, M.V.F., Dub, S.N., et al. (2006). Surface alloying of stainless steel 316 with copper using pulsed electron-beam melting of film-substrate system. Surf. Coat. Technol. *200*, 6378–6383.

Stinville, J.C., Villechaise, P., Templier, C., Riviere, J.P., and Drouet, M. (2010a). Plasma nitriding of 316L austenitic stainless steel: Experimental investigation of fatigue life and surface evolution. Surf. Coat. Technol. *204*, 1947–1951.

Stinville, J.C., Villechaise, P., Templier, C., Rivière, J.P., and Drouet, M. (2010b). Lattice rotation induced by plasma nitriding in a 316L polycrystalline stainless steel. Acta Mater. *58*, 2814–2821.

Sun, Y. (2013). Sliding wear behaviour of surface mechanical attrition treated AISI 304 stainless steel. Tribol. Int. *57*, 67–75.

Suryanarayana, C., and Koch, C.C. (2000). Nanocrystalline materials – Current research and future directions. Hyperfine Interact. *130*, 5–44.

Van Swygenhoven, H., Farkas, D., and Caro, A. (2000). Grain-boundary structures in polycrystalline metals at the nanoscale. Phys. Rev. B *62*, 831–838.

Tao, N.R., Zhang, H.W., Lu, H., and Lu, K. (2003). Development of nanostructures in metallic materials with low stacking fault energies during surface mechanical attrition treatment (SMAT). Mater. Trans. *44*, 1919–1925.

Templier, C., Stinville, J.C., Villechaise, P., Renault, P.O., Abrasonis, G., Riviere, J.P., Martinavicius, A., and Drouet, M. (2010). On lattice plane rotation and crystallographic structure of the expanded austenite in plasma nitrided AISI 316L steel. Surf. Coat. Technol. *204*, 2551–2558.

Thomas, B., and Schmitt, J.-H. (2002). Durcissement des aciers - Mécanismes. *M4340*.

Tong, W.P., Tao, N.R., Wang, Z.B., Lu, J., and Lu, K. (2003). Nitriding iron at lower temperatures. Science *299*, 686–688.

Tong, W.P., He, C.S., He, J.C., Zuo, L., Tao, N.R., and Wang, Z.B. (2006). Strongly enhanced nitriding kinetics by means of grain refinement. Appl. Phys. Lett. *89*.

Tong, W.P., Liu, C.Z., Wang, W., Tao, N.R., Wang, Z.B., Zuo, L., and He, J.C. (2007). Gaseous nitriding of iron with a nanostructured surface layer. Scr. Mater. *57*, 533–536.

Waltz, L., Retraint, D., Roos, A., and Olier, P. (2009). Combination of surface nanocrystallization and co-rolling: Creating multilayer nanocrystalline composites. Scr. Mater. *60*, 21–24.

Wang, L., Ji, S., and Sun, J. (2006a). Effect of nitriding time on the nitrided layer of AISI 304 austenitic stainless steel. Surf. Coat. Technol. *200*, 5067–5070.

Wang, Z.B., Tao, N.R., Tong, W.P., Lu, J., and Lu, K. (2003). Diffusion of chromium in nanocrystalline iron produced by means of surface mechanical attrition treatment. Acta Mater. *51*, 4319–4329.

Wang, Z.B., Lu, J., and Lu, K. (2005). Chromizing behaviors of a low carbon steel processed by means of surface mechanical attrition treatment. Acta Mater. *53*, 2081–2089.

Wang, Z.B., Lu, J., and Lu, K. (2006b). Wear and corrosion properties of a low carbon steel processed by means of SMAT followed by lower temperature chromizing treatment. Surf. Coat. Technol. *201*, 2796–2801.

Zhang, Z.L., and Bell, T. (1985). STRUCTURE AND CORROSION RESISTANCE OF PLASMA NITRIDED STAINLESS STEEL. Surf. Eng. *1*, 131–136.

Zhang, H.W., Hei, Z.K., Liu, G., Lu, J., and Lu, K. (2003). Formation of nanostructured surface layer on AISI 304 stainless steel by means of surface mechanical attrition treatment. Acta Mater. *51*, 1871–1881.

Zhang, K.M., Zou, J.X., Grosdidier, T., Gey, N., Weber, S., Yang, D.Z., and Dong, C. (2007). Mechanisms of structural evolutions associated with the high current pulsed electron beam treatment of a NiTi shape memory alloy. J. Vac. Sci. Technol. A *25*, 28–36.

Zou, J.X., Qin, Y., Dong, C., Wang, X.G., Wu, A.M., and Hao, S.Z. (2004a). Numerical simulation of the thermal-mechanical process of high current pulsed electron beam treatment. J. Vac. Sci. Technol. A *22*, 545–552.

Zou, J.X., Wu, A.M., Dong, C., Hao, S.Z., Liu, Z.M., and Ma, H.T. (2004b). Beam treatment oxidation protection of AISI H13 steel by high current pulsed electron. Surf. Coat. Technol. *183*, 261–267.

Zou, J.X., Grosdidier, T., Zhang, K.M., and Dong, C. (2006a). Mechanisms of nanostructure and metastable phase formations in the surface melted layers of a HCPEB-treated D2 steel. Acta Mater. *54*, 5409–5419.

Zou, J.X., Zhang, K., Dong, C., Qin, Y., Hao, S., and Grosdidier, T. (2006b). Selective surface purification via crater eruption under pulsed electron beam irradiation. Appl. Phys. Lett. *89*.

Zou, J.X., Grosdidier, T., Zhang, K.M., Gao, B., Hao, S.Z., and Dong, C. (2007a). Microstructures and phase formations in the surface layer of an AISI D2 steel treated with pulsed electron beam. J. Alloys Compd. *434–435*, 707–709.

Zou, J.X., Grosdidier, T., Bolle, B., Zhang, K.M., and Dong, C. (2007b). Texture and microstructure at the surface of an AISI D2 steel treated by high current pulsed electron beam. Metall. Mater. Trans. -Phys. Metall. Mater. Sci. *38A*, 2061–2071.

Zou, J.X., Zhang, K.M., Grosdidier, T., Dong, C., Qin, Y., Hao, S.Z., and Yang, D.Z. (2008). Orientation-dependent deformation on 316L stainless steel induced by high-current pulsed electron beam irradiation. Mater. Sci. Eng. -Struct. Mater. Prop. Microstruct. Process. *483-84*, 302–305.

Zou, J.X., Grosdidier, T., Zhang, K.M., and Dong, C. (2009). Cross-sectional analysis of the graded microstructure in an AISI D2-steel treated with low energy high-current pulsed electron beam. Appl. Surf. Sci. *255*, 4758–4764.

List of figures

List of tables

Chapter II

The studied materials and characterization techniques

The aim if this chapter is to give a description of the treated materials and the experiments techniques used for the characterization.

In the first part, a review of the microstructure and properties of the studied materials are summarized. Two materials are studied: The AISI 316L (two grades: the 316LM and 316LS) and AISI 660 austenitic stainless steels. The typical microstructure of these materials as well as their mechanical properties are described.

The second part summarizes the techniques used to characterize the evolution of the microstructure, the chemical composition and the associated mechanical properties (hardness and residual stress). A rapid review of the Electron BackScattered Diffraction (EBSD) is given. The procedure of the determination of the Geometrically Necessary Dislocation (GND) is detailed. Then, the residual stress measurement by X-Ray Diffraction is described recalling the basic principles and assumptions. Concerning the chemical composition quantification, the Glow Discharge Emission Optical Spectrometry (GD-OES) principle is presented. Finally, the surface hardness measurement procedure is described.

Summary

I. <u>Materials</u>

I. 1.   **Introduction to the stainless steels**

The stainless steels are a suitable class of alloys for many industrial applications where a high corrosion resistance is required. This resistance is imparted to the alloy by adding at least about 11 wt. % of Chromium. Contrarily to the carbon steels, which corrode rapidly by the formation of an iron oxide film, the amount of Chromium present in stainless steel is sufficient to form a passive film of chromium oxide, blocking the oxygen diffusion to the steel surface. The stainless steels class can be divided into four basic groups based on their crystalline structure: *austenitic*, *ferritic*, *martensitic and Duplex* (Lo, Shek, and Lai 2009). Another group of stainless steels known as *precipitation-hardened* steels are a combination of austenitic and martensitic steels.

1 - The ferritic stainless steels are magnetic non heat-treatable steels that contain chromium but not nickel. They have good heat and corrosion resistance, in particular in sea water, and good resistance to stress-corrosion cracking. Their mechanical properties are not as strong as the austenitic grades, however they have better decorative appeal.

2 - Martensitic grades: Martensitic grades are magnetic and can be heat-treated by quenching and tempering. They contain chromium but usually contain no nickel, except for 2 grades. Martensitic steels are not as corrosive resistant as austenitic or ferritic grades, but their hardness levels are among the highest of the all the stainless steels, due to the high content of carbon in the martensitic stainless steels.

3 - The austenitic stainless steels are non heat-treatable non-magnetic steels that are usually annealed and cold worked. Some austenitic steels tend to become slightly magnetic after cold working. They have excellent corrosion and heat resistance with good mechanical properties over a wide range of temperatures. There are two subclasses of austenitic stainless steels: chromium-nickel and chromium-manganese-low nickel steels. Chromium-nickel steels are the most general widely used steels and are also known as 18-8(Cr-Ni) steels. The chromium nickel ratio can be modified to improve formability; carbon content can be reduced to improve intergranular corrosion resistance. Molybdenum can be added to improve corrosion resistance.

4   - Duplex stainless steel: they have a mixed microstructure of austenite and ferrite, the aim usually being to produce a 50/50 mix, although in commercial alloys the ratio may be 40/60. Duplex stainless steels have roughly twice the strength compared to austenitic stainless steels and also improved resistance to localized corrosion, particularly pitting, crevice corrosion and stress corrosion cracking. They are characterized by high chromium (19–32%) and molybdenum (up to 5%) and lower nickel contents than austenitic stainless steels. The properties of duplex stainless

steels are achieved with an overall lower alloy content than similar-performing super-austenitic grades, making their use cost-effective for many applications. Duplex grades are characterized into groups based on their alloy content and corrosion resistance.

5 - The precipitation-hardened steels (also called age hardening steels) are chromium and nickel containing steels that provide an optimum combination of the properties of martensitic and austenitic grades. Like martensitic grades, they are known for their ability to gain high strength through heat treatment and they also have the corrosion resistance of austenitic stainless steels. The high tensile strengths of precipitation hardening stainless steels come after a heat treatment process that leads to precipitation hardening of a martensitic or austenitic matrix. Hardening is achieved through the addition of one or more of the elements Copper, Aluminum, Titanium, Niobium, and Molybdenum.

In the present study, two alloys are studied: the AISI 316L and the AISI 660 precipitation-hardened stainless steels. The chemical composition and mechanical properties are detailed in the following sections.

I. 2.   The AISI 316L austenitic stainless steels

The AISI 316L austenitic stainless steel is widely used in applications requiring very high corrosion resistance or good elevated temperature strength. Its crystallographic structure is face centered cubic (fcc). It should be noted that this steel could be called differently depending on the designation system: 1.4404 (numerical designation), X2CrNiMo17-12-2 (NF EN 10088-3). In the present work, the designation "AISI 316L" will be used.

Two grades of this steel are treated: a "standard" AISI316L grade, commonly used in the industrial domain, and the AISI316LS an austenitic stainless steel re-sulfurized to a tightly controlled level, in order to provide to the alloy an excellent machinability while retaining a good corrosion resistance. This grade was chosen in the treatment by HCPEB (described in Chapter I) essentially to form higher density of craters before the Plasma Nitriding. The chemical compositions of the two treated grades of AISI 316L are given in Table II. 1.

wt. %											
Fe	C	Mn	Si	S	P	Cr	Ni	Mo	Cu	Co	N
62.724	0.017	1.790	0.380	0,002	0.019	17.430	14.700	2.740	0.160		0.040

(a)

wt. %											
Fe	C	Mn	Si	S	P	Cr	Ni	Mo	Cu	Co	N
68.184	0.020	1.520	0.524	0.028	0.027	16.700	10.140	2.080	0.522	0.203	0.052

(b)

Table II. 1: Chemical composition of (a) the "standard" AISI 316L and (b) the AISI316LS stainless steels.

A notable difference in the Ni contents observed, where the AISI 316L more Ni (14.7 wt.%) than the AISI316LS (10.14 wt.%). Actually, the normalized AISI 316L chemical composition is given within a wide range (10.5 to 15 wt.%). In addition, the AISI 316LS higher cupper content, which enhances the chemical resistance in the corrosive fields.

The mechanical properties of the AISI316L grades, given by the supplier company, are given in Table II. 2.

	Hardness [HV]	Density [g.cm^3]	Tensile strength [MPa]	Yield strength Rp$_{0.2}$ [MPa]	Young's modulus [MPa]
AISI316L	200	7.9	604	331	205
AISI316LS	200	7.9	539	447	206

Table II. 2: The mechanical properties of the two AISI316LSS grades

Prior to all the treatments, the samples are polished mechanically until diamond paste (1 µm) then chemically using Oxide Polishing Suspension (OP-S).

As observed in Fig. II. 1, the initial microstructure of the AISI316L is composed of large austenitic grains with thermal twins. The initial AISI316LS microstructure (Fig. II. 2) presents quite similar morphology, with the presence of Manganese Sulphides (arrowed). A notable difference between these AIS 316L grades can also be seen. Actually, the density Sigma 3 twins ((111)<60°>) -presented in in red lines- is higher in the case of the AISI 316LS.
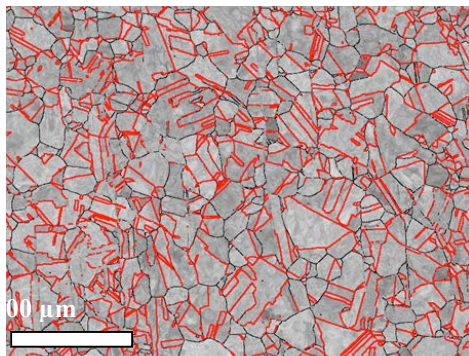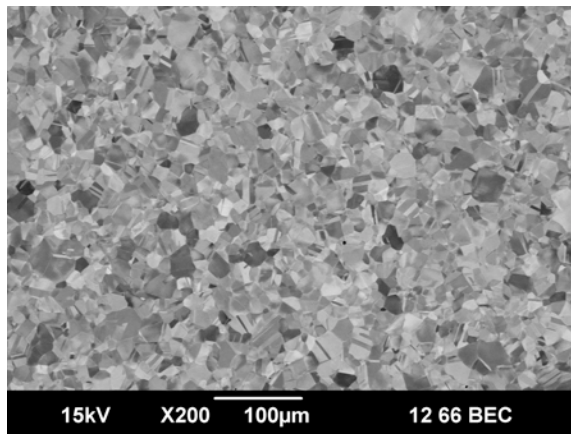
————— Sigma 3 twin boundaries (111) <60°>

Fig. II. 1: SEM image of the AISI 316L initial microstructure and the distribution of the Sigma-3 boundaries (thermal twins).
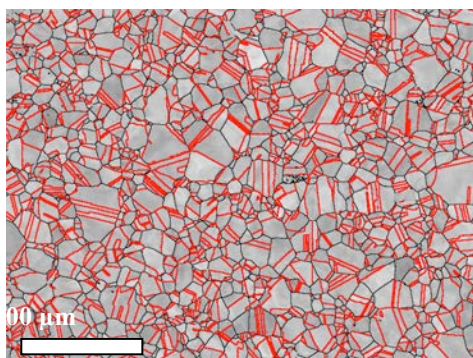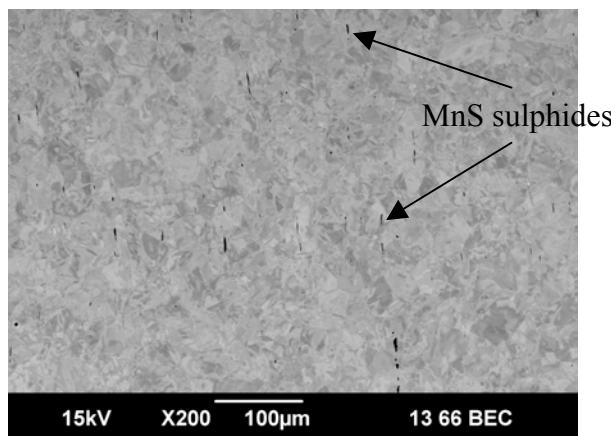
Fig. II. 2: SEM image of the AISI316LS initial microstructure and the distribution of the Sigma-3 boundaries (thermal twins).

————— Sigma 3 twin boundaries (111) <60°>

I. 3.   **The AISI 660 precipitation hardening stainless steel**

In general, the material can be hardened primarily by cold working or quenching and tempering. The stainless steels can also be hardened in a similar way, but an additional strengthening technique exists and called "precipitation hardening" or "age hardening". The strengthening process in this case performed in the following three steps (Muraca and Whittick 1972):

1- Solution treatment: all the precipitates and alloying elements are dissolved (or go into a supersaturated solution) in a relatively high temperature around 600 °C for most of stainless steels.

2- Quenching or cooling: Once the alloy is brought into solution, it is cooled to room temperature. The cooling can be carried out in air, water or oil, but must be done fast enough to obtain a supersaturated solid solution. The material properties can then be improved by creating a finer grain size.

3- Precipitation (or age hardening): The obtained supersaturated solid solution decomposes with temperature or time as the alloying elements form small precipitates clusters. These precipitates are in form of intermetallic phases (such as Ni_3Al, Ni_3Ti, Ni_3Cu). The formation of these clusters acts to significantly strengthen the material. However, prolonged aging causes the coarsening of these intermetallic phases, which can declines the strength, due to the fact that dislocations can bypass coarse intermetallic phases.

In the case of stainless steels, the precipitation-hardening alloys are iron-nickel-chromium alloys, which contain one or more precipitation hardening elements such as titanium, aluminum, niobium, copper and molybdenum. These steels have two main characteristics: high strength and high corrosion resistance, comparable to the standard AISI 304L and 316L austenitic alloys.

There are three types of precipitation-hardening stainless steels (depending on the martensite start and martensite finish temperatures (M_s and M_f) as well as the as-quenched microstructure):

- Martensitic precipitation-hardening stainless steels,
- Semi-austenitic precipitation-hardening stainless steels,
- Austenitic precipitation-hardening stainless steels.

The present work focuses on the last type, and especially the called AISI 660 alloy, which can be found in the literature under the following designations: 1.4980 or A286. This non-magnetic iron-based alloy combines high strength (obtained through solution heat treating and age hardening) and good corrosion resistance for use at temperatures up to 700 °C. It is widely used in the offshore

oil and gas industry where the components are subject to high levels of stress and temperature. The chemical composition and mechanical properties oft his alloy is given in Table II. 3.

Fe	C	Mn	Si	Ti	S	P
Balance	<0.08	<2	<1	1.9-2.35	<0.025	<0.025

Cr	Ni	Mo	Cu	V	Al	B
13.5-16	24-27	1-1.5	<0.5	0.1-0.5	<0.35	0.003-0.008

(a)

	R [MPa]	Re [MPa]	A [%]	Hardness [HV]
AISI660	960-1200	≥ 660	≥ 16	≥ 290-360

(b)

Table II. 3: (a) The AISI 660 chemical composition (in wt. %), (b) the conventional mechanical properties of the AISI 660 ("Properties of the AISI660 Stainless Steel").

The initial microstructure of the AISI 660 is characterized by the presence of large austenitic grains containing thermal twins, as well as the presence of precipitates as it can be observed in the EBSD map given in Fig. II. 3.
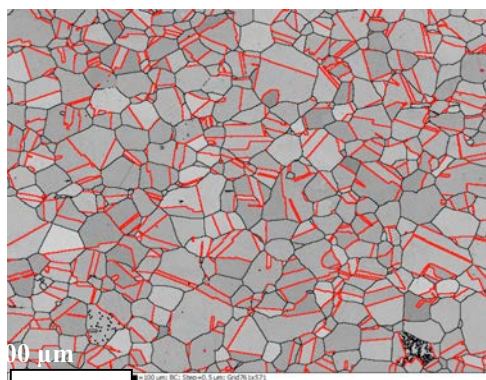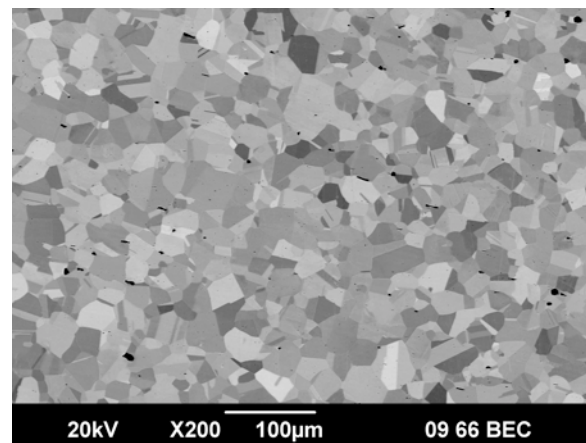
Sigma 3 twin boundaries (111) <60°>

Fig. II. 3: SEM image of the AISI 660 initial microstructure and the distribution of the Sigma-3 boundaries (thermal twins).

II. <u>The characterization techniques</u>

Various techniques of characterization are employed to investigate the surface microstructure, chemical composition as well as the stress state and hardness. These characterization techniques include essentially a Scanning Electron Microscope (SEM) with a Field Emission Gun (FEG), type Jeol-6500F; A Siemens D-5000 X-Ray Diffractometer and also a Glow Discharge-Optical Emission Spectroscopy (GD-OES). The surface hardness is measured using a Vickers hardness machine. The EBSD, GD-OES, residual stress measurement by XRD and hardness are described in the following sections.

II. 1. **The Electron BackScattered Diffraction technique: orientations maps and determination of the Geometrically Necessary Dislocation (GND)**

II. 1. 1. *Principle of the technique*

A scanning Electron Microscope (SEM) is a type of electron microscopes that images the materials surface by scanning it with a high-energy beam of electrons in a raster scan pattern. The SEMs have also an Electron BackScattered Diffraction (EBSD) system that allows combined SEM/EBSD mapping in order to compare the observed microstructure and crystallographic information.

EBSD provides, through the crystal orientation information, the texture measurements, the identification of the different phases present in a material, boundary characterization, and misorientations due to plastic deformation. The development of EBSD can be dated back to 1928, in which year the electron diffraction by mica was first recorded by Kikuchi (Kikuchi 1928). The electron diffraction pattern contains some intersected paralleled line pairs, which were later named Kikuchi bands in honor of Kikuchi. Two years after the presence of the first commercially available SEM, Coates observed pseudo-Kikuchi bands in SEM (Coates 1967). Later in the 1970's, Venables et al. (Venables and Binjaya 1977) advanced the concept of electron backscattered patterns (EBSP), even though the electron backscattered diffraction map was called backscattered Kikuchi map for a long period of time. From 1982 to 1984, the computer-aided indexing of EBSD patterns received much development. In 1991, the Hough transform implement the automated recognition and indexing of EBSD patterns, which has played a critical role for the further development of the EBSD technique. The first commercial EBSD system was available in 1994, named "Orientation Imaging Microscope (OIM^{TM})" or "Automated Crystal Orientation Mapping (ACOM)". In the following years EBSD has become a well-established technique for the SEM, and has gained wide applications in many fields.
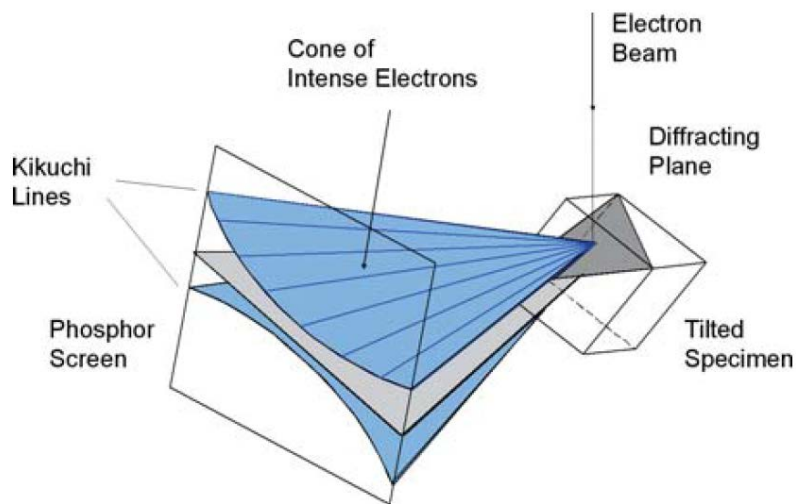
Fig. II. 4: Schematic of diffracting cones with respect to the reflecting plane, the specimen, and the phosphor screen.

The generation of EBSD is a process in which electrons undergo various interactions with the atoms in the crystal lattice and some of the electrons emerge from the sample during the irradiation of electron beam acting on the sample. As illustrated in Fig. II. 4 (Schwarz, Kumar, and Adams 2000), if a fluorescent phosphor screen is placed close to the sample, a pattern of a serial of intersected Kikuchi bands is formed on the screen because of Bragg diffraction. It is worth noting that the angle in relation to the width of Kikuchi band equals to $2\theta_B$, where θ_B stands the Bragg angle. A typical EBSD pattern is shown in Fig. II. 5 (Schwarz, Kumar, and Adams 2000). In the map, every Kikuchi band pattern corresponds to a specific crystal plane, and the point where Kikuchi bands intersected indicates a zone axis. In order to get clear Kikuchi band contrasts, the sample is usually tilted 70°.
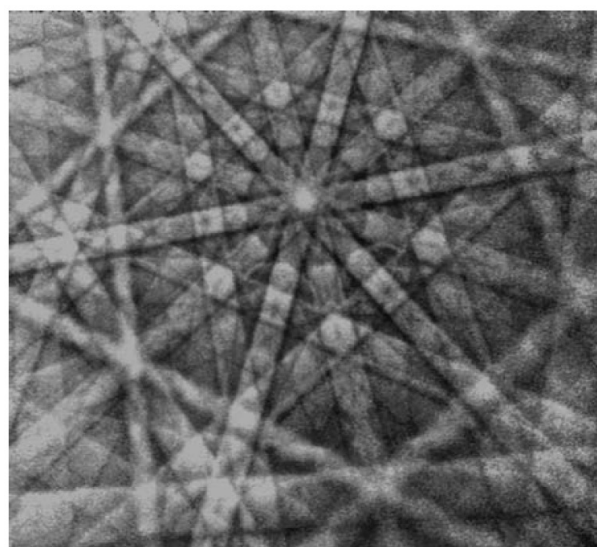
Fig. II. 5: Example of the formed backscatter Kikuchi patterns.

II. 1. 2.   The Geometrically Necessary Dislocation: Calculation using the EBSD data

The use of EBSD technique is for obtaining crystallographic information from samples in the scanning electron microscope. In general, the use of EBSD and automated imaging of crystal orientation can definitively reveal the sample microstructure including grain size, distribution of grain boundary misorientations and special boundaries and their specific locations in the sample. It also gives local misorientations at individual points in a regular grid on a planar surface of the material, as shown in Fig. II. 6 (Schwarz, Kumar, and Adams 2000).
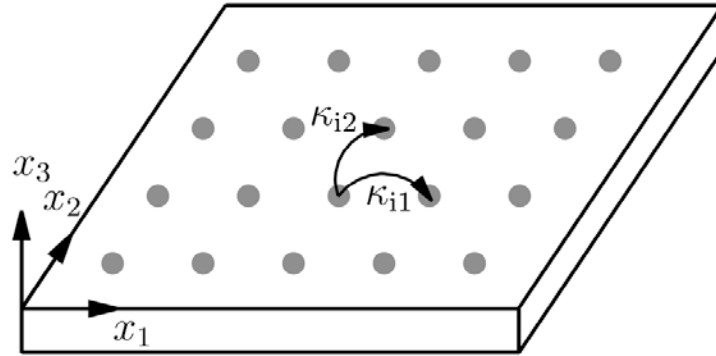
Fig. II. 6: Sketch of the sample coordinate system used for Electron BackScattered Diffraction (EBSD). The local misorientations are calculated at each of the grey points.

Using the differences in orientation between neighboring points, the lattice curvature and (if elastic stresses are not considered) the dislocation density tensor can be calculated. These dislocations are line defects, which cause crystal distortion, described by line vector $\vec{l^t}$ indicating the direction, a Burger vector $\vec{b^t}$, which indicates the displacement and also a position vector $\vec{x^t}$. Nye introduced the local dislocation tensor (Nye 1953), which describes all the dislocations present, using the following equations (Pantleon 2008):

$$\alpha_{ij} = \sum_t b_i^t l_j^t \; \delta \; (\vec{x} - \vec{x^t}) \qquad Eq. \; II. \; 1$$

As shown by Kröner et al. (Kröner 1980), its components ($\alpha_{ik} = -\epsilon_{klj} \frac{\partial \beta_{ij}^{el}}{\partial x_l}$) are determined entirely by the elastic distortion tensor $\beta_{ij}^{el} = \varepsilon_{ij}^{el} + \omega_{ij}$, which is the sum of the elastic strain tensor ε_{ij}^{el} and the lattice rotation tensor ω_{ij}:

$$\omega_{ij} = -\epsilon_{ijk} \theta_k \qquad\qquad Eq. \; II. \; 2$$

The later is given using the lattice rotation vector $\theta_k = -\epsilon_{kij} \frac{\omega_{ij}}{2}$. Introducing curvature tensor:

$$\kappa_{ij} = \frac{\partial \theta_i}{\partial x_j} =: \theta_{ij} \qquad\qquad Eq. \; II. \; 3$$

the dislocation density tensor becomes (Kröner, 1981; Kroner, 1955)

$$\alpha_{ik} = \kappa_{ki} - \delta_{ki}\kappa_{mm} - \epsilon_{klj}\frac{\partial \epsilon^{el}_{ij}}{\partial x_l} \qquad Eq.\ II.\ 4$$

This equation shows that dislocations are related with the heterogeneous lattice rotations. When the elastic strains are assumed absent ($\epsilon^{el}_{ij} \equiv 0$), Eq. II. 4$\alpha_{ik} = \kappa_{ki} - \delta_{ki}\kappa_{mm} - \epsilon_{klj}\frac{\partial \epsilon^{el}_{ij}}{\partial x_l}$ simplifies to Nye's relations between the dislocation density tensor and the crystalline lattice curvature

$$\alpha_{ik} = \kappa_{ki} - \delta_{ki}\kappa_{mm} \qquad Eq.\ II.\ 5$$

$$\kappa_{ki} = \alpha_{ik} - \frac{1}{2}\delta_{ki}\alpha_{mm} \qquad Eq.\ II.\ 6$$

In addition, a crystalline lattice orientation is defined by the necessary rotation to achieve the particular orientation from a chosen reference orientation. This rotation was described by the Bunge orientation matrix (more details in (Bunge 1982)). An orientation difference between two orientations in analogously defined by the rotation required to obtain orientation (B) from another (A), described by a disorientation angle $\Delta\theta$ and rotation axis $\vec{r}$. Then, the disorientation vector $\Delta\theta_i = \Delta\theta_{ri}$ in the sample coordinates can also be calculated from the disorientation matrix ($\Delta g = (g_A)^{-1}g_B$), as

$$\Delta\theta_k = -\epsilon_{kij}\Delta g_{ij}\frac{\Delta\theta}{2\sin\Delta\theta} \qquad Eq.\ II.\ 7$$

with $\Delta\theta = arc\cos(\Delta g_{ii} - 1)/2$.

From the disorientation between two neighboring points separated spatially by $\Delta\vec{x}$, the lattice curvatures

$$\kappa_{kl} = \frac{\partial\theta_k}{\partial x_l} \approx \frac{\Delta\theta_k}{\Delta x_l} \qquad Eq.\ II.\ 8$$

in sample coordinates are easily depicted when the orientation data are issued from a square grid aligned with the sample coordinate system, as shown in Fig. II. 6. However, as the orientations maps are determined only in the sample plane (along x_1 and x_2), only six components of the curvature tensor can obtained (κ_{i1} and κ_{i2}, with i = 1, 2, 3).

From these six accessible curvature components, five components of the dislocation density tensor can be derived:

$\alpha_{12} = \kappa_{21}$ $\alpha_{23} = \kappa_{32}$

$\alpha_{13} = \kappa_{31}$ $\alpha_{33} = -\kappa_{11} - \kappa_{22}$ *Eq. II. 9*

$\alpha_{21} = \kappa_{12}$

From these equations, a truncated scalar value of ρ_{GND} can be calculated; we call it $\rho^{(2D)}_{GND}$:

$$\rho^{2D}_{GND} = \alpha_{12} + \alpha_{13} + \alpha_{21} + \alpha_{23} + \alpha_{33} \qquad Eq.\ II.\ 10$$

In the present work, raw orientation maps (without noise reduction) were used to extract the GND density according to the method proposed. In order to quantify the GND densities only within the grains, the adjacent pixels across boundaries displaying a disorientation exceeding 5° were not considered in the calculation. For the sake of visual clarity, only the band contrast was plotted for densities smaller than 10% of the GNDs density maximum (see legend). It also should be noted that the values of GND density are the average along each horizontal line parallel to the treated surface. Actually, the purpose id to analyze the evolution of the GND density from the top treated surface towards the material core.

II. 1. 3.   The surface preparation

The first step in collecting EBSD data is preparing the specimen so that high quality Kikuchi patterns are observed and obtained with the imaging system.

The near-incident energy backscattered electrons form the EBSD patterns. Backscattered electrons that have experienced inelastic events inside the bulk of the specimen do not contribute to the pattern. This fact, combined with the high tilt angle of the specimen (70°), results in a diffraction region that forms within the extreme top surface of the specimen. The crystal lattice in this region should be strain-free and clean from contamination or oxide layers for diffraction to occur. If these conditions are not respected, the resulting EBSD patterns will be of poor quality or will not be visible at all, as shown in the example below (Fig. II. 7) in the case of a duplex steel (Singh Ubhi 2009).

(a)   (b)
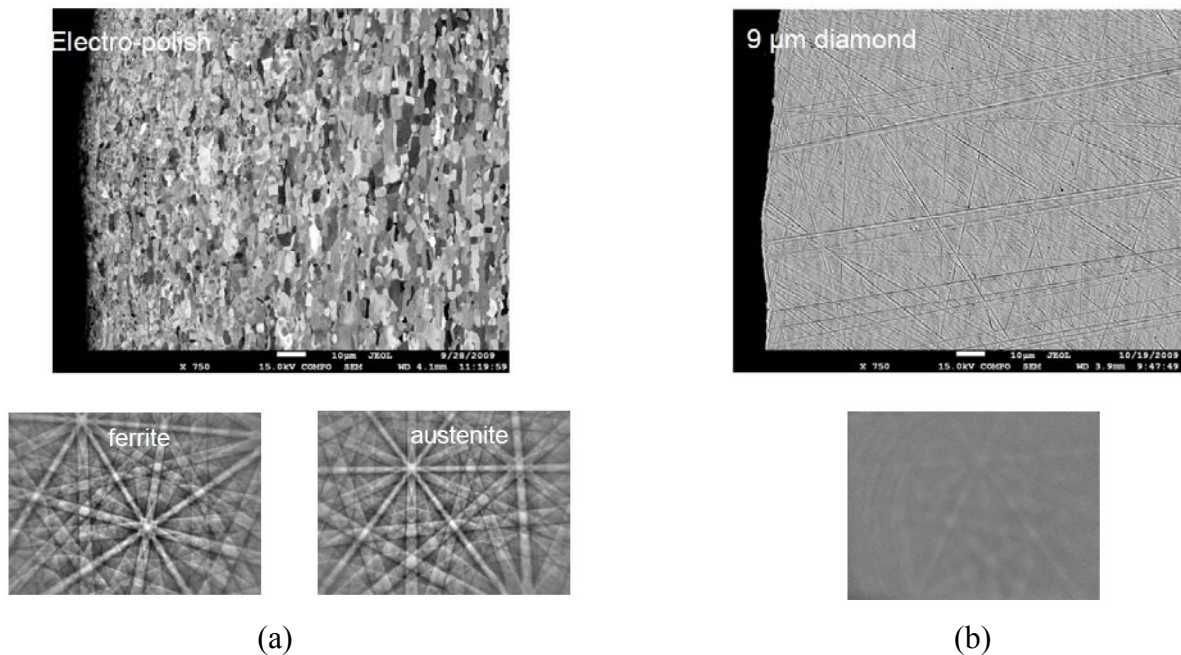
Fig. II. 7: Examples of the evolution of EBSD patterns as function of the surface preparation of a duplex steel: (a) after electro-polishing, (b) after 9μm polishing.

Proper specimen preparation will address these issues and help in obtaining reliable Kikuchi patterns. All the samples are then mechanically polished then finished with Oxide Polishing Suspensions (OPS from the company Struers) to remove the top surface deformed layer.

II. 2. **Residual stress measurement by X-Ray Diffraction**

II. 2. 1. *Generalities about the residual stress*

Residual stresses are self-equilibrating stresses within materials and they are the result of elastic and/or plastic deformation non-homogeneously distributed over the volume. Effectively it means that the resulting force and the resulting moment produced by them are zero. The total stress in externally loaded parts containing residual stresses, will always equal the sum of the residual stresses and the loading stresses (Macherauch 1987). Residual stresses are traditionally classified as residual stresses of the 1st, 2nd and 3rd kind (Fig. II. 8).
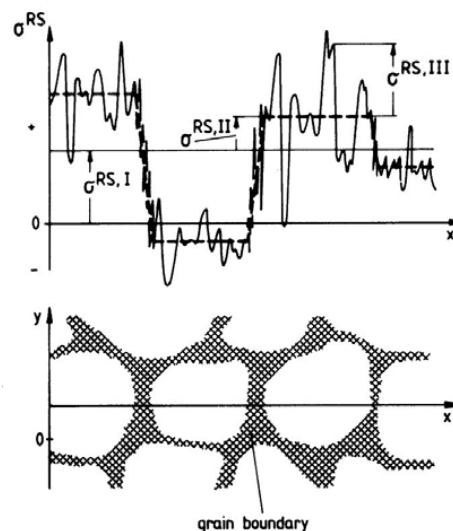
Fig. II. 8: Total residual stress distribution along several grains of a polycrystal and their separation in 1st, 2nd and 3rd residual stresses.

According to Macherauch et al (Macherauch 1987) the different kinds of stresses are defined as:

1. Residual stresses of the 1st kind are nearly homogeneous across large areas i.e. several grains and they are in equilibrium over the bulk of the material. A change in the equilibrium of forces and moments of a volume containing 1st kind of residual stresses will cause a change in its dimensions.

2. Residual stresses of the 2nd kind are nearly homogeneous across microscopic areas i.e. one grain or parts of a grain and are equilibrated across a sufficient number of grains.

Macroscopic changes of the dimensions of a volume comprising 2nd kind residual stresses may only occur if distinct disturbances of this equilibrium will happen.

3.   Residual stresses of the 3rd kind are inhomogeneous across submicroscopic areas, i.e. some atomic distances within a grain and are equilibrated across small parts of a grain. No macroscopic changes of the dimensions of the stressed material will happen if this equilibrium is disturbed.

The different kinds of stresses are commonly divided into macro residual stresses and micro residual stresses. Macro residual stresses are residual stresses of the 1st kind and micro residual stresses are generally regarded as combinations of residual stresses of the 2nd and 3rd kind.

The total (local) residual stress is given by:

$$\sigma^{RS} = \sigma^{RS,I} + \sigma^{RS,II} + \sigma^{RS,III} \qquad \textit{Eq. II. 11}$$

Residual stresses may be advantageous for many technical purposes, e.g. for increasing the fatigue strength of a material. However, the opposite may also apply; residual stresses can have detrimental effects. Consequently, it is very important to have knowledge of the amount and sign of the residual stresses and the stress distribution within a material.

II. 2. 2.   Residual stress measurement by X-Ray diffraction

The measurement of stresses with X-ray diffraction is founded in the elasticity theory. The definitions and notations of the stress component are defined as in the figure hereafter:
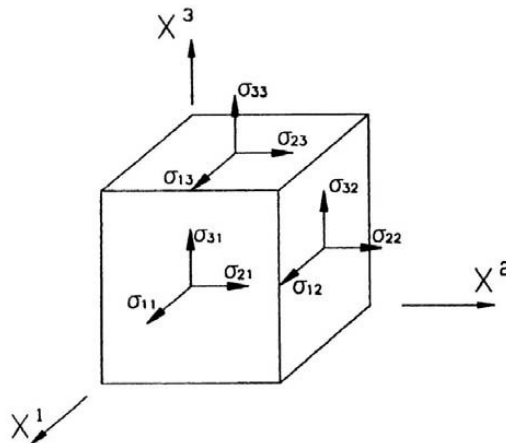
Fig. II. 9: Definition of the stress components (Hauk 1997).

The stresses and strains can be written as tensors i.e. they both form symmetrical 2nd rank tensors. They each have 9 components σ_{ij}, ε_{ij}, which in matrix form are written as (Hauk 1997):

$$\sigma = \begin{bmatrix} \sigma_{11} & \sigma_{12} & \sigma_{13} \\ \sigma_{21} & \sigma_{22} & \sigma_{23} \\ \sigma_{31} & \sigma_{32} & \sigma_{33} \end{bmatrix} \qquad \varepsilon = \begin{bmatrix} \varepsilon_{11} & \varepsilon_{12} & \varepsilon_{13} \\ \varepsilon_{21} & \varepsilon_{22} & \varepsilon_{23} \\ \varepsilon_{31} & \varepsilon_{32} & \varepsilon_{33} \end{bmatrix}$$

The symmetry $\sigma_{ij} = \sigma_{ji}$ and $\varepsilon_{ij} = \varepsilon_{ji}$ dictate that only 6 of the 9 components are independent and are sufficient to describe the stress and strain at a volume element in the material. It is possible to transform the axes so that only normal stresses are present in the coordinate system (zeroes above and below the matrix diagonal). Within this kind of system the normal stresses are known as principal stresses. Normal stresses (same indices) are stresses that act along the normal of the plane in consideration and will cause dimensional changes without changes in shape. Shear stresses are stress components that act along the plane in consideration and will cause deformations due to changes in shape. Shear stresses have mixed indices, where the first index indicates the direction and the second index indicates the normal of the plane in which the stress acts.

Generally, two systems are considered i.e. the sample and the measurement systems, which are described by a Cartesian coordinate system, thus designated the sample system (Si) and the laboratory system (Li), respectively (the figure hereafter).
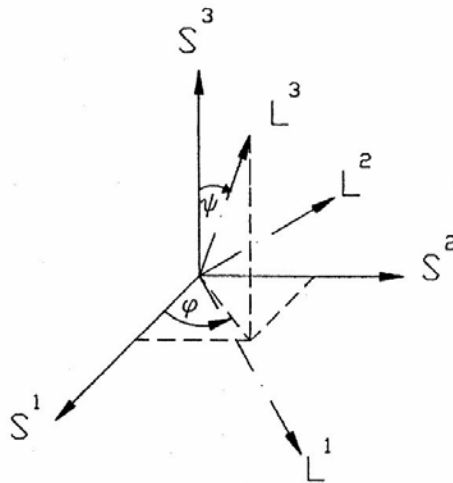
Fig. II. 10: Descriptions of the measurement direction and the sample and laboratory system (Hauk 1997).

Rotation and tilting of the sample relative to the coordinate system (S^1, S^2, S^3) are described by the azimuth angle ϕ and the pole angle ψ, respectively. S^3 defines the sample normal and S^1 and S^2 are in the sample surface. Measurement is performed in the direction L^3. Diffraction (information) occurs from the lattice planes perpendicular to the scattering vector defined as the bisector (B) of the incident and diffracted beam. The quantities actually measured are scattered intensity and the scattering angle, $2\theta°$, which directly yield the lattice spacing. The strain follows from the measured lattice spacing.

The strain measured in the direction L^3, $\varepsilon_{\phi\psi}$, can be expressed as a projection of the strain tensor in the measurement direction (ϕ, ψ) within the sample system or as the ε_{33} component in the laboratory system. Accordingly, the strain in the measurement direction is given as (Hauk 1997):

$$\varepsilon_{\varphi,\psi} = <\varepsilon_{11}>^x \cos^2\varphi \sin^2\psi + <\varepsilon_{22}>^x \sin^2\varphi \quad \sin^2\psi + <\varepsilon_{33}>^x \cos^2\psi +<$$
$$\varepsilon_{12}>^x \sin 2\varphi \sin^2\psi + <\varepsilon_{13}>^x \cos\varphi \sin 2\psi + <\varepsilon_{23}>^x \sin\varphi \sin 2\psi \quad Eq.\ II.\ 12$$

The $<\varepsilon_{11}>^x$ are the average of the strain components taken over the contributing crystallites considering the attenuation of the X-rays (see below).
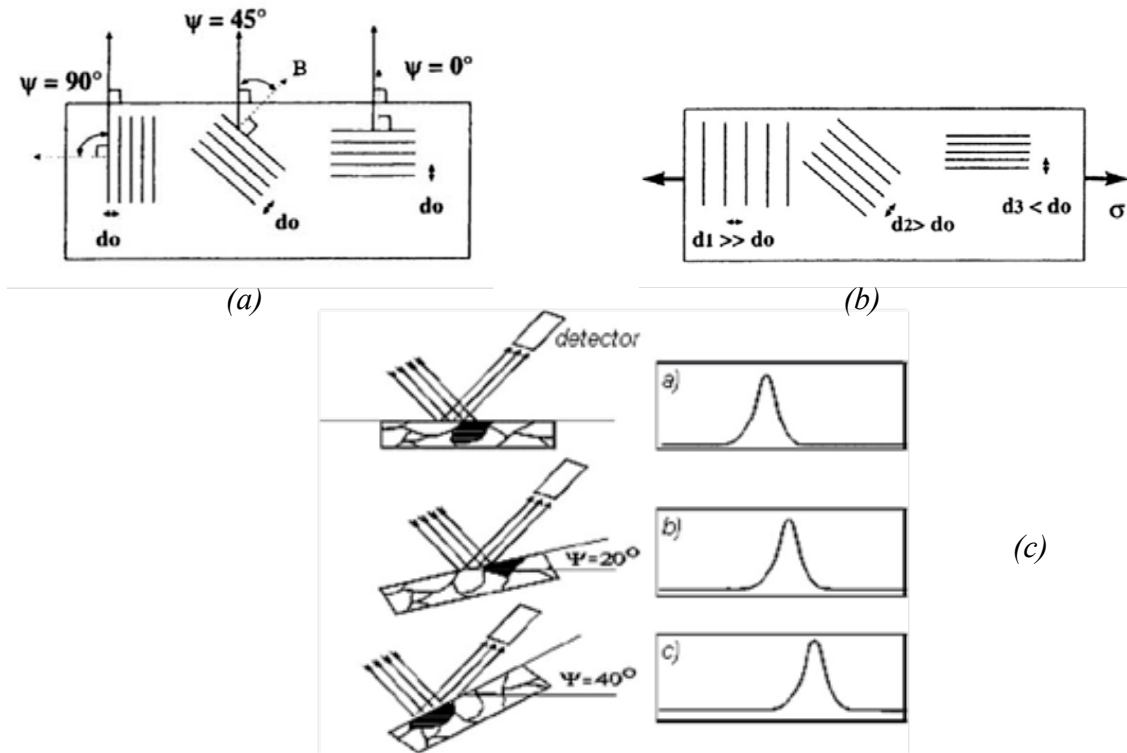
Fig. II. 11: Tilting in a direction defined by pole angle ψ. (a and b) Diffraction occurs from lattice planes perpendicular to the bisector B. The measured strain (lattice spacing) is dependent on the angle of the lattice planes in mention with the (applied) effective stress (Lu and Retraint 1998). (c) Diffraction occurs from grains oriented with lattice planes perpendicular to the bisector B. The measured quantity is the scattering angle 2θ°.

It is assumed that the ε_{ij} are homogeneous within the penetration depth of the X-ray and that the material is elastically isotropic. Hooke's law of isotropic materials, relating strain and stress, is introduced (Hauk 1997):

$$E\varepsilon_{ij=(1+v)}\sigma_{ij} - v\delta_{ij}(\sigma_{11} + \sigma_{22} + \sigma_{33}) \qquad Eq.\ II.\ 13$$

where E is Young's modulus, v is Poisson's ratio and δ is the Kronecker delta:

$$\delta_{ij} = \begin{cases} 1\ if\ i = j \\ 0\ if\ i \neq j \end{cases} \qquad Eq.\ II.\ 14$$

The relationship between $\varepsilon_{\phi,\psi}$ and σ_{ij} for an elastically isotropic body can now be established (Hauk 1997):

$$\varepsilon_{\varphi,\psi} = \frac{d_{\varphi,\psi} - d_{\varepsilon=0}}{d_{\varepsilon=0}} = \tfrac{1}{2}S_2^m (\sigma_{11} \cos^2\varphi \sin^2\psi + \sigma_{22} \sin^2\varphi \sin^2\psi + \sigma_{33} \cos^2\psi)$$
$$+ \tfrac{1}{2}S_2^m (\sigma_{12} \sin 2\varphi \sin^2\psi + \sigma_{13} \cos\varphi \sin 2\psi + \sigma_{23} \sin\varphi \sin 2\psi) + S_1^m (\sigma_{11} + \sigma_{22} + \sigma_{33}) \qquad Eq.\ II.\ 15$$

where $d_{\phi,\psi}$ is the lattice plane spacing, $d_{\varepsilon}=0$ is the strain free lattice plane spacing, ϕ is the azimuth angle, ψ is the pole angle between the normal to the reflecting plane (hkl) and the normal to the specimen surface. The macroscopic elastic data is given by:

$$\tfrac{1}{2}S_2^m = \frac{1+v}{E} \qquad\qquad S_1^m = \frac{-v}{E} \qquad\qquad Eq.\ II.\ 16$$

Using diffraction methods only a small part of all crystallites contributes to diffraction, depending on the lattice plane under study. Only crystallites oriented perpendicular to the measurement direction will diffract. The elastic behavior of the actually diffracting crystallites may differ from the macroscopic one due to the elastic anisotropy of the crystals. In order to take the elastic anisotropy into consideration it is necessary to replace the macroscopic elastic constants $\tfrac{1}{2}S_2^m$ and S_1^m with {hkl}-dependent X-ray Elastic Constants (XEC) $S_1(hkl)$ and $\tfrac{1}{2}S_2(hkl)$.

Finally, considering a biaxial stress state to simplify the general equation, assuming that the stress components involving the surface normal direction (X_3) are zero; the fundamental equation in stress measurement by diffraction takes the form (Hauk 1997):

$$\varepsilon_{\varphi,\psi} = \frac{d_{\varphi,\psi} - d_{\varepsilon=0}}{d_{\varepsilon=0}} = \tfrac{1}{2}S_2(hkl)(\sigma_{11}\cos^2\varphi + \sigma_{12}\sin 2\varphi + \sigma_{22}\sin\varphi)\sin^2\psi + S_1(hkl)(\sigma_{11} + \sigma_{22}) \quad Eq.\ II.\ 17$$

The lattice spacing $d_{\varphi\psi}$ is measured for each direction of the φ and ψ angles. In the case of the present residual stress determination, the procedure was done for both the γ and α phases using the (220)γ and (211)α planes for the AISI 316L stainless steel. The calculation of the residual stress is based on the general Hook's law:

$$\sigma_{ij} = \frac{E}{1+v}\left(\varepsilon_{ij} + \frac{v}{1-2v}Tr(\varepsilon)\delta_{ij}\right) \qquad\qquad Eq.\ II.\ 18$$

Here, σ_{ij} is the stress component and ε_{ij} the strain component. Two usual assumptions are used for the stress analysis. First, the stress strain states are considered homogeneous in each phase for the samples. This means that possible stress gradients in the very top surface layer are not considered and that the measured residual stress values determined here for each phase are averaged within the penetration depth of the X-ray beam.

It should be noted also here that a Siemens D5000 diffractometer equipped with an Eulerian cradle and a linear Position Sensitive Detector (PSD Braun) which is able to cover a domain of 12° in 2θ. The Cr-Kα radiation was selected for the measurement in order to avoid the fluorescence from the studied material. The maximum penetration depth of the X-ray beam using this radiation is estimated to be about 5 μm.

The (average/isotropic) Young's modulus E and the Poisson ratio y were used as elastic constants. They were taken as $E_\alpha \approx 210$ GPa and $\upsilon_\alpha = 0.28$ for the α phase and $E_\gamma \approx 180$ GPa and $\upsilon_\gamma = 0.28$ for the γ-phase.

II. 3.   The chemical composition analysis: The Glow Discharge – Optical Emission Spectrometry (GD-OES)

GD-OES is known since 1967 when Grimm published the first results from hisanalytical source(Grimm 1967). Starting from that time the interest in Grimm's source incombination with optical emission spectrometry has steadily grown. Nowadays GD-OES is employed for the analysis of steels and steel surfaces, other metallic coatingsand metals, PVD/CVD coatings, semiconductors, polymers, ceramics.

The principle of GD-OES is shown in Fig. II. 12. The principle is the following: atoms of the sample are sputtered, ionized, excited and emit characteristic light in the GD plasma (discharge gas - Ar); this characteristic light is detected by an optical spectrometer. The detectors can be either PMTs or CCD arrays mounted into a Rowland-circle or in combination with a monochromator.
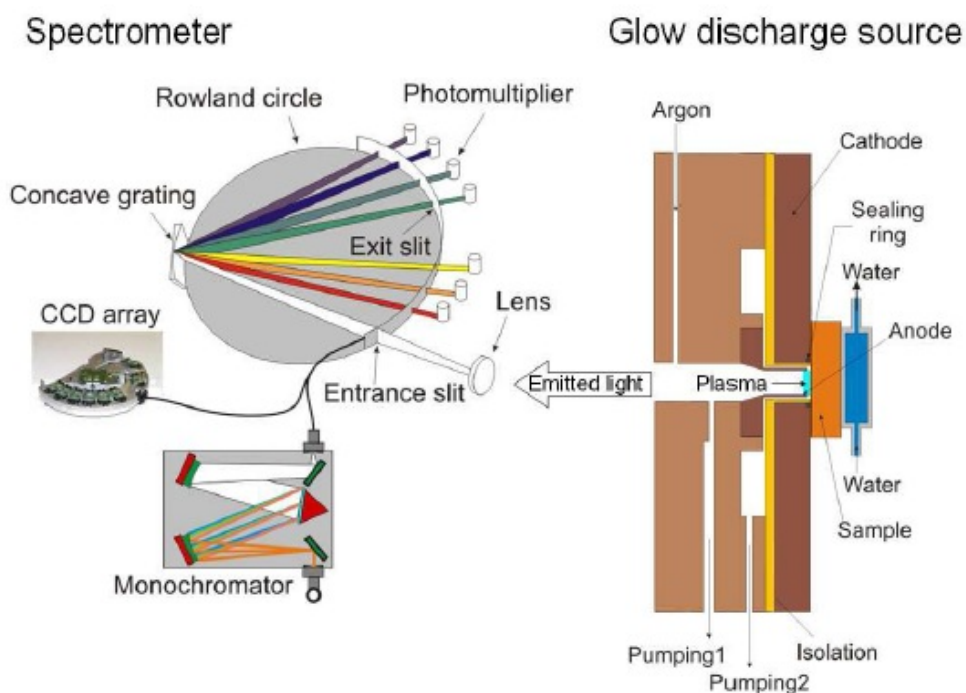
Fig. II. 12: Schematic illustration of the GD-OES principle.

GD-OES is suitable for the analysis of nearly all elements (including the light elements H, C, N, O) in films of 1 nm up to more than several mm thickness. The depth resolution of the method is about 5 % of the sputtered depth, but higher than the ultimate depth resolution (3 nm). However it should be mentioned that to reach the best depth resolution, the shape of the sputtered crater should be optimized (by varying the discharge parameters, in the simplest case - voltage, current and pressure). In addition GD-OES is characterized by a high sensitivity (detection limit 0,1-10 μg/g) and high dynamic range (μg/g up to main components).

In the present study, the GD-OES system is HORIBA Jobin Yvon, type RF1000. It is used to quantify the evolution of the chemical composition from the top surface towards the material core.

II. 4.   The surface hardness measurements

The hardness is a measure of how resistant solid matter is to various kinds of permanent shape change when a force is applied. Among the techniques used for the characterization of this property, the indentation hardness is widely used and known. It allows to measure the resistance of a sample to material deformation due to a constant compression load from a sharp object. They are primarily used in engineering and metallurgy fields.

As the different surface treatments studied in the present work affect directly the material hardness, this section describes the technique used to investigate the hardness evolution. The

Vickers hardness test method is used. It consists of indenting the test material with a diamond indenter, in the form of a right pyramid with a square base and an angle of 136 degrees between opposite faces subjected to a load of 1 to 100 kgf (Fig. II. 13). The full load is normally applied for 10 to 15 seconds. Under each load, in order to obtain a relevant statistic, the hardness value indicated corresponds to the measurement of at least of 10 different hardness tests (NF EN ISO 4507:2007-11-01, 2007–11–01).
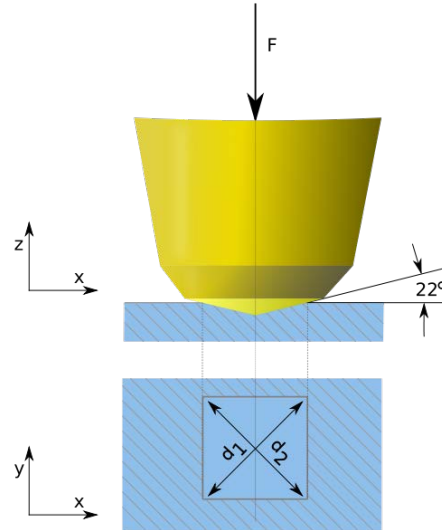
Fig. II. 13: Description of the Vickers hardness principle.

This technique allows the determination of hardness profiles on the cross section, i.e. the hardness evolution from the top surface to the material core. In addition, as the zones of interests after duplex treatments are very thin (~3 µm), indentation loads in the range of 10 to 500 gf are applied to the material surface. As the indentation load increases, the contributing material volume increases too. In consequence, in the case of the nitrided surface for example, the effect of the nitrided layer can be observed as the load increases. To observe more clearly the evolution of the surface hardness, the indentation depth is used instead of the indentation load. Actually, the indentation depth (noted h) can be expressed using geometrically relationship as function of the diagonal "d":

$$h = \frac{\sqrt{2}}{4} d. \cot 68° \approx \frac{d}{7} \qquad \text{Eq. II. 19}$$

References

Bunge, Hans Joachim. 1982. *Texture Analysis in Materials Science: Mathematical Methods*. Butterworths.

Coates, Dg. 1967. "Kikuchi-Like Reflection Patterns Obtained with Scanning Electron Microscope." *Philosophical Magazine* 16 (144): 1179–&. doi:10.1080/14786436708229968.

Grimm, W. 1967. "Glow Discharge Lamp for Routine Spectroanalytic Measurements." *Naturwissenschaften* 54 (22): 586–&.

Hauk, V. 1997. *Structural and Residual Stress Analysis by Nondestructive Methods*. Elsevier.

Kikuchi, S. 1928. "Diffraction of Cathode Rays by Mica." *Japanese Journal of Physics* 5: 83–96.

Kröner, E. 1980. "Continuum Theory of Defects Con."

Lo, K.H., C.H. Shek, and J.K.L. Lai. 2009. "Recent Developments in Stainless Steels." *Materials Science and Engineering: R: Reports* 65 (4–6): 39–104. doi:10.1016/j.mser.2009.03.001.

Lu, J., and D. Retraint. 1998. "A Review of Recent Developments and Applications in the Field of X-Ray Diffraction for Residual Stress Studies." *Journal of Strain Analysis for Engineering Design* 33 (2): 127–36. doi:10.1243/0309324981512869.

Macherauch, E. 1987. *International Guide Book on Residual Stresses, Advances in Surface Treatments*. Vol. 4.

Muraca, R. F., and J. S. Whittick. 1972. *Materials Data Handbook - Stainless Steel Alloy A-286*. Western Applied Research and Development, Inc.

NF EN ISO 4507:2007-11-01. "Sintered Ferrous Materials, Carburized or Carbonitrided - Determination and Verification of Case-Hardening Depth by a Micro-Hardness Test."

Nye, Jf. 1953. "Some Geometrical Relations in Dislocated Crystals." *Acta Metallurgica* 1 (2): 153–62. doi:10.1016/0001-6160(53)90054-6.

Pantleon, W. 2008. "Resolving the Geometrically Necessary Dislocation Content by Conventional Electron Backscattering Diffraction." *Scripta Materialia* 58 (11): 994–97. doi:10.1016/j.scriptamat.2008.01.050.

"Properties of the AISI660 Stainless Steel." *Thyssen France*. http://www.thyssenfrance.com/fich_tech_fr.asp?product_id=11290.

Schwarz, A. J., M Kumar, and B. L. Adams. 2000. *Electron Backscatter Diffraction in Materials Science*. Eds. New York: Kluwer Academic/Plenum Publishers.

Singh Ubhi, H. 2009. "Characterisation of Materials Using EBSD (part I)" presented at the Oxford Instruments.

Venables, Ja, and R. Binjaya. 1977. "Accurate Micro-Crystallography Using Electron Backscattering Patterns." *Philosophical Magazine* 35 (5): 1317–32. doi:10.1080/14786437708232955.

List of figures

List of tables

Chapter III

Investigation of the Surface Mechanical Attrition Treatment (SMAT) effects on the microstructure and contamination of the AISI 316L and AISI 660 stainless steels surfaces

In this chapter, the AISI 316L and AISI 660 austenitic stainless steels are subjected to the Surface Mechanical Attrition Treatment (SMAT) using different treatment parameters (duration of the treatment, amplitude of vibrations, nature of the impacting balls) in order to determine quantitatively their general effects on the deformation induced microstructure modifications.

The first part of this chapter summarizes the SMAT processing parameters used for treating the two steels. These processing conditions will be used in the second and third part of this chapter to quantitatively characterize the effectiveness of the plastic deformation to modify the microstructure and also to investigate the pollution associate with the treatment.

The second part presents the mechanical effects of the SMAT parameters on the microstructure of the AISI 316L and the AISI 600 stainless steels. Firstly, the AISI 316L microstructure is analyzed using Scanning Electron Microscopy (SEM) coupled with Electron BackScattered Diffraction (EBSD). The EBSD data are then used to develop a new technique to quantitatively describe the induced plastic deformation. The procedure is firstly developed and tested on the AISI 316L treated under different SMAT parameters for validation. It is then applied to the case of the AISI 660 treated under wider range of amplitudes and treatment durations as well as different natures of balls. The influence of these parameters on the evolution of the microstructure is then discussed.

The last part of this chapter deals with the surface modification after SMAT in term of chemical composition. The surface of the AISI 316L was firstly investigated by Transmission Electron Microscopy (TEM) coupled with Energy-Dispersive X-ray spectroscopy (EDX). Surface contamination by materials coming from the SMAT chamber parts is revealed. Further investigations were then carried out on the surface of the AISI 660 using X-Ray Diffraction to describe, quantitatively and using a non-destructive approach, the effect of processing parameters on the nature and content of the surface pollution.

Summary

I.   The SMAT experimental conditions used for treating the AISI 316L and AISI 660 SS surfaces

Two materials are chosen to be treated by SMAT: the AISI 316L and the AISI 660 stainless steels. As the AISI 316L austenitic microstructure after SMAT has been investigated in previous works (Roland et al. 2007; Roland et al. 2006), this will facilitate the development and understanding of the new approach of plastic deformation quantification developed in this chapter. On the other hand, the AISI 660 precipitation hardened, which is richer in Ni content than the AISI 316L, is more stable and has been treated for industrial applications of the AREVA Company. The SMAT experimental conditions are given in this section.

I. 1   The SMAT treatment and its parameters used for the AISI 316L

The specimens of AISI 316L were 25 mm diameter and 8 mm thick disks. Prior to the SMAT, the samples were mechanically polished to mirror-finish (OPs suspension). The chemical composition and mechanical properties of the material are given in the previous chapter. Fig. III. 1 is an image showing the typical surface morphology after SMAT. The material flows at the edge of the sample under the severe plastic deformation during SMAT.
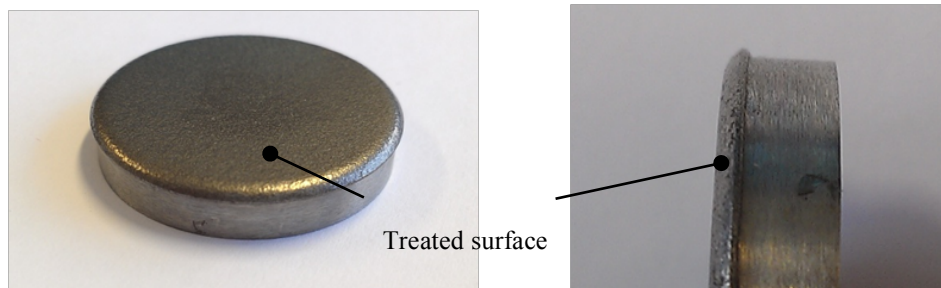
Fig. III. 1: Close up view of the AISI 316L treated samples.

The SMAT was performed by SONATS company under argon atmosphere (to avoid oxidation), using intercrossed variations of different parameters: the treatment duration (3 and 20 min), the amplitude of the sonotrode vibration (60 and 80 μm), and balls nature (100Cr6 and Zirshot balls); the other conditions remain similar. All the experimental conditions are given in Table III. 1

Condition	Balls			SMAT conditions				Designation in the work
	Nature	Diameter (mm)	Weight (g)	Amplitude of vibration (µm)	Treatment duration (min)	Vibrating frequency (kHz)	Distance Sonotrode – sample (mm)	
1	100Cr6 steel	1	7.6	60	3	20	30	D1A60T3.00
2			7.6	60	20			D1A60T20.00
3			7.6	80	3			D1A80T3.00
4			7.6	80	20			D1A80T20.00
5	Zirshot		5.9	60	3			D1A60T3.00**Z**
6			5.9	60	20			D1A60T20.00**Z**

Table III. 1: SMAT parameters used for treating the AISI 316L stainless steel.

I. 2   The SMAT treatment and its parameters for the AISI 660

The rectangular shape of the AISI 660 samples - an example of which is shown in Fig. III. 2- has been chosen by AREVA. SEM observations and EBSD analysis were carried out in the arrowed zone on the right side of the sample (20 mm from the boundary); while XRD and chemical composition measurements were carried out at the zone in the symmetric part of the sample (see Fig. III. 2a). It is also interesting to note in the enlargement given in Fig. III. 2b that the same phenomenon of the plastic flow already observed in the case of the AISI 316L is present at the edge of the AISI 660 samples.
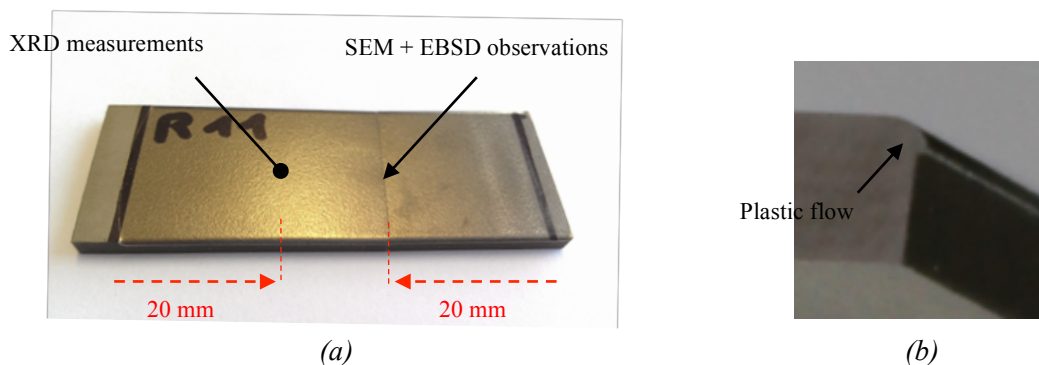
Fig. III. 2: Close up view of the (a) the AISI660 surface and (b) the plastic flow observed at the edge of the sample after SMAT.

The SMAT parameters used for treating the AISI 660 are given in table 2. The samples were treated using intercrossed variations of more parameters in comparison with the AISI 316L: the balls diameter (1 and 2 mm), the amplitude of the sonotrode (30, 50 and 80 µm) and the covering ratio (100, 3000 and 10000 %). It should be noted that the covering ratio is used here instead of the treatment duration previously used for the AISI 316L. In fact, the covering ratio is a qualitative parameter determined by the operator. A covering ratio of 100% is reached when the operator estimates that at least one impact has been done at each zone of the surface. The time corresponding to a covering ratio of 100% is measured and used to obtain higher covering ratios. For example, to

obtain a covering ratio of 3000 % and 10000 % (the used rates in the present case), the measured 100% "covering ratio time" is multiplied by 30 and 100, respectively. All the parameters are summarized in Table III. 2.

	Ball			SMAT conditions					
Reference	Nature	Diameter (mm)	Weight (g)	Amplitude of vibration (µm)	Covering ratio (%)	Treatment duration (min)	Vibrating frequency (kHz)	Distance Sonotrode – sample (mm)	Designation
R40	100Cr6 steel	1	5.87	30	100	0.50	20	30	D1A30T0.50
R41				50		0.33			D1A50T0.33
R42				80		0.17			D1A80T0.17
R68				30	3000	15.00			D1A30T15.00
R43				50		10.00			D1A50T10.00
R44				80		5.00			D1A80T5.00
R1		2	11.7	30	100	0.66			D2A30T0.66
R2				50		0.50			D2A50T0.50
R3				80		0.25			D2A80T0.25
R7				30	3000	20.00			D2A30T20.00
R8				50		15.00			D2A50T15.00
R9				80		7.50			D2A80T7.50
R10				30	10000	67.00			D2A30T67.00
R11				50		50.00			D2A50T50.00
R12				80		25.00			D2A80T25.00

Table III. 2: Summary of the different SMAT parameters used for treating the surface of the AISI 660 stainless steel.

To ease the citation of the different treated samples, a designation has been adapted to recognize the treatment conditions directly as follows:
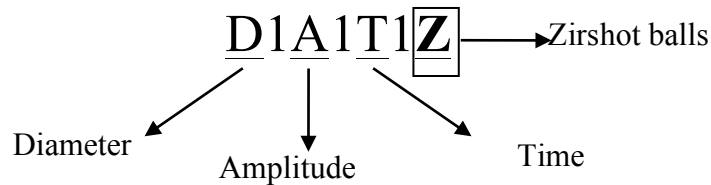
D: the balls diameter (mm)

A: the vibration amplitude (µm)

T: the treatment duration (min)

Z is added when balls used are in Zirshot.

II. <u>Quantitative analysis of the mechanical effects of the SMAT on the induced microstructure modifications</u>

The microstructure of the AISI 316L, subjected to SMAT under the conditions given in the previous section, is detailed hereafter by EBSD analysis. Using these analyses, a new method to quantitatively describe the induced plastic deformation is given and tested firstly on the case of the 316L. The procedure is then applied in the case of the AISI 660 treated by SMAT using larger range of processing parameters.

II. 1 Limitations and strength of the new approach and the GND calculation procedure

It should be noted that the developed procedure still has some limitations. Firstly, the calculated Geometrically Necessary Dislocation (GND) density depends on the acquisition of the EBSD data. In fact, it has been established by Jiang et al (Jiang, Britton, and Wilkinson 2013) that increasing the step size results in lowering the recorded GND density. In addition, depending on SMAT conditions, the roughness of the surface can be very important. During the analysis of the cross section, it is difficult to determinate of the exact location of the extreme surface.

Despite that, this new approach allows to quantitatively describe the induced plastic deformation after SMAT (and after severe plastic deformation in general). It gives a first approach to the study of the effect of the different SMAT parameters on the evolution of the induced microstructure. It also presents an advantage in term of the limitation of the experimental characterization analysis duration. Many pieces of information about the microstructure and the plastic deformation levels and witness marks can be revealed within a relatively short time, in comparison with other techniques, such as TEM observations, where in addition to the limited analyzed zone, the sample preparations require a more significant delay.

II. 2 Development of a new approach for rapid quantification of microstructure modifications induced by the SMAT

II. 2. 1   *Surface and in-depth microstructure investigation:*

The changes in the surface morphology and in-depth microstructure after SMAT are shown in Fig. III. 3. Using Secondary Electron Imaging (SEI), the top treated surface morphology is given in Fig. III. 3a. The treated surface is very rough after the repeated impacts of the balls. Some 'dark' zones (arrows in black in Fig. III. 3a) are also observed at some regions of the surface. The roughness of the surface was not studied in the present work, which focuses more on the microstructure modification within the material. Fig. III. 3b gives an example of the microstructure

morphology after SMAT with 100Cr6 balls under amplitude of 60 μm for 20 minutes. The cross section observations reveal the induced plastic deformation signs as well as the whole affected zone of the material. The initial austenitic grains are not visible anymore at the top surface after SMAT and the microstructure was gradually refined within a depth of more than 100 μm. In addition, at the extreme top surface, a 'dark' layer and zones similar to the ones observed at the top surface are visible. In the next part of this chapter, chemical composition analysis will show that these zones are essentially contaminated by the Sonotrode elements (Ti, Al and V elements).

As observed in Fig. III. 3b, the material was gradually refined from the top surface towards the depth. However, it is impossible at this state to depict precisely the deformation mechanisms. As SEM observations are not sufficient to gain more information about the induced deformation mechanisms and to determine precisely the affected zone thicknesses, EBSD measurements were carried out.
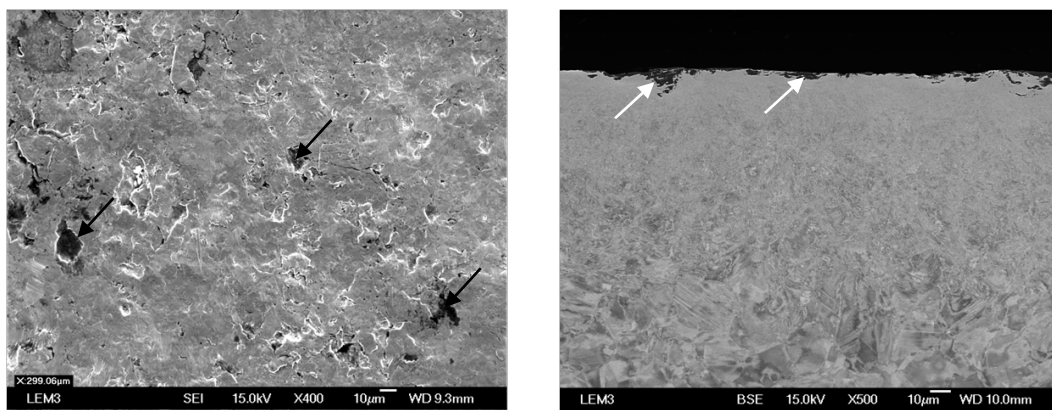
Fig. III. 3: Typical surface (a) and cross section (b) microstructure morphology of the AISI 316L stainless steel SMAT-ed sample (100Cr6 balls – 60 μm of amplitude for 20 minutes)

EBSD measurements with a very low step size were firstly then used (as shown in Fig. III. 4) to determinate as precise as possible the resulting microstructure and to analyze the deformation mechanisms. Fig. III. 4a gives a typical Band Contrast (BC) and Inverse Pole Figure (IPF) maps of the cross section of the 316L stainless steel after SMAT, recorded using a step size of 30 nm in the area of high strain regime below the surface. These maps are raw (not corrected) in which the black areas correspond to heavily strained regions, giving rise to blurred or overlapped Kikuchi patterns that could not be indexed. As shown in Fig. III. 4a, at the top of the images (near the top treated surface), the EBSD technique was not able to resolve the structure of a layer having a thickness of about 4 μm below the surface. Indeed, this area corresponds to the heavily deformed microstructure containing nanograins or domains having sizes as low as 20 nm (Roland et al. 2006; Roland et al.

2007) and, as a consequence, the indexing ratio at different distances from the surface in this area is very low.

(a)

(b)
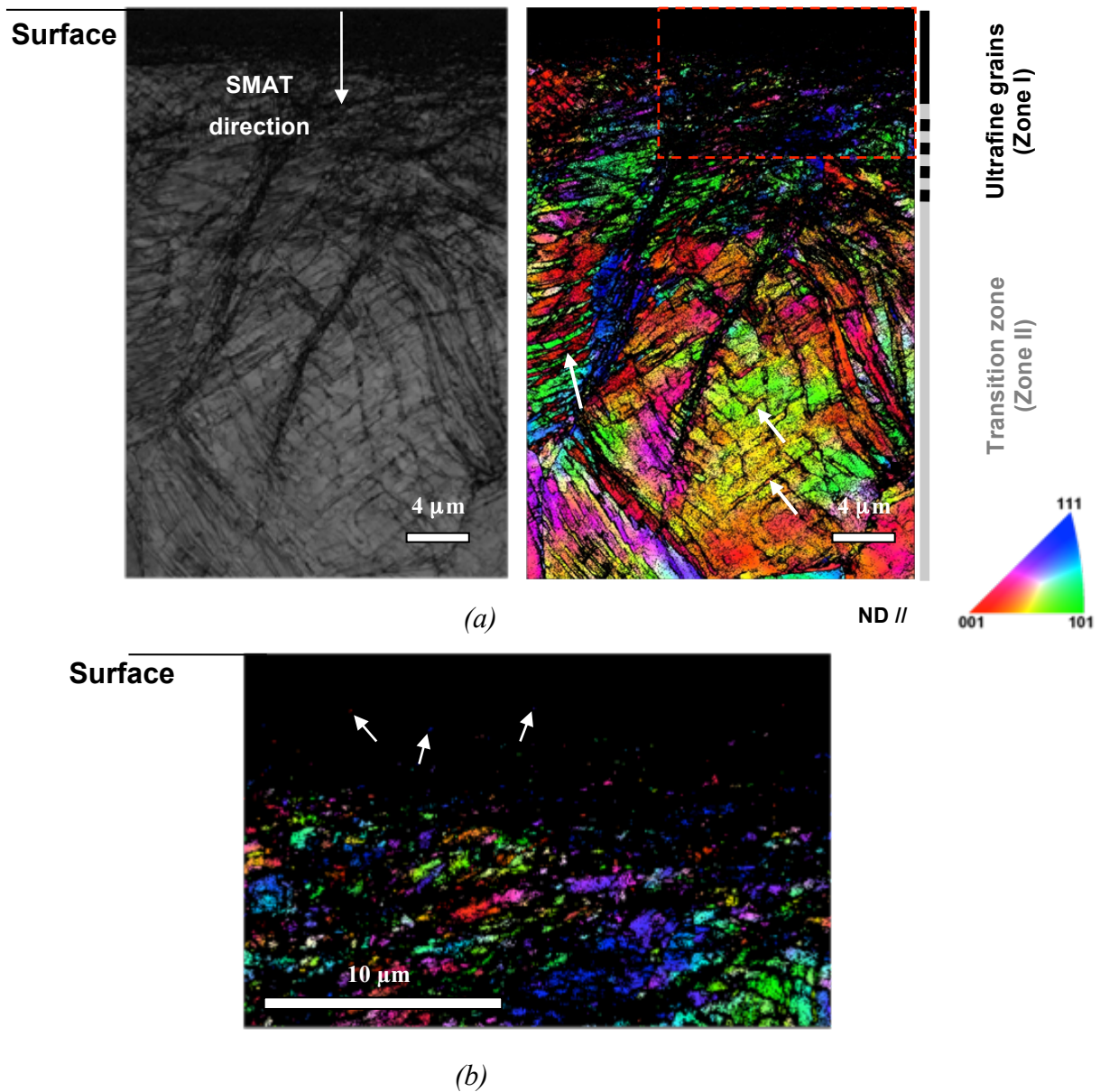
Fig. III. 4: (a) Typical example of EBSD maps of the cross section obtained after SMAT with a very fine step size (30 nm). (b): Close loop of the outlined zone in red in Fig. III.4a.

Fig. III. 4b is an enlargement of the outlined red zone that shows that in this extreme surface layer, only few points were indexed (arrowed). As the distance from the surface increases, the indexing rate increases and the EBSD technique starts recording fine domains that clearly originate from grain and subgrain divisions. Most of these domains are highly misoriented. At a distance of about 6 μm from the surface (top of Fig. III. 4b), most of these domains still have a largely sub-micrometric size. As the distance from the surface further increases and the local strain decreases, it

becomes easier to depict the presence of deformation twins (arrowed in the IPF map in Fig. III. 4a), as reported by Roland et al. (Roland et al. 2006; Roland et al. 2007).
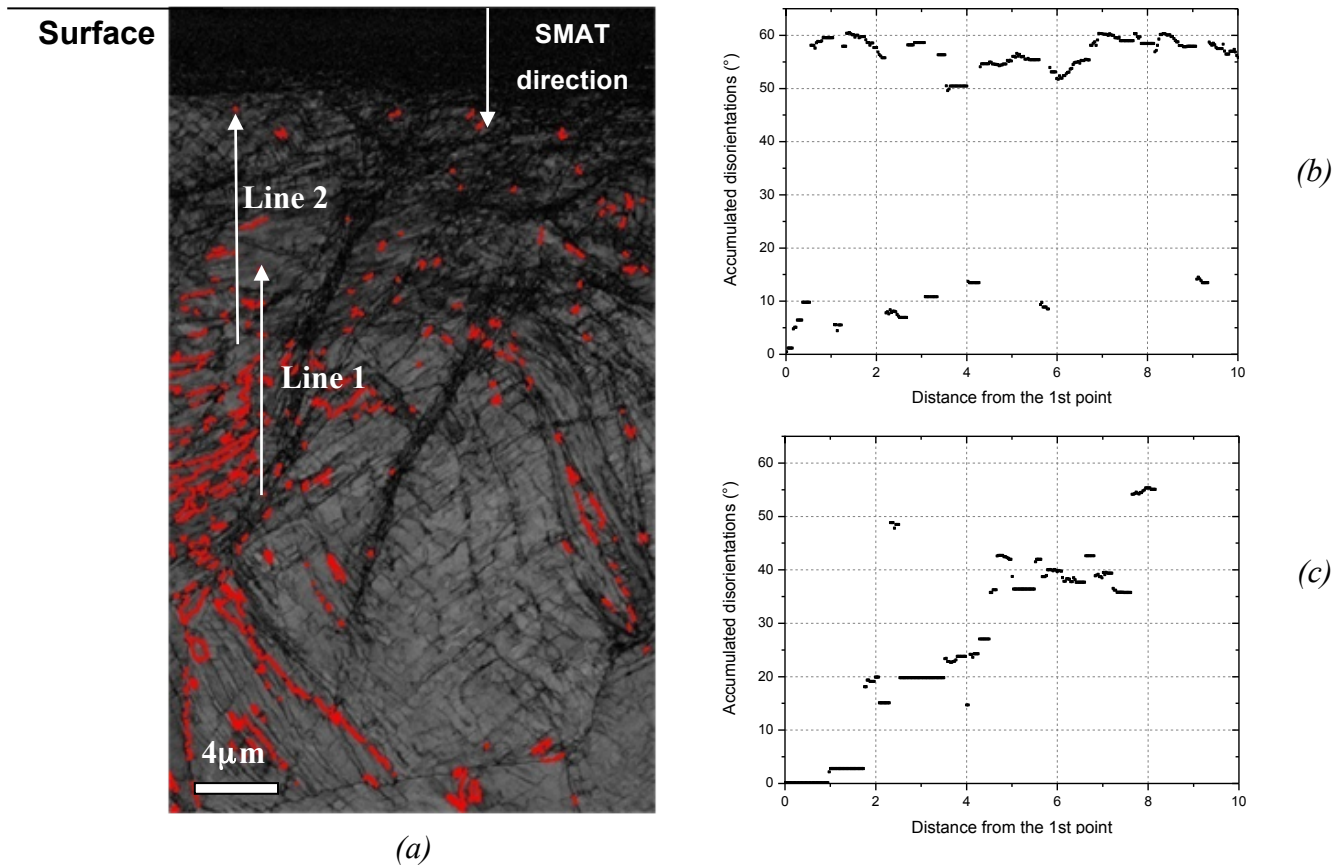
Fig. III. 5: (a) The Sigma 3 twin boundaries (111) <60°> map (red lines) and the evolution of misorientation (b) in the subsurface and (c) at the top surface.

Fig. III. 5 give more information concerning the misorientation degree within the microstructure in the same area. In the Band Contrast map in Fig. III. 5a are drawn red lines corresponding to the Sigma-3 ((111) <60°± 2>) twin boundaries. Consistently with the result of Roland et al (Roland et al. 2006; Roland et al. 2007), a high density of deformation twins is observed. It is also clear that, even if the BC map is revealing long and thin deformation twins, the exact (111) <60°> twin boundary misorientation is generally not maintained over long distances. As suggested by the variation of shades of colors in the IPF map in Fig. III. 4a, this is due to the accumulation of dislocations along the twin boundaries that creates a local misorientation gradient. For illustration, Fig. III. 5b and c present the local accumulated misorientation relative to the first point following the two white arrows. In Fig. III. 5b, a high number of Sigma-3 twin boundaries is detected and misorientation of about 10° can be depicted in the matrix between the twin boundaries. In Fig. III. 5c, closer to the surface where the level of strain sustained by the material is higher, in addition to a fewer number of Sigma-3 boundaries, broader and higher levels of accumulated misorientations are observed.

Clearly, this kind of high resolution EBSD map authorizes to depict the main features revealed by TEM concerning the grain refinement and associated deformation mechanisms(Lu, Liu, and Liu 2004). However, even if the analysis is much faster than a detailed TEM analysis, the drawback of such high-resolution map is the necessary limitation of the covered surface if one wants to keep a reasonable duration of analysis (here, for this small map, about 8 hours). Also, the statistical relevance of the observed phenomena may be questioned because the analyzed length on the surface remains of the order of the initial grain size (20 to 30 μm) and the depth of analysis is still restricted to about 40 μm, much below the depth of the area affected by the plasticity which may reach 200μm(Roland et al. 2007; Zhu et al. 2004).Therefore, other procedure, always using EBSD data, will be applied in order to quantitatively describe the plastic deformation imparted to the material, and in consequence the effect of the different processing parameters. In particular, it is important to be able to determine the thickness of the 3 different zones usually depicted in SMAT-ed samples: (i) the so-called nano-crystalline domain, or more currently for metallurgists the domain of UltraFine Grains (UFG) having largely sub-micrometric sizes, that correspond to the ultimate stage of grain refinement under heavy deformation, (ii) the transition zone where the initial micrometric grains are fragmented under heavy deformation and (iii) the deformed zone where the initial grains are simply plastically deformed.

It appears that it is possible to extract from EBSD maps important information on the plastic deformation induced by SMAT. It is then important to analyze differently the orientation maps obtained from EBSD measurements to get a quantitative description of the level of plastic deformation imparted to the sample and, in consequence, determine the effect of the processing parameters.

II. 2. 2   *Exploitation of the EBSD data in the development of a new method of quantification of the induced plastic deformation*

This section describes how to use data obtained from EBSD to depict, more rapidly and in a quantitative way, the overall mesoscopic plastic strain gradients generated at the material subsurface by the SMAT treatment. In his pioneer paper on non-homogeneous deformation, Ashby has introduced the distinction between statistically stored dislocations and Geometrically Necessary Dislocations (GND) (Ashby 1970). More details about the GND are given in the "Materials and experiments techniques" chapter. The GND accommodate the incompatibility of the elastic/plastic distortion, which arises only in the non-homogeneously deforming regions(Ashby 1970; Nye 1953; Kröner 1980). Thus, while the statistically stored dislocations -which develop in homogeneous deformation- have a predominant density at small strain, the amount of GND becomes more

important at high strain and its local density is actually proportional to the rotational of the elastic/plastic distortion(Nye 1953). Therefore, a good indicator of the plastic deformation imparted by the SMAT can be the distribution of the GND density as a function of the distance from the top treated surface. It is well established that the dislocation structure in a deformed material consists of cells, sub-grains and/or walls, which accommodate the misorientation between dislocation-poor areas. The quantification of the dislocation structure heterogeneity in deformed polycrystals by EBSD is then possible (see for example (Field et al. 2012; Dillien et al. 2010; Beausir and Fressengeas 2013)). As the strain imparted to the material increases, the size of these domains decreases and the average misorientation between them increases. Consequently, as will be seen hereafter, this evolution can be depicted for SMAT-ed sample by direct measurements of local misorientation at different depth using low magnification EBSD maps and the associated quantification of GND densities. However, at very high strain close to the surface, the ultimate stage of the deformation process under SMAT is the transformation of these domains in ultrafine grains having high angle grain boundaries within which dislocations are not stable anymore. In this regime, the properties of the material are not any more GND-governed but more closely related to the grain size (Hall-Petch effect). Thus, this switching between different types of microstructure configurations requires other indicators for following the structure evolution in the vicinity of the surface where the highest strains were imparted. In this case, for which the indexing rate by EBSD decreases significantly, the apparent grain size will be used as the main criterion. The details of the procedure for depicting quantitatively the microstructure evolution is given hereafter and illustrated in Fig. III. 6 and Fig. III. 7.

By omitting the elastic deformation, a part of GND density can be extracted from the orientation maps (Pantleon 2008). In the present work, raw orientation maps (without noise reduction) were used to extract the GND density according to the method proposed by Pantleon (Pantleon 2008). In order to quantify the GND densities only within the grains, the adjacent pixels across boundaries displaying a disorientation exceeding 5° were not considered in the calculation. Five components of the GND tensor (α), known also as the Nye tensor, can be determined from the 2D mappings (Nye 1953; Pantleon 2008).

Fig. III. 6a gives a map of the entry-wise norm of GND density tensor recorded with a step size of 200 nm. This step size is arbitrarily chosen to optimize the acquisition map duration (~ 8 hours). Note that for the sake of visual clarity, only the band contrast was plotted for densities smaller than 10% of the GND density maximum (see legend). In Fig. III. 6b are given the corresponding in-depth evolutions of GND density and indexation rate. It should be noted that the values of GND density are the average along each horizontal line parallel to the treated surface. The low GND

density observed at the top surface is not necessary due to the plastic deformation induced, but also probably to the low indexation rate in this zone.

At the top of Fig. III. 6a, is present the top surface black layer for which the indexation rate is nearly 0, as confirmed in Fig. III. 6b. In this last figure, it can be seen that below this layer, the density of GND increases continuously to reach a maximum at about 50 µm. At this maximum of GND density, the indexation rate is now about 65 %; the remaining 35 % of non-indexed data points are due to the high strain and grain subdivision mechanisms taking place, which still result in blurred or overlapped Kikuchi patterns and appear as black dots in the map. The low GND level in this low-indexed zone is then due to the very low size of grains. Actually, no dislocations can be observed below a given critical grain size. As the depth increases further, the GND density starts decreasing and reaches the initial level of the bulk material at approximately 180 µm. The indexation rate within this zone continues to increase and reaches a maximum of about 95 %. The difficulty is thus to depict quantitatively using relevant and reliable criteria the thicknesses of the different domains. For this, several criteria were selected and represented in Fig. III. 7.

In Fig. III. 7a are plotted, as a function of the distance from the top surface towards the bulk, the evolution of the average GND density (black dots), its derivative (solid blue line) and the evolution of the apparent grain size (red dots) obtained by the line intercept method along horizontal lines. The latter consists in placing horizontal lines (one line is placed on each pixel line along Y) on the EBSD map and counting the number of times a new grain boundary is intercepted. Using these three pieces of information, the thickness of the domains described before can be determined quite precisely.

(a)

(b)
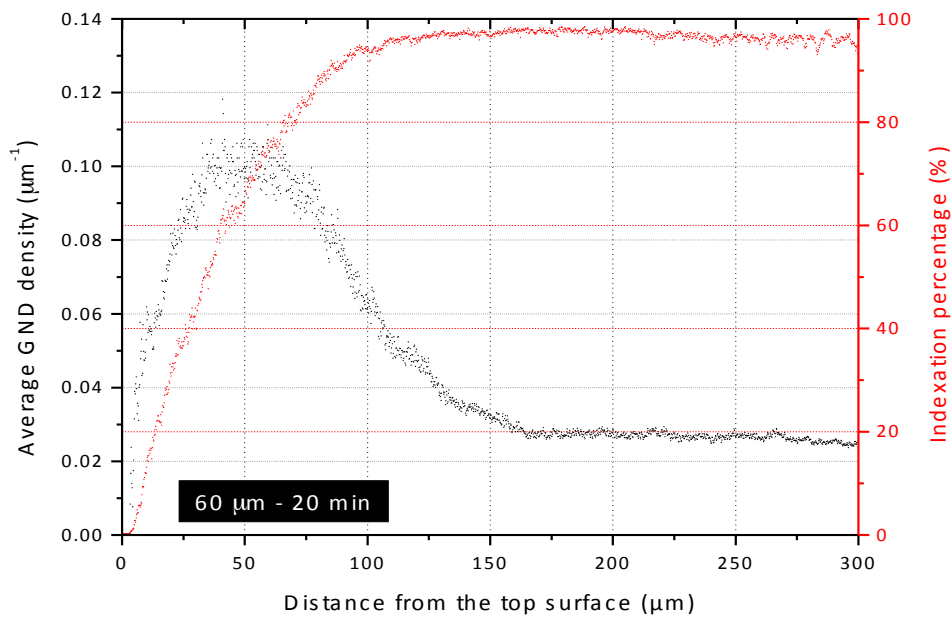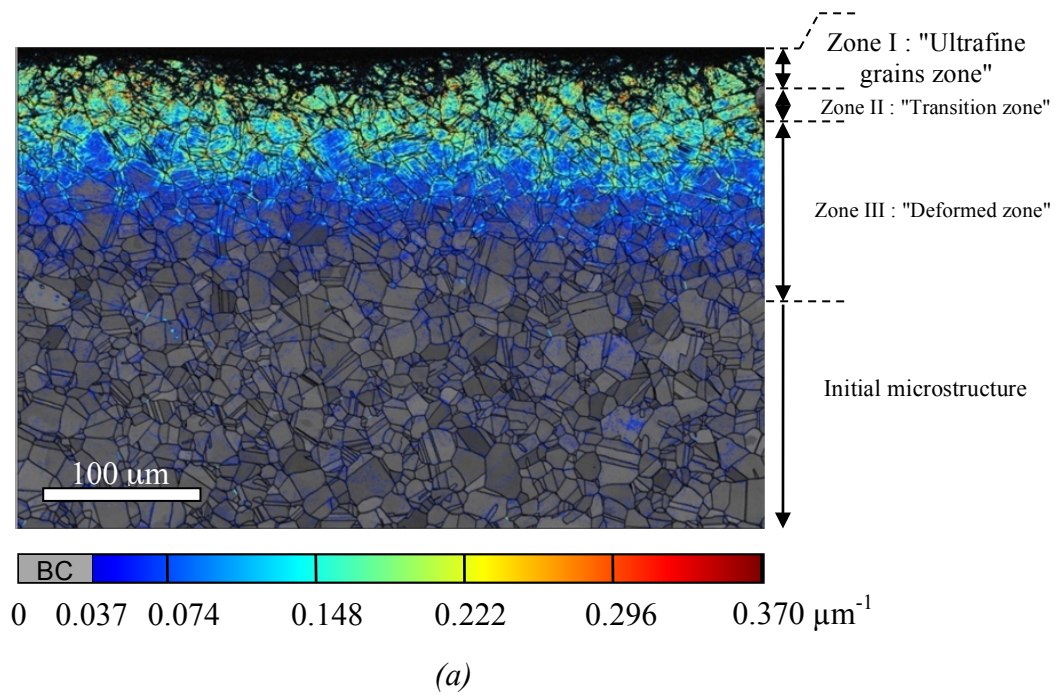
Fig. III. 6: (a) Map of GND density obtained from EBSD measurement (step size of 200 nm) in 316L stainless steel after 20 minutes SMAT with 60µm vibrating amplitude. For intensities less than 0.037 µm⁻¹ (bottom 10%), the Band Contrast (BC) was plotted. (b) The corresponding evolution of the average GND density (black dots) and the indexing rate (red dots) from the top surface.
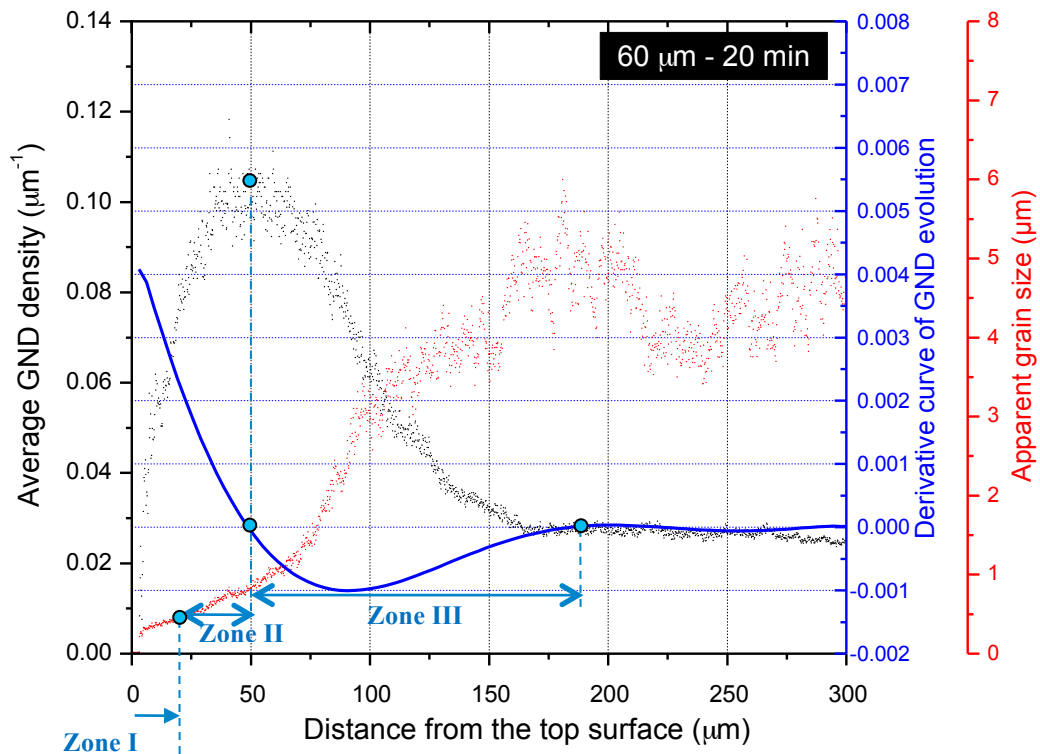
(a)
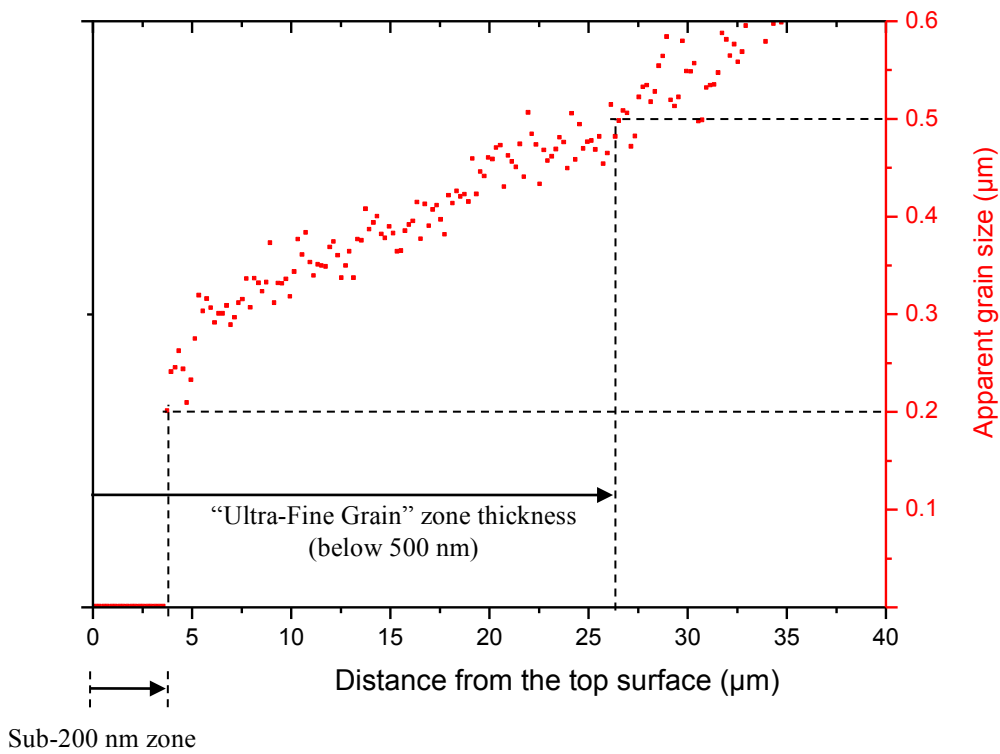
(b)

Fig. III. 7: (a) Evolution of the average GND density (black dots), its derivative (blue dots) and the evolution of grain size (red dots), (b) zoom of the grain size evolution within the first 40 μm.

The thickness of the UFG layer (Zone I) can be characterized by a corresponding grain size obtained by the line intercept method (red dots in Fig. III. 7a). In a fairly arbitrary way, two equivalent grain sizes were selected here to characterize this domain: a "nano" range below 200 nm and another having an ultrafine grain size below 500 nm. The 200 nm value was chosen because it is the step size used for the acquisition of the EBSD maps. So, sub-200 nm zones cannot be depicted by the EBSD analysis. These grain size ranges were fairly arbitrarily chosen because no conventional size range of the nano-crystalline domains is properly defined and a wide range of values are given in the literature. Using this criterion and Fig. III. 7b, which is an enlargement of the apparent grain size evolution near the top surface, the thickness of this first "nano" zone below 200 nm is about 4 μm while the sub-500 nm domain reaches about 26.5 μm.

The thickness of the "transition zone" (Zone II) can be depicted in Fig. III. 7a using the derivative of the GND density evolution. The derivative nullifies when the GND density reaches the highest level, which corresponds to the end of the transition zone. Thus, the transition zone stretches approximately down to a depth of about 50 μm. Using these criteria, the thickness of this transition zone, where the grains are significantly fragmented by the heavy deformation but do not reach the ultrafine grain range, is therefore about (50 – 26.5 μm) 23.5 μm.

Finally, going further within the depth of the material, the last characteristic zone – the deformed zone - (Zone III) is characterized by a continuous decrease of the GND density. The derivative curve in this zone is negative and nullifies when the GND density becomes low and constant in the unaffected zone, at about 183 μm. The thickness of this zone is then about (183-50 μm) 133 μm. In this zone, plastic deformation took place but the initial structure dominated by large grains is still visible. The apparent grain size, revealed by the line intercepts method, changes in this domain because of the formation of a few deformation twins and the presence of dislocations creating possible misorientation superior to 5°. It is also important to recall here that, even if the size of the grains in the initial material is about 20μm, the apparent grain size for the base material in Fig. III. 7a reaches a steady plateau at about 4.5 μm because of the presence of annealing twins that are counted as high angle boundaries in the automated analysis. The three so-obtained zones and their thicknesses are indicated in Fig. III. 6a.

This developed technique can be considered fairly precise for the determination essentially of the zones II and III. Actually, for the zone I, the thickness estimation is very sensible to the determination of the sample edge. The SMAT induces very high deformation near the top surface, leading to none of very low indexed zones. Another factor that should be considered is the surface roughness after SMAT. The beginning of zone I can also be affected by the formation of an "edge effect" during sample polishing for microscopic observations. Unfortunately, at this stage of this

work, these parameters could not be taken in consideration. The estimation of the zone I thickness is then done with the assumption that the layer is continuous and with no surface roughness.

Now that the procedure is developed, it will be tested on the AISI 316L treated under different SMAT conditions.

II. 3   Application of the quantification procedure: effected of the processing parameters

II. 3. 1   Application to the AISI 316L

The AISI 316L is treated under the conditions given in table 1 (section I). As it is well established that increasing the step size results in lowering the recorded GND density (Jiang, Britton, and Wilkinson 2013)*,* all samples were analyzed using exactly the same procedure and step size for EBSD measurements (200 nm) in order to compare all the samples and to avoid the step size effect between different maps. Fig. III. 8ashows the evolution of the GND density in six samples of the 316L stainless steel for which the vibration amplitude and treatment duration were varied, and to ease the comparison between the different samples, it also presents the different estimated thickness of the different constitutional layers as well as the total affected zone (*Fig. III. 8*b).

A first striking feature revealed by this analysis is that the depth of the overall affected zones depends very little on the tested processing conditions. Indeed, the two samples treated under 60 µm amplitude as well as the one processed under 80 µm for the shortest time (3 min) have a rather close affected depth around 180 µm. Only a long treatment of 20 min at the highest amplitude (80 µm) increases the overall depth by about 20% (220 µm). Comparatively, the differences in the thicknesses of the UFG and transition zones are much more important and depend very much on the processing conditions (Fig. III. 8b).

When using 100Cr6 balls, for the sample treated using the "softest" conditions (60 µm of vibration amplitude for 3 minutes), the so-called "Ultra-fine grain" domain corresponds to a 1.2 µm layer of sub-200 nm grains followed by a thickness of about 6.1 µm of grains in the 200-500 nm range. The thin size of the whole UFG layer (1.2+6.1=7.3 µm) indicates that the deformation imparted to the material leads to a limited fragmented layer. The subsequent transition zone has indeed a thickness of about 20 µm (19.7µm), which leads to a total thickness of "fragmented" zone of 27 µm (7.3+19.7=27µm) before reaching the so-called deformation zone.

(a)

(b)
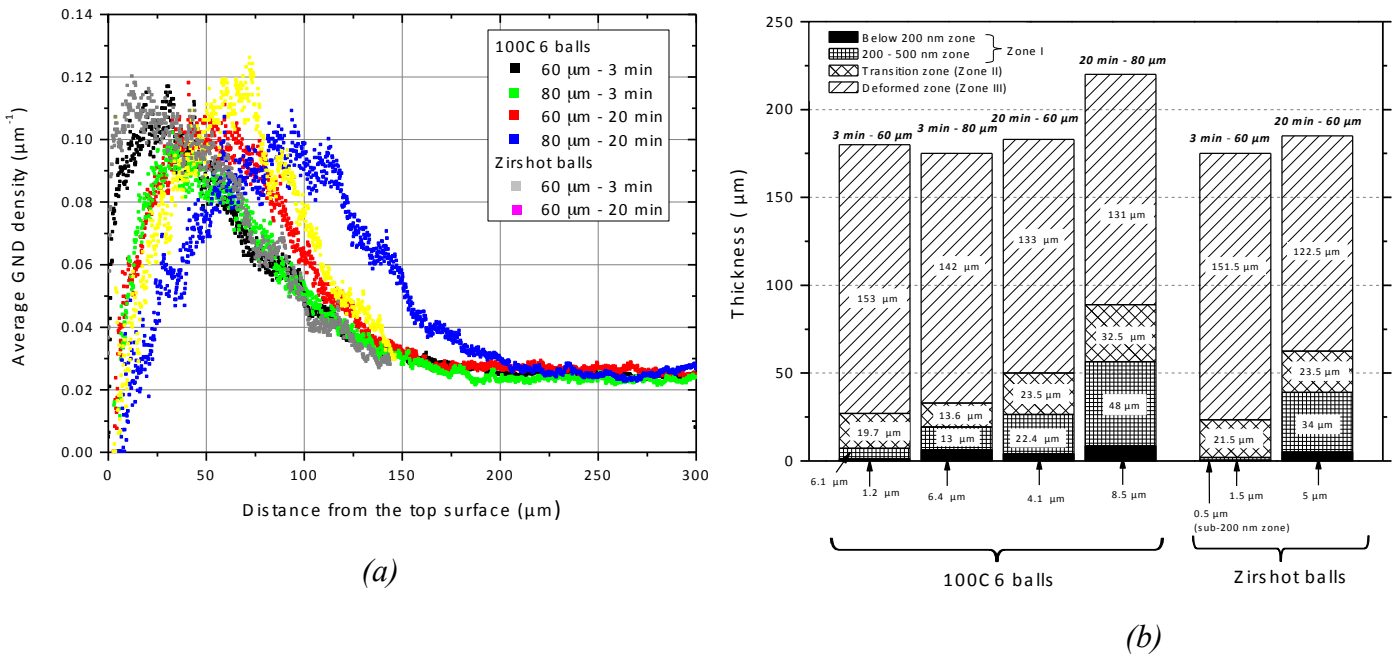
Fig. III. 8: Evolution of the average GND density from the top surface to the bulk for different SMAT conditions, (b) Thickness evolution of the different layers depending of the SMAT conditions.

Type of the affected domain	SMAT conditions			
	60 μm – 3 min	*60 μm – 20 min*	*80 μm – 3 min*	*80 μm – 20 min*
Overall affected zone (Zones I + II + III)	*180 μm*	*183 μm*	*175 μm*	*220 μm*
			x1.2 →	
Total fragmente zone (Zones I + II)	*27 μm*	*x 1.8* → *50 μm*	*33 μm* *x 1.8* →	*x 2.7* → *89 μm*
		x 1. 2 →		
'UFG' zones (Zone I)	*7.3 μm*	*x 3.6* → *26.5 μm*	*19.4 μm* *x2.1* →	*x 2.9* → *56.5 μm*
		x2.7 →		

Table III. 3: Thickness (from the top surface) of the different formed layers after treatment of the AISI 316L.

Increasing the vibration amplitude to 80 µm for the same treating time of 3 min has a moderate effect on increasing the depth of the total fragmented zone, which reaches only 33 µm

(6.4+13+13.6=33 µm). However, the higher vibration amplitude leads to a more advanced grain refinement process close to the surface. This leads to a total "Ultra-fine grain" domain increased by almost a factor of 3 (19.4 µm versus 7.3 µm), and corresponding to a successive 6.4 µm + 13 µm thick layers of sub-200 nm and 200-500 nm grains, respectively.

When the treatment duration in increased from 3 to 20 minutes, the thicknesses of the UFG domains are multiplied by a factor of about 3 or more while the overall fragmented domains increase by factors of about 1.8 and 2.7, under vibration amplitudes of 60 and 80 µm, respectively All the details are summarizes in Table III. 3.

To investigate the effect of the nature of the balls, the affected thicknesses of the samples treated under only the amplitude of 60µm for 3 and 20 minutes, and using the two types of balls (100Cr6 and Zirshot), are given in Table III. 4. After 3 min of SMAT, the UFG thickness is decreased by a factor of 2.7 when using balls of Zirshot, while the same zone thickness is increased by a factor of 1.5 at higher treatment duration (20 min).

The thickness of the total fragmented zones is almost constant at low treatment duration (3min) whatever the nature of the balls used. However, it is increased by a factor of 1.2 at high SMAT duration (20 min) when balls in Zirshot are used. It should be noted that this increase is related to the increase of UFG zones thickness, where the Zone II thickness remains similar when using 100Cr6 (50-26.5 = 23.5 µm) or Zirshot balls (62.5-39 = 23.5 µm).

The overall affected zone seems to be not sensible to the nature of balls used at low or high SMAT duration. The decrease of the UFG zones thickness of the D1A60T3Z sample may be related to the roughness of the surface or a low indexation rate in the extreme surface of this sample.

These results show that the developed procedure can be very interesting in the quantification of the induced plastic deformation by SMAT, and to depict fairly precisely the different defined layers thicknesses in the case of the AISI 316L. The procedure will be then applied to the AISI 660 treated with wider range of SMAT parameters.

Type of the affected domain	Amplitude of 60 µm			
	3 min		20 min	
	100Cr6 balls	Zirshot	100Cr6 balls	Zirshot
Overall affected zone (Zones I + II + III)	180 µm	175 µm	183 µm	185 µm
Total fragmented zone (Zones I + II)	27 µm	23.5 µm	50 µm *x 1.2*	62.5 µm
'UFG' zones (Zone I)	7.3 µm ÷2.7	2 µm	26.5 µm x1.5	39 µm

Table III. 4: Thickness (from the top surface) of the different formed layers after treatment of the AISI 316L.

II. 3. 2   Application of the GND procedure to the AISI 660 stainless steel

The SMAT conditions are given in Table III. 2 (section I). The ASISI 660 is chosen because, firstly, it is the subject of industrial research on materials treated by SMAT (AREVA), and also, it is interesting to investigate the effect of SMAT on more stable and harder austenitic stainless steel containing precipitates.

Fig. III. 9 are given typical Banc Contrast (BC) images and Inverse Pole Figure (IPF) maps obtained on a cross section of the D2A50T50 sample (in AISI 660). Here also the step size was kept at 200 nm for the EBSD analysis. The cross section morphology is similar to the AISI 316L one in the sense that three types of zones characterized by different microstructures is obtained. At the extreme top surface, a 'black' layer with very low indexation rate is observed (the so-called "Zone I"). Then, going further within the material, fragmented grains (Zone II) followed by deformed grains (Zone III) within which the plastic deformation signs are visible (white arrows). The zones I, II and III are represented in Fig. III. 9a only to indicate qualitatively the three characteristic layers in the orientation map.

(a)   (b)
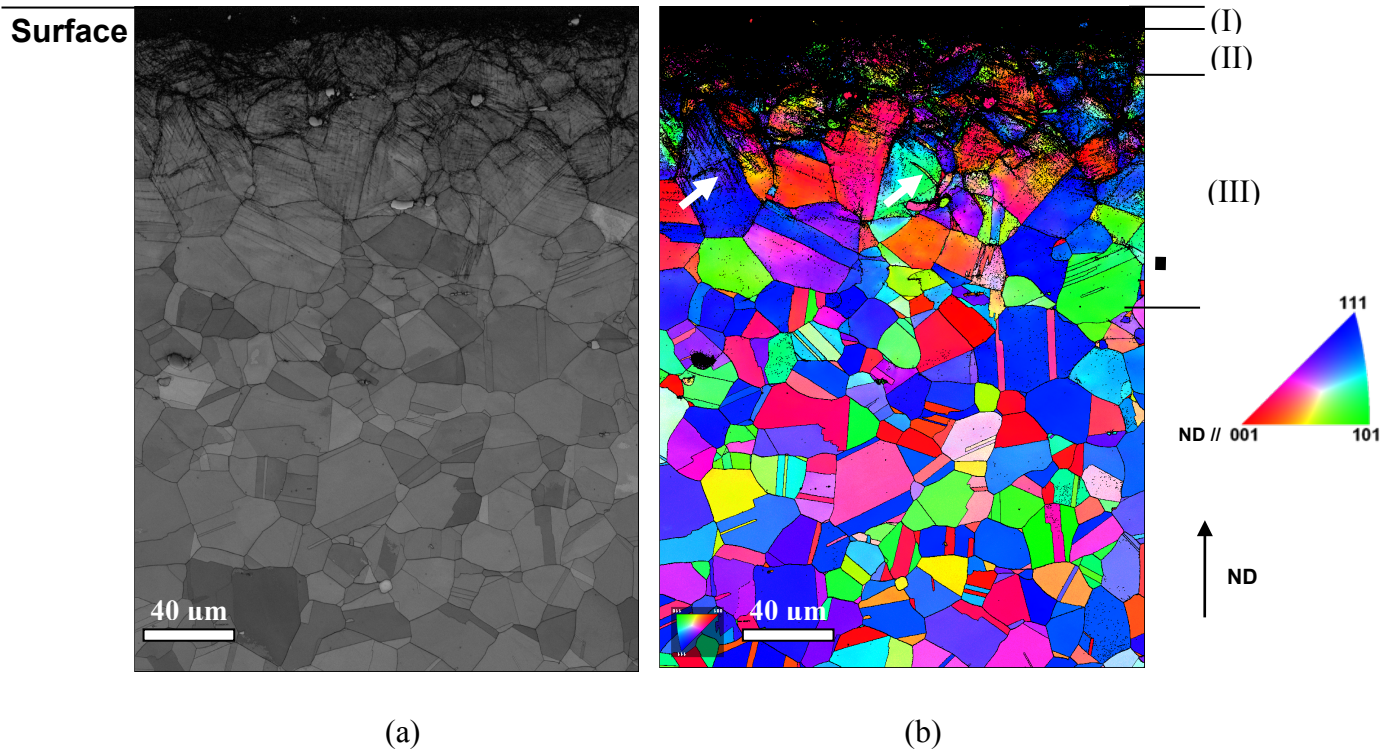
Fig. III. 9:Typical (a) Banc Contrast and (b) IPF maps of the cross section obtained on after SMAT of the AISI 660 with a step size of 200 nm (D2A50T0.50).

BC						
0	0.037	0.074	0.148	0.222	0.296	0.370 μm^{-1}
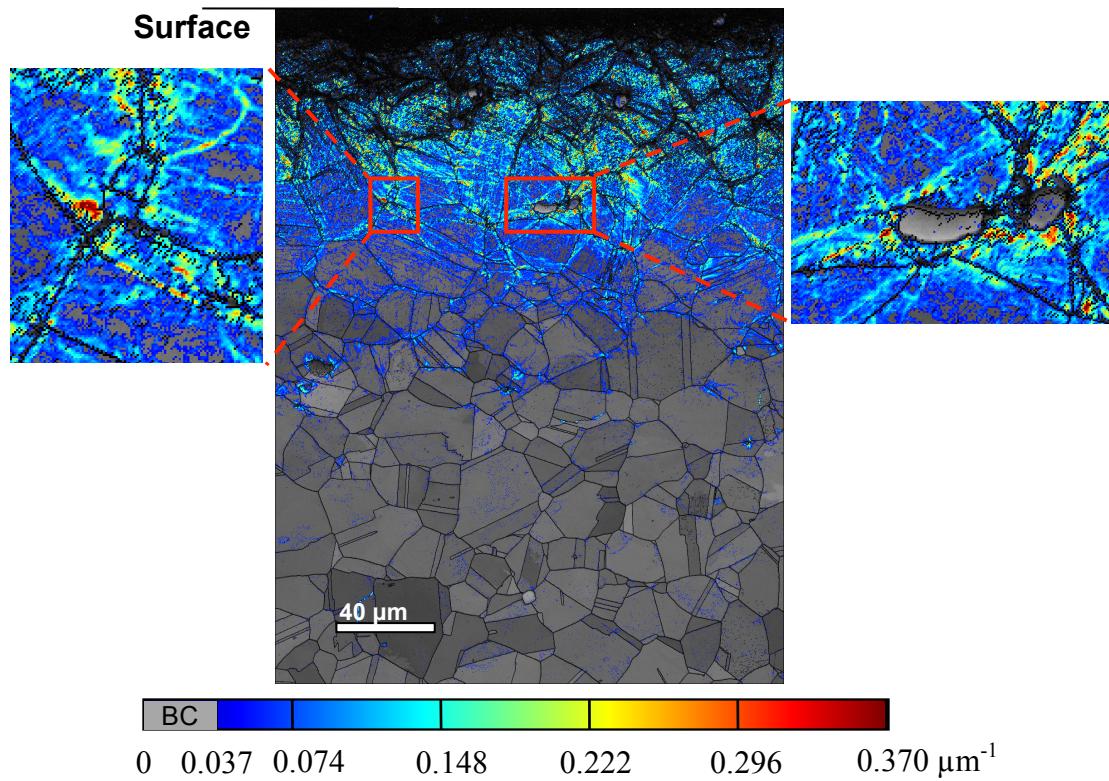
Fig. III. 10: Typical GND density map after the SMAT and close loop of examples precipitates region.

Fig. III. 10 gives the corresponding GND map of the same sample (D2A50T50). As for the previous presented GND maps, the BC is plotted for densities smaller than 10 % of the GND density maximum. As for the AISI 316L, the top surface layer (black layer) presents low GND densities, because of the low indexation rate (highly deformed zone). As the distance from the top surface increases, the GND density increases and seems to reach the maximum at a depth of about 50 µm, then decreases to reach the initial material level at approximately 200 µm. It is also interesting to note that high GND density is obtained near the precipitates (outlined ref zones in Fig 10), reaching higher values than the neighbor grains, as shown in the high magnification of the outlined red zones in Fig. III. 10. This phenomenon was observed by Humphreys et al in previous studies of the deformation of particle-containing alloys (F. J. Humphreys and Stewart 1972; F. Humphreys and Kalu 1990; F. Humphreys and Ardakani 1994) where it has been shown that the particles prevent a slip system, which is activated in the matrix, from occurring in a region adjacent to the particle. In this adjacent region, high misorientations can be observed.

To gain more information about the evolution of GND density as function of the SMAT parameters, the procedure developed in the previous section is applied to all the AISI 660 samples. The evolutions of GND density as a function of the distance from the surface are given in Fig. III. 11 and the different thicknesses estimated from these curves (using the criteria defined at the beginning of this chapter) are given in Fig. III. 12. The evolutions of the UFG (Zone I) and transition (Zones II) as well as the deformed (Zone III) thicknesses are then depicted. It should be noted that in this particular case (AISI 660), the derivative of the GND evolution curve in the deformation zone is very sensitive to the perturbations (due to precipitates visible in Fig. III. 10), the limit of the deformation zone can be under or overestimated using the derivative criterion. This is why it is estimated simply by the linear fit of the initial material GND level.

From Fig. III. 11, the presented curves have almost the same form as the ones obtained on the AISI 316L treated by SMAT in the previous sections, where the average GND density increases continuously to reach a maximum, then decreases to reach the GND density level in bulk material. A notable difference with the AISI 316L is the apparition of peaks at different locations on the GND curve. These peaks are originated from the concentration of GND around the large precipitates, as shown in Fig. III. 10b.
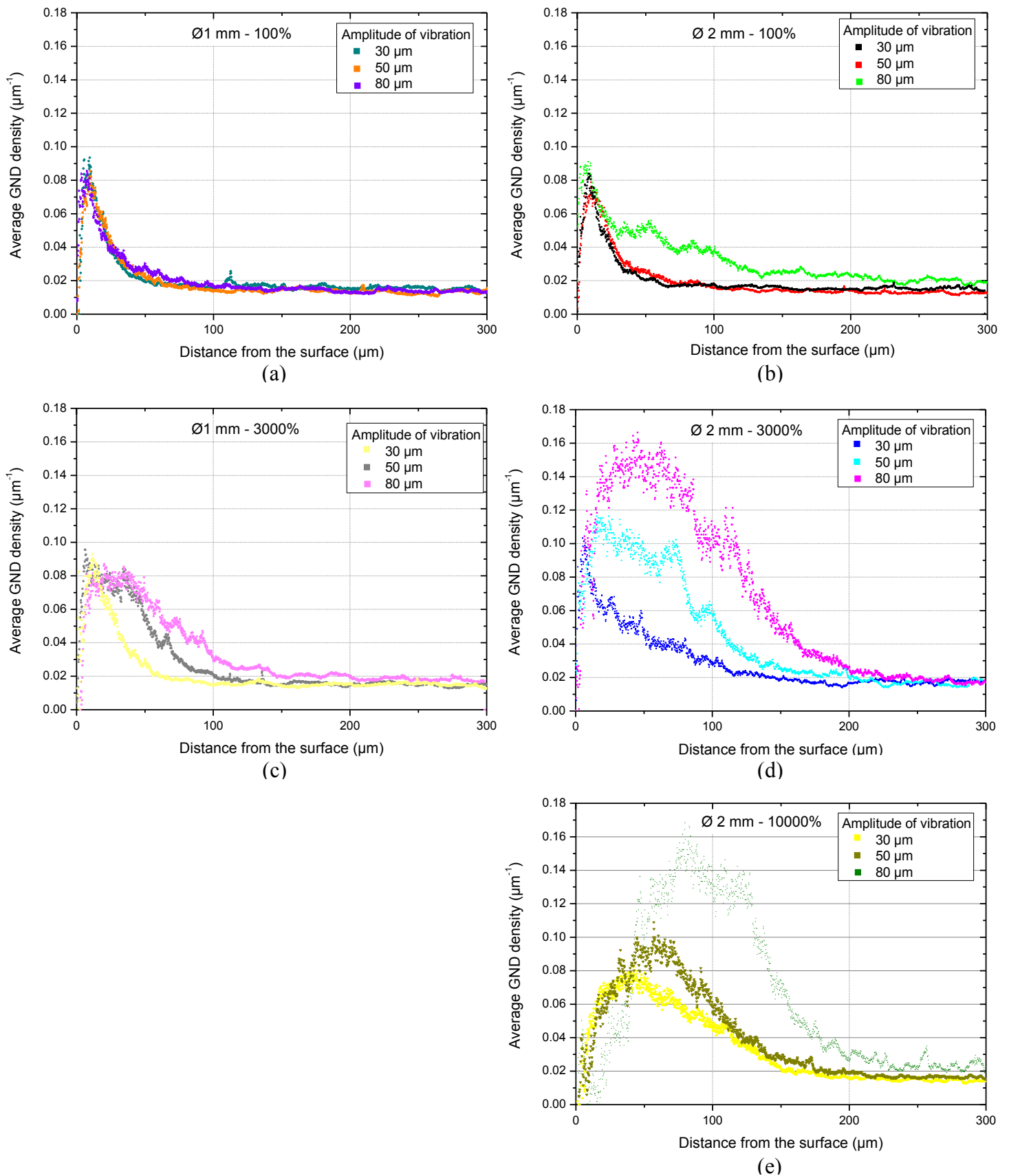
Fig. III. 11: In-depth evolution of the GND density for different amplitudes of vibrations, covering ratios and balls diameter.

Concerning the effect of the SMAT parameters on the zones thickness, Fig. III. 11a and c give the evolution of the GND density for the samples treated with balls of 1 mm diameter. At 100 % of covering ratio (Fig. III. 11a), the three treated samples have GND density evolutions which are quite similar near the top treated surface. However, a difference is observed in the deformed zone, where GND density seems to be higher under 80 μm and 50 μm of vibration amplitude, and the GND level of the initial material is reached at deeper depth than for the sample treated under 30 μm. With higher covering ratio (Fig. III. 11c), no significant changes are observed when the amplitude of vibration remains low (30 μm), where the evolution of the profile is quite similar to the samples treated under 100 % of covering ratio under the same amplitude. However, when the amplitude increases from 50 to 80 μm, the affected layer seems to be thicker. These results are confirmed by the estimations of the different characterized zones, given in Fig. III. 12, where the overall affected depth increases respectively with the amplitude of vibration for the two covering ratios. In addition, the thicker thickness of the fragmented zone is obtained at longer treatment duration (3000%).

For balls of 2 mm diameter, the evolutions of GND density for different covering ratios (100, 3000 and 10000 %) are given in Fig. III. 11b, d and e. At low covering ratio (100 %), the evolution of the GND density under 30 and 50 μm seems to be quite similar to the samples treated with balls of 1 mm diameter (in Fig. III. 11a). When the vibration amplitude is increased to 80 μm, the maximum of GND density remains constant, but the affected depth is higher and reaches about 175 μm.

When the covering ratio is increased from 100 to 3000 %, the effect of the balls diameter is more visible, as shown in Fig. III. 11d. Both the maximum GND density and corresponding depth are increased when the amplitudes of vibration are 50 and 80 μm.

Comparatively, increasing further the covering ratio (treatment duration) from 3000 to 10000 % has a direct effect on the position of the maximum of GND density, corresponding to the fragmented zones (Zones I and II), while the overall affected zone thickness seems unchanged.

These evolutions are clearly confirmed in Fig. III. 12. Different information can be extracted from this graph. On one hand, the effect of the vibration amplitude is visible under all the covering ratios and for the two ball diameters. In fact, the overall affected thickness increases when the vibration amplitude increases from 30 to 80 μm. It should be noted that under the covering ratios of 3000 and 10000 % (balls of 2 mm diameter), the thickness of the overall affected layer does not increases significantly for amplitudes of vibration of 50 and 80 μm.

On the other hand, the ball diameter (when increasing from 1 to 2 mm) does not seem to have an important effect on the zone thicknesses when the covering ratio is 100 %. Only an increase of the deformed zone is observed under the amplitude of vibration of 80 μm.

At higher covering ratios (3000 and 10000 %), the effect of balls size is more visible. Indeed, higher overall deformed zones are obtained under the whole range of amplitudes of vibration. It is also important to note that almost similar overall deformed zones are obtained under the two covering ratios of 3000 and 10000% for the amplitudes of vibrations of 50 and 80 μm. However, it is clearly observed that the thicknesses of the fragmented zones are higher at the covering ratio of 10000 %.
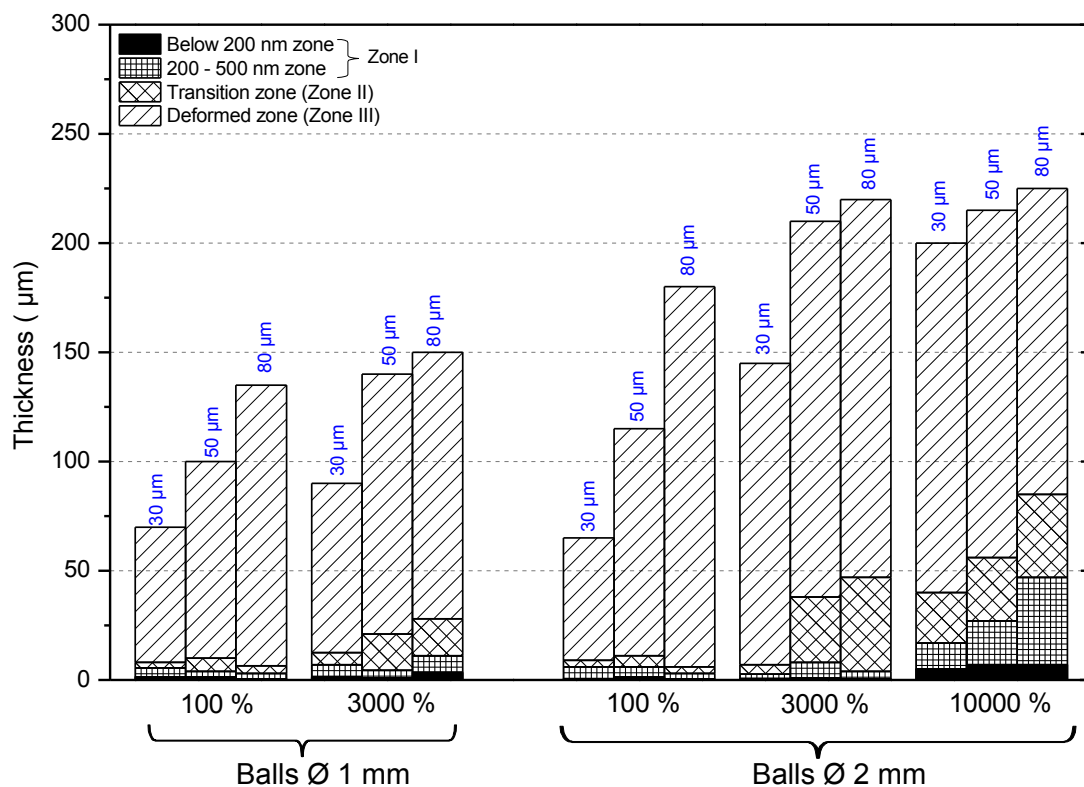
Fig. III. 12: Thickness evolution of the different layers of the AISI 660 SS for balls diameters of 1 mm

To observe more clearly the effect of SMAT parameters, the evolutions of the different layers thicknesses as function of the vibration amplitude and the covering ratio are given in Fig. . To ease the comparison, the evolutions were fitted using a linear function, and the slope is noted on the curves. Under the softest conditions (Fig. a), it is observed that only the deformed zone is significantly affected by the increase of the vibration amplitude, where the thickness increased from about 60 to 130 μm. The UFG and transition zone thicknesses remain stable and in the same range (below 5 μm). Using balls of 2 mm diameter (Fig. b) does not have an important effect on the evolution of the UFG and fragmented zones thicknesses, which are quite similar to the ones obtained with a lower diameter; while the overall affected depth increases from about 60

to170μmwhen the amplitude increases from 30 to 50 μm. It should be reminded (as mentioned in the material and experiments chapter) that the balls at the beginning of the experiment cover 50 % of the sonotrode surface. Therefore, when the balls diameter is multiplied by 2, the balls number is in fact divided by 4. As the covering ratio is determinate by the surface aspect, 100 % covering ratio is reached after a slightly longer SMAT duration with larger balls.

Increasing the covering ratio from 100 to 3000 % (for balls of 1 mm diameter) results essentially in the formation of a thicker transition zone, which increases from about 5 (under 30 μm of vibration amplitude) to about 17 μm (under 50 and 80 μm of vibration amplitudes) as shown in Fig. c. In addition, the effect of balls size is more noticeable at 3000 % of covering ratio than at 100 %. As it can be observed in Fig. d, the transition and deformed layers thicknesses were increased from about 5 to 42 μm, and from 140 to 175 μm, respectively.

When the covering ratio is further increased to 10000 %, the thickness of the sub-200 nm zone is higher that under covering ratios of 100 and 3000 %, and remains stable at the different amplitudes of vibration (30 to 50 μm). The 200-500 nm and transition zone thicknesses are significantly increased within the range of the 30-80 μm of vibration amplitude, from about 12 to 35 μm, and from 22 to 32 μm, respectively. The deformed zone thickness remains almost constant when the vibrations amplitude increases from 30 to 80 μm, having a thickness of about 160 to 140 μm, respectively.

To describe more in details the effect of the SMAT parameters on the deformed zone evolution, Fig. III. 14gives the evolution of this zone thicknesses as function of the amplitude of vibration for the samples treated with balls of 1 and 2 mm, and for covering ratios of 100, 3000 and 10000 %. From this figure, when the covering ratio is 100 % (the black and red lines), the thickness of the deformed layer is approximately the same when using balls of 1 or 2 mm diameter, except at the highest amplitude of vibration, where the deformed layer thickness reaches about 170 μm when using balls of 2 mm diameter. This latter significantly increases under covering ratios of 3000 and 10000 % when balls of 2 mm are used. It can be considered that for these two samples the deformed layer thickness is in the same range.
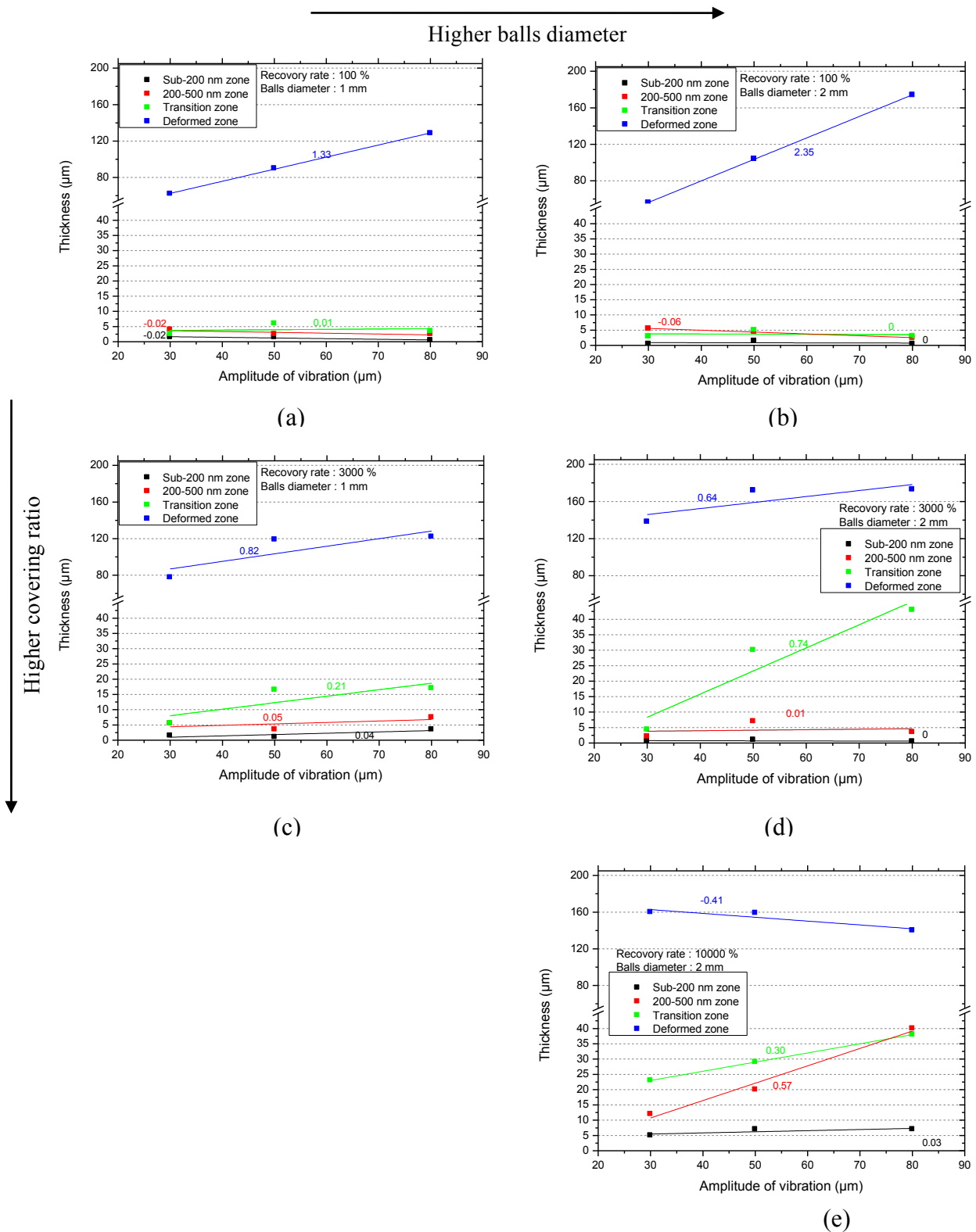
Fig. III. 13: Thickness evolution of the three formed layers as function of the amplitudes of vibration for different covering ratios: (am) 100 %, (c, d) 3000%, and (e) 10000 %.

For the sample treated under 3000 % covering ratio (blue curve), the thickness increases from about 140 to 170 μm when the vibration amplitude increases from 30 to 80 μm. When the treatment duration is longer (covering ratio of 10000 %), the thickness of the deformed layer remains in the

same range as under 3000 % of covering ratio, where it is about 160 µm for the vibration amplitudes of 30 and 50 µm, and decreases slightly under the highest vibration amplitude (80 µm). A saturation effect in term of the induced-defects density seems to be present. It can be also shown by the decrease of the curves slope (in Fig. III. 14).
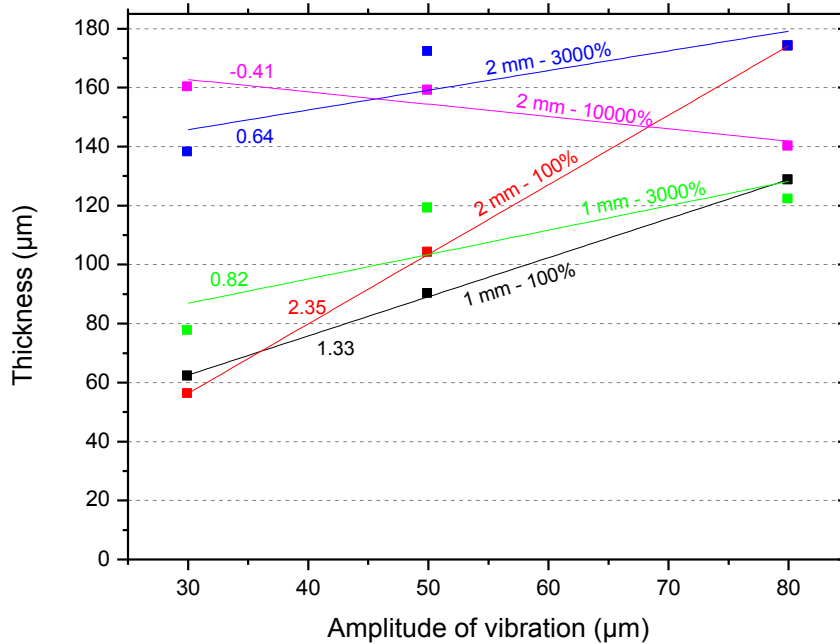
Fig. III. 14: Evolutions of the deformed zones thicknesses as function of the amplitude of vibration.

It is also clearly observed that the maximum of the average GND density depends on the SMAT parameters. This is illustrated in Fig. III. 15. This figure shows that, whatever the amplitude of vibration, the maximum of the GND density (calculated along each X-line) is constant for the samples treated with balls of 1 mm reaching about 0.08 µm^{-1}. When using the 2 mm balls and under low covering ratio (100 %), the maximum of GND is quite identical to the samples treated with 1 mm ones. However, it can be clearly seen that this maximum increases from 0.10 to approximately 0.15 µm^{-1} for the covering ratio of 3000 %, and from about 0.07 to 0.14 µm^{-1} for 10000%. In comparison with the maximum that can be reached using our criterion ($\frac{maximum\ of\ disorientation}{step\ size} = \frac{5\times(\pi/180)}{0.2} = 0.43$ µm^{-1}), the maximum GND calculated from our EBSD maps gives values 3 times lower than this maximum. Actually, the latter one is reached in the case where from one pixel to another along the X-direction with a step size of 0.2 µm, the disorientation is 5 °. However, in the analyzed maps, the misorientation can reach 5° but not along the whole X-line, which lower the X-direction average disorientation, and thereby the average GND density.
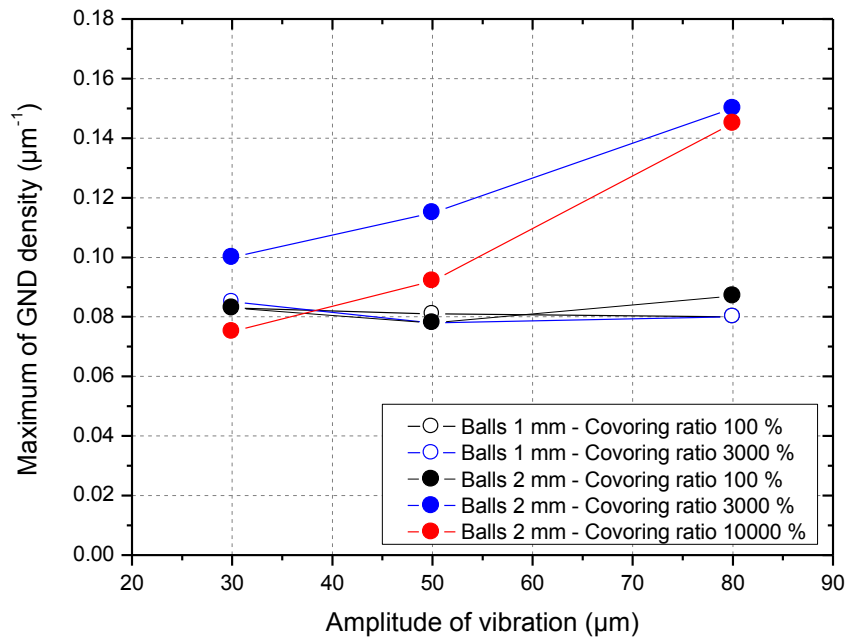
Fig. III. 15: Evolution of the maximum of the GND density as function of the amplitude of vibration, balls diameter and covering ratio.

To summarize, these comparisons show that:

- Increasing the vibration amplitude has a slight influence on the sub-500 nm layers except when using balls of 2 mm diameter and high covering ratio (10000 %), where the thicknesses of the 200-500 nm zone increases significantly and reaches about 45 μm when the vibration amplitude is 80 μm.

- The transition zone thickness seems to be not sensitive to the increase of the amplitude of vibration when the covering ratio is 100%, while it increases under higher covering rates of 3000 and 10000 %. The highest increase was observed for the covering ratio of 3000%.

- For the deformed zone, the thickness is sensitive to the increase of the amplitude of vibration when using the covering ratio is 100 %, while this effect is less visible under higher covering ratios. A saturation effect is even observed under more severe conditions (Diameter of 2 mm, covering ratios of 3000 and 10000 %), where the overall affected thickness remains quite stable when the amplitude of vibration increases.

II. 4   Discussion

The AISI 316L and 660 stainless steels have been treated by SMAT under different processing parameters. As observed for severe plastic deformation treatments, grain refinement of coarse-grained materials under SMAT involves various dislocation activities and the creation of subgrain boundaries. Using raw orientation maps obtained from the ESBD measurements, the microstructure and general features on the surface layers were then characterized. The new established procedure for quantifying the effect of processing parameters allowed to determinate precisely the thickness of the different layer. The discussion in this part will be divided into two essential parts. Firstly, the deformation mechanisms under the SMAT as well as a comparison between the AISI 316L and AISI 660 are discussed. Secondly, the effects of the SMAT parameters on the microstructure evolution are explained.

II. 4. 1   Deformation under the SMAT

II. 4. 1. a The deformation and nanocrystallization mechanisms and comparison between the AISI 316L and AISI 600 stainless steels

The mechanisms of grain refinement for the AISI 316L stainless steel have been detailed using Transmission Electron Microscopy (TEM) by Roland et al. (Roland et al. 2006; Roland et al. 2007). At low strain, the microstructure is characterized by high density of mechanical twins and dislocation arrays. As the strain increases, twin-twin interactions occur which subdivide the original austenitic grains into smaller blocks and, ultimately, lead to the formation of randomly oriented nanocrystallites (50 ~ 400 nm) involving boundary sliding and rotation of crystalline domains. Consequently, SMAT produces gradients in grain size and structural defects through the depth below the surface. The magnitude of this gradient, which is directly related to the local strain sustained by the material, depends on the numerous processing parameters.

Concerning the specific deformation of these austenitic stainless steels, some comments need however to be made. First, as the deformation twins are often very fine, many of them are not directly depicted in the map with a step size of 200 nm. As sufficient amount of misorientation is generated by the plastic deformation along these twins, it is however possible to see them in the GND density map as shown in Fig. III. 16, done with a low step size (50 nm). Second, it is also worth noting that the nucleation of strain induced martensitic variants at twin-twin boundaries previously reported in the 316L stainless steel treated by SMAT (Roland et al. 2006; Roland et al. 2007) was not revealed in the present study by EBSD neither also by XRD and TEM.

As the grain fragmentation process requires a sufficiently high amount of multidirectional impacts, the increase in the treatment duration from 3 to 20 min has a significant effect on the thicknesses of the UFG and transition zones of the AISI 316L, where the combination of dislocations is the major driving mechanism.
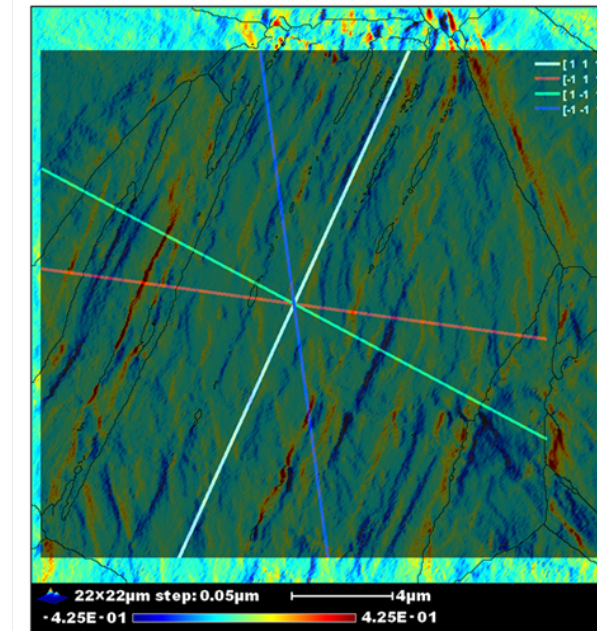
Fig. III. 16: Example of GND density distribution in a deformed grain carried out with a step size of 50 nm
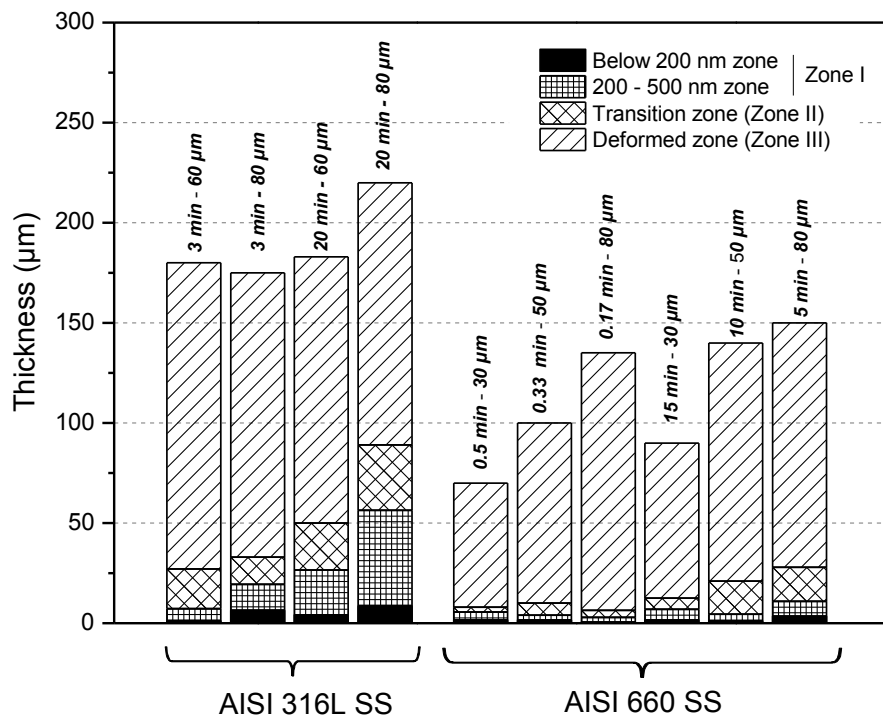
Fig. III. 17: Comparison of the different zones thicknesses after SMAT (balls of 1 mm diameter) of the AISI 316L and AISI 660 stainless steels.

As for the AISI 316L, for the deformation of the AISI 660, a graded microstructure is obtained after SMAT. However, there is a notable difference in comparison with the AISI 316L. Actually, the AISI 660 is characterized by a higher SFE (80mJ/m²) than the AISI 316L (38 mJ/m^2), and shows then extensive dynamic recovery which do not undergo the mechanical twinning and thereby the strain hardening. More comparison elements are given in the following section.

II. 4. 2   Evolution of the affected depths as function of the stainless steel nature (AISI 316L versus AISI 660)

As shown in Fig. III. 17, the whole affected zone of the AISI 660 is thinner that the AISI 316L one. The total fragmented zone of the AISI 316L is clearly thicker. To illustrate this, the two samples in AISI 316L (D1A80T3) and in AISI660 (D1A80T5) are compared. These two samples are treated under the same amplitude of vibration and with identical balls diameter. Only the AISI660 treatment duration is higher (5min against 3min for the AISI 316L). This difference is originated, as explained in the first section of this chapter, from the fact that the covering ratio is used for treating the AISI 660, while the duration is chosen for the AISI 316L.

On one hand, to explain the difference of the overall affected thicknesses, regarding the stress distribution within the material depth and according to Hertz theory (Cornet and Deville 1998), the maximum of shear stress is reached at the sub surface (as shown in Fig. III. 18). A schematic figure of the stress evolution as a function of the distance from the top surface is given in Fig. III. 19. The curve gives the typical stress distribution within the material in the case of a ball-plan contact. In this figure, the yield strength of the AISI 316L and 660 stainless steels are also represented. The depths are not given because the aim of this figure is to compare qualitatively the two materials. As mentioned in the "Materials and Experiments techniques" chapter, the yield strength of the AISI 316L and 660 are about 200 and 660 MPa, respectively. From this figure, it appears clearly that the whole affected depth of the AISI 316L must be more important than in the AISI 660 one.
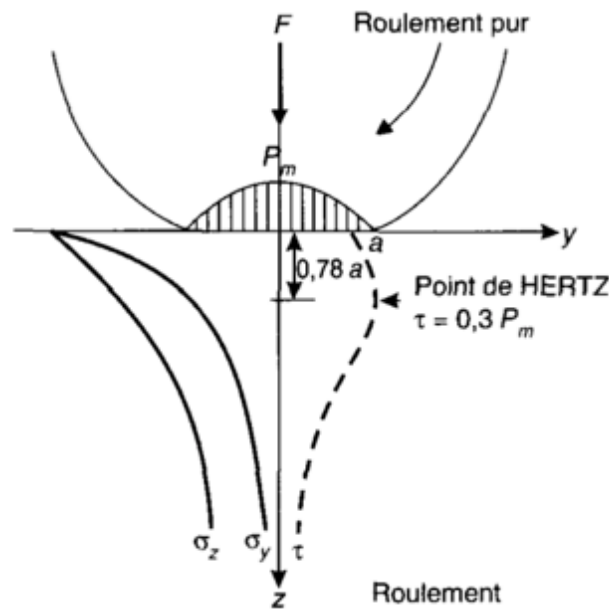
Fig. III. 18: Stress distribution in a sphere-plan contact (Cornet and Deville 1998)
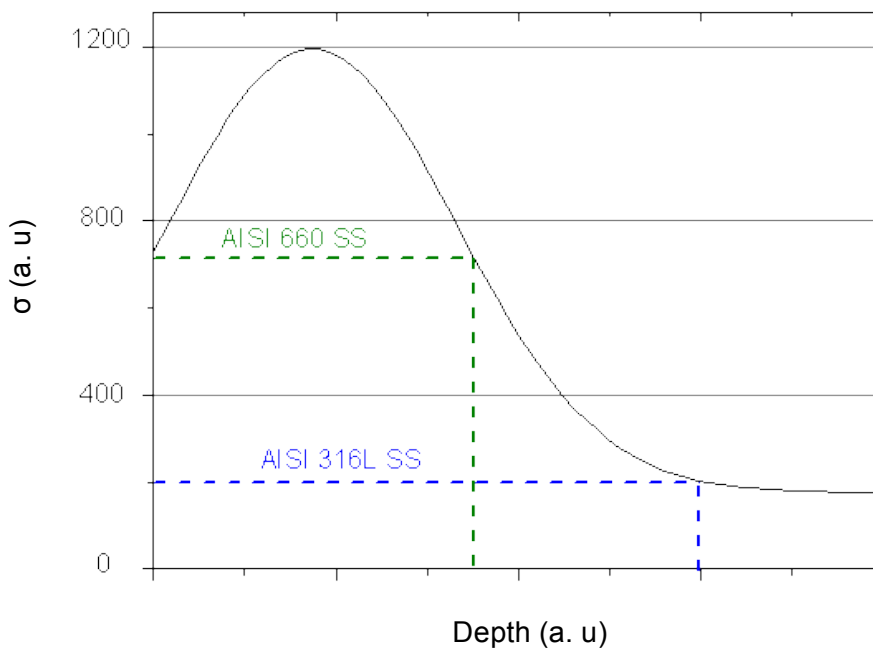
Fig. III. 19: Schematic representation of the stress distribution as function of the distance from the treated surface in the case of ball-plan contact.

On the other hand, it is also interesting to discuss the difference in the fragmented zones (Zones I + II) thicknesses between the two steels (as observed in Fig. III. 17). Comparing two samples treated at quite similar conditions (samples D1A80T**3** in AISI 316L and D1A80T**5** in AISI 660), the thickness of the fragmented zone represents about 8 % of the overall affected zone of the D1A80T3 sample (in AISI 316L), while it is only about 16 % for the AISI 660 (D1A80T5 sample). This can be explained by the Stacking Fault Energy (SFE) of the two materials. Because of the

difference in chemical composition (Lacombe and Baroux 1990), the SFEs of the AISI 316L and AISI 600 are about 20 and 80 mJ/m², respectively. The AISI 316L is characterized by a low SFE, promoting the formation of twins induced by the plastic deformation. This initiates the fragmentation mechanisms, where the austenitic grains are subdivided into smaller blocks because of the twin-twin interactions. When the strain increases, the AISI 660 is characterized by a high SFE (80mJ/m²), and shows extensive dynamic recovery. Comparatively, it does not undergo mechanical twinning and thereby the strain hardening is less effective. It seems clear that the SFE and the mechanical properties of the materials have a direct effect on the deformation mechanisms that occur during SMAT and on the thickness of the affected zones.

II. 4. 2. a Effect of the SMAT parameters on the microstructure refinement:

The developed procedure of plastic deformation quantification allowed to describe the effect of the individual SMAT parameters on the microstructure evolution (in section II.2 and II.3). It is now interesting to discuss the results. Therefore, this section focuses on the energy transmitted by the balls to the surface. Hereafter are detailed the calculations used to estimate the cumulated energy. The equations are issued from the work of Thiriet et al.(Thiriet 2010).

Firstly, assuming that the sonotrode movement is sinusoidal and the balls store energy at the contact with the sonotrode, the sonotrode displacement is following the equation:

$$u = \frac{A}{2} \cdot cos(2\pi.f.t) \quad \textit{Eq. III. 1}$$

Where A and f are respectively the sonotrode amplitude and frequency of vibration, and t is the treatment duration.

The speed of the sonotrode is then the derivative of the displacement:

$$\frac{du}{dt} = v(t) = -A.\pi.f.sin(2\pi.f.t) \quad \textit{Eq. III. 2}$$

The maximum of speed reached by the sonotrode is:

$$v_{max} = A.\pi.f \qquad \textit{Eq. III. 3}$$

The ball weight is simply given by:

$$m_b = \frac{\pi}{6}.\rho.d_b^3 \quad \textit{Eq. III. 4}$$

Where ρ is the ball material density (kg.m^{-3}) and d_b is the ball diameter (m).

The maximum kinetic energy stored by the ball is then given by:

$$Ec_{max} = \frac{\pi}{12}.\rho.d_b^3.(A.\pi.f)^2 \qquad \textit{Eq. III. 5}$$

The total cumulated energy at the surface can be expressed by the following equation:

$$E_{tot} = E_{cmax} \cdot N_b \cdot t \cdot Ni \qquad\qquad Eq.\ III.\ 6$$

Where E_{tot}: the total energy accumulated at the top surface (J),

Ec: maximum of the kinetic energy of one ball (J),

N_b: the number of balls,

Ni : number of impacts per min,

t : the treatment duration (min).

The number of impacts per seconds is missing in the present study, because no experimental measurements were available. As the aim is to compare the samples relatively, it will be given equal to 1.

The balls number is related to the balls diameter. Actually, the criterion used for the SMAT is that the balls should cover 50% of the sonotrode surface. To ease the analysis, the interaction between the balls is not considered in the calculation.

The expression of the cumulated energy is then given by:

$$E_{tot} = \frac{\pi}{12} \cdot \rho \cdot d_b^3 \cdot (A \cdot \pi \cdot f)^2 \cdot N_b \cdot t \qquad Eq.\ III.\ 7$$

However, the cumulated energy (given in Eq. III.7) is not completely imparted to the material surface. Depending on the treated material, only a part of this energy is retained. Actually, after the contact with the surface, and depending on mechanical properties (especially the hardness), the balls rebound differently from one material to another. The balls restitution depends also on the surface plastic deformation state. Bagur et al. (Bagur et al. 2012)have established an empiric relationship between the hardness and the restitution coefficient, using experiments data of different materials impacts with steels balls. The expression of the restitution coefficient (noted k_r) evolution as function of the material hardness (HV) is then given by the following equation:

$$k_r = 0.2397\times \ln(HV) - 0.696 \qquad Eq.\ III.\ 8$$

This function is represented in Fig. III. 20. The materials used in the present study have an initial hardness of about 200 HV (AISI 316L) and 350 HV (AISI 660), corresponding to restitution coefficients of 0.57 and 0.67, respectively. It is important to note that the hardness increases continuously during the SMAT treatment. So, the restitution coefficient increases also depending on the SMAT parameters. At this state of the present work, this is not taken in consideration in the calculation.

This coefficient is then introduced in the calculation of the cumulated energy, and the equation for calculation of the cumulated energy becomes (Thiriet 2010):

$$E_{tot} = E_c \cdot N_b \cdot t \cdot (1 - k_r) \qquad\qquad Eq.\ III.\ 9$$
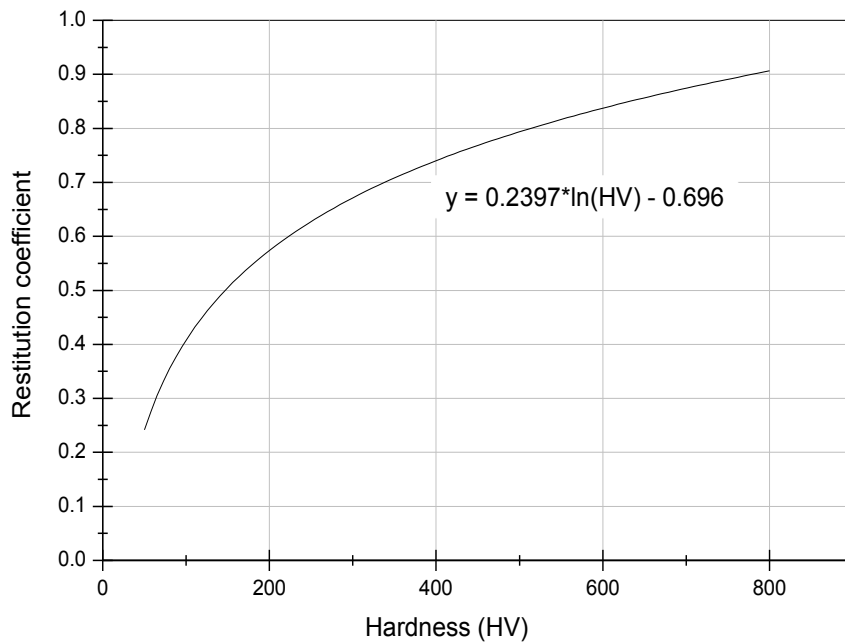
Fig. III. 20: Empiric evolution of the restitution coefficient as function of the hardness (HV) established by Bagur et al (Bagur et al. 2012).

The introduction of this coefficient in the calculations decreases the cumulated energy. The calculated values for the AISI 316 are multiplied by (1 - 0.57 = 0.43) and those of the AISI 660 by (1- 0.67 = 0.33). The cumulated energy is calculated for the whole range of parameters used in this study, and the evolutions of the 3 zones as function of this energy are given in Fig. III. 21. Data corresponding to the AISI 660 and AISI 316L treated with the 100Cr6 steel balls is represented in black, and in red, respectively. The AISI 316L samples treated with Zirshot balls are presented in green.

A "log-log" presentation is used to better visualize the evolutions at low energies, and linear fits (log(Thickness)=a*log(Energy)) with slopes (a) are also given. It should be noted that the slope corresponds in a linear mode to the power of the fit function (Thickness=Energy^a). When the value of "a" decreases, the thickness tends to stabilize at higher energy values. The results are given in Fig. III. 21.
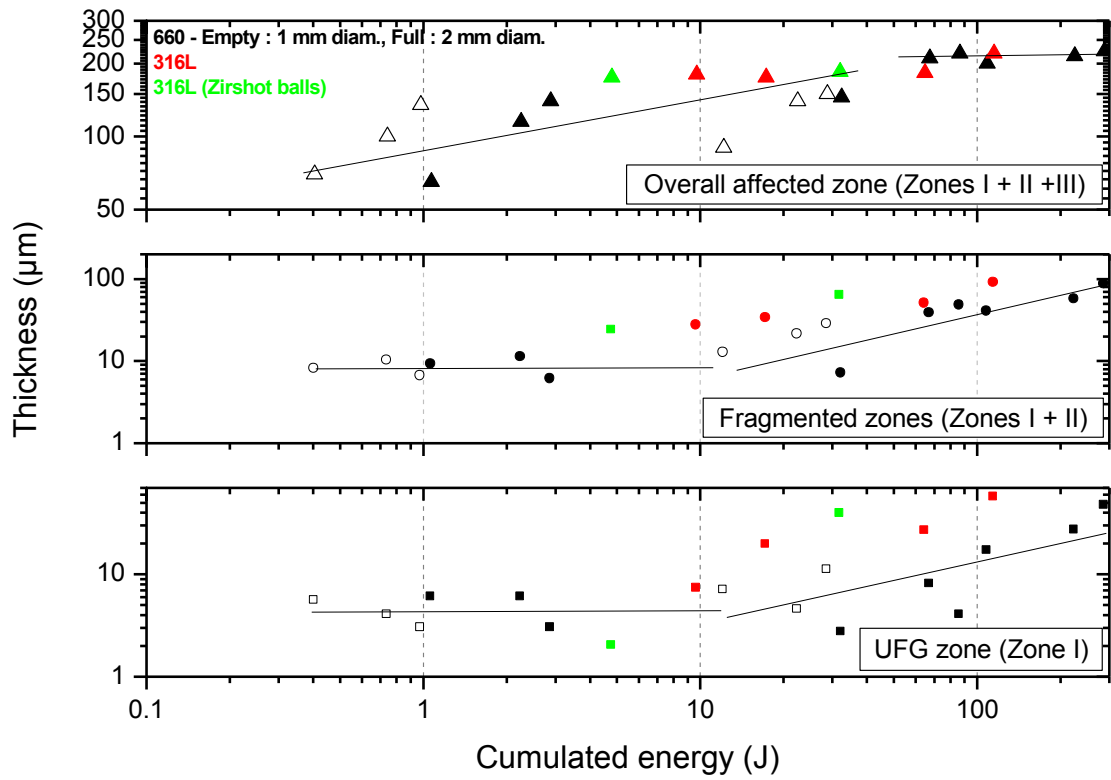
(a)
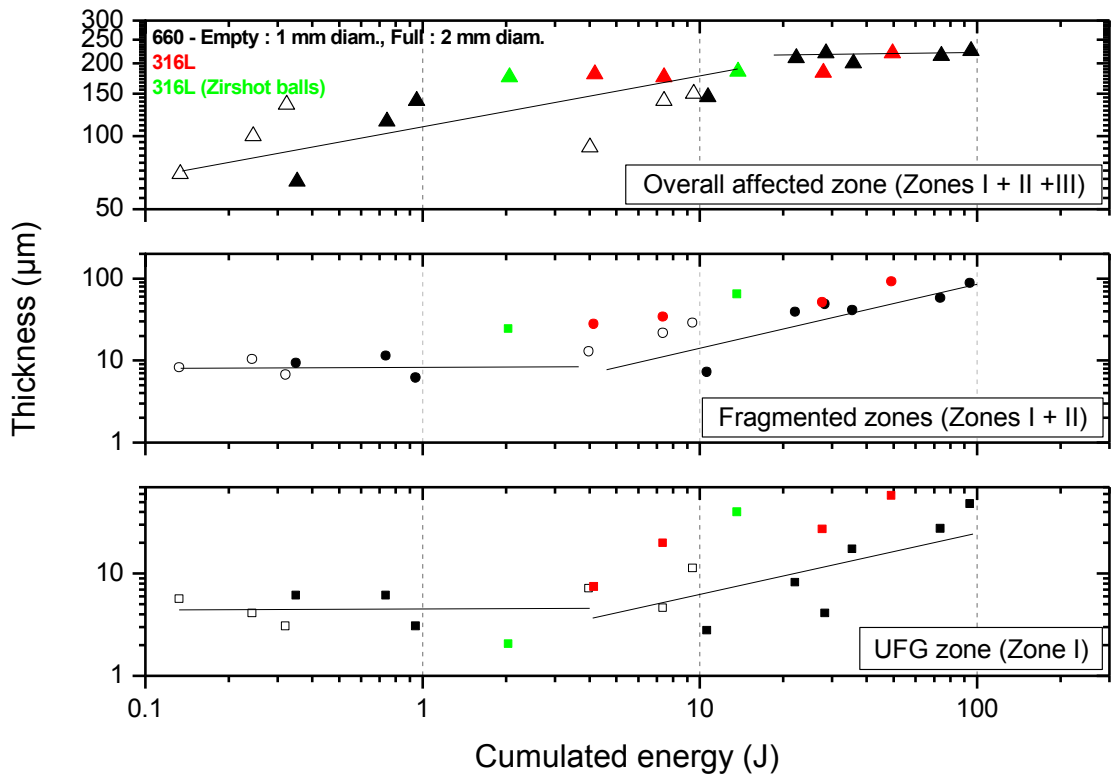
(b)

Fig. III. 21: The evolution of the (a) UFG, (b) fragmented and (c) overall affected zones thicknesses as function of the calculated cumulated energy taking in consideration the restitution coefficient.

From Fig. III. 21a and b, It can be firstly observed that the use of the restitution coefficient results in a shift of the data to lower cumulated energies. Higher shift to lower energies is logically observed for the AISI 660 samples, as the restitution coefficient is higher (0.67), while for the AISI 316L samples, the shift is less important (restitution coefficient of 0.57).

Concerning the thickness evolution of the AISI 660 different zones as function of the cumulated energy, two tendencies can be observed in Fig. III. 21b. Within the range of about 0 to 10 J of cumulated energy, the overall affected thickness increases and the fragmented and UFG ones remain fairly constant. However, when the cumulated energy is higher than about 10 J, the opposite effect is observed, where the thickness of the UFG and fragmented layers increase continuously and the overall affected thickness saturates and remains constant (about 230 µm). These results show that a minimum cumulated energy is required to increase the fragmentations mechanisms of the surface microstructure, leading to the formation of thick UFG and fragmented layers.

For the AISI 316L (red and green symbols), the evolution is quite different. The overall affected depth is almost the same within the whole analyzed energy range. It is also worth noting that for the UFG and fragmented layers, the thickness increases continuously, and in comparison with the AISI 660 samples, no threshold is observed. Wider parameters range is maybe needed to depict more precisely the evolution of the different zones thicknesses within larger cumulated energy range.

II. 5   Summary and conclusions

It has been shown in this section that low magnification maps (step size of 200 nm) could be used to extract the GND density, which is a good indicator of the plastic deformation imparted by the SMAT treatment. The apparent grain size and the derivative of the GND density evolution were used to establish criteria allowing to depict quantitatively the thickness of the three zones present through the SMAT affected layer: (i) the "ultrafine grain (UFG)" zone having sustained high strain at the top surface, (ii) the sub-surface transition zone in which the extend of deformation is sufficient to activate grain sub-division of the initial grains and, finally, (iii) the deformed zone where the initial grains are simply plastically deformed.

This procedure was applied to compare the effect of different processing parameters: the vibration amplitude of the sonotrode and the treatment duration as well as the balls nature (in the case of the AISI 316L). Firstly, for the AISI 316L, it was noticed that more modifications occurs within the UFG and fragmented layers, where the increases when higher cumulated energy is imparted to the surface, while the overall affected depth remains quite constant. On the other hand,

for the AISI 660, the thicknesses of the UFG and fragmented layers remain constant until a threshold cumulated energy of about 10 J, then increase. Meanwhile, the overall affected depth present the opposite effect, where its thickness increases for cumulated energies lower than 10 J, then saturates and remains stable.

The degree of advancement of the refinement process observed obviously depends on the local strain sustained by the material and, consequently, creates gradients in grain size and amount of structural defects through the depth below the surface. The magnitude of these gradients depends on the processing parameters. This part presents then the interest of the analyzing technique developed in the present work to correlate the SMAT parameters (amplitude, duration, balls nature) to the final deformed SMAT structure. This type of approach - using the evolution of GND – should be helpful to quantitatively estimate the effectiveness of other treatments in which the SMAT process is used as a precursor prior to nitriding (Tong et al. 2003), co-rolling (Waltz et al. 2011) or microarcing (Wen et al. 2011) as well as, more generally speaking, duplex treatments generating, on purpose, surface deformation gradients (Zhang and Zou 2012; Grosdidier et al. 2008; Kamikawa, Huang, and Hansen 2008) or spatially heterogeneous microstructures (Kamikawa, Huang, and Hansen 2008; Grosdidier et al. 2010; Witkin et al. 2003).

III. Effects of the SMAT parameters on the surface contamination

During the SMAT and depending on the process conditions, the balls impact "severely" the surface of the material and may enhance its chemical reactivity with the chamber parts elements. The sonotrode is for example in titanium alloy Ti-6Al-4V and the chamber in steel or polymer. In the first part of this chapter, chemical composition investigations (using GD-OES) are carried out on AISI 316L samples. In-depth quantification of the chemical elements present in the material shows the evolution of this contamination as function of the SMAT parameters. The second part describes a new qualitative method of analysis of SMAT-induced contamination by XRD. Actually, the presence of Titanium on the surface affect the background noise of the diffraction patterns, which is modified depending on the SMAT

III. 1 Surface contamination of the AISI 316L stainless steel surface after SMAT

III. 1. 1   The experimental results of the chemical composition analysis

In order to investigate the surface contamination, the sample treated under the "highest" severity condition is analyzed (D1A80D20). The extreme top surface morphology after SMAT under BSE detector is given in Fig. III. 22. The presence of "dark zones" distributed fairly heterogeneously on the treated surface is observed in Fig. III. 22a. These zones are clearly detected within the material cross section as shown in Fig. III. 22b. Their thickness can reach about 4 μm in some zones.

(a)   (b)
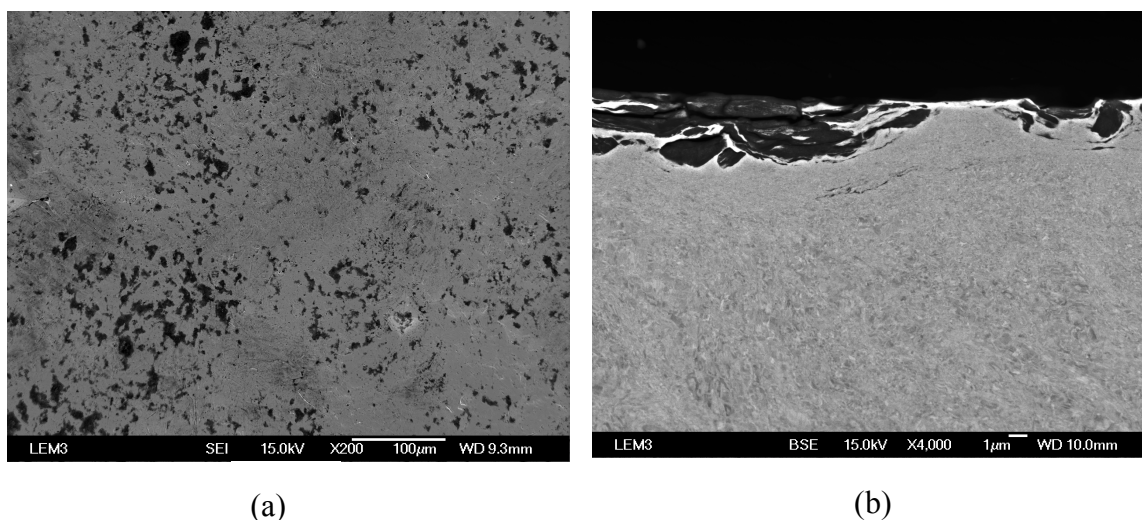
Fig. III. 22: SEM images showing the (a) surface morphology and (b) the cross section microstructure after 316L SMAT-ed under 80 μm of amplitude for 20 min with 100Cr6 balls (see table 1).

In order to investigate more locally this modified layer, Transmission Electron Microscopy (TEM) observations were carried out. Fig. III. 23gives a combination of Bright Field (BF) images

of the extreme top surface of the same sample. It is observed that the microstructure is essentially formed of 2 layers in this zone: a layer reaching about 1 µm with low contrast present at the extreme top surface (as shown in Fig. III. 22b), which is probably corresponds to the beginning of so-called zone I (UFG zone), and a severely deformed microstructure at the subsurface.
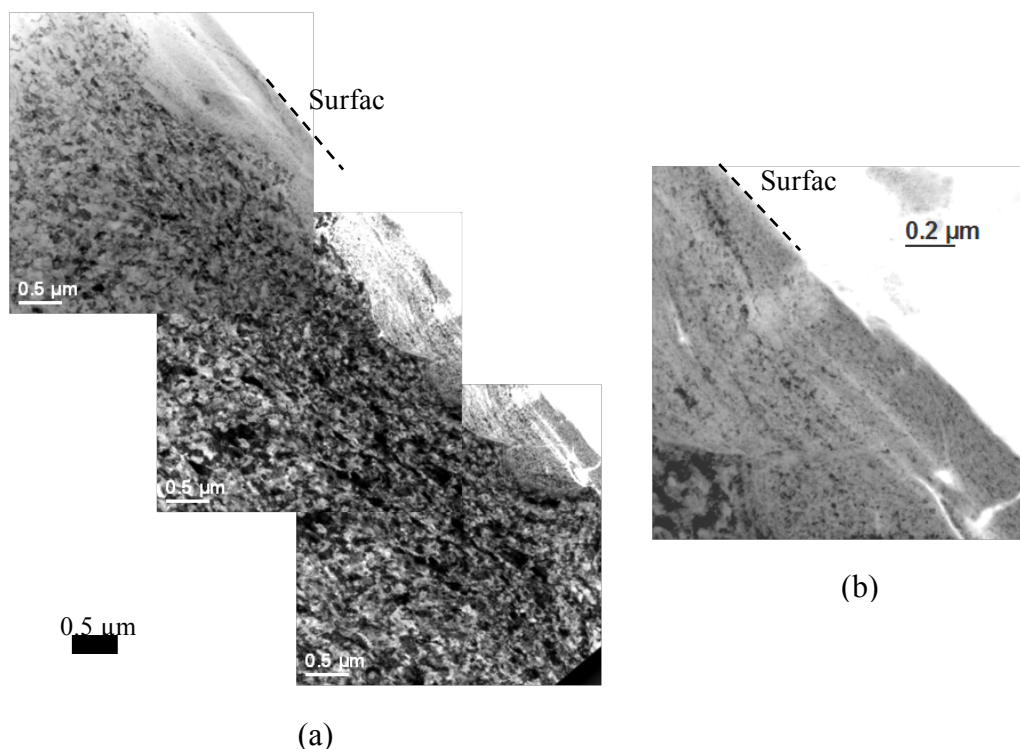
Fig. III. 23: (a) Bright Field images of the top extreme top surface of the 316L SS sample treated under 80 µm of amplitude for 20 min with 1 mm diameter 100Cr6 balls. (b) Close loop of the microstructure morphology at the extreme top surface.

To analyze the nature of these modified layers, local chemical analyses were carried out by Energy-Dispersive X-ray spectroscopy (EDX). The results are given in Fig. III. 24.Two zones having different aspects and different chemistry are observed. The local EDX chemical analyses of the two zones are given in Figs. 2 b and c. The bottom left of the image in Fig. 2a corresponds to the base material in which is observed that the heavy deformation has generated the presence of nano-grains. Consistently with the chemistry of the base austenitic steel, peaks of Fe, Ni, Cr, Mn and Mo are clearly depicted. It is important to note that the high intensity of the Cu peak is due to electrons interacting with the sample holder in the TEM. The top right of the image corresponds to a contaminated domain revealed in Fig. III. 22. In addition to some of the initial chemical elements present in the 316L sample, the analysis of the top surface reveals the presence of other elements such as Ti, Al and V. This indicates that external elements were introduced during the SMAT treatment. In the present case of the specific contamination analyzed here, the chemical species introduced within the surface are the constituting elements of the Ti-6Al-4V alloy from which the sonotrode is made of.

120

(c)
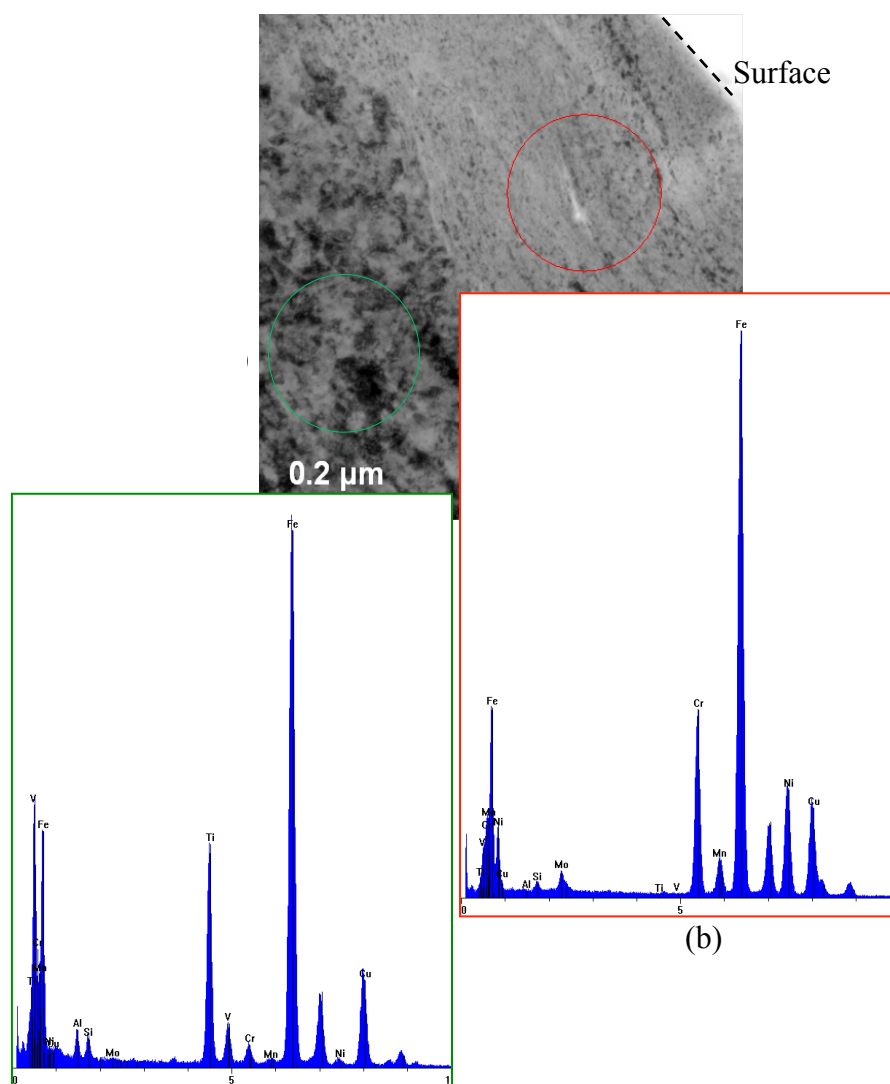
Fig. III. 24: (a) Bright Field image presenting the zones where the EDX analysis was carried out. (b) At the top surface layer, (c) at the subsurface

To gain a more statistical insigth on the exact nature of the surface contaminations, a GD-OES analysis was carried out on different samples treated under various SMAT conditions. Fig. III. 25shows the GD-OES results corresponding to the content (wt. %) of the different chemical elements expressed as a function of the distance from the top surface. As the data are averaged over a surface of about 12 mm^2 and because of the surface roughness induced by the SMAT process, the curves only give a qualitative trend of the amount of contamination. It is firstly observed (in Fig. III. 25a, b and c) that Ti is present in a significant amount at the surface in comparison with the other contaminating elements. Its content reaches an average of about 10 wt. % at the top surface and its presence is detected over a maximum depth of about 9 μm for the sample treated with the most severe conditions (80 μm / 20 min). On the same sample, contents are reaching about 4 wt. % in Al

and 2 wt. % in V, for the same maximum affected depth of about 9 µm. Their relative content and their similar penetration depths confirms that these 3 elements were introduced as the consequence of some material removal from the sonotrode, they subsequent transfer to the sample surface and incorporate into the substrate under the peening process. Concerning the nature of the surface pollution, a second interesting result is the detection of zirconium for the sample treated with the Zirshot balls (Fig. III. 25d). Its amount is globally low with content that do not exceed 1wt. % for a maximum depth of 4 µm.
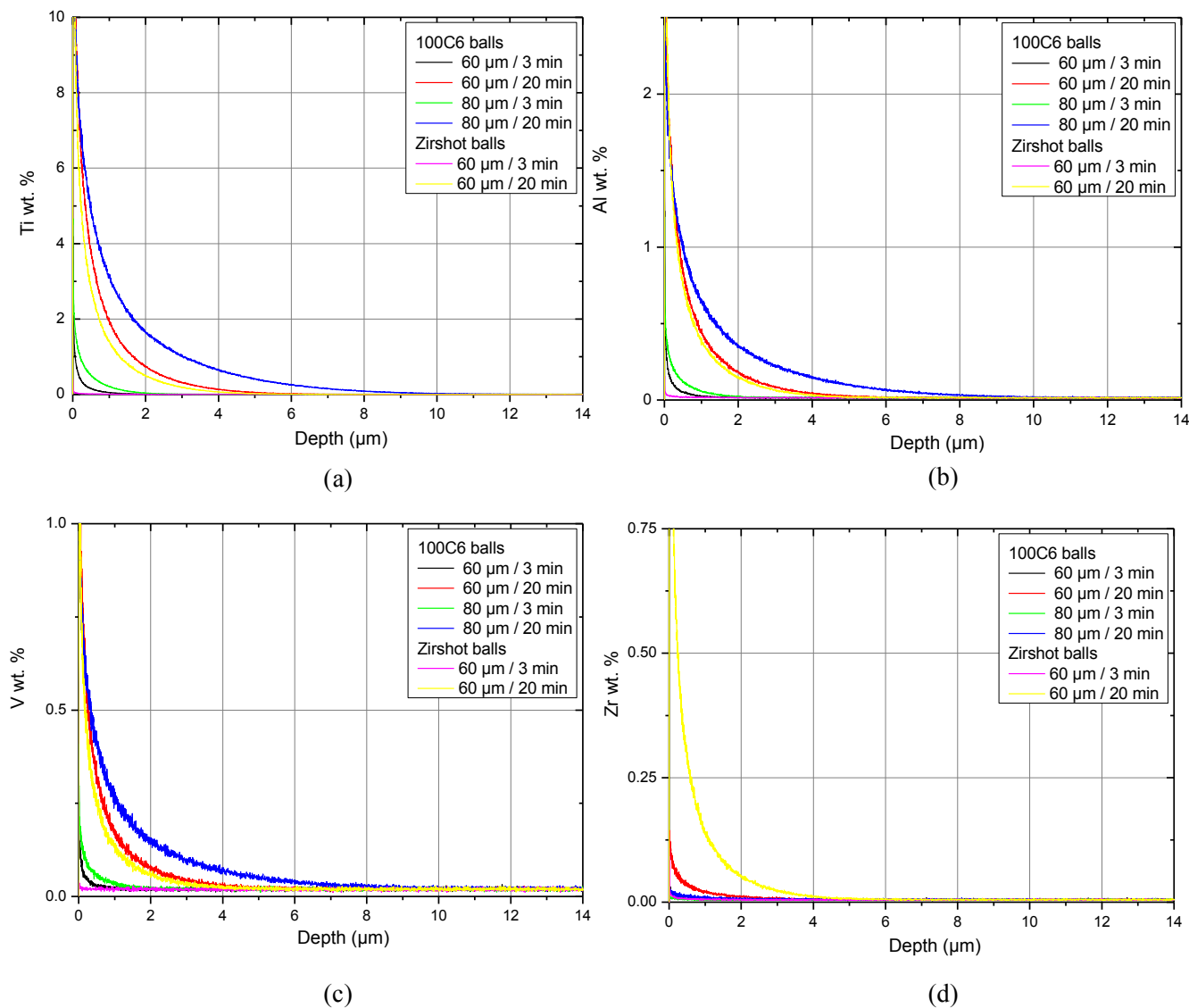
Fig. III. 25: In-depth evolution of the chemical composition (wt.%) of (a) Titanium, (b) Aluminum, (c) Vanadium and (d) Zirconium after SMAT under different conditions.

In addition, it is observed (in Fig. III. 25a, b and c) that increasing the treatment duration results in an increase in the Ti, Al and V concentrations as well as an increase of the contaminated depths. These phenomena are less noticeable when increasing the vibrations amplitude. Indeed, the

increase of the vibration amplitude, for a given treatment duration, gives rise essentially to a slight increase in the contaminated depth.

Beside the contamination by these sonotrode elements, a decrease of the Iron and Nickel concentrations was depicted. As shown in Fig. III. 26a, an important decrease of the Fe content is observed notably for the samples treated for 20 minutes. A decrease of the Ni content (in Fig. III. 26b), especially for the D1A80T20 sample, is depicted. It should be noted near the top surface, an increase of the Ni content can be observed. This decrease can be due to the formation of Ni_3Ti or Ni_3Al nitrides (Ti-6Al-4V / 316L mechanosynthesis).
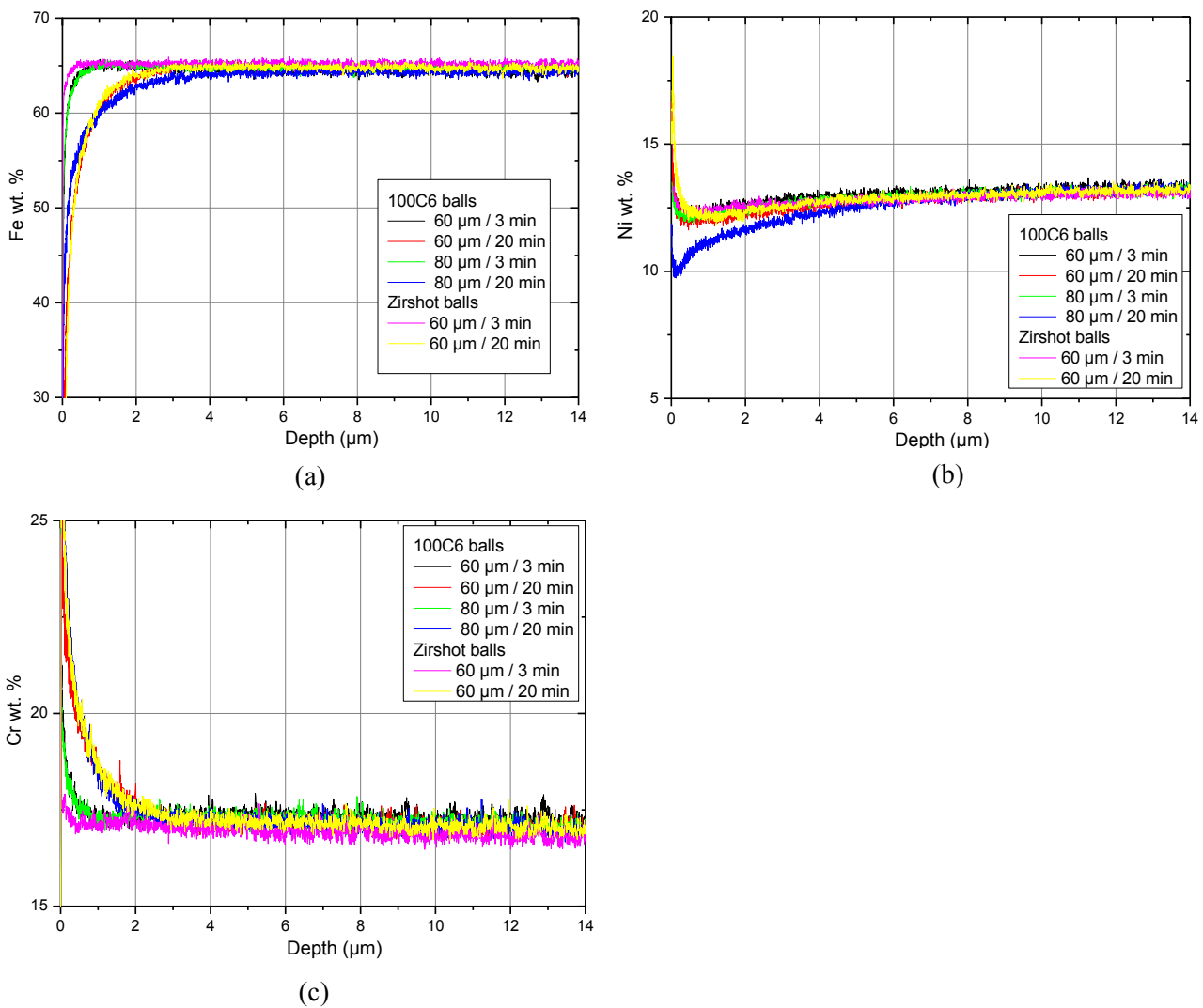
Fig. III. 26: In-depth chemical composition (wt. %) evolution of (a) Iron, (b) Nickel and (c) Chromium after different SMAT conditions.

It was also observed that the Chromium content increases at the top surface, as observed in Fig. III. 26c. The Cr contamination reaches about 25 wt. % and affects about 2 μm in-depth, when the treatment duration is 20 minutes. This contaminated "layer" is less important for the low treatment duration (3 min), with a depth of less than 1 μm and concentration of about 20 wt. %.

III. 1. 2   Discussion of the AISI 316L surface contamination

The chemical composition investigations reveal the presence of a contaminated layer on the surface of the SMAT-ed samples by the chemical elements of the sonotrode and probably the treatment chamber. It is observed that the contaminated depths and the elements concentration are different as a function of the SMAT parameters. These elements are deposed on the surface by the balls. This phenomenon has been observed in previous works. After treating the HASTELLOY C2000 (a nickel alloy resistant to corrosion) by Surface Nanocrystallization and Hardening (SNH), the surface was contaminated by balls in Tungsten carbides (WC) for treatment duration superior to 2h (Villegas et al. 2005). In other works, the presence of Fe_2O_3 and Fe_3O_4 oxides on the surface of the AISI316L after plastic deformation for 2 hours by ball milling has been revealed (Cemin et al. 2010). More generally, the process of incorporation of other chemical elements using colliding balls had been used to create surface alloying.

From the results presented in the last section, it is also clear that the balls nature has an influence on the surface contamination, especially at low treatment durations. The balls in Zirshot contaminates less the surface, in term of the deposited concentration and affected depth. In fact, these balls are "lighter" that the 100Cr6 ones. During the SMAT process, the impact of these balls with the sonotrode and the chamber does not generate enough energy to transfer the Ti, Al and V elements; therefore, it is probable that less content of these elements is transferred to the material surface.

The chemical analysis of the surface contamination also revealed a high contamination by the Chromium. As the AISI 316L is alloyed with higher content of Cr than the balls, it is then not expected that this contamination is issued from the balls. The sonotrode is in Ti-6Al-4V and does not contain Cr. A plausible hypothesis is that Cr is originating from the chamber. Actually, the chamber is in D2 die steel that contains carbides of MC type (M_7C_3), which are very rich in Cr. During the SMAT process, it is then possible that the repeated impacts with the chamber allow to extract these carbides from the matrix and to deposit it on the treated material surface.

III. 2 Contamination effect on the XRD analysis of the AISI 660 stainless steel samples

In the previous section, the contamination effect was investigated using destructive technique (GD-OES), forming craters of about 4 mm in diameter on the analyzed surface. These results reveal that the surface is contaminated by the sonotrode element of Ti-6Al-4V (Ti, Al and V) and also by the elements issued from the chamber (Cr) and the balls (Zr). However, this method is not always convenient and cannot be used for all the shapes of samples and for industrial applications. In the present section, XRD data (in form of θ-2θ traces) will be employed to investigate the contamination of the AISI 660 surfaces. Different radiations (Chromium, Iron or Cupper) can be used to induce the fluorescence of the Titanium element. In this study, Chromium radiation (K_α=0.2291 nm).

Fig. III. 27 gives as examples the θ-2θ traces of the initial material and the samples treated with balls of 2 mm diameter with 100, 3000 and 10000 % of covering ratio. For the initial material, diffraction peaks corresponding to the γ-phase are observed. After SMAT under a covering ratio of 100 %, the diffraction peaks of the γ-phase are larger, which can be due to the refinement of the structure induced by the SMAT process. After longer treatment duration (3000 %), the γ-peaks become larger than 100 % one. When the covering ratio is 10000%, the γ-peaks enlargement is more visible and the XRD trace is significantly shifted to higher intensities.
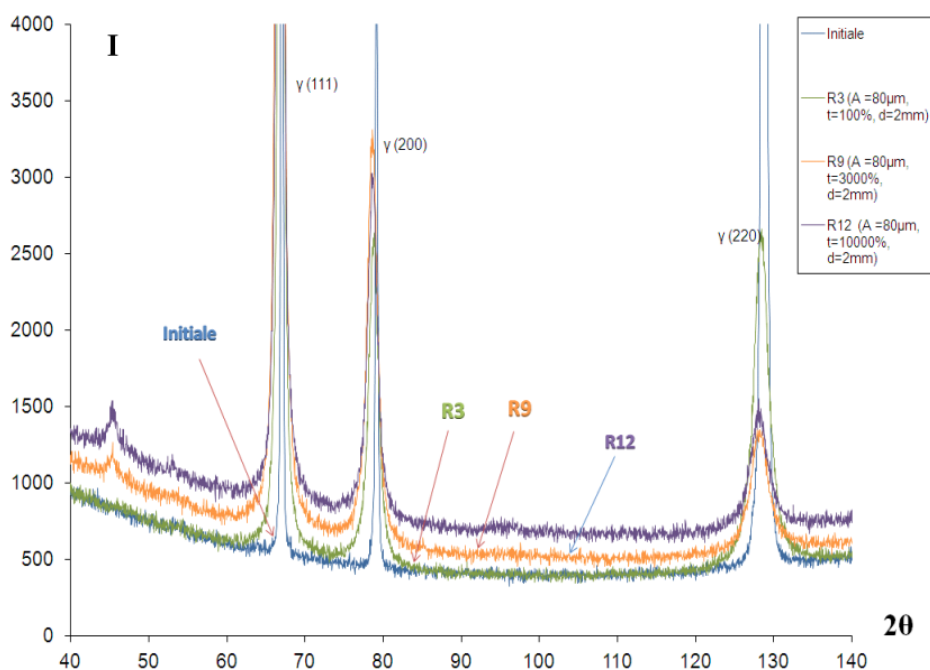

Fig. III. 27: XRD patterns of the AISI 660 treated under different conditions of SMAT (see table 2)

These results show also that depending on the SMAT parameters, the background noise level is modified. This is due to the contamination by the Titanium during the SMAT process as described in the previous section. As illustrated in Fig. , the presence of Titanium atoms in (and within) the treated surface generates the emission of fluorescence X-Rays. Actually, the Chromium -used as X-Ray radiation source- is energetic enough to expel electrons from the inner orbital of the titanium atoms. This makes the electronic structure of Titanium unstable, and electrons in higher orbitals "fall" into the lower orbital to fill the hole left behind. In falling, energy is released in the form of photons. These photons are depicted by the XRD detector because their energy is close enough to the Cr one and also because no energy range discrimination is used in the detector. When the quantity of Titanium increases in the surface, the quantity of photons emitted increases, as shown in Fig. b and c. This is traduced in the XRD analysis by the addition of the substrate signal to the Titanium one, and thereby a shift in the Y-axis of the final XRD pattern as observed in Fig. III. 27.
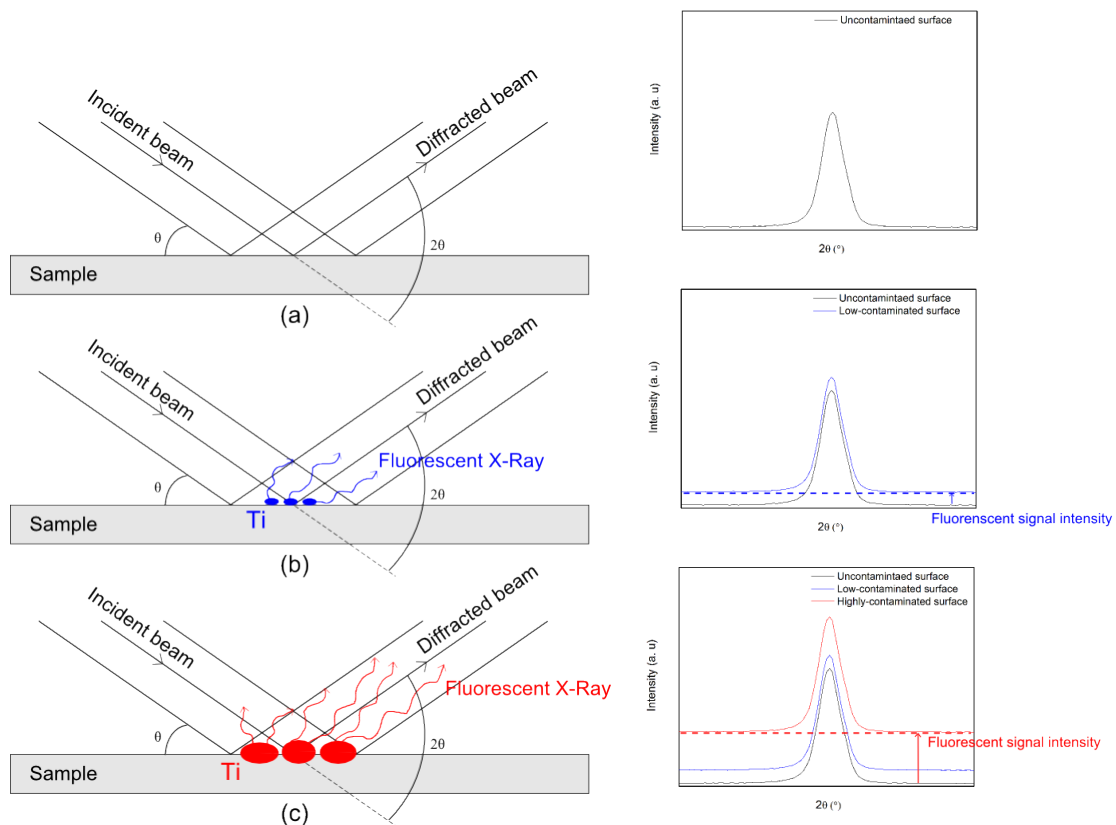
Fig. III. 28: Schematic illustration of the effect of Titanium presence in the surface of the AISI 600 SS. (a): when the surface is uncontaminated, only the diffracted signal is depicted by the detector. (b) and (c) : The presence of Titanium in the surface is characterized by the emission of fluorescent X-Rays in different directions (Red lines).

As illustrated in Fig. III. 29, the background noise varies as the amplitude of vibration and covering ratio increase. It is observed that the background noise level increases from about 400 (D2A30T20) to 575 (D2A30T15), and from about 675 (D2A30T67) to 750 (D2A30T50),

respectively. At high vibration amplitude of 80 μm, the background noise remains almost at the same level at low covering ratio R12 and slightly decreases at high one (D2A80T7.5).
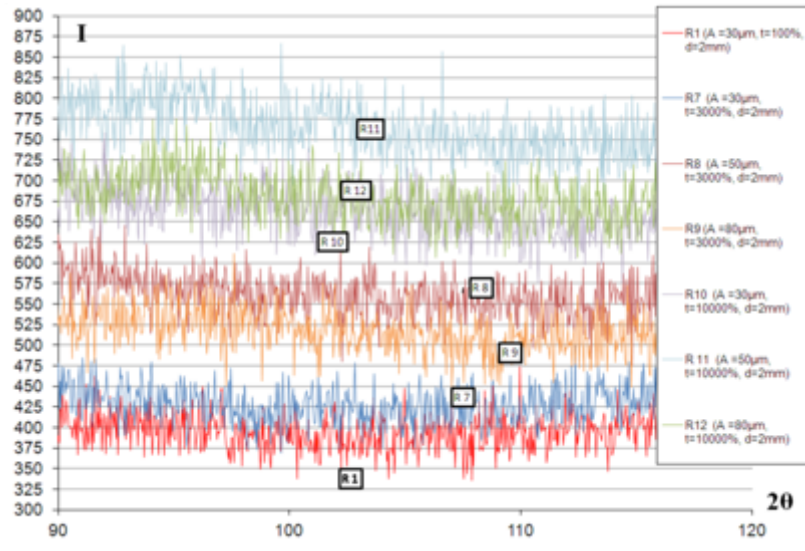
Fig. III. 29:XRD pattern showing the difference of the background noises for different SMAT conditions.

In order to quantify the contamination of this steel, the relative background intensity (noted I) was measured for all samples, using the following equation:

$$I = \frac{I_{sample} - I_{ini}}{I_{ini}} \times 100 \quad \textit{Eq. III. 10}$$

The variation of the relative background noise as function of the covering ratio and the treatment duration are given in Fig. III. 30. It is firstly observed that the relative background is directly related to the covering ratio, as observed in Fig. III. 30a. When the covering ratio increases, the relative background noise also increases. In addition, for a given covering ratio, it is clearly observed that the vibration amplitude of 50 μm generates more contamination that a vibration amplitude of 80 μm. This apparently surprising result is probably due to the different treatment durations required to achieve the targeted covering ratio. Actually, to reach a covering ratio of 100 %, longer treatment duration is needed under low vibration amplitudes, as mentioned in Table III. 2.
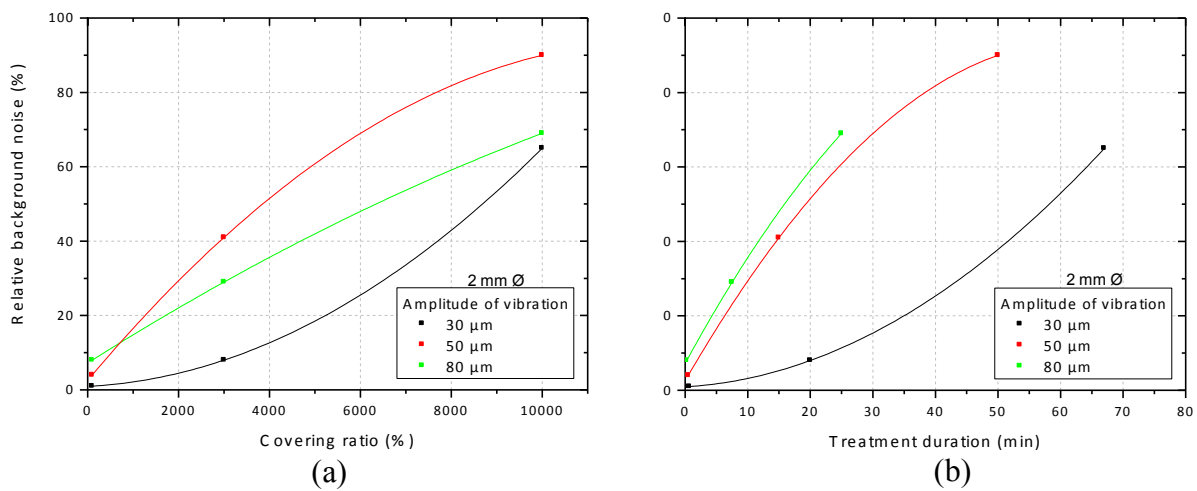
Fig. III. 30: The relative intensity evolution as function of (a) the covering ratio, (b) the treatment duration.

The evolution of the background relative intensity as function of the treatment duration (for samples treated with 1 mm diameter balls) is given in Fig. III. 30b. It can be seen clearly that under vibration amplitude of 30 µm, the relative intensities are low in comparison with other samples, showing that under this amplitude, less contamination on the surface is introduced. It can also be also observed that increasing the treatment duration results in an increase of the background relative intensities for all vibration amplitudes.

At a given treatment duration, the 50 and 80 µm amplitudes generate more contamination, but the results also confirm that the highest amplitude (80 µm), which generates the most energetic conditions, also results in a slightly higher level of contamination. Consequently, it is clear that the apparent surprising result of background level increase (shown also in Fig. III. 27) is due to the higher treatment duration required to generate the targeted covering ratio.

IV. **Summary and conclusions**

The investigations of the SMAT effects on the AISI 316L and AISI 660 surfaces give rise to interesting results. The mechanical effect of the SMAT on the microstructure is firstly investigated, and then the analysis focused on the surface contamination occurred during the process.

Firstly, the induced plastic deformation by the SMAT was quantified using a new technique, based on Electron Back Scatter Diffraction (EBSD) measurement (step size of 200 nm). This method consisted on the determination and exploitation of the Geometrically Necessary Dislocations (GND), which is a good indicator of the plastic deformation, to characterize the microstructure and to identify the different layers formed on the surface after SMAT. Actually, the evolution of the average GND density was calculated from the top surface to the material bulk, and using new established criteria, the three SMAT characteristic zones were identified: (i) Zone I: the Ultra Fine Grains (UFG) zone composed of with grains having sub-micrometric size; (ii): Zone II: the transition zone where the initial grains are fragmented to fine grains under the heavy deformation and finally (iii) Zone III: the deformed zone, where the initial grains are simply plastically deformed. This procedure was firstly tested on the AISI 316L, as it is a widely studied steel, and its deformation mechanisms are extensively studied. It was noticed that the UFG and transition zones thicknesses are more significantly affected when increasing the amplitude of vibration, while the whole affected layer remains constant (except under the highest conditions where an increase is observed).

This refinement process clearly depended on the local strain sustained by the material inducing by consequence a gradient in grain size and high defects density. This induced gradient depended on the processing parameters. Therefore, the AISI 660 was treated under a wider range of SMAT parameters. For this steel, it was noticed that the UFG zone is more sensible to the vibration amplitude when using balls of 2mm diameter and treating for long durations, while the thickness of the overall affected layer increases when balls of 1 mm diameter are used, and a saturation effect is observed under 50 and 80 µm of vibration amplitude when the covering ratio is 3000 % or more where the thickness of this zone tends to stabilize.

This developed procedure allowed to give a new approach to quantify the plastic deformation induced by the SMAT, however, some it is limited by some factors. It should be noted firstly that this procedure is sensible to the surface preparation and the EBSD acquisition conditions. In addition, as the surface after SMAT is rough, it is very difficult to determinate precisely the extreme surface, so the calculation of the UFG thickness can be over or sub-estimated.

On the other hand, the last part this chapter treated the chemical composition modifications occurred after the SMAT. The analysis of the AISI 316L surface by Glow Discharge Optical Emission Spectroscopy (GD-OES) showed a contamination by the sonotrode (in Ti-6Al-4V) and chamber (in D2 die steel) elements where high contents of essentially Titanium were depicted. It was also observed that increasing the treatment duration led to more contamination than when increasing the vibration amplitude. In addition, when using balls in Zirshot, the contamination is less important. This was probably due to the lower weight of these balls, resulting in a lower cumulated energy transferred the material surface.

However, the GD-OES is a destructive analysis method, which is not always convenient in the industrial field and for some special shape of industrial parts. The surface contamination of the AISI 660 was then analyzed based on the fluorescence phenomenon occurring during the X-RD measurements. Actually, as this steel contained high content of Titanium, the contamination by the Ti of the sonotrode can be depicted by the background noise level, which varied as function of the content of Ti deposed on the surface. The comparison between the different AISI 660 samples was done by calculating the background noise relative intensity.

References

Ashby, M. F. 1970. "The Deformation of Plastically Non-Homogeneous Materials." *Philosophical Magazine* 21 (170): 399–424. doi:10.1080/14786437008238426.

Bagur, J, A Houpert, A Hazotte, and Thierry Grosdidier. 2012. "Etude de L'effect de L'écrouissage Sur Le Coefficient de Restitution de Surfaces Métalliques, Lors D'éssais D'impacts de Particules, Assimiliés À Un Traitement de Surface Du Type Grenaillage Par Ultrasons". Laboratoire d'Etude des Microstructures et Mécanique des Matériaux (LEM3), Metz.

Beausir, Benoit, and Claude Fressengeas. 2013. "Disclination Densities from EBSD Orientation Mapping." *International Journal of Solids and Structures* 50 (1): 137–46.doi:10.1016/j.ijsolstr.2012.09.016.

Cemin, Felipe, Fernando G. Echeverrigaray, Ane C. Rovani, Cintia L. G. Amorim, Rodrigo L. O. Basso, Israel J. R. Baumvol, and Carlos A. Figueroa. 2010. "Influence of Atomic and Mechanical Attrition on Low Temperature Plasma Nitriding of Ferrous Alloys." *Materials Science and Engineering a-Structural Materials Properties Microstructure and Processing* 527 (13-14): 3206–9. doi:10.1016/j.msea.2010.02.012.

Cornet, A, and J Deville.1998. *Physique et Ingénierie Des Surfaces,.*EDP Sciences.

Dillien, Steven, Marc Seefeldt, Sebastien Allain, Olivier Bouaziz, and Paul Van Houtte. 2010. "EBSD Study of the Substructure Development with Cold Deformation of Dual Phase Steel." *Materials Science and Engineering a-Structural Materials Properties Microstructure and Processing* 527 (4-5): 947–53.doi:10.1016/j.msea.2009.09.009.

Field, D. P., C. C. Merriman, N. Allain-Bonasso, and F. Wagner. 2012. "Quantification of Dislocation Structure Heterogeneity in Deformed Polycrystals by EBSD." *Modelling and Simulation in Materials Science and Engineering* 20 (2).doi:10.1088/0965-0393/20/2/024007.

Grosdidier, T., D. Goran, G. Ji, and N. Llorca. 2010. "On the Processing of Hetero-Nanostructured Metals for Improved Strength/ductility Balance by ECAE and SPS Techniques." *Journal of Alloys and Compounds* 504, Supplement 1: S456–S459. doi:10.1016/j.jallcom.2010.03.035.

Grosdidier, T., J. X. Zou, N. Stein, C. Boulanger, S. Z. Hao, and C. Dong. 2008. "Texture Modification, Grain Refinement and Improved Hardness/corrosion Balance of a FeAl Alloy by Pulsed Electron Beam Surface Treatment in the 'Heating Mode.'" *Scripta Materialia* 58 (12): 1058–61.doi:10.1016/j.scriptamat.2008.01.052.

Humphreys, F.J., and A.T. Stewart. 1972. "Dislocation Generation at SiO2 Particles in an A-Brass Matrix on Plastic Deformation." *Surface Science* 31: 389–421. doi:10.1016/0039-6028(72)90269-5.

Humphreys, Fj, and Mg Ardakani. 1994. "The Deformation of Particle-Containing Aluminum Single-Crystals." *Acta Metallurgica Et Materialia* 42 (3): 749–61. doi:10.1016/0956-7151(94)90272-0.

Humphreys, Fj, and Pn Kalu. 1990. "The Plasticity of Particle-Containing Polycrystals." *Acta Metallurgica Et Materialia* 38 (6): 917–30. doi:10.1016/0956-7151(90)90164-C.

Jiang, J., T. B. Britton, and A. J. Wilkinson. 2013. "Measurement of Geometrically Necessary Dislocation Density with High Resolution Electron Backscatter Diffraction: Effects of Detector Binning and Step Size." *Ultramicroscopy* 125 (February): 1–9. doi:10.1016/j.ultramic.2012.11.003.

Kamikawa, Naoya, Xiaoxu Huang, and Niels Hansen. 2008. "Tailoring Structures through Two-Step Annealing Process in Nanostructured Aluminum Produced by Accumulative Roll-Bonding." *Journal of Materials Science* 43 (23-24): 7313–19. doi:10.1007/s10853-008-2964-8.

Kröner, E. 1980. "Continuum Theory of Defects Con."

Lacombe, P, and B Baroux. 1990. *Les Aciers Inoxydables*. Edp Sciences.

Lu, A. Q., G. Liu, and C. M. Liu. 2004. "Microstructural evolution of the surface layer of 316L stainless steel induced by mechanical attrition." *Acta Metallurgica Sinica* 40 (9): 943–47.

Nye, Jf. 1953. "Some Geometrical Relations in Dislocated Crystals." *Acta Metallurgica* 1 (2): 153–62. doi:10.1016/0001-6160(53)90054-6.

Pantleon, W. 2008. "Resolving the Geometrically Necessary Dislocation Content by Conventional Electron Backscattering Diffraction." *Scripta Materialia* 58 (11): 994–97.doi:10.1016/j.scriptamat.2008.01.050.

Roland, T., D. Retraint, K. Lu, and J. Lu. 2006. "Effect of SurfaceNanoCrystallization on Tribological Properties of Stainless Steel." In *Residual Stresses Vii*, edited by W. Reimers and S. Quander, 524-525:717–22. Zurich-Uetikon: Trans Tech Publications Ltd.

Roland, T,Retraint, D, Lu, K, Lu, J. 2007. "Enhanced Mechanical Behavior of a Nanocrystallised Stainless Steel and Its Thermal Stability." *Materials Science and Engineering: A* 445–446: 281–88. doi:10.1016/j.msea.2006.09.041.

Thiriet, Tony. 2010. "Traitements mécaniques et thermochimiques couplés sur acier inoxydable et alliage base nickel austénitiques". Ecole des Mines de Nancy.

Tong, W P, N R Tao, Z B Wang, J Lu, and K Lu. 2003. "Nitriding Iron at Lower Temperatures." *Science*.

Villegas, Juan C., Kun Dai, Leon L. Shaw, and Peter K. Liaw. 2005. "Nanocrystallization of a Nickel Alloy Subjected to Surface Severe Plastic Deformation." *Materials Science and Engineering: A* 410–411 (November): 257–60. doi:10.1016/j.msea.2005.08.087.

Waltz, L., D. Retraint, A. Roos, C. Garnier, and P. Olier. 2011. "Effect of Interfacial Oxidation Occurring during the Duplex Process Combining Surface Nanocrystallisation and Co-Rolling." *Surface and Coatings Technology* 205 (19): 4608–13.doi:10.1016/j.surfcoat.2011.03.140.

Wen, Lei, Y.M. Wang, Yan Liu, Y. Zhou, L.X. Guo, J.H. Ouyang, and D.C. Jia. 2011. "EIS Study of a Self-Repairing Microarc Oxidation Coating." *Corrosion Science* 53 (2): 618–23.doi:10.1016/j.corsci.2010.10.010.

Witkin, David, Z. Lee, R. Rodriguez, S. Nutt, and E. Lavernia. 2003. "Al–Mg Alloy Engineered with Bimodal Grain Size for High Strength and Increased Ductility." *Scripta Materialia* 49 (4): 297–302.doi:10.1016/S1359-6462(03)00283-5.

Zhang, K.M., and J.X. Zou. 2012. "Formation of Ultrafine Twinned Austenite on a Cold Rolled 316L Stainless Steel Induced by Pulsed Electron Beam Treatment under Heating Mode." *Thin Solid Films* 526: 28–33. doi:10.1016/j.tsf.2012.10.024.

Zhu, K.Y., A. Vassel, F. Brisset, K. Lu, and J. Lu. 2004. "Nanostructure Formation Mechanism of A-Titanium Using SMAT." *Acta Materialia* 52 (14): 4101–10.doi:10.1016/j.actamat.2004.05.023.

List of figures

List of tables

Chapter IV

Effect of the surface activation by mechanical and thermo-mechanical treatments on the nitrogen diffusion in the surface of the AISI 316L

In this chapter, the effects of the surface activation by plastic deformation techniques before the Plasma Nitriding (PN) treatment are investigated. The goal is to determine the potential of various plastic deformation pre-treatments to improve the nitrogen diffusion on the AISI 316L during a given nitriding treatment of 8 hours at 350 °C. Three activation techniques were used. The plastic deformation was imparted by (i) shooting balls under SMAT and by (ii) the conventional cold rolling. Some tests were also carried out after plastic deformation (iii) induced by the thermo-mechanical stresses generated by the High Current Pulsed Electron beam (HCPEB) treatment.

This chapter is divided into two parts. ***The first part*** is dedicated to the activation by SMAT. In a first section, the cross section microstructure and the evolution of the nitrided layers thickness are analysed using Scanning Electron Microscope (SEM) and Electron BackScattered Diffraction (EBSD), and the modification of the surface hardness is also investigated. The second section is a detailed study about the effect of the SMAT-induced contamination on the nitriding layer and surface hardness.

The second part deals with other surface "activators" used prior to Plasma Nitriding. The AISI 316L samples are cold-rolled using three reduction ratios. Cold rolling is used because it is a "simple" deformation process, and it introduces a high density of defects within the material. The nitrided layer thicknesses and the surface harnesses are evaluated after the duplex treatment "cold rolling + Nitriding". In the second section of this part, because of the industrial application limitation of the cold rolling (complex shapes of industrial parts are not possible to achieve), the HCPEB is also used as a possible surface activator, which could be more convenient in the industry. Two grades of the AISI 316 (the AISI 316LM: medical grade and 316LS: with higher content of S to improve the machinability) are treated under high and low energy before nitriding. As explained in the literature review chapter, the HCPEB treatment leads to the eruption of the second phase particles present at the

subsurface layer and thereby to the formation of craters on the surface. This is why the AISI 316LS is chosen to investigate the effect of the surface purification and chemical homogenization on nitriding. The evolutions of the nitrided layers thickness as well as the surface hardness and residual stress are also detailed.

Summary

Part. 1.   Effect of the SMAT on the evolution of the nitrided depths and surface hardness of the AISI 316L

After revealing a significant surface pollution in the previous chapter, we will study in the following the effect of nitriding directly on a raw SMAT-ed surface and after selective electro-polishing, used to remove the contamination layer. Thus, in the next sections, for sake of clarity, the following abbreviations will be used:

SN: SMAT + Nitriding.

SPN: SMAT + Polishing + Nitriding.

I.   Plasma Nitriding of "raw" SMAT-ed samples

I. 1.   SMAT parameters used for treating the AISI 316L surface

AISI 316L specimens of 8 mm thickness were cut from a rolled hyper-quenched 25 mm diameter bar. This grade is identical to the one used in chapter III and its chemical composition is given in section I. The samples are mechanically polished to a mirror-like finish (1 μm diamond paste). Prior to nitriding, the SMAT is carried out under an argon atmosphere in order to limit oxidation. The treatment conditions are summarized in Table IV. 1.Untreated and SMAT-ed samples were placed together into the plasma nitriding reactor to be treated under the same conditions (at 350 °C for 8h.).

Balls			SMAT conditions			
Nature	Diameter (mm)	Weight (g)	Amplitude of vibration (μm)	Treatment duration (min)	Vibrating frequency (kHz)	Distance Sonotrode – sample (mm)
100Cr6 steel	2	15.2	60	20	20	30

Table IV. 1: SMAT parameters used for treating the AISI 316L stainless steel before plasma nitriding.

I. 2.   Cross-section microstructure modifications induced by the duplex treatment "SMAT + Nitriding"

Fig. IV. 1presents the X-Ray Diffraction (θ-2θ) patterns obtained after SMAT, direct Nitriding and SMAT + Nitriding (SN) sample surfaces. After SMAT, characteristic diffraction lines of the austenite phase (γ) are observed and no martensitic peaks are depicted. After nitriding only, in addition to the γ-peaks from the substrate, the formation of the larger peaks at diffraction angles lower than that of the parent γ-phase is observed. These peaks correspond to the γ_N-phase (described in Chapter II).

The SN sample presents the same phases as the only nitrided one where, in addition to the γ-peaks, the γ_N phase peaks also appear. In order to compare the thickness of the nitrided layers, the XRD intensities of the γ and γ_N peaks are used (noted I and Iγ_N, respectively). Actually, as the XRD diffraction volume is constant during the phases analysis and assuming that the crystallographic texture is identical in the γ and γ_N-layers, the relative intensity Iγ_N/Iγ will changes as function of the thickness of the γ_N layer, where thicker γ_N layer will results in a high value of this ratio, and vice versa.

Applying this method to the (111) peak, it can be then found that higher Iγ_N/Iγ value is obtained for the only nitrided layer (~ 1.4 µm) in comparison with the SN sample (~ 0.84µm). This indicates that the nitrided layer after SN is thinner than after only nitriding.
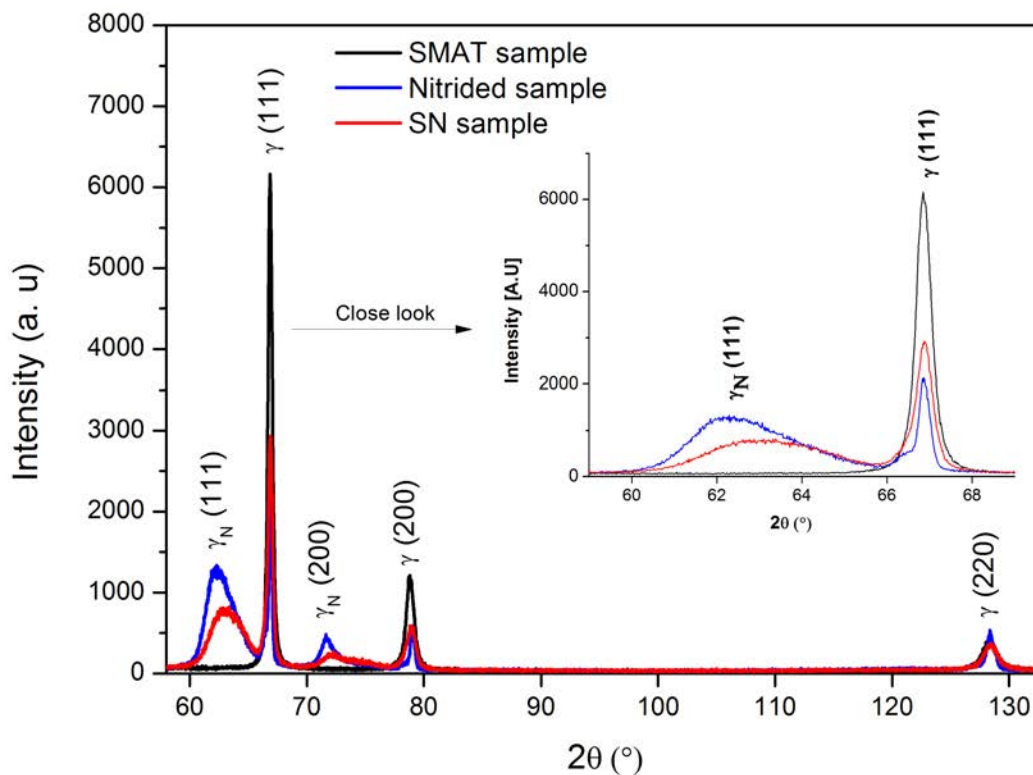
Fig. IV. 1: X-ray diffraction patterns of the SMAT, plasma nitrided and SN samples.

In addition, the $\gamma_N$peaks present a dissymmetry as can clearly seen in the close loop ofFig. IV. 1. This is possibly due to chemical composition heterogeneity in the formed nitrided layer. Previous studies tried to explain the phase formed and explained the dissymmetry of the γ_N phase (Dalibon, Bozzano, and Bruehl 2013; Adachi and Ueda 2012; Asgari et al. 2011). As explained in Chapter I, this dissymmetry is attributed to the heterogeneity of the nitrogen content within the nitrided layer, leading thereby to a gradient of the lattice parameter.

To observe the microstructural modifications, Fig. IV. 2presents SEM cross section micrographs (Backscattered Electrons images) of the treated samples. The SMAT sample (Fig. IV. 2a) exhibits a high density of plastic deformation signs (slip lines and twinning). The mechanisms responsible for the plastic deformation generated by SMAT on the 316L stainless steel have been detailed previously in this work. From these micrographs, it can also be seen that the layer formed on the surface of nitrided sample (Fig. IV. 2b) is more continuous and uniform (~ 2 µm) in comparison with the SN sample (~ 1.8 µm as observed in Fig. IV. 2c).High magnification images(Fig. IV. 3) show also that the nitrided layer formed on the SN sample presents discontinuities (arrows).

(a)   (b)   (c)
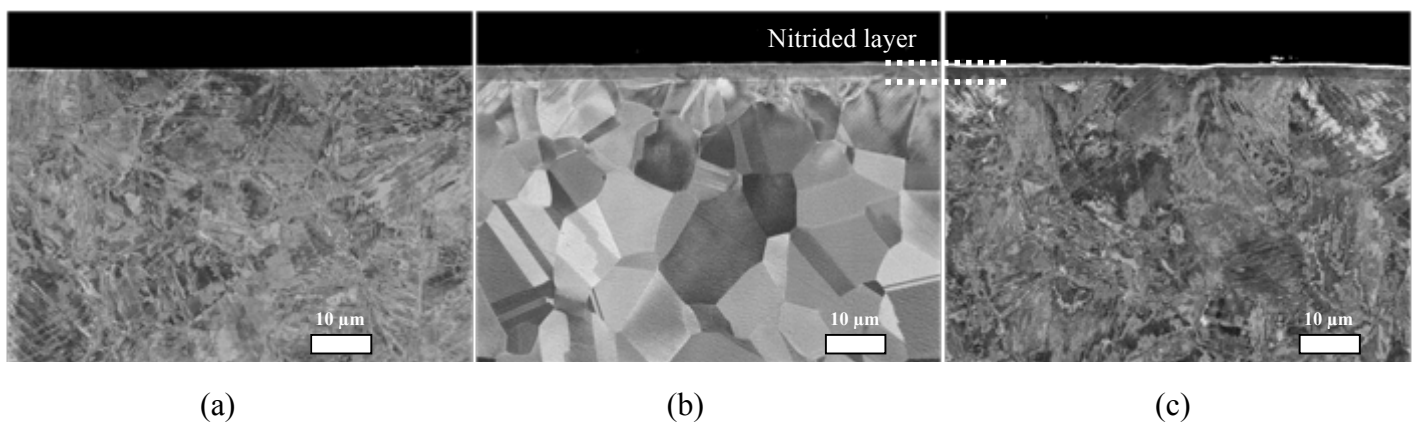
Fig. IV. 2: SEM cross-section microstructure after (a) SMAT, (b) Nitriding and (c) SMAT+ plasma nitriding.

(a)   (b)
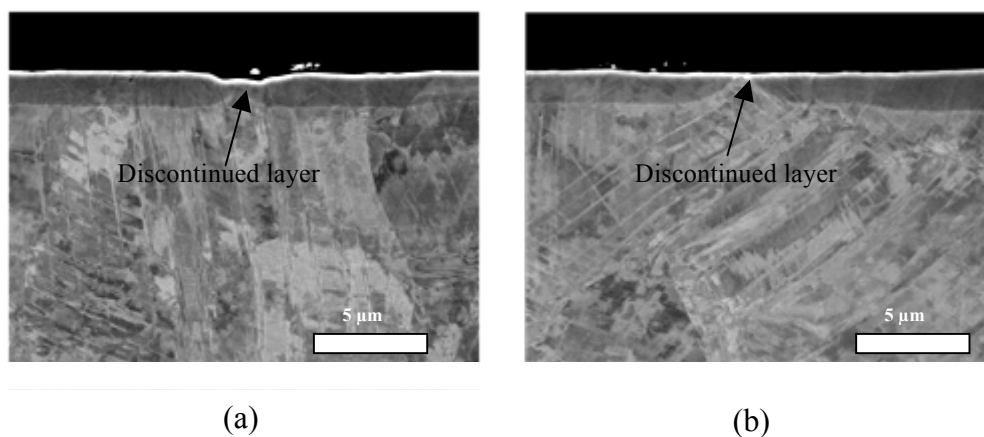
Fig. IV. 3:Cross section images showing that the nitrided layer formed on the SMAT-ed surface is not continuous.

Complementary EBSD analyses were carried out to give more details about the microstructure evolution and the nature of plastic deformation.Fig. IV. 4gives the orientation maps corresponding to the SMAT (a), the Nitrided (b) and the SN samples (c), carried out with a step size of 0.1 µm. The colors are given following the standard triangle colors, where the <001> direction is parallel to the treatment direction. The SMAT-ed sample orientation map (Fig. IV. 4a) shows the presence of

high amount of crystallographic rotations inside the initial grains. Microstructure refinement is also observed in some zones near the top treated surface, presenting very refined grains. The details about the microstructure refinement and deformation after SMAT observed here are similar to the ones described in Chapter III.

For the nitrided sample, the EBSD map -given inFig. IV. 4b- shows that rotation inside grains occurs within the nitrided layer, sign of the deformation induced by the nitriding process (Stoneville et al. 2010). Under this layer, no significant rotation is observed. In Fig. IV. 4c, which corresponds to the orientation map of the SN sample, high rotation inside grains in the whole analyzed area is observed. This map is quite similar to the SMAT-ed sample one. In addition, misorientations inside grains in the top layer can also be seen, which is probably due, as for the nitrided sample, to the deformation induced within the nitrided layer(Stinville et al. 2010; Templier et al. 2010).

(a)

(b)

(c)
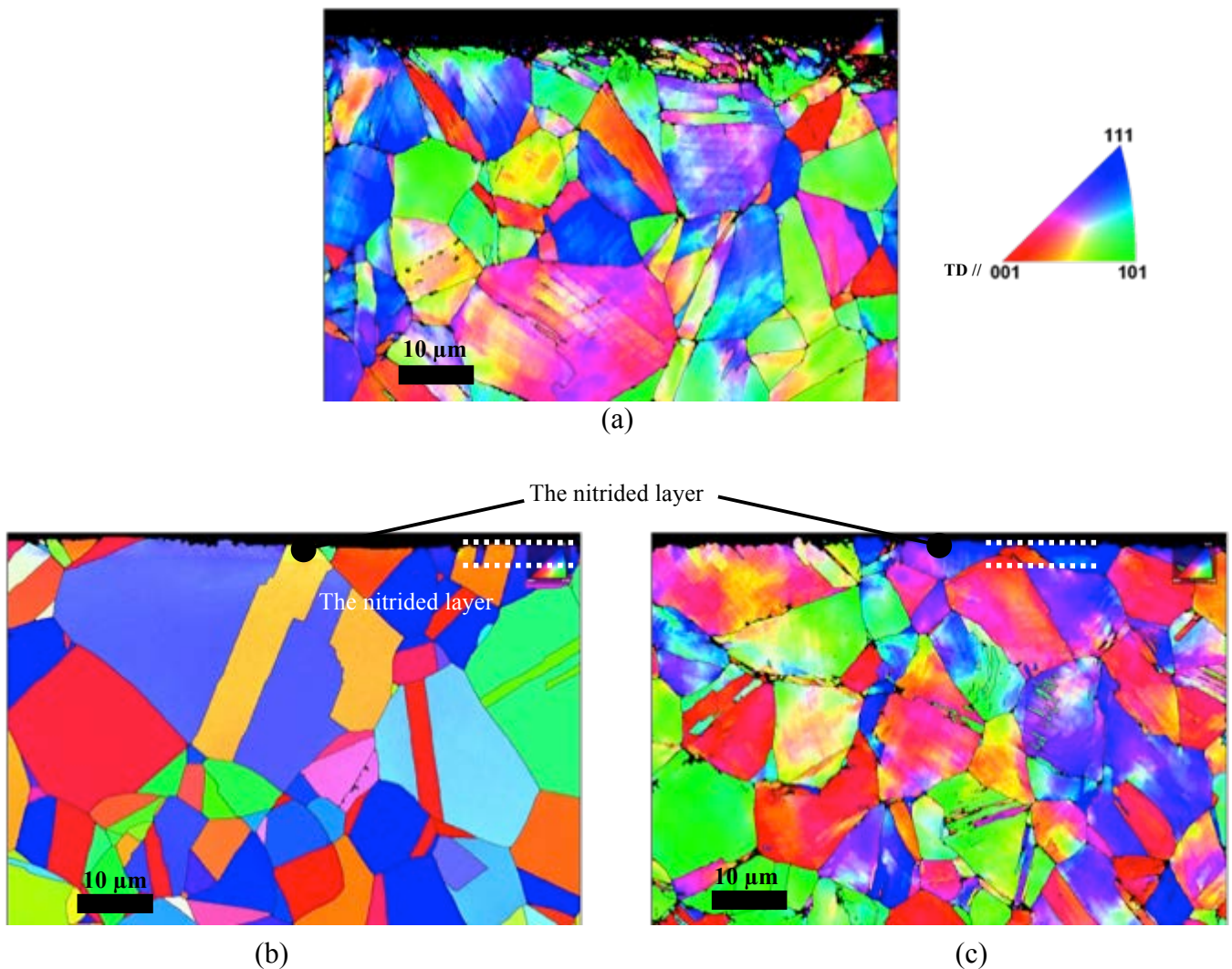
Fig. IV. 4: Cross section IPF maps of the (a) SMAT-ed, (b) Nitrided and (c) SN samples. The <001> direction is parallel to the treatment direction.

I. 3.   **Hardness evolution after SMAT, nitriding and the duplex treatment SN**

Surface indentations under different loads and in-depth hardness measurements on cross section were carried out. The results are given inFig. IV. 5. The depth indentation corresponds to the indenter penetration and is estimated using the equation given in Chapter II. From the surface indentation measurements in Fig. IV. 5a, the nitrided sample presents a hardness of about 360 HV at the extreme surface and then decreases when increasing the indentation load to reach a hardness of about 200 HV, close to the initial material hardness (~180 HV). The decrease of the hardness can be explained by the decreasing contribution of the nitrided layer as compared to the bulk, when the indentation load is increased. For the SMAT-ed surface, the hardness is relatively constant at about 360 HV, which is due to the important depth affected by the SMAT treatment. The higher hardness increase is obtained after SN. The top surface hardness is significantly increased by about 400%, reaching almost 720 HV in comparison with the initial material (~180 HV for the untreated material), and doubled in comparison with the only nitrided one (~ 360 HV). As the indentation load increases, the hardness decreases but remains at a higher level at the maximum load used (500 g).

To analyse the hardness evolution within deeper thickness of the material (until about 500 µm in depth), cross-section measurements were carried on using a load of 25 g. The results are given in Fig. IV. 5b. It should be noted that the hardness values given for a depth of 1 µm are the ones measured by surface indentation with the lowest load (Fig. IV. 5a). For the nitrided sample, the surface hardness reaches a maximum of about 360 HV. Just below the nitrided layer, the hardness drops down to the initial hardness of the material (about 180 HV). The nitriding treatment only affects the near surface hardness over a depth that corresponds to the nitrided layer thickness. Comparatively, the top surface hardness of the SMAT sample is close to that of the nitrided sample, but the hardness below decreases slowly and is still modified until a depth of 250 µm.

In the case of the SN sample, only the top surface hardness has been increased by about 200 % in comparison with the SMAT-ed or nitrided samples (Fig. IV. 5b). This is due to the formation of the nitrided layer. In addition, the hardness underneath the top surface of the SN sample remains very close to the SMAT one. This indicates that the temperature of the nitriding treatment (350 °C) do not affect the sub-surface hardness. The SMAT effects on microstructure are then not affected.
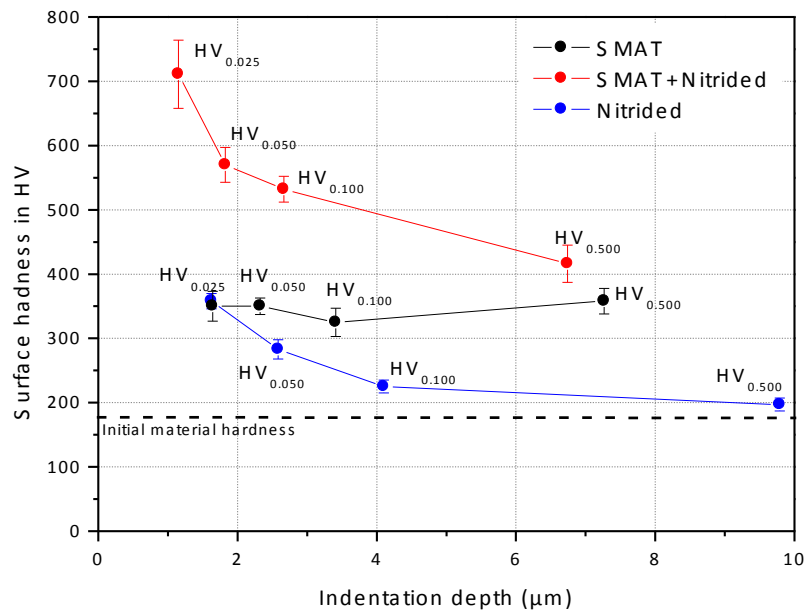
(a)
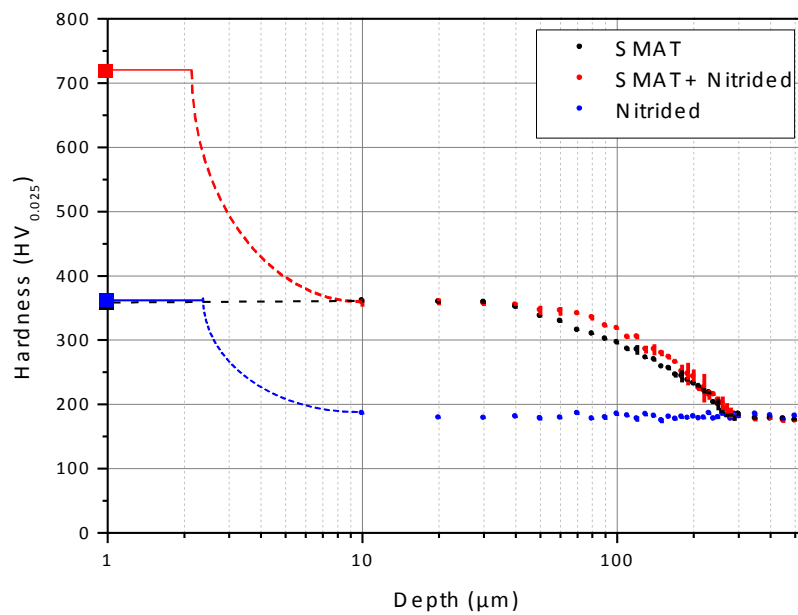
(b)

Fig. IV. 5: (a) surface hardness evolution of the SMAT, nitrided and SMAT+nitrided sample using (a) surface indentation by different loads and (b) cross-section measurements (load of 25 g).

I. 4.   **Discussion**

The 316L stainless steel microstructure modifications and hardness evolutions observed after SMAT are consistent with previous studies. For example, Roland et al. 2007 observed that the hardness was increased from 250 HV in the bulk material to about 460 HV at the extreme surface, a value higher than the hardness obtained in the present work (~360 HV). This is due probably to the

higher balls diameter used in the cited work (3 mm) in comparison with our treatment (2 mm). The surface hardness enhancement was related to the strong refinement of the grain size by SMAT, which leads to an increase of the strength (the Hall-Petch relationship) and the high density of dislocations induced.

After nitriding, a new phase replaces the γ-phase in both the nitrided and SN-ed samples, corresponding to the $γ_N$-phase. As observed in the experimental results (Fig. IV. 1), the peak broadening is due to the gradient of nitrogen near the surface, leading then to a gradient of the lattice parameter over the depth analyzed by the X-ray beam. It has been shown by Shedden et al. (Shedden et al. 1997)that more nitrogen contents result in an increase of the lattice parameter of the $γ_N$-phase, as shown inFig. (taken from Stinville 2006). From this figure and our XRD results, the estimated superficial nitrogen content is about 25 at. %. However, it should be noted that the lattice parameter does not simply depend on the nitrogen content, but also on the elastic anisotropic strain due to the very important compressive residual stress (1 to 4 GPa) introduced by nitrogen incorporation in the expanded austenite layer. A method was proposed by Czerwiec et al. (Czerwiec et al. 2009) to separate the contribution of nitrogen incorporation from the stress one. Nevertheless, for the only nitrided sample, the $γ_N$ peaks are is shifted to lower diffraction angle as compared to the SN sample. This can be interpreted as lower as lower nitrogen content for the SN sample as compared to the only nitrided sample.
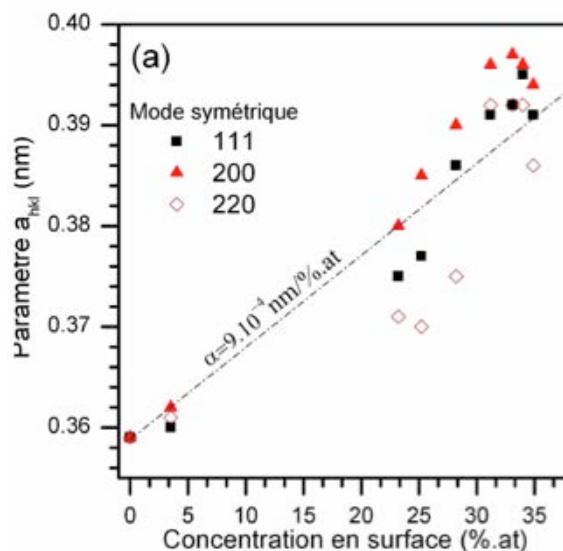
Fig. IV. 6: Lattice parameter a of nitrogen stabilized expanded austenite ($γ_N$) as a function of surface nitrogen content(J.-C. Stinville 2006).

Concerning the surface hardness, the results presented in Fig. IV. 5show that the hardness of the nitrided sample was only increased within few micrometers, reaching a maximum of about 360 HV. This result is consistent with the SEM structural observations, where it is seen that the nitrided layer does not exceed 2μm. Previous works also showed that the hardness is only enhanced near the

extreme surface after nitriding of 316L. In the work of Mingolo et al., the surface hardness after plasma nitriding (at 400 and 550 °C for 12h) could reach about 1500 HV (Mingolo, Tschiptschin, and Pinedo 2006), 4 times higher than the hardness measured in the present work. This is due to the formation of iron and chromium nitrides, which harden the material surface. In the present case, as the nitriding temperature is lower (350 °C), no nitrides are formed and the surface hardness

The highest hardness is obtained after SN for which the surface hardness (~720 HV) is more than 100 % higher than for the nitrided sample only (~360 HV). The first assumption of this significant hardness increase is the possible formation of nitrides during the nitriding process. It has been shown for example that after nitriding under 400 °C for 30 h of a SMAT-ed38CrMoAl ferritic steel, the hardness was increased by 30 % in comparison with the only nitrided samples (Micoulaut et al. 2007). The same tendency is observed after SN treatment of a pure iron, where the hardness was 55 % higher that of the only nitrided pure iron (Ruan, Chen, and Lu 2010). The hardness enhancement in these works was explained by the formation of a nanostructured layer and precipitation of iron nitrides. It should also be noted that iron and the steels used in these two studies are α-type, whereas γ steels with no phase transformation is used in the present study. In our work, as the nitriding temperature does not exceed 350 °C, the formation of nitrided is inhibited. No evidence of CrN is available from the XRD diffraction pattern presented in Fig. IV. 1

The second assumption that can explain this hardness increase is the cumulative effect of both the SMAT and the nitriding processes. Actually, the measured surface hardness value may represent a cumulative effect of the SMAT treatment and of the subsequent nitrogen insertion. The final material hardness (after SN) can be expected to follow the equation:

$$HV_{final} = HV_{initial} + \Delta HV_{SMAT} + \Delta HV_{Nitriding}$$

where ΔHV_{SMAT} (180 HV) and $\Delta HV_{Nitriding}$ (180 HV) are the gain of hardness induced by the SMAT and Nitriding treatments, respectively.

$$HV_{final} = 180 + 180 + 180 = 540$$

However, the HV_{final} calculated is inferior to the measured hardness here (~720 HV). This shows that the harness obtained after the duplex treatment SMAT+PN is not simply cumulative (addition) of each treatment. The combined-effect is more complex and the nitriding of a coarse-grained material can lead to different hardened layers than the one of a severely deformed material.

As observed in Chapter III, the SMAT leads to a surface contamination by different chemical elements, such as Titanium, Aluminium and Vanadium. These elements may react with the nitrogen to form hard nitrides, for example, Titanium nitrides (TiN) or Aluminium nitrides (AlN). Their

presence is not depicted in this work because probably of the small size of this precipitated and there amount, not detected by the experimental tools used.

In the sub-layer, the hardness of the two samples decreases slowly to the bulk value. These results show that the subsequent nitriding treatment does not affect the sub-surface hardness imparted to the material by SMAT. This is consistent with the work of Roland et al.(Roland et al. 2007)where it is shown that the AISI 316L nanometer scaled microstructure is retained up to 600 °C.

To investigate the influence of nitriding at 350 °C on the microstructure obtained by the SMAT in the sub-surface, complementary analysis of the microstructure were done using EBSD technique. Data post-treatment allowed the study of the induced defects density in the form of GND. The GND density is used in this case to observe the stability of the structure after nitriding at 350 °C. The GND densities are displayed in Fig. IV. 7following the given colours code. For densities smaller than 10% of the maximum, the colour code was not used and the band contrast was simply plotted. The red zones are those with high GND density, while very low GND density corresponds to the blue ones. The average value of GND density was calculated from 3 EBSD maps. From these maps, after SMAT and SMAT+PN (Fig. IV. 7a and c), the affected depths as well as the level of the GND density seem quite similar, which probably mean that the nitriding treatment does not lead to a decrease of the defects and of the new grains boundaries induced by the SMAT. For the only nitrided sample (Fig. IV. 7c), the nitrided layer contains higher GND density in comparison with the initial material, due to the plastic deformation induced by the nitrogen insertion.

To compare these samples quantitatively, the average GND density evolutions are shown in Fig. IV. 8 as a function of the distance from the top surface towards the material. These evolutions are given in linear scale (Fig. IV. 8a) as well as in log-log scale (Fig. IV. 8b) in order to observe more clearly the evolution near the top surface. From this figure, it is observed that the nitrided sample presents an average GND density of about $4.\,10^{-2}$ μm^{-1}until about 3 μm in depth, which is higher that the untreated sample GND density ($\sim 2.\,10^{-2}\mu m^{-1}$). From this depth, the GND density decreases quickly to reach the initial level at about 5 μm.

For the SMAT-ed and SN samples, within the first 5 microns, the calculation of the GND density is not precise, as the indexation rate in this zone is very low (sub-micron zone as described in Chapter II). From a depth of 10 μm, the average GND densities of the two samples remain constant and similar (in a range of 6 to $8.\,10^{-2}$ μm^{-1}), until a depth of about 70 μm, then decreases continuously to reach the initial level at a depth of about 250 μm. These results show that the

defects induced by the SMAT are not affected by the nitriding post-treatment of nitriding (at 350 °C).
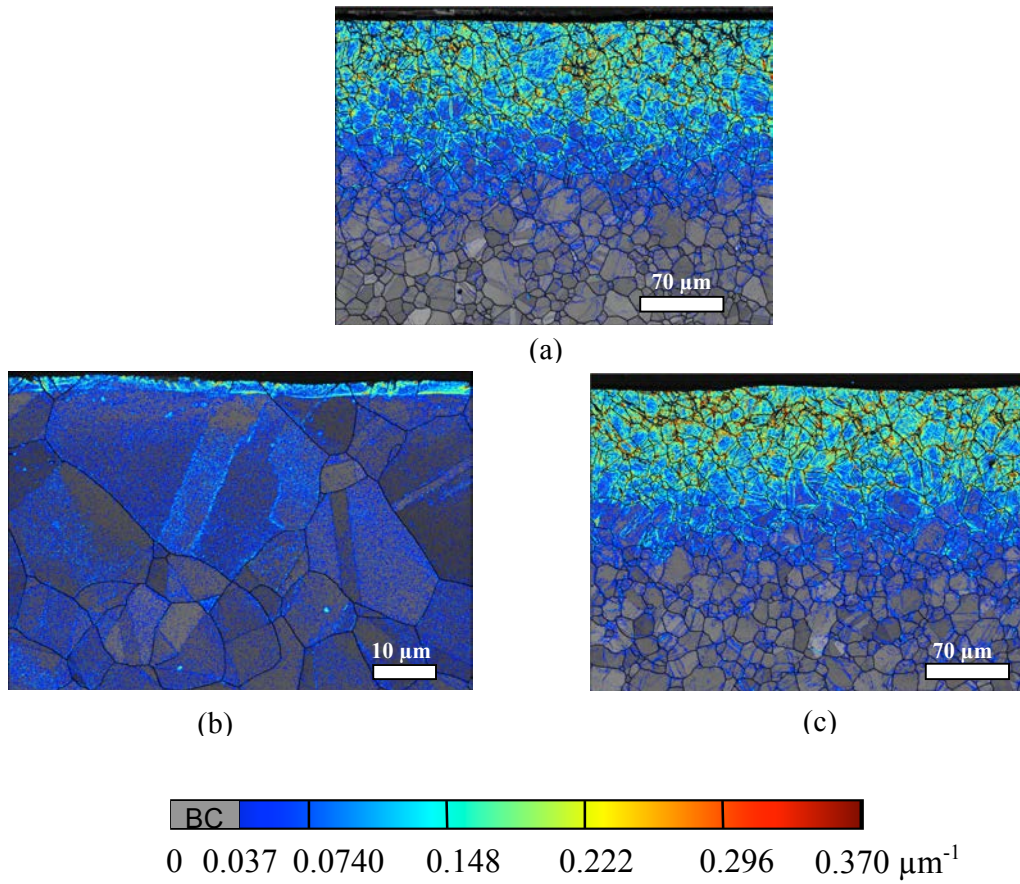
Fig. IV. 7: GND density maps of the (a) SMATed, (b) Nitrided and (c) SN samples.
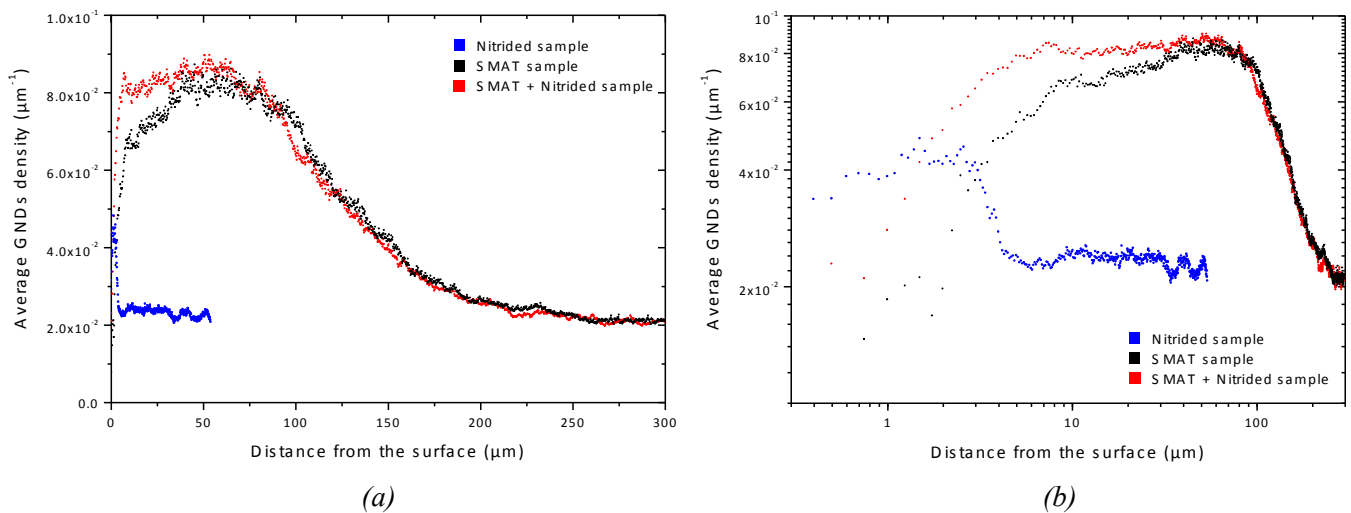
Fig. IV. 8: (a) Linear and (b) log-log evolutions of the average GND density as function of the distance from the top surface for the three treated samples.

I. 5.   **Summary**

In conclusion, three essential results are revealed:

(i)The hardness of the subsurface is not affected by the Nitriding temperature (350 °C). This is believed to be due to the absence of recrystallization and grain growth during the nitriding process of the SMAT deformed microstructure.

(ii) The SMAT apparently does not enhance the nitrogen diffusion and leads to the formation of thinner (in comparison with the only nitrided sample) and non-continuous nitrided layer. This is probably due to the contamination by the Sonotrode (Ti, Al and V), the chamber (Cr) and the balls (Zircon). Actually, these elements may limit the diffusion of nitrogen in the AISI 316L matrix.

(iii) A considerable increase of the top surface hardness of the SMAT+Nitrided sample (~720 HV) by a factor of more than 2 in comparison with the only nitrided one (~360 HV) is observed. This enhancement could not be explained by a simple cumulative effect of the SMAT and the nitriding treatments. A more complex combination of the effect of each treatment may exist.

(iv) This increase of hardness may be due to formation of hard nitrides (such as TiN or AlN) after the reaction of nitrogen with the contamination elements induced by the SMAT.

II. <u>Plasma Nitriding after surface "cleaning" by electro-polishing</u>

II. 1.   **Experimental conditions**

4 samples are selected for this investigation: 2 treated with balls in 100Cr6and 2 other with balls in Zirshot. Unfortunately, no samples treated at identical conditions as the ones in the previous chapter (section I) are available. Samples treated for a quasi-similar duration are then used. All the conditions used are summarized in Table IV. 2.

Reference	Balls			SMAT conditions			
	Nature	Diameter (mm)	Weight (g)	Amplitude of vibration (µm)	Treatment duration (min)	Vibrating frequency (kHz)	Distance Sonotrode – sample (mm)
D1A60T5	100Cr6 steel	1	7.6	60	5	20	30
D1A60T17			7.6		17		
D1A60T5**Z**	Zirshot		5.9		5		
D1A60T17**Z**			5.9		17		

Table IV. 2: The samples used for the plasma nitriding after surface electro-polishing.

The SMAT-ed surfaces are partially subjected to electro-polishing before PN in order to remove the surface contamination and also to understand the effect of the highly deformed structure (present at the top surface of SMAT-ed samples) on the nitrogen diffusion. Two electro-polishing conditions are used: 60V for 20 and 60 seconds, each condition in one side of the sample, as shown inFig. IV. 9. The choice of these parameters was done after testing several conditions to obtain a smooth surface and without pitting. After polishing for 20 and 60s, a layer of about 10-15 µm and about90 to 110 µm are removed respectively, and all the samples are nitrided (at the same time) under a temperature of 350 °C for 8h. As mentioned, the samples analyzed in this part are treated almost at the same conditions as the samples analyzed in Chapter III. Therefore, Fig. IV. 10, showing the evolution of the average GND density from the top treated surface, is used to estimate approximately the surface defects density state after the electro-polishing. This figure is issued from Chapter III because no GND analysis was carried out on the samples studied in the present section. It is observed that for the short electro-polishing duration (20s), the samples surfaces correspond to the transition zone, while for higher the duration (60s), the surface structure corresponds to the deformed zone one. The so-called "UFG" zone is removed after the electro-polishing.
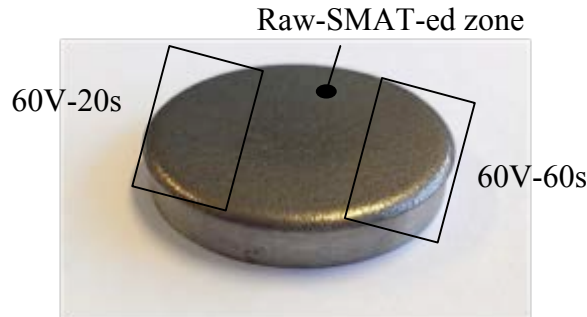
Fig. IV. 9: Schematic figure of the electro-polished zones on the surface of the SMATed sample.
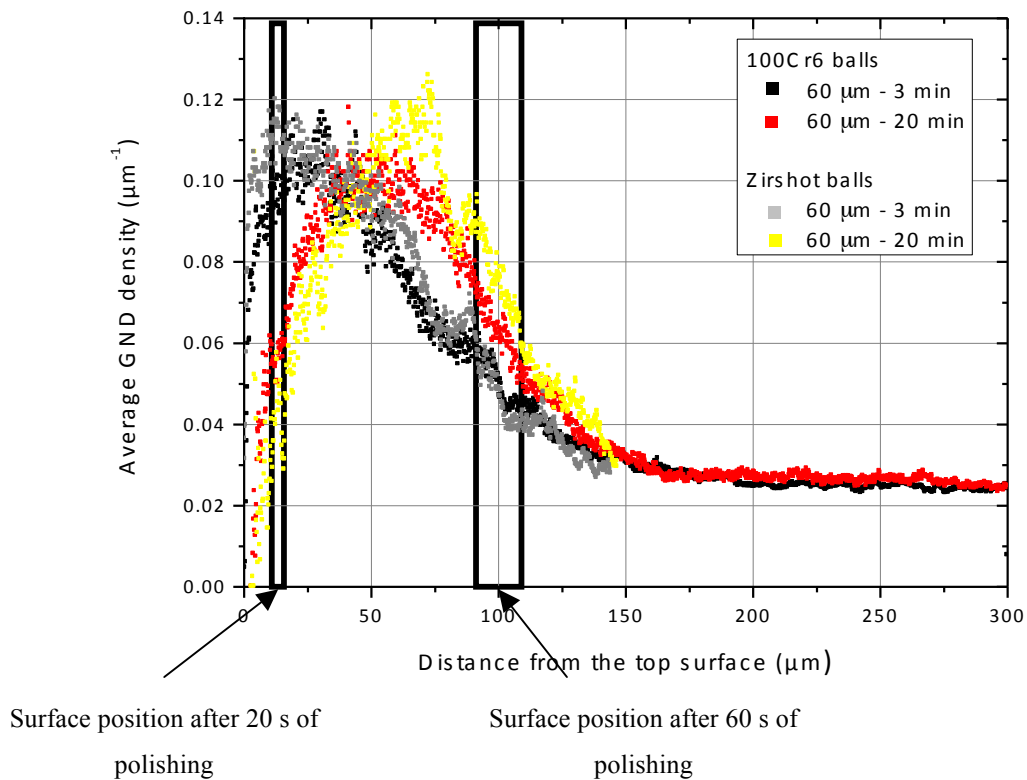
Fig. IV. 10: Evolution of the average GND density from the top treated surface of the AISI 316L samples treated under the amplitude of vibration of 60 µm and representation of the surface position after "electro-polishing". In black and gray hatchings after 20 s and 60 s of electro-polishing, respectively.

II. 2.   **Investigation of the surface microstructure and of the formed nitrided layer**

Fig. IV. 11gives the XRD patterns of the different zones of all the nitrided samples. After nitriding, it is observed -for all the samples-that the polishing step leads to the formation of γ_N peaks of higher intensity. It can also be seen that γ_N diffraction peaks of the SPN zones are shifted to lower angles, which must be associated to higher nitrogen content in the γ_N layer. Actually, higher nitrogen content increases the lattice parameters (a_N) and thereby the interplanar distance (d). It corresponds to a lowering of the scattering angle θ used in the Bragg's law.

To describe the evolution of γ_N layer thicknesses from these XRD results, the relative intensity $I\gamma_N/I\gamma$ is used. $I\gamma_N$ and $I\gamma$ intensities correspond to the air under the peaks. Actually, the XRD signal is issued from both the γ_N layer and the substrate γ, and as the diffraction volume of the sample ($\gamma_N + \gamma$) is identical for a given 2θ position, the $I\gamma_N/I\gamma$ indicates then the contribution of each related zones. The results are given in Table IV. 3. It is clearly observed that the raw-SMAT-ed nitrided zones present the lowest value of $I\gamma_N/I\gamma$. This indicates that more intensity is coming from the substrate (γ-phase), so a thin nitrided layer is formed. In addition, these results also show also that for the samples SMAT-ed for a long duration (17 min), the SN regions present a very low $I\gamma_N/I\gamma$ (0.13 for the D1A60T17 and 0.06 D1A60T17**Z** samples). In the zones polished during 20 and 60s before PN, the $I\gamma_N/I\gamma$ values are higher and quite similar. This shows that the formed γ_N layer is thicker.
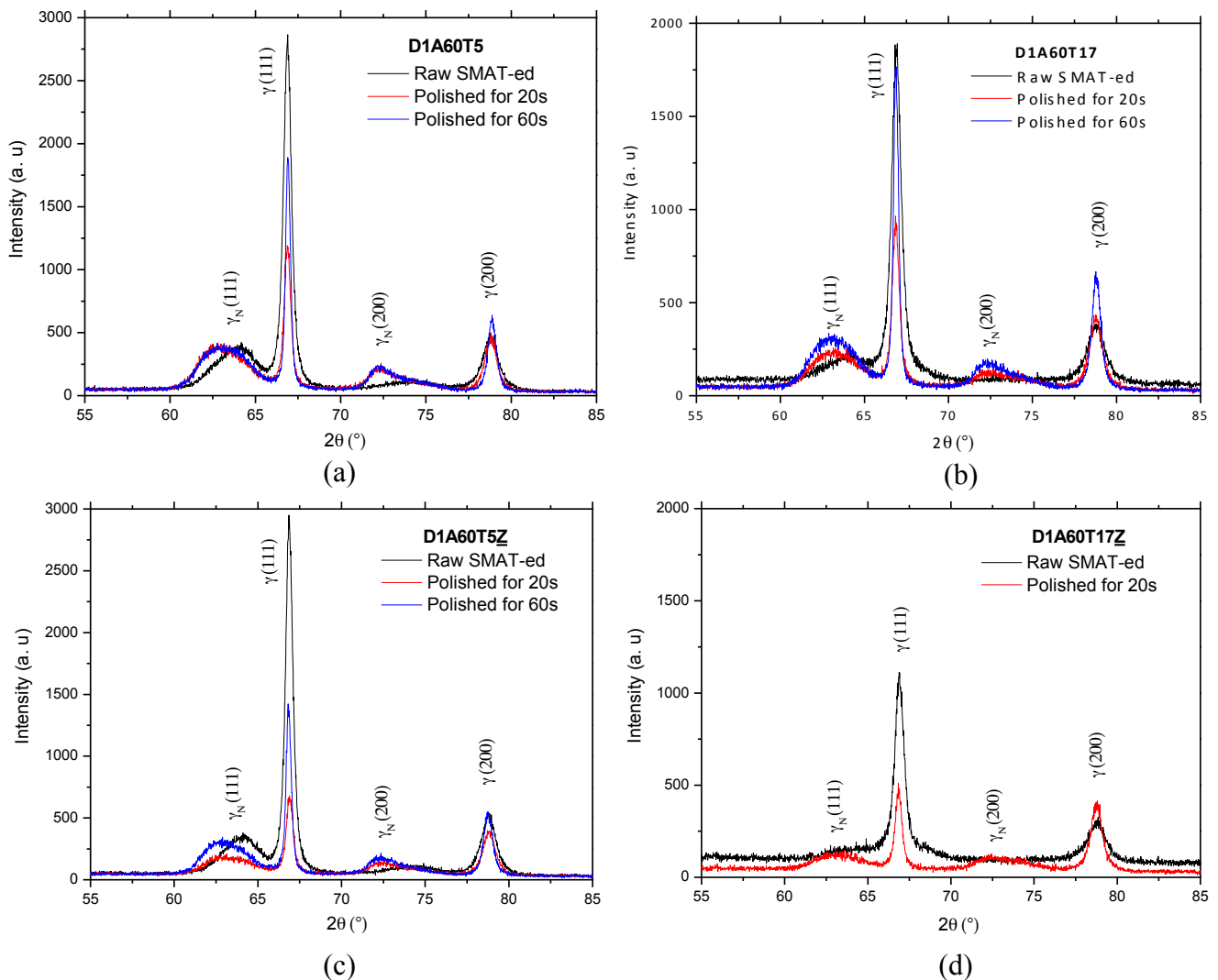
Fig. IV. 11: XRD patterns of the samples treated with (a and b) 100Cr6 samples and (c and d) with Zirshot balls for 5 and 17 min then nitrided.

| | | $I\gamma_N/I\gamma$ (peaks area ratio) - (111) peak | | |
		SN	SP20sN	SP60sN
Sample	D1A60T5 (Fig. IV. 11a)	0.35	1.53	1.27
	D1A60T17 (Fig. IV. 11b)	0.13	0.84	0.92
	D1A60T5Z (Fig. IV. 11c)	0.26	1.06	1.10
	D1A60T17Z (Fig. IV. 11d)	0.06	0.83	N. A.

Table IV. 3: Calculations of the intensity ratio $I\gamma_N/I\gamma$ for the (111) peak of all the samples.

Another interesting result that can be extracted from these XRD patterns results is the effect of SMAT duration on the surface contamination. Actually, after nitriding of the raw SMAT-ed samples, the background noise intensity when the SMAT duration increases. It can also be observed in Fig. IV. 11b and d that the background noise decreases after polishing steps of 20 and 60s. This effect was previously described in Chapter III, where it was attributed to the surface contamination by the Sonotrode elements (fluorescence induced by the presence of Ti).

(a) (b) (c)
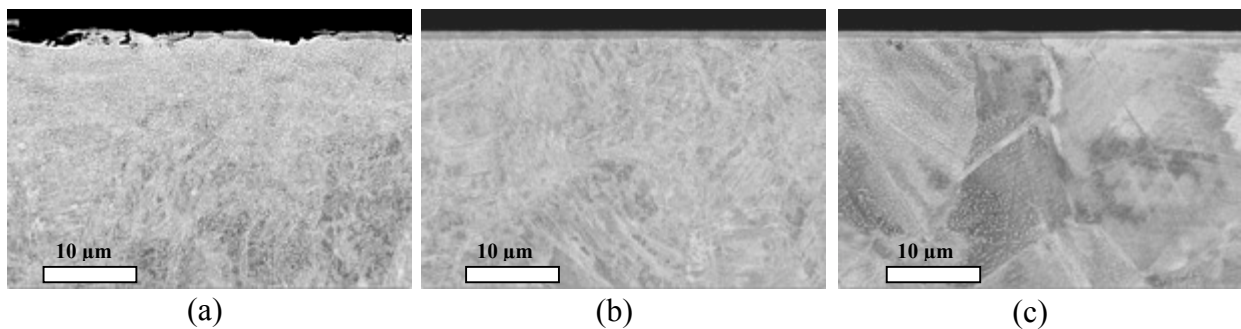
Fig. IV. 12: SEM cross section images showing the nitrided layer in the case of (a) the raw SMAT-ed surface nitrided, (b) SMATed+electropolishing for 20s+ nitrided and (c) SMATed+electropolishing for 60s+ nitrided. The sample was treated with 100Cr6 balls for 17 min.

From these XRD results, it is clear that the nitrided layer thickness depends on the surface structure. To compare the 4 treated samples, the thicknesses of nitrided layers are firstly estimated from SEM observations (Fig. IV. 12). The raw-SMAT zone presents a high density of defects and a discontinuous nitrided layer (Fig. IV. 12a), similar to the one observed in the first section of this chapter. After polishing for 20 and 60s (Fig. IV. 12b and c, respectively), the nitrided layer is continuous and uniform. Logically, the microstructure of the sample polished for 20s is less deformed and the initial grains shape can be easily seen.

The evolution of the nitrided layer thicknesses for the different SMAT conditions are summarized inFig. IV. 13. For the samples treated with the 100Cr6 balls for 5 minutes, the nitrided layer in the raw SMAT-ed region has the lowest thickness (~ 1.3 μm). The polishing for 20 and 60s results in the formation of thicker nitrided layers, reaching about 1.6 and 1.7 μm, respectively. When the treatment duration increases (17 min), the nitrided layer is very thin in the raw SMAT-ed

region (< 1 µm), and then the thickness increases slightly after polishing for 20 and 60s, to reach about 1 µm.

For the sample treated with balls in Zirshot, the nitrided depths for all the conditions (in comparison with the samples treated with 100Cr6- balls) are quite thinner at low SMAT duration and similar when the treatment duration is 17 min. However, similar tendency is observed after successive polishing. In fact, for the treatment duration of 5 min, the nitrided depths change very slightly (1 to 1.5 µm), and for a treatment duration of 17 min, the depth increases from about 1 µm (in the raw SMAT-ed sample) to about 1.2 µm (in the 60s-polished zone).

It should also be noted that these values are always below the thickness of the nitrided layer formed on the surface of untreated AISI 316L (at 350 °C for 8h), which is around 2 µm. This is probably due to the surface preparation method. In the present study, the samples cross-section were simply mechanically polished until a mirror-like finish (1 µm diamond paste) then polished by Oxide Polishing Suspension (OP-S) for 30 min.
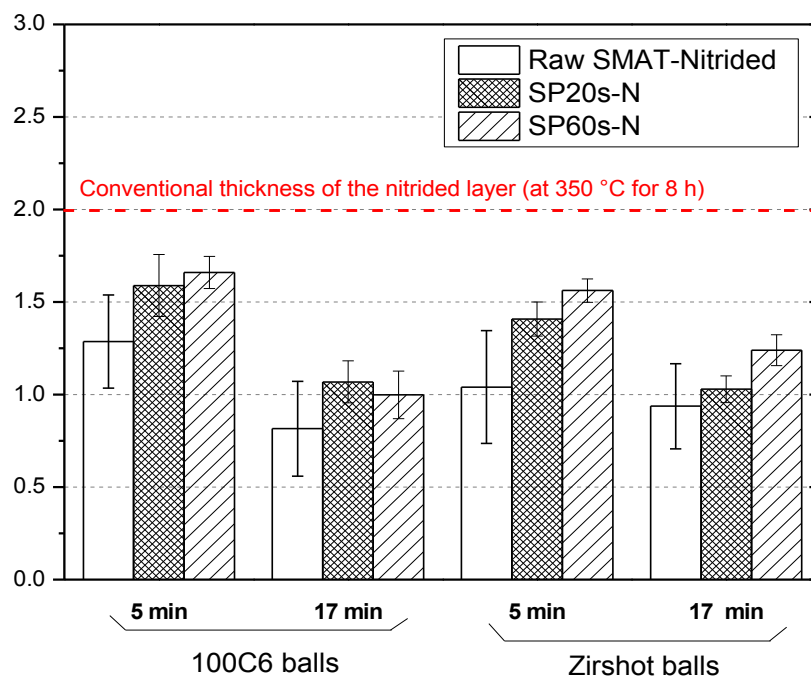
Fig. IV. 13: The evolution of the nitrided layer thickness as function of SMAT parameters and surface electro-polishing parameters.

To depict more precisely the thickness of the nitrided layer, other techniques are used.Fig. IV. 14shows for example the nitrogen concentration measured by Glow Discharge Optical Emission Spectroscopy (GD-OES) for the sample treated with the 100Cr6 balls for 5 minutes. The tendency is quite similar to the one observed by SEM and XRD. The thicknesses depicted by GD-OES are more important in the raw SMAT-ed and 20s polished zones, where the nitrided depths reach about

2.5 and 3 µm, respectively (~1.2 and 1.6 µm estimated by SEM observations). Thicknesses determined by GD-OES are maximum thicknesses because such measurement is performed over several grains on large area. This result confirms the XRD observations, where the γ_N peaks shift to lower angles after polishing for 20 s (higher nitrogen content $\rightarrow$ increase of the lattice parameter $\rightarrow$ lower diffraction angle).
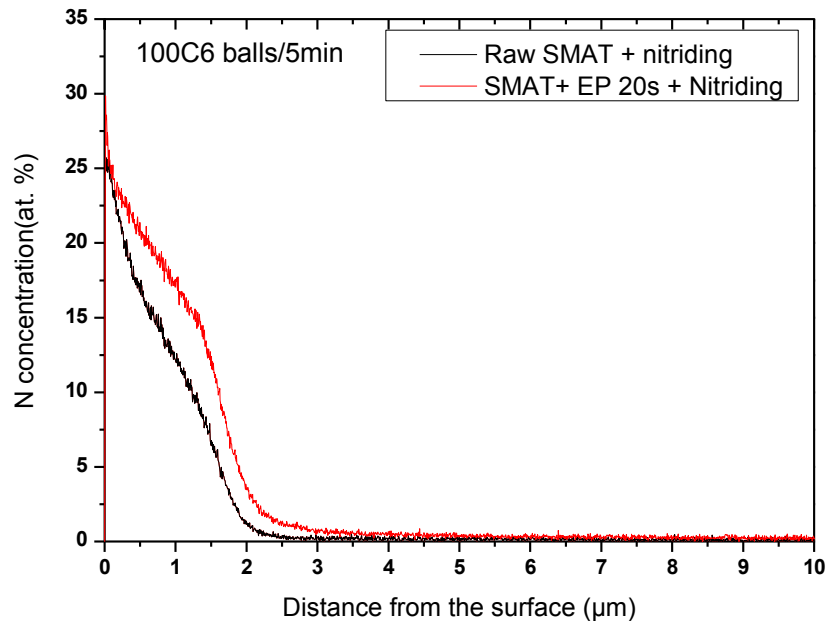
Fig. IV. 14: Nitrogen concentration profiles in the raw SMAT region (Black line) and after polishing for 20 s (Red line) for the sample treated with 100Cr6 balls for 5 min.

II. 3.   **The surface hardness evolution after Surface polishing**

The surface hardness of the different regions (raw SMAT-ed, polished for 20s and 60s then nitrided) is measured using different loads (25$\rightarrow$ 500 g). The results are summarized in Fig. IV. 15 and Fig. IV. 16.

- *Samples treated with 100Cr6 balls:*

For the sample treated with the 100Cr6 balls for 5 min (Fig. IV. 15a), the hardness of the raw SMAT-ed zone then nitrided has the highest hardness, reaching about 600 HV at the extreme surface and decreases to reach about 450 HV at a depth of about 6.5 µm. For the regions polished for 20 and 60s, the hardness is lower than the raw SMAT-ed region one. However, it remains high in the 20s polished zone (>400 HV) in comparison with the 60 s polished one, as the latter is less deformed (less defects after polishing).

When the SMAT duration is increased to 17 min, the hardness of the raw SMAT-ed nitrided region reaches about 650 HV (near the hardness obtained after SMAT+PN inFig. IV. 15b). The

hardness of the region polished for 20s remains quite similar to the sample treated for 5 min (in Fig. IV. 15a), while it is higher in the region polished for 60s and nitrided. It may be maybe explained by the presence of defects at this depth, in comparison with of the sample treated for a low SMAT duration, where the overall affected layer is thinner (Chapter III).
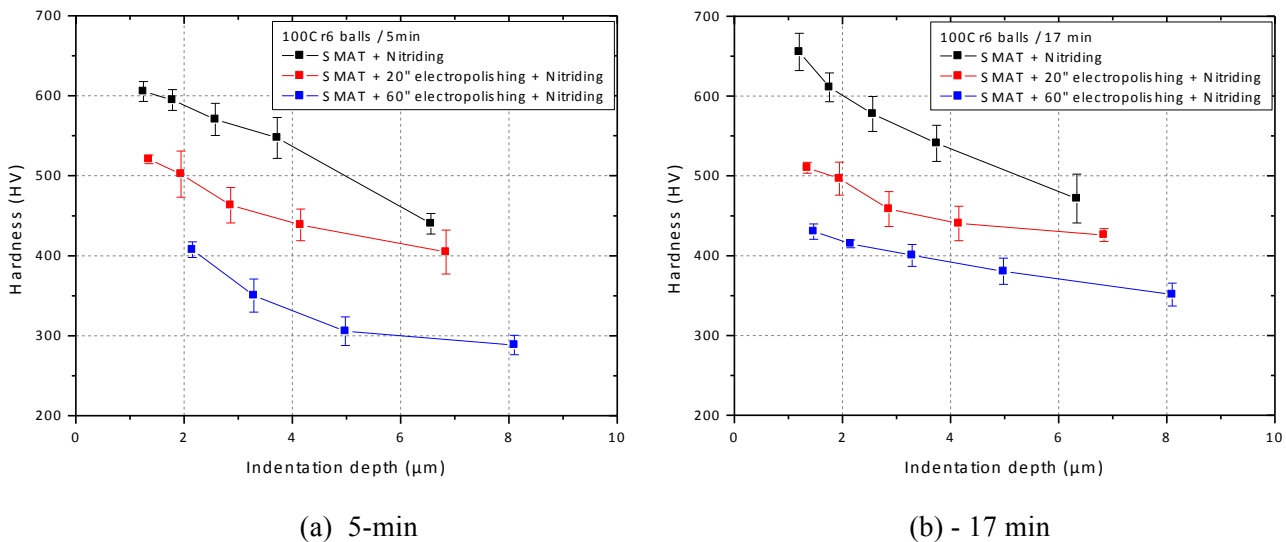
(a) 5-min

(b) - 17 min

Fig. IV. 15: Surface hardness evolutions of the samples SMAT-ed with 100Cr6 balls prior to nitriding. Two SMAT durations: (a) 5 min and (b) 17 min.

- *Samples treated with Zirshot balls:*

For the samples treated with the Zirshot balls, the surface hardness of the three regions is lower than the one of the samples treated with the 100Cr6 balls. At low SMAT duration (Fig. IV. 16a), the hardness of the raw SMAT-ed Nitrided region reaches about 500 HV at the extreme surface and then decreases to reach about 375 HV for an indentation depth of 7 µm. The polishing of the surface for 20s before nitriding results in a significant decrease of the hardness, where it reaches about 375 HV and then decreases until about 300 HV corresponding to an indentation depth of 8 µm. When the surface is polished for 60s, it is observed that after nitriding, the surface hardness reaches about 360 HV at the extreme top surface and then decreases to about 280 HV. These hardness values are slightly lower than the 20s polished sample, but remain higher in comparison with the samples treated for 5 min (thinner deformed layer).

For the treatment duration of 17 min, the results are given in Fig. IV. 16b. The nitrided raw SMAT-ed region has a highest hardness reaching more than 500 HV and remains constant until an indentation depth of about 3 µm then decreases to about 450 HV (for an indentation depth of about 6 µm). In the SMAT-ed20s-polished zone, the hardness decreases to about 470 HV at the extreme

surface and then stabilizes at a depth of 3 μm (~400 HV). However, the surface hardness is only increased to about 350 HV within less than 4 μm then decreases to about 300 HV in the 60s-polished zone (less deformed layer in comparison with the 20s polished zone).

(a) - 5 min   (b) - 17 min
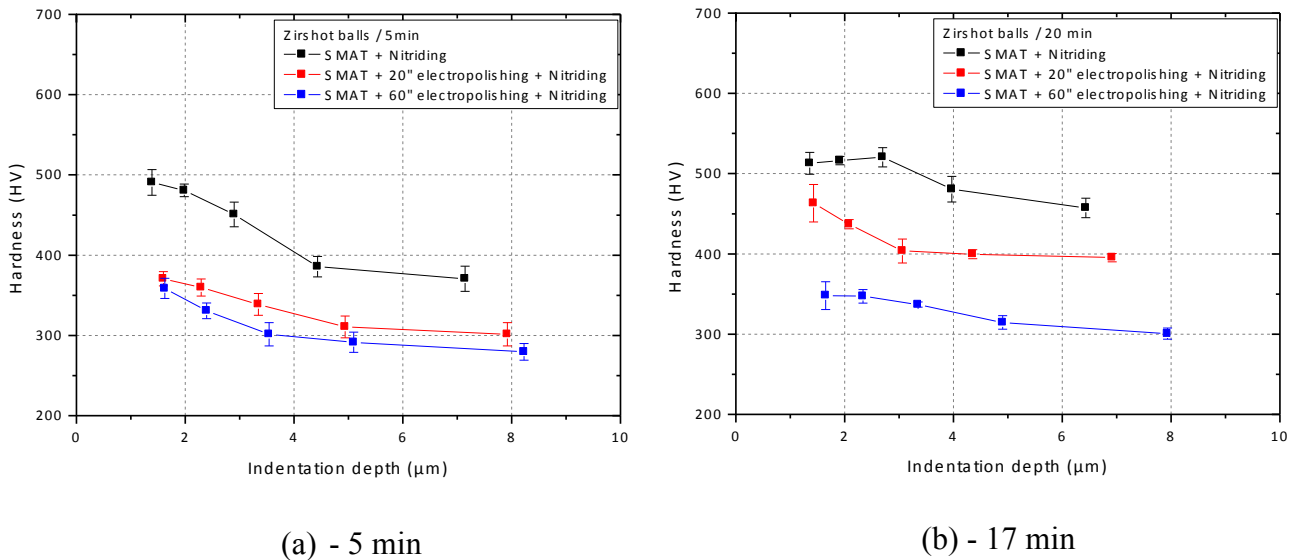
Fig. IV. 16: Surface hardness evolution for samples treated with Zirshot balls.

II. 4.   **Discussion**

The investigation of the raw SMAT-ed surface (in Chapter III) has confirmed the presence of a contamination "layer" on the top surface, composed of elements coming from the sonotrode (Ti, Al and V), the chamber (Cr) and the balls (Zr). The presence of these external elements blocks the diffusion process of the nitrogen and thereby leads to the formation of a non-continuous nitrided layer (continuous only in the zones where no contamination occurs). This phenomena was observed in the literature for the ball milling process(Chemkhi et al. 2013), where the AISI 316L was oxidized leading to decreasing the nitrided layer thickness. The same kind of oxides was observed on the surface of the AISI 316L(Waltz et al. 2011). In the present work, the electro-polishing allows to remove the contaminated layer and partly conserve (only after polishing for 20s) the deformed structure induced by SMAT, leading to higher surface hardness. However, the nitriding kinetics in not improved after the removal of the contamination layer in contrary to what was observed by Thiriet et al. (Thiriet et al. 2012). It is not clear for the moment why the nitriding kinetics is not improved in our study, but the plastic deformation state is probably different from the one reported by Thiriet et al.

III.   <u>Conclusions of Part I</u>

In this first part, the activation of the AISI 316L surface by SMAT before plasma nitriding was investigated. It was revealed that the nitrogen diffusion is not enhanced when the raw SMAT-ed surfaces are directly nitrided. Even after an intermediary step of polishing to remove the contamination layer formed during the SMAT, the nitrided depths remain smaller than the one of the nitrided material without SMAT.

It was also observed that the surface hardness is significantly increased after the duplex – treatment SN even if the nitrogen diffusion is not enhanced. It reaches about 700 HV (HV$_{0.025}$) at the extreme surface after SN, while it is about 360 HV after only Nitriding or SMAT. In addition, the subsurface hardness after SMAT remains quite similar after Nitriding at 350 °C for 8h. Using the GND as plastic deformation indicator, it was proved that the defects density induced by SMAT remains constant after Nitriding. This was attributed to the lack of recrystallization and grain growth during the nitriding process (350 °C, much lower than the microstructure recrystallization and recovery temperatures). This increase of hardness was not simply a cumulative effect (addition of the SMAT and nitriding hardening contributions). More complex processes, such as reaction of nitrogen with the surface contamination elements leading to the formation of hard nitrided, such as TiN or AlN. However, why believe that the plastic deformation state after the SMAT+PN duplex treatment can have a major rule in increasing the surface hardness.

Furthermore, it was observed that the SMAT-ed surface polished before nitriding results in a decrease of the surface hardness, essentially for the samples treated for a low SMAT duration (5 min). Actually, as the overall affected depth of these samples was not very important, and the polishing removed the layer containing a high density of defects, and thereby, the low increase of the surface hardness was only due to the contribution of the formed nitrided layer. When the SMAT duration is higher (17 min), the surface hardness of the SPN regions is lower than the SN one, but remains higher than the only SMAT-ed sample.

All these results show that removing the contaminated layer can enhance the nitrogen diffusion as compared to rough SMAT-ed samples (example inFig. IV. 13), leading to the formation of thicker nitrided layer. However, the thickness of the nitrided layer for SMAT-ed+nitrided samples is always thinner than the initial material nitrided one. Even if the surface hardness is decreased in comparison with the SN regions, the obtained hardness after SPN is still higher than after only SMAT or nitriding. Therefore, the SMAT increases significantly the surface hardness and could also be a promising surface activator before nitriding to enhance both the diffusion of nitrogen, but

it should be optimized to obtain a convenient microstructure (continuous nitrided layer) and ''clean'' surface (no contamination by the balls and sonotrode elements).

Part. 2. Investigation of other surface activation processes before nitriding of the AISI 316L: Cold Rolling (CR) and High Current Pulsed Electron Beam (HCPEB)

Part. 1. showed that the surface activation by SMAT does not automatically lead to the enhancement of nitrogen diffusion in AISI 316L. This was essentially attributed to the surface contamination by the sonotrode elements (Ti), which may slow down the nitrogen diffusion. In this part, the surface activation by SMAT will be firstly substituted by the Cold Rolling (CR), which is a simple deformation treatment, and then by the thermo-mechanical treatment "High Current Pulsed Electron beam". The effect of these pre-treatments on the microstructure and the nitrided depths of the AISI 316L will be investigated. The surface hardness evolution is also detailed.

I. <u>The effect of cold rolling on the nitrogen diffusion and surface hardness of the AISI 316L</u>

I. 1. The experimental conditions

The studied material is the same as in the last part: AISI 316L with the same composition (see chapter II for more details). The specimen are 25 mm in diameter and 8 mm thickness. The surfaces of all the samples were mechanically polished until a mirror like finish (1 µm diamond paste) then cold-rolled at different rolling reduction of 45, 55 and 75 %. The samples were then nitrided at 350 °C for 8 hours. The conditions of cold rolling and nitriding are summarized in Table IV. 4.

Rolling reduction (%)			
0	45	55	75
The Nitriding conditions	350 °C / 8h		

Table IV. 4: The cold rolling and plasma nitriding treatment conditions.

Prior to nitriding, all the surfaces were again mechanically polished to remove the layer where a high shear stress is present. The surface state is verified by the pole figures measurement by XRD. Fig. IV. 17 presents the γ-(111) pole figure evolution for the different rolling reduction ratios. It can be seen that it is typical cold-rolling texture of fcc metals and no shear component is depicted, which confirm the effect of polishing to remove the induced sheared layer.

(a) (b) (c)
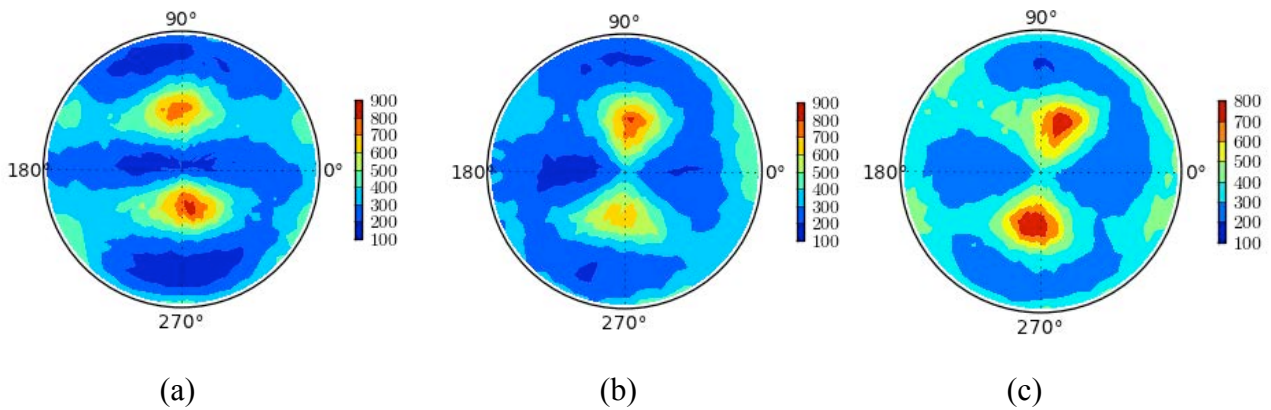
Fig. IV. 17: The (111) pole figure evolution of the upper surface after (a) 45%, (b) 55% and (c) 75 % of cold rolling reduction. ND is in the center and RD is pointing down in all figures.

I. 2. **The nitrided layer evolution of the CR-N samples**

Fig. IV. 18 shows the θ-2θ patterns of the CR and CR-N samples. Before nitriding, as shown in Fig. IV. 18a, only the peaks corresponding to the γ-phase are depicted. No peak corresponding the martensite/ferrite phase is revealed. A broadening of the γ peaks is also observed after CR. This is due to the grain refinement and plastic deformation.

After nitriding of the CR samples, the XRD patterns, given in Fig. IV. 18b reveal the presence of the expanded austenite γ_N. The samples rolled for 45 and 55 % then nitrided present higher γ_N-peak intensity in comparison with the only nitrided one. This intensity is even higher when the rolling reduction is 75 %. The CR45%-N and CR55%-N samples seem to have the same nitrided layer thickness, while a thicker nitrided layer seems to be formed on the surface of the CR75%-N sample.
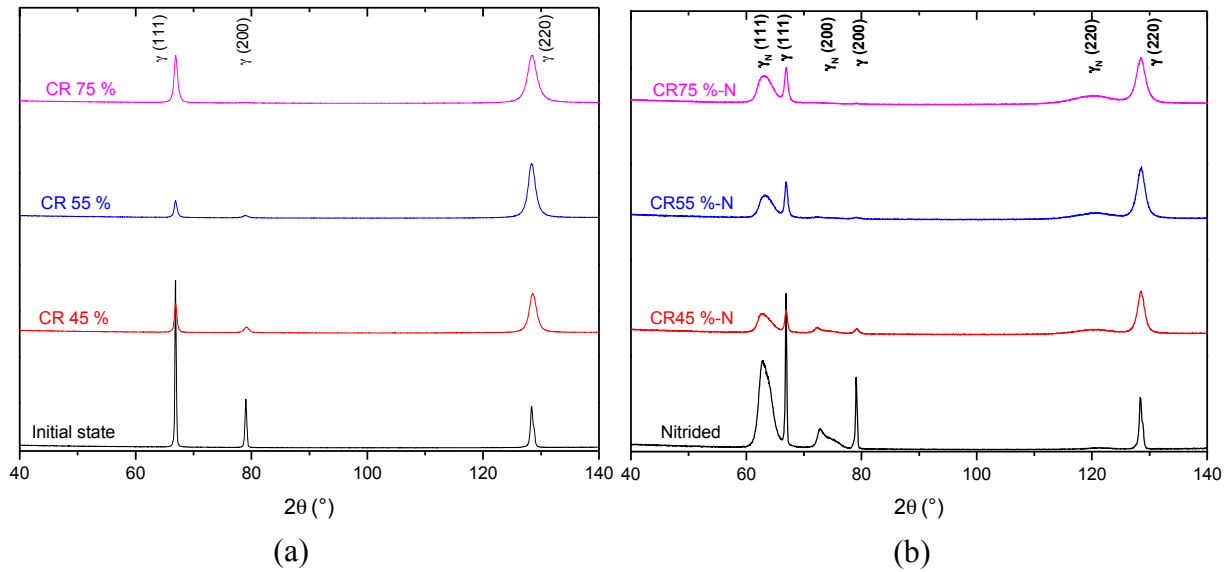
Fig. IV. 18: X-ray diffraction patterns of (a) the Cold-Rolled and (b) the cold rolled+Nitrided samples.

To confirm these results, cross sectional observations were carried out. Fig. IV. 19 gives the microstructure morphology of the four treated samples, and Fig. IV. 20 summarizes the thicknesses of the nitrided layers estimated from these observations. In Fig. IV. 19a, a continuous nitrided layer of about 2µm is formed on the coarse grains of the only nitrided sample. For the sample CR45%-N (Fig. IV. 19b), the initial grains are visible but contain high density of defects. The nitrided layer formed on the surface of this sample is about 3 µm in thickness. When the rolling rate is increased to 55%, the initial grains are not visible anymore, and a very high density of defects can be clearly seen inFig. IV. 19c. However, the nitrided layer seems to have similar thickness as the one of the CR45%-N. When the reduction rate further increases, the structure is more deformed and contains logically very high defects density, as shown in Fig. IV. 19d. It is also observed that the nitrided layer formed on this sample surface is thicker (~ 4 µm).

From Fig. IV. 20, it is clearly observed that the nitrided thickness is strongly increased when the material is subjected to CR before nitriding. The nitrided thickness was increased by a factor of about 45 % when reduction rates of 45 and 55 % are applied. The thickness is further enhanced when a very high reduction rate is used (75%) when it is increased by about 95 %, reaching 4.2 µm.

(a)

(b)

(c)

(d)

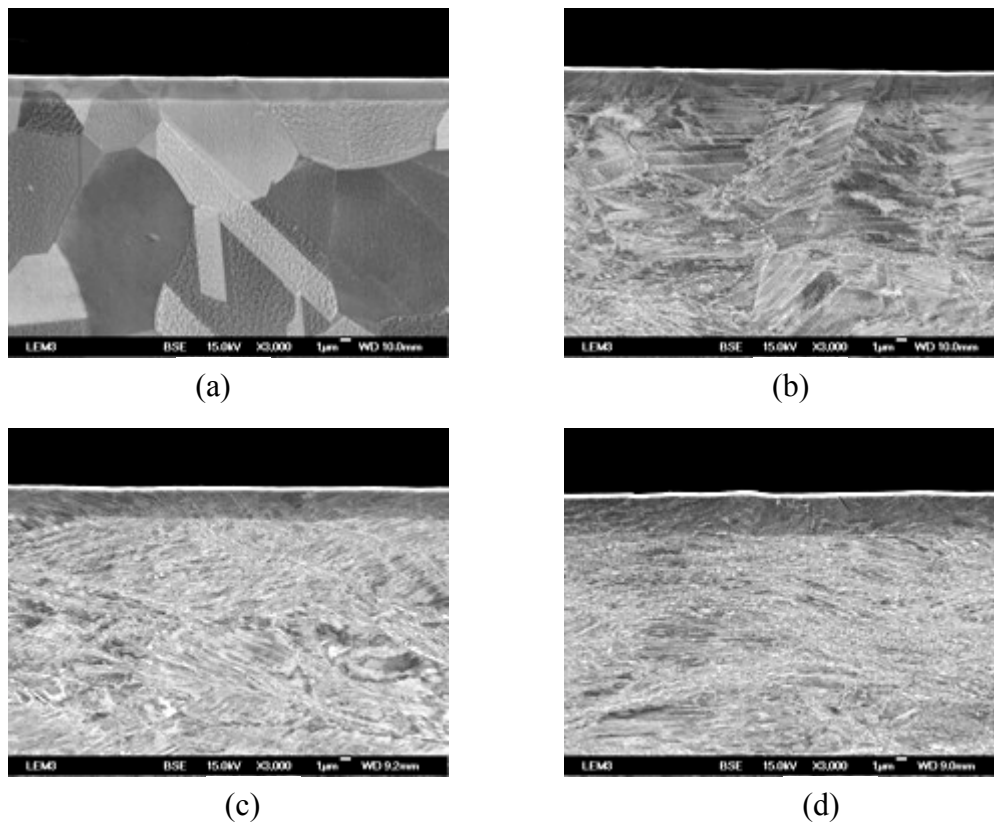*Fig. IV. 19: Microstructure of the surface layers formed on the AISI 316LSS after nitriding of (a) an untreated material and cold-rolled samples with a rolling reduction of (a) 45 %, (b) 55% and (c) 75 %.*

As mentioned previously, the thickness of the nitrided layer revealed by SEM observations is underestimated. To depict it more precisely, GD-OES analysis is carried out and the nitrogen content evolution as a function of the distance from the top surface is given inFig. IV. 21. Similar trend, as the one observed after SEM observations (Fig. IV. 19 and Fig. IV. 20), can be seen. As expected, thicker nitrided layers are measured. For the nitrided sample (black line), the nitrogen diffusion reaches about 2 µm. The highest nitrided depth is obtained on the sample deformed with a rolling rate of 75% prior to nitriding (pink line), where the thickness reaches about 4.5 µm more than two time higher than the only nitrided one). The samples deformed with rolling rates of 45 and 55 % have intermediary nitrided layer thickness of approximately 3,5 µm.

It should also be noted that the nitrogen concentration in the top surface is different between the initial and CR nitrided samples, as observed inFig. IV. 21. Actually, the nitrogen concentration reaches more than 30 at. % on the surface of the initial nitrided sample, but on the CR-N samples, this concentration is around 25 at. %, and the diffusion depth is much higher than within the initial nitrided sample. The CR45%-N and CR55%-N samples present quite similar nitrogen profiles, which is consistent with the cross section SEM observations where the nitrided layer thickness for both samples was about 3 µm.
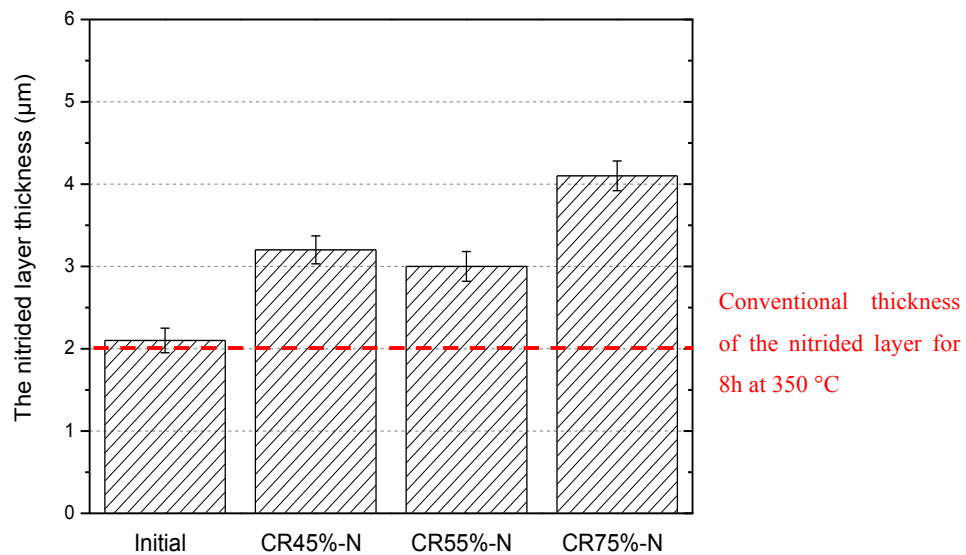
Fig. IV. 20: The evolution of the nitrided layer thickness as function of the rolling reduction.
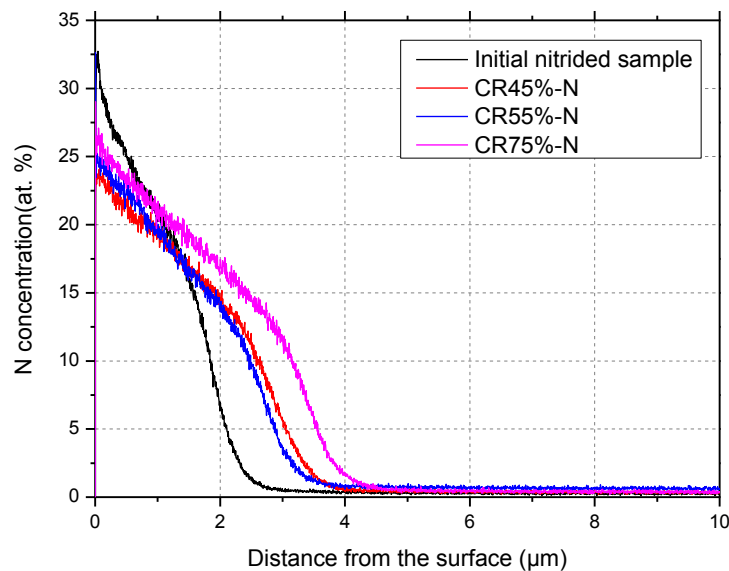
Fig. IV. 21: In-depth GD-OES profiles of nitrogen for the all the nitrided samples.

I. 3.   **The surface hardness evolution after the CR-N duplex treatments**

In order to investigate the influence of the duplex treatment CR-N on the mechanical properties of the treated material, the surface hardness was measured using the same procedure as for the SMAT-Nitrided samples (surface indentations using different loads 25g – 500g). The results are summarized inFig. IV. 22. One can notice that for the only nitrided sample (black curve), the hardness was increased to about 325 HV, and remains higher within the first 3-4 µm (corresponding approximately to the nitrided layer thickness) than the initial level (~ 180 HV).
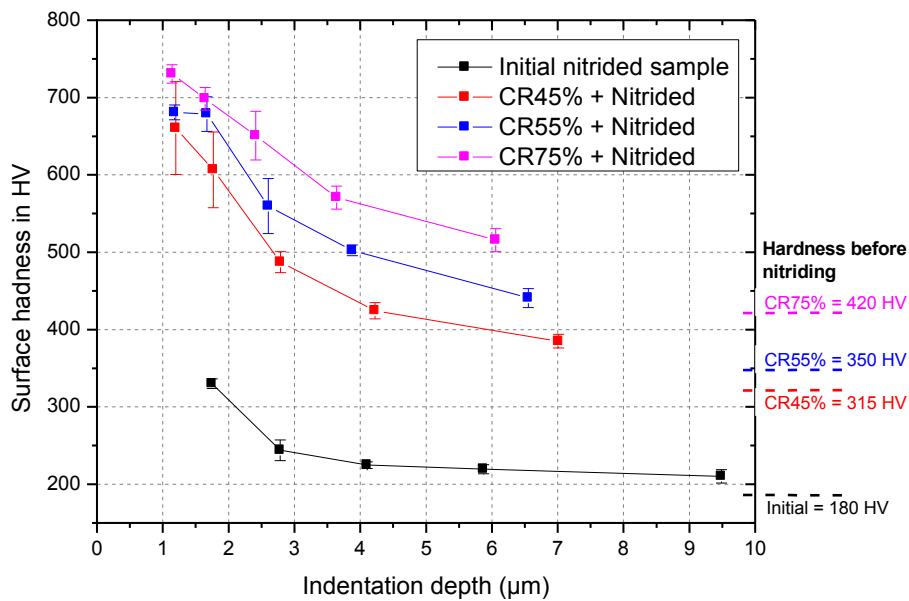
Fig. IV. 22: Surface hardness evolution after cold rolling + Nitriding measured using different indentation loads.

The CR coupled with nitriding seems to have an important effect on the hardness from the lowest rolling reduction. Actually, for the CR45%-N sample (red curve), the surface hardness is about 660 HV, almost 220% higher than the only nitrided sample one. As the indentation loads increase, the hardness decreases to reach finally about 400 HV (for the highest indentation load).

When the rolling reduction is increased to 55% before nitriding, the hardness further increases as observed in the blue curve. The extreme surface hardness is about 675 HV then decreases to about 450 HV for the maximum indentation load, quite similar to the surface hardness of the CR45%-N sample (~ 660 HV).

The highest hardness is obtained on the surface of the CR75%-N sample, where it reaches about 740 HV on the extreme top surface and then decreases to about 520 HV for the highest indentation load (at about 6 µm).

In comparison with the SMAT+PN duplex treatment, the hardness decreases more "slowly" when the indentation load increases. This is due to the fact that the nitrided layer is thicker after nitriding of cold-rolled surfaces.

In addition, as for the SMAT+PN treatment, the hardness after the CR+N duplex treatment is also not simply cumulative. This can confirms that this increase of hardness is not related to the surface pollution and an eventual reaction of nitrogen with the contamination elements (formation of TiN, AlN). Another effect, related to the plastic deformation state, should be responsible for the increase of the nitrogen diffusion. This effect can be more easily studied and understood using the cold

rolling as surface activator, because the surface strengthening by this process is easier to control than by SMAT.

I. 4. **Summary**

The experimental results presented in this section give the evolution of the nitrided layers thickness and the surface hardness after the duplex treatment CR-N. Prior to nitriding, the samples were rolled using three reduction rates (45, 55 and 75 %). The SEM observations show that a continuous nitrided layer is formed on the surface of the four treated samples, and that the thickness increased with an increase of the rolling reduction. The nitrided depths of the samples cold-rolled under 45 and 55%ratios have quasi-similar thickness. The nitrogen content profiles (measured by GD-OES) confirm this trend.

In addition, the extreme surface hardness of CR-N samples presented an important enhancement. In comparison with the only nitrided sample, the hardness was increased by about 220 % for the samples with rolling reductions of 45 and 55 %, and by about 240 % for the sample rolled for 75%.

As for the SMAT, the final increased hardness is not only a cumulative effect of the CR and nitriding hardness. This enhancement is also probably related to the plastic deformation state after the CR process. It is not to the formation of nitrides such as TiN or AlN, as during the cold rolling, no contamination by the Ti and Al or other elements is induced.

II. Plasma-Nitriding of the AISI 316L surface activated by the thermo-mechanical treatment "High Current Pulsed Electron Beam"

In this last section, a new surface activation before plasma nitriding will be investigated. Actually, as shown in this chapter, the SMAT induces a surface contamination by the sonotrode and chamber elements, leading to decrease the nitrogen diffusion in the surface of the AISI 316L. On the other hand, the cold rolling gives interesting results in term of surface-activator before plasma nitriding. However, the shape of the samples to be treated limits this process. In the case of complex shapes in the industrial applications, the use of this process is impossible. Therefore, in this section, a recently developed technique of surface treatments, the High Current Pulsed Electron beam (HCPEB), is suggested as a new surface activator. It has different advantages firstly to treat parts of different shapes, and second to avoid direct contact with the treated surface. The effects of this process on the nitriding diffusion of the AISI 316L are detailed in the following paragraphs.

II. 1.   Materials and HCPEB experimental conditions

As mentioned in the "Materials and Experimental techniques" chapters, two grades of AISI 316L are subjected to the HCPEB treatment: the "conventional" AISI 316LM and the AISI 316LS grade more rich in Sulphide. The last grade contains Manganese Sulphides (MnS), which give very consistent machining characteristics to the alloy. The presence of these sulphides will allow the formation of higher density of craters on the surface during the HCPEB treatment. More details about the materials studied and the typical microstructure modifications after HCPEB are given in Chapter I. In the present work, the samples are treated for 20 pulses under 2 accelerating voltages: 19 kV and 27 kV.

The chemical compositions of the two 316L grades used in this part are given in the tables below (Table IV. 5). It should be noted that the Ni content in the AISI 316LS in significantly low in comparison with the AISI 316LM one, which can affect the stability of this alloy during surface treatment. The ($\gamma \rightarrow \alpha'$) phase transformation is then possible.

316LM wt. %											
Fe	C	Mn	Si	S	P	Cr	Ni	Mo	Cu	Co	N2
62.724	0.02	1.79	0.38	<0,002	0.02	17.43	14.7	2.74	0.16		0.04

(a)

316LS wt %											
Fe	C	Mn	Si	S	P	Cr	Ni	Mo	Cu	Co	N2
68.184	0.020	1.520	0.524	0.028	0.027	16.700	10.140	2.080	0.522	0.203	0.052

(b)

Table IV. 5: The chemical composition of the two AISI 316L grades studied in the present section.

II. 2.   **Microstructure modifications and nitrided layer thickness evolution**

The HCPEB treatment induces modifications in the microstructure morphology of the surface layer. XRD analyses are then carried out on the surface of the different samples before and after HCPEB and the results are grouped in the figure here after (Fig. IV. 23). It can be clearly observed inFig. IV. 23a that the microstructure remains formed bythe γ-phase after HCPEB under low and high accelerating voltage, while in the case of the AISI 316LS, a new peak corresponding to the transformation martensite (α') appears clearly. The formation of these phases will probably modify the diffusion during the post Plasma Nitriding treatment.
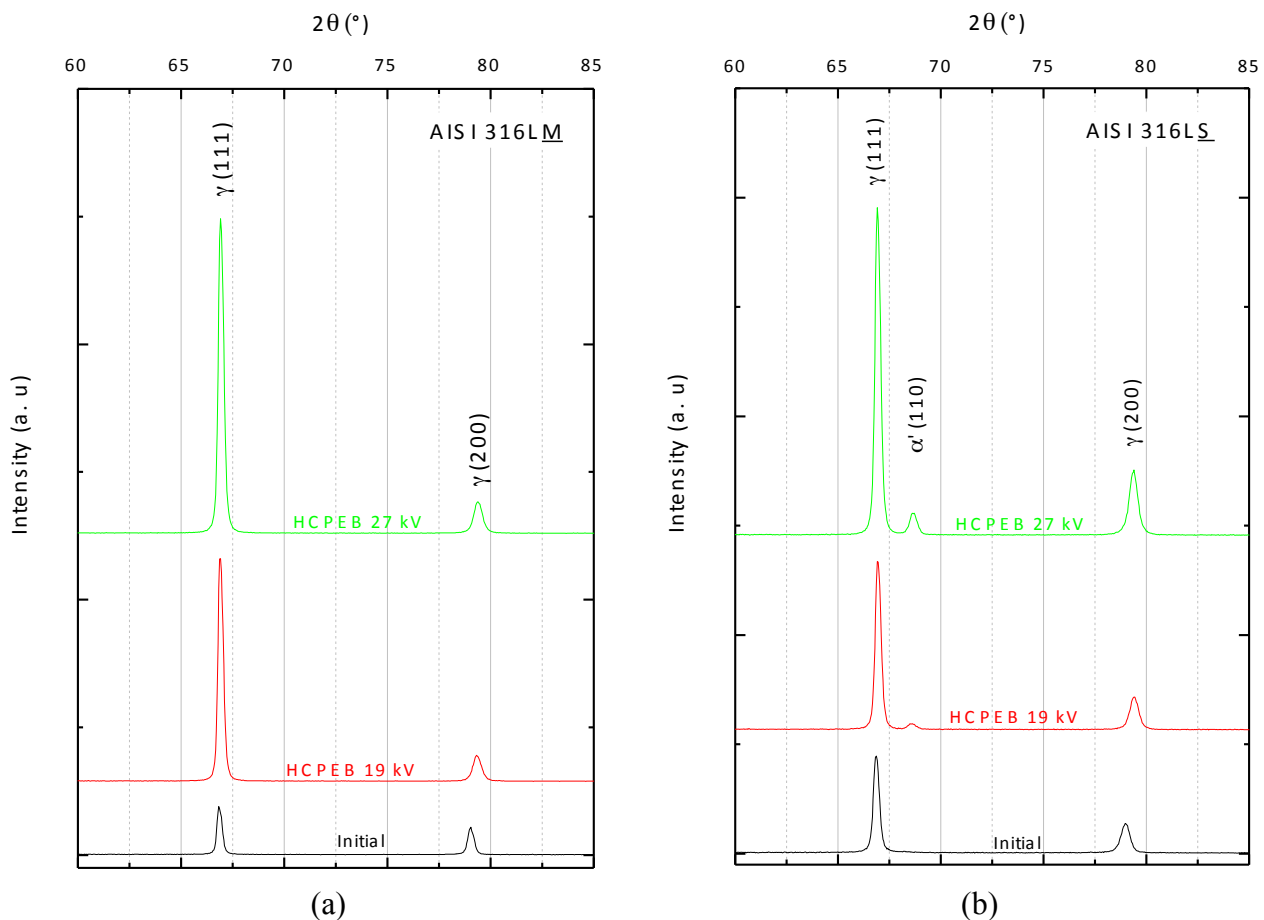

Fig. IV. 23: XRD pattern of (a) the AISI 316LM and (b) the AISI 316LS before and after treatment by HCPEB.

To observe the evolution of the formed microstructure and the nitrided layer thickness, SEM observations are given inFig. IV. 24. The associated estimations of the thicknesses are presented inFig. IV. 25. For the AISI 316LM (Fig. IV. 24a to c), after nitriding of the initial material, a continuous nitrided layer of about 2 μm is observed. However, the thickness of the nitrided layers formed on the surface of samples pre-treated by HCPEBseems to increase, reaching approximately 2.8 and 3 μm under low and high energy, respectively. Concerning the AISI316LS, the nitrided

layer formed on the initial material (Fig. IV. 24d) and pre-treated sample at low energy (Fig. IV. 24e) is continuous and has almost the same thickness as the AISI 316LM sample (~ 2.3 on the initial sample and 2.7 μm for the pre-treated HCPEB sample then nitrided). However, when the sample is pre-treated under high energy (Fig. IV. 24f), the formed nitrided layer is thinner (~ 2 μm).

In addition, it should be noted that the surface after the HCPEB treatment of the AISI 316LS (as observed in Fig. IV. 24e and f) presents more important roughness than the AISI 316LM one. This is due to the higher density of craters formed on the surface of the AISI 316LS as it contains a high density of manganese sulphides.
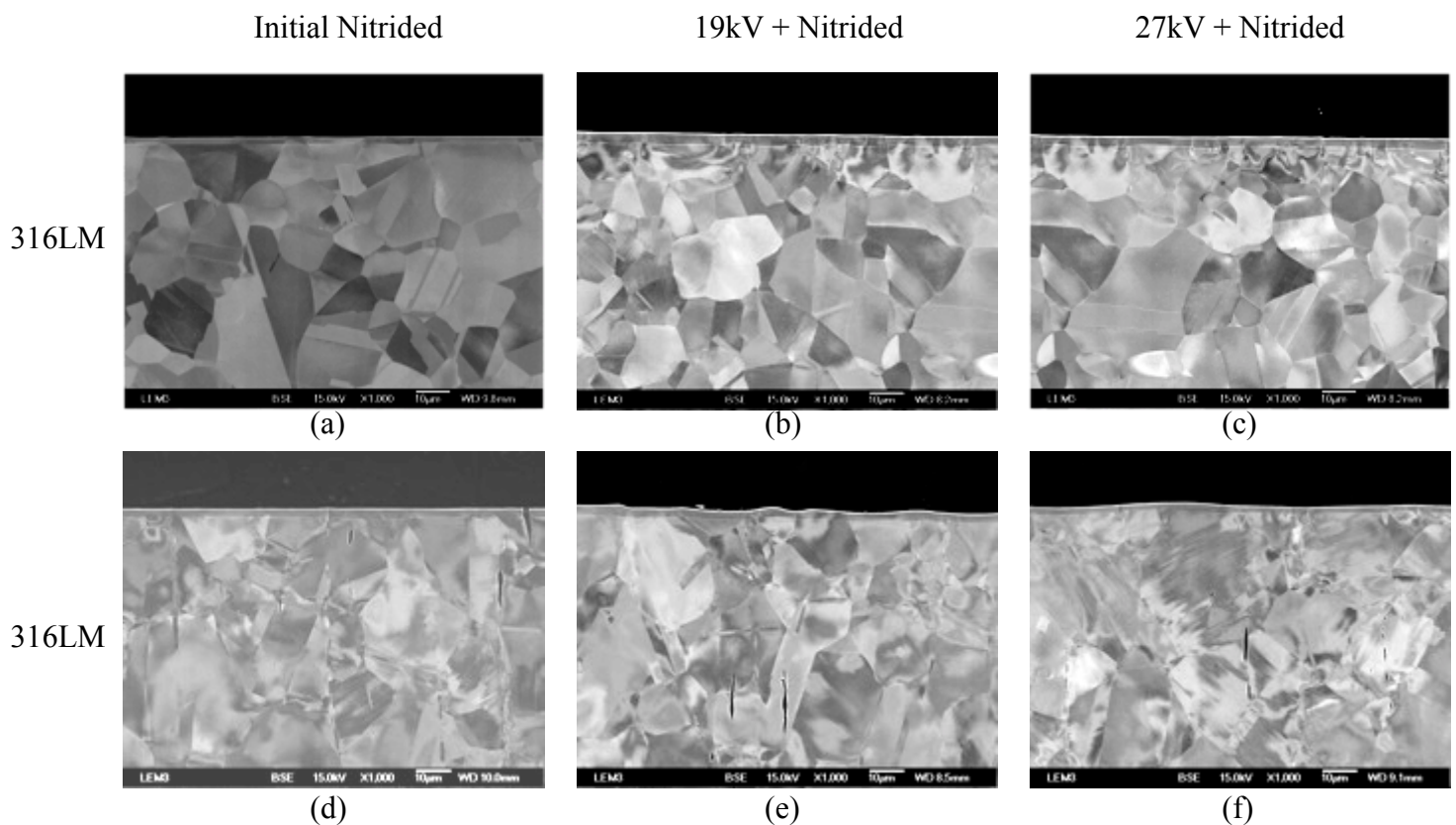

Fig. IV. 24: Cross-section microstructure after nitriding of (a, b et c) the AISI 316LM and the 316LS (d, e and f) before and after the HCPEB treatment. The nitrided layer can be seen at the extreme top surface.
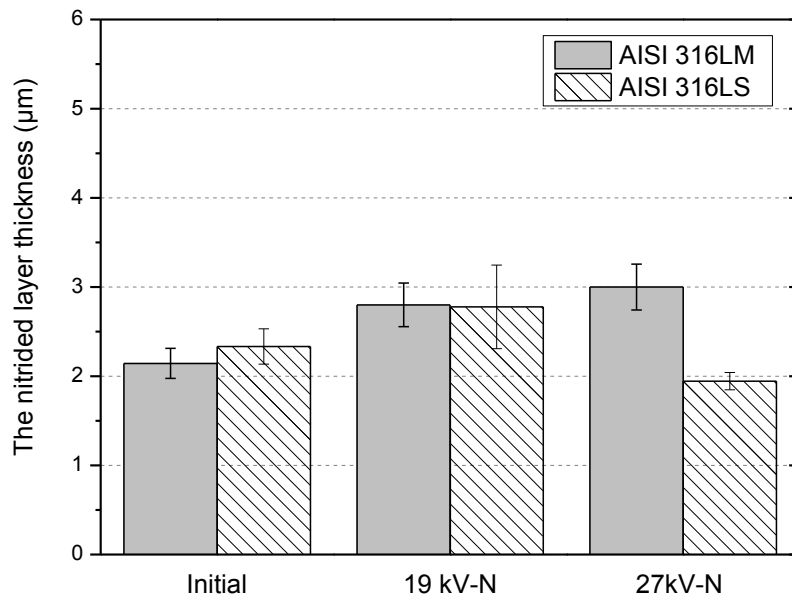
Fig. IV. 25: Evolution of the nitrided layer thicknesses as function of the accelerating voltage used for the HCPEB treatment of the AISI 316LM and 316LS stainless steels.

Fig. IV. 26 summarizes the nitrogen concentration measured by GD-OES. It is shown that for the AISI 316LM (Fig. IV. 26a), the HCPEB treatment under 19kV of accelerating voltage leads to the increase of the nitrided layer thickness, where the thickness reaches approximately 3.5 µm (about 2.5 µm for the initial nitrided sample). This thickness further increases when the accelerating voltage is higher (27kV) to reach approximately than 4 µm.

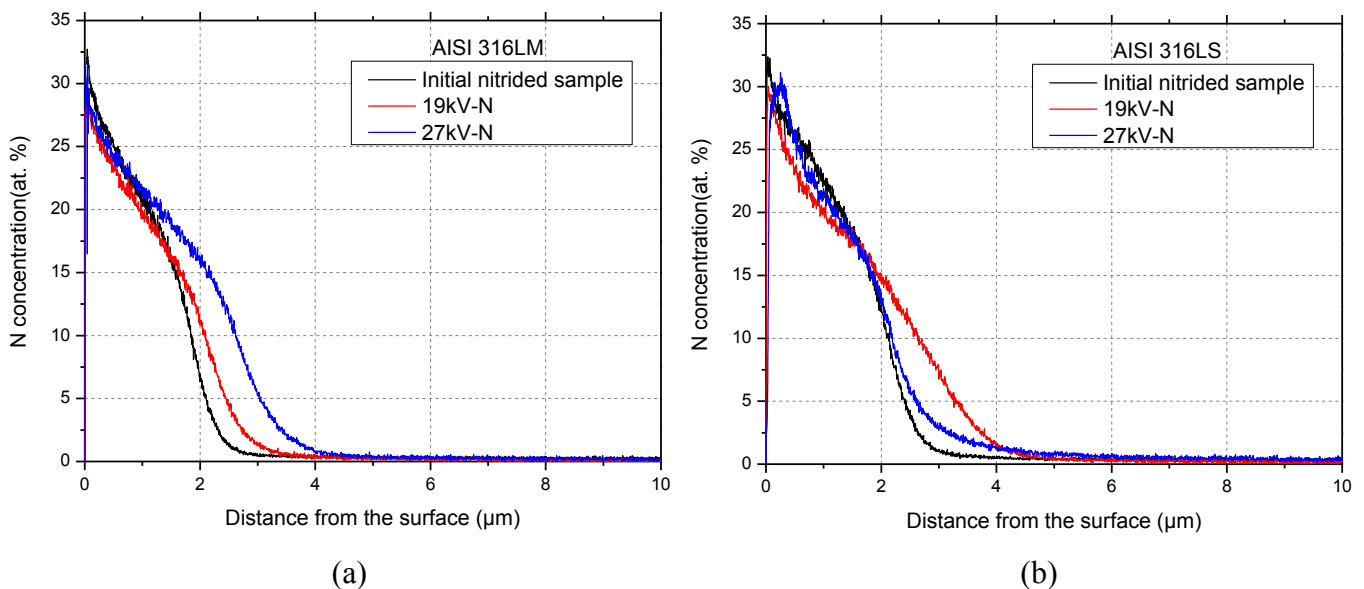(a)   (b)

Fig. IV. 26: Nitrogen profiles of the (a) AISI 316LM and (b) AISI 316LS samples after nitriding and HCPEB-N treatments.

For the AISI316LS (Fig. IV. 26b), the initial and the treated under 19kV of accelerating voltage samples present quite similar evolution as compared to the AISI 316LM. The initial nitrided

material presents a nitrided layer of about 3 µm in thickness. This thickness in increased when the material is treated by HCPEB (19kV) and reaches about 4µm. When the HCPEB energy is higher (Blue line - 27kV), the diffusion depth seems to be quite identical to the 19 kV-N one, but less nitrogen content in present in the nitrided layer (blue curve below the red one in the 2 - 4 µm range).

The HCPEB treatment before PN enhances then the nitrogen diffusion in the AISI 316LM surface under low and high energy, but an improvement of diffusion is observed only under low energy in the case of the AISI 316LS grade. It is now interesting to observe the effect of surface activation by the HCPEB on the mechanical properties of these AISI 316L surface grades. In the next section, the evolution of the surface hardness and residual stress are investigated.

II. 3.   Evolution of the surface hardness and residual stress

II. 3. 1. The surface hardness evolution

As described in Chapter I, the HCPEB treatment leads to the surface and subsurface hardness modification, due to surface melting (formation of new phases) and the propagation of the stress wave. In the present work, the surface hardness of the HCPEB treated samples is investigated before and after nitriding. The results are given inFig. IV. 27.

After only the HCPEB treatment, the extreme surface hardness of the AISI 316LM (Fig. IV. 27a) -for both acceleratingvoltages- is quite lower (about 170 HV) than the initial hardness (200 HV). The initial material hardness is reached quite quickly at about 3 µm (27 kV accelerating voltage) and 4 µm (19 keV).

For the AISI 316LS, the hardness evolutions are somewhat different (Fig. IV. 27b). Actually, after the HCPEB under 19kV, the surface hardness remains almost similar to the initial material one (~ 200 µm). However, the treatment under 27 kV of accelerating voltage results in (i) a softening of the material near the extreme top surface, where the hardness decreases to about 170 HV, and (ii) an enhancement of the hardness in the subsurface, where the hardness reaches about 250 HV at about 5.5 µmof indentation depth, and remains quite higher (~ 215 HV) than the initial material at about 9.5 µm.
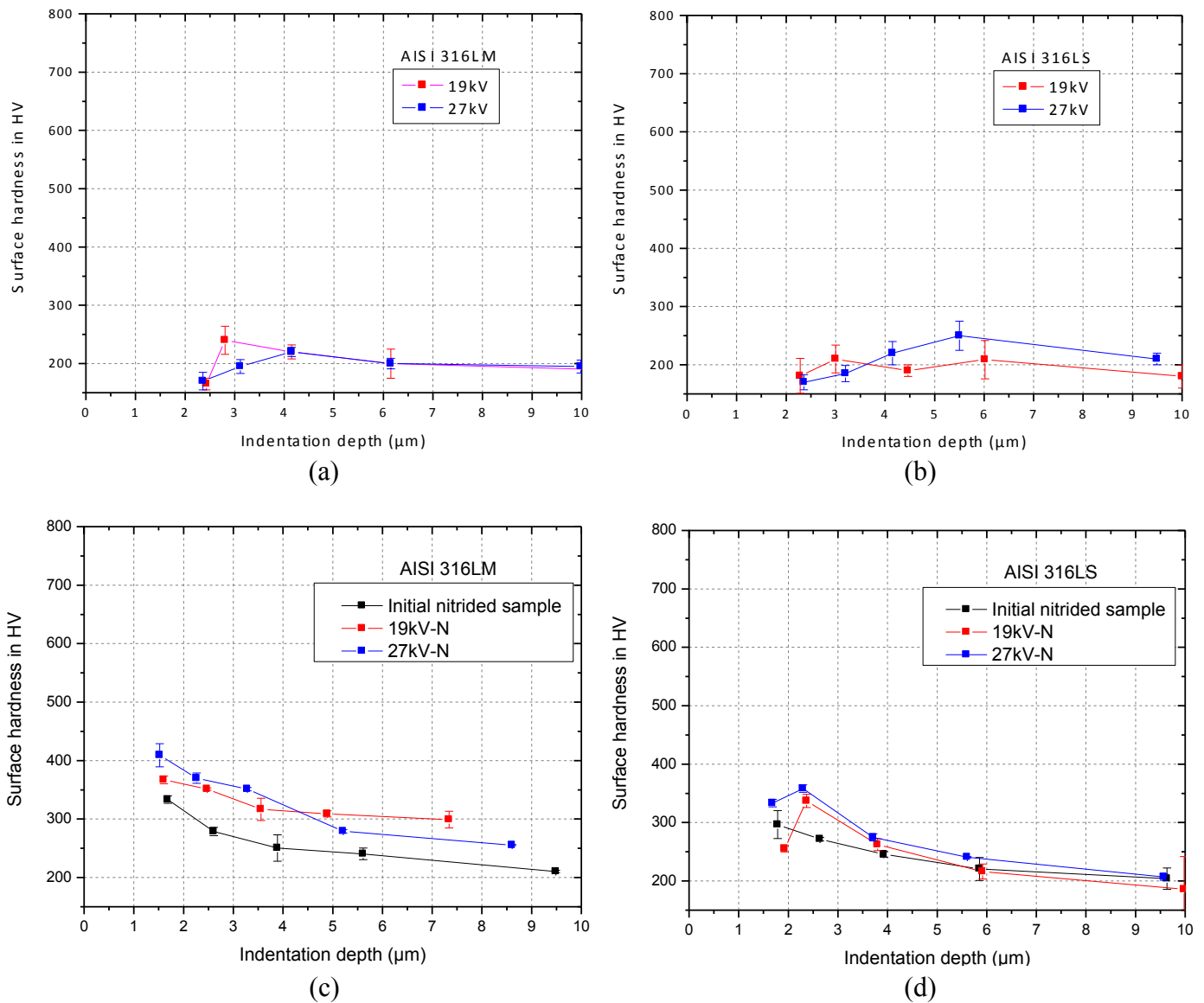
Fig. IV. 27: Surface hardness evolution of the AISI 316LM and AISI 316LS after (a, b) the HCPEB treatment and (c, d) after the duplex treatment HCPEB-N.

After the HCPEB-N duplex treatment, the surface hardness is increased in comparison with the PN nitriding treatment. For the AISI316LM (Fig. IV. 27c), the surface hardness reaches about 340 HV after the PN, then decreases continuously to reach almost the initial material hardness at a depth of 9.5 µm. After the HCPEB(19kV) and nitriding, the extreme surface hardness is higher (~ 360 HV) and decreases slightly to stabilize at 310 HV for an indentation depth of 3.5 µm. When the HCPEB energy is higher (27 kV), the extreme surface of the HCPEB27kV-N sample exhibits a higher hardness (~400HV), which remains higher than the HCPEB19kV-N until a depth of about 4 µm and then decreases to about 250 HV.

For the AISI 316LS grade (Fig. IV. 27d), the surface hardness seems to be lower. For the initial nitrided sample, the hardness evolution is relatively identical to the AISI 316LM one. The extreme

surface hardness is about 300 HV (lower than the AISI 316LM), then decreases continuously to attain approximately the initial material hardness (200 HV at a depth of 9.7 µm). However, for the two samples treated by the HCPEB-N duplex treatment, a 'softening' effect appears at the extreme surface. For the HCPEB19kV-N sample, the extreme surface hardness is about 250 HV, and increases to reach a maximum at about 2.3 µm (~ 330 HV), then decreases continuously to join the surface hardness of the initial nitrided sample. The same tendency is observed on the surface of the HCPEB27kV-N sample, where the hardness increases from 340 to 360 HV at the top surface (< 3 µm), then decreases and follows somewhat the initial nitrided sample profile.

II. 3. 2. *The evolution of the residual stress after the surface activation treatments*

In addition to the microstructure modification induced by the surface activation techniques (i.e.: the SMAT, the cold rolling and the HCPEB), and which may affect the nitrogen diffusion, the surface residual stress changes significantly. Using XRD analysis, and more particularly the peak-shifting, the stress state on the surface of the different samples can be determined using the technique described in Chapter II. The error of the measurement is estimated to be ±50 MPa.

(a) Residual stress after the SMAT:

The stress state of the initial material (prior to the SMAT treatment) is compressive with a main stress component σ_{11} = -90 MPa, and the shear components ($\sigma_{12}, \sigma_{13}, \sigma_{23}, \sigma_{21}, \sigma_{31}$ and σ_{32}) are fairly weak having their values smaller than 30 MPa:

$$\begin{pmatrix} \sigma_{11} & \sigma_{12} & \sigma_{13} \\ \sigma_{21} & \sigma_{22} & \sigma_{23} \\ \sigma_{31} & \sigma_{32} & \sigma_{33} \end{pmatrix} = \begin{pmatrix} -110 & -30 & 20 \\ -30 & -80 & 20 \\ 20 & 20 & 0 \end{pmatrix} \text{ MPa} \quad \textit{\underline{(Initial material)}}$$

After SMAT and shot peening,the compressive stress is typical of the materials treated by SMAT and shot-peening treatments(Wang et al. 1998). It is usually considered as the major factor in increasing the fatigue strength of materials.

The analysis of the D1A60T20.00 samplefor example shows that the main stress components σ_{11} and σ_{22} have quite similar values, about -330 and -380 MPa, respectively, sign of a mainly compressive stress in the surface layer. The other shear components are weak, with values smaller than 60 MPa:

$$\begin{pmatrix} -330 & -50 & 20 \\ -50 & -380 & 10 \\ 20 & 10 & 0 \end{pmatrix} \text{ MPa}$$

(b) Residual stress after the cold rolling:

On the other side, the residual stresses in the surface layers of the cold rolled samples with regard to different reduction rations, as well as the initial stateare listed below:

$$\begin{pmatrix} -90 & -10 & 20 \\ -10 & -100 & 30 \\ 20 & 30 & 0 \end{pmatrix} \text{MPa}\textit{(Initialmaterial)} \qquad \begin{pmatrix} 250 & 80 & -30 \\ 80 & 110 & -30 \\ -30 & -30 & 0 \end{pmatrix} \text{MPa} \qquad \textit{(CR45\%)}$$

$$\begin{pmatrix} -90 & 130 & 10 \\ 130 & -20 & 60 \\ 10 & 60 & 0 \end{pmatrix} \text{MPa} \qquad \textit{(CR55\%)} \qquad \begin{pmatrix} -40 & 140 & -130 \\ 140 & -180 & -100 \\ -130 & -100 & 0 \end{pmatrix} \text{MPa} \qquad \textit{(CR75\%)}$$

It is observed that for the lowest reduction ratio of the cold rolling (45 %) that surface is a tensile state of stress, where the main stress components σ_{11} and σ_{22} are about 250 and 110 MPa, respectively. However, the shear stress components are low an reach a maximum of to 80 MPa. As the reduction ration increases, the stress state changes to a compressive one, with $\sigma_{11} = -90$ MPafor the reduction ratio of 45 %, and $\sigma_{22} = -180$ under reduction ratio of 75 %. It is also interesting to note that shear stresses components increase when the reduction ratio becomes more important, and reaches the highest values when reduction ratio of 75 % is applied. In comparison with the stress state of SMAT-ed sample, the cold rolling results in 'lower' compressive state but a higher shear stress is clearly depicted.

(c) Residual stress after the HCPEB:

In the case of the samples treated with the HCPEB process, the stress state is very different. Actually, global feature of residual tensile stress is observed for two treatment conditions, and remains at the same level when increasing the accelerating voltage, with a maximum of $\sigma_{11} = 280$ MPa and $\sigma_{22} = 300$ MPa. This phenomenon has already been observed and discussed in a previous work (Zhang et al. 2013). During the solidification process, the shrinkage of solidification is constrained by the solid mater below the melted layer. Therefore, the resolidified layer has a tensile state of stress.

$$\begin{pmatrix} -190 & 50 & 40 \\ 50 & -100 & -20 \\ 40 & -20 & 0 \end{pmatrix} \text{MPa} \qquad \begin{pmatrix} 280 & 50 & -10 \\ 50 & 270 & 10 \\ -10 & 10 & 0 \end{pmatrix} \text{MPa} \begin{pmatrix} 260 & 20 & 0 \\ 27 & 300 & 20 \\ 0 & 20 & 0 \end{pmatrix} \text{MPa}$$

(Initial material) *(HCPEB-19 kV)* *(HCPEB-27 kV)*

Comparing the AISI 316L treated by these different processes prior to plasma nitriding, the stress state is different. The SMAT-ed sample surface is purely in compression, and after cold rolling, the surface stress passes from a tensile stress state with weak shear components under the

lowest reduction ratio, to a quite low compressive state (lower than the one obtained after the SMAT) with high shear stress components.

At this state of the study, it is quite difficult to depict exactly the effect of the stress state on the nitrogen diffusion. However, some assumptions can be given. As it was observed, the SMAT induces high density of defects within a high depth, but the compression of the lattice may limit the movement of nitrogen towards the interstitial positions, and thereby may limiting the nitrogen diffusion and the formation of a thin nitrided layer. On the other side, the cold rolling induces higher density of defects, as observed in the cross section observations (Fig. IV. 19), with grains highly sheared. The compression is less pronounced with higher shear components. Finally, even if the surface was in tension, the HCPEB introduces a 'light' plastic deformation in comparison with the two previous processes (SMAT and CR). Another phenomenon that can block the diffusion of nitrogen is the surface contamination by the carbon. Actually, during the HCPEB treatment, the surface in contaminated by the carbon coming from the cathode, which is in graphite (the results are not given in the present study).

To have an enhancement of the nitrogen diffusion, it seems then than severe plastic deformation of the surface should be carried out, producing a microstructure with high density of defects, and also a surface with low compression state and high shear stress. Further analysis should be carried out in order to investigate more in details this problematic.

II. 4.   **Summary**

In this part, it was observed that the nitrogen diffusion in the surface of the AISI316LM was increased when a prior HCPEB treatment is done. This effect was also observed in the surface of the AISI 316LS but only when the HCPEB is carried out at a low energy (19kV). In addition, it was found that HCPEB-N duplex treatment enhances the surface hardness of the AISI 316L.

For the AISI 316LS, on one hand, the surface activation by HCPEB allows the formation of a thicker nitrided layer at low energy of HCPEB. On the other hand, the surface hardness increases in the sub-surface (less than the AISI 316LM) and 'softening' phenomena was observed at the extreme top surface.

The surface activation by the mechanical and thermomechanical treatments lead to the formation of a different stress state. After SMAT, a typically compressive state is obtained, while cold rolling leads to the formation of a tensile state of stress under low reduction ratio, and a compression stress state under the highest reduction ratio (together with the presence of high shear stress components). After the HCPEB treatment, the rapid solidification of the melted layer leads to the formation of a tensile stress state. These different stress states may have an important rule in the nitrogen diffusion. In particular, the presence of shear stress after cold rolling could increase the nitrogen diffusion. Further investigations should be done to understand the detailed effects of the surface stress state on the nitrogen diffusion.

III.   Conclusions of part 2

The surface activation of the AISI316L was carried out using the cold rolling process. It has been found that thicker nitrided depths are obtained when increasing the reduction ratios, where the thickness was 2 times higher after CR at 75 % (~ 4 µm) than the initial material one. The surface hardness was also significantly increased and reaches 660-740 HV, about 4 times higher than the initial material hardness. In comparison with the SMAT treatment, the CR allowes to increase both the nitrided depth and the surface hardness, without any surface contamination by elements such as Ti, Al or V. The assumption of formation and reaction of these elements with nitrogen is then not valid, and the enhancement of nitrogen was probably due to the imparted plastic deformation. The effect of the latter can be easily observed and understood, as long as the strengthening by CR is easier to control in comparison with SMAT, where many parameters interact simultaneously.

The High Current Pulsed Electron Beam (HCPEB) was also suggested as surface activator before plasma nitriding. The advantages of this treatment are its ability to treat different samples shapes, and also to avoid contact with the treated surface. Two grades of the AISI 316L were treated: the AISI 316LM conventional grade, and the AISI 316LS, richer in sulphide. The second grade was used to change the surface morphology after the HCPEB treatment (higher density of craters). When the energy of the electron beam increased from 19 to 27 kV, it has been shown that the nitrided layer thickness of the AISI 316LM increased also to about 2.7 and 3 µm, higher than the 2 µm obtained on the surface of the onlynitrided material. However, for the AISI316LS, the nitrided layer increased to about 2.7 µm when 19 kV energy was used, then decreased to 2 µm for 27 kV of energy of HCPEB, a thickness similar the onlynitrided material. The HCPEB under some specific conditions seems also to be an efficient technique for increasing both the nitrided layer thickness and the surface hardness of the AISI 316L.

Comparing the different activation techniques used in the present study, the cold rolling seems to be the most convenient. As a matter of fact, the highest increase in the nitrogen content was observed in the CR+ nitrided samples. The HCPEB can also be a promising technique to accelerate the diffusion, however, further investigations should be achieved to understand the effects of the surface stress state and also the probable contamination by carbon, issued from the cathode (in the HCPEB chamber), which may limit the incorporation of nitrogen.

References

Adachi, Shinichiro, and Nobuhiro Ueda. 2012. "Formation of S-Phase Layer on Plasma Sprayed AISI 316L Stainless Steel Coating by Plasma Nitriding at Low Temperature." *Thin Solid Films* 523 (November): 11–14. doi:10.1016/j.tsf.2012.05.062.

Asgari, M., A. Barnoush, R. Johnsen, and R. Hoel. 2011. "Microstructural Characterization of Pulsed Plasma Nitrided 316L Stainless Steel." *Materials Science and Engineering a-Structural Materials Properties Microstructure and Processing* 529 (November): 425–34. doi:10.1016/j.msea.2011.09.055.

Chemkhi, M., D. Retraint, A. Roos, C. Garnier, L. Waltz, C. Demangel, and G. Proust. 2013. "The Effect of Surface Mechanical Attrition Treatment on Low Temperature Plasma Nitriding of an Austenitic Stainless Steel." *Surface & Coatings Technology* 221 (April): 191–95. doi:10.1016/j.surfcoat.2013.01.047.

Czerwiec, Thierry, Huan He, Grégory Marcos, Tony Thiriet, Sylvain Weber, and Henri Michel. 2009. "Fundamental and Innovations in Plasma Assisted Diffusion of Nitrogen and Carbon in Austenitic Stainless Steels and Related Alloys." *Plasma Processes and Polymers* 6 (6-7): 401–9. doi:10.1002/ppap.200930003.

Dalibon, E. L., P. B. Bozzano, and S. P. Bruehl. 2013. "Microstructure of Nitrided Layers in Aisi 316l Stainless Steel After Low Temperature Ion Nitriding." *Acta Microscopica* 22 (1): 4–11.

Micoulaut, M., S. Mechkov, D. Retraint, P. Viot, and M. Francois. 2007. "Granular Gases in Mechanical Engineering: On the Origin of Heterogeneous Ultrasonic Shot Peening." *Granular Matter* 9 (1-2): 25–33. doi:10.1007/s10035-006-0018-y.

Mingolo, N., A.P. Tschiptschin, and C.E. Pinedo. 2006. "On the Formation of Expanded Austenite during Plasma Nitriding of an AISI 316L Austenitic Stainless Steel." *Surface and Coatings Technology* 201 (7): 4215–18. doi:10.1016/j.surfcoat.2006.08.060.

Roland, T., D. Retraint, K. Lu, and J. Lu. 2007. "Enhanced Mechanical Behavior of a Nanocrystallised Stainless Steel and Its Thermal Stability." *Materials Science and Engineering: A* 445–446: 281–88. doi:10.1016/j.msea.2006.09.041.

Ruan, H. H., A. Y. Chen, and J. Lu. 2010. "Characterization of Plastically Graded Nanostructured Material: Part I. The Theories and the Inverse Algorithm of Nanoindentation." *Mechanics of Materials* 42 (5): 559–69. doi:10.1016/j.mechmat.2010.02.005.

Shedden, B.A, F.N Kaul, M Samandi, and B Window. 1997. "The Role of Energetic Neutrals in Reactive Magnetron Sputtering of Nitrogen-Doped Austenitic Stainless Steel Coatings." *Surface and Coatings Technology* 97 (1–3): 102–8. doi:10.1016/S0257-8972(97)00138-2.

Stinville, J. C., P. Villechaise, C. Templier, J. P. Riviere, and M. Drouet. 2010. "Lattice Rotation Induced by Plasma Nitriding in a 316L Polycrystalline Stainless Steel." *Acta Materialia* 58 (8): 2814–21. doi:10.1016/j.actamat.2010.01.002.

Stinville, Jean-Charles. 2006. *Evolution Des Microstructures et Textures Locales Par Nitruration Plasma de L'acier 316L. Répercussion Sur Sa Durabilité En Fatigue.*

Templier, C., J. C. Stinville, P. Villechaise, P. O. Renault, G. Abrasonis, J. P. Riviere, A. Martinavicius, and M. Drouet. 2010. "On Lattice Plane Rotation and Crystallographic Structure of the Expanded Austenite in Plasma Nitrided AISI 316L Steel." *Surface & Coatings Technology* 204 (16-17): 2551–58. doi:10.1016/j.surfcoat.2010.01.041.

Thiriet, T., T. Czerwiec, D. Hertz, G. Marcos, T. Toll-Duchanoy, S. Migot, B. Brugier, M. Foucault, and T. Belmonte. 2012. "Nitrogen Diffusion at Low Temperature in Fcc Materials

Deformed by Attrition Peening." *Defect and Diffusion Forum* 323-325 (April): 471–76. doi:10.4028/www.scientific.net/DDF.323-325.471.

Waltz, L., D. Retraint, A. Roos, C. Garnier, and P. Olier. 2011. "Effect of Interfacial Oxidation Occurring during the Duplex Process Combining Surface Nanocrystallisation and Co-Rolling." *Surface and Coatings Technology* 205 (19): 4608–13. doi:10.1016/j.surfcoat.2011.03.140.

Wang, Shengping, Yongjun Li, Mei Yao, and Renzhi Wang. 1998. "Compressive Residual Stress Introduced by Shot Peening." *Journal of Materials Processing Technology* 73 (1–3): 64–73. doi:10.1016/S0924-0136(97)00213-6.

Zhang, K. M., J. X. Zou, B. Bolle, and T. Grosdidier. 2013. "Evolution of Residual Stress States in Surface Layers of an AISI D2 Steel Treated by Low Energy High Current Pulsed Electron Beam." *Vacuum* 87 (January): 60–68. doi:10.1016/j.vacuum.2012.03.061.

List of figures

List of tables

Conclusions and perspectives

Previous works reported in the literature suggested that the nitrogen diffusion could be increased when the materials surface was deformed using mechanical treatments, such as shot peening or high-pressure torsion. Such a mechanical activation was used to decrease the nitriding temperature and duration as well as to increase the nitrided depths.

One of the aims of this work was to improve our understanding of the effect of the duplex surface activation treatment, using – to start with - the Surface Mechanical Attrition Treatment (SMAT) on improving surface nitriding of the AISI 316L stainless steel. This work was also done to determine the effectiveness of other alternative surface activation treatments such as cold rolling and High Current Pulsed Electron Beam (HCPEB). While the first technique is faster and more reliable than SMAT to introduce dislocations in elongated products, the second one can be used to treat more complex shapes (but of small size) while avoiding any contact with the treated surface (thus avoiding contamination by external chemical elements).

Before investigating the effectiveness of SMAT on enhancing the nitriding potential, the effects of SMAT parameters (balls diameter, amplitude of vibration, balls nature, treatment duration) on the microstructure modification were firstly investigated. The treatments were carried out on the AISI 316L and AISI 660 austenitic stainless steels. Firstly, a new technique based on the Geometrically Necessary Dislocation (GND) theory and using the Electron BackScattered Diffraction (EBSD) data allowed to establish a new quantification method of the microstructure formed after SMAT. This method allowed, using newly defined criteria, to determine fairly precisely the thickness of the three characteristic zones formed after the SMAT: (i) the UltraFine Grains zone (UFG), (ii) the transition zone and (iii) the deformed one. For the AISI 316L, quite similar layer thicknesses were formed after treating under 60 µm for 20 minutes and 80 µm for 3 minutes.

The developed quantification technique was then applied to the AISI 660 treated with wider range of SMAT parameters. When 1 mm diameter balls are used, it was found that increasing the duration of the treatment resulted essentially in an increase of the transition layer thickness, sign of higher grains fragmentation near the top treated surface, while the overall affected depth remained quite constant. With balls of 2 mm diameter, the overall affected and deformed zones thicknesses saturated when the treatment durations increased. Only the UFG and transition zone continued to increase. To analyse more quantitatively the evolution of these zones as function of the SMAT conditions, the energy imparted (cumulated energy) to the material was estimated, based on the

balls kinetic energy and other parameters such as treatment duration and balls number. When the energy increased, the overall affected depth increased continuously and stabilized at a given value of about 10 J. However, it was found that the fragmentation became more important when the energy reached about 5 J. The UFG and transition zone thicknesses remained quite constant at energies below this value (5 J), then started to increase continuously in the range of calculated energies, reaching a maximum of about 50 μm for the highest cumulated energy (~ 95 J). It seemed then that an energy threshold was necessary to activate the fragmentation mechanism. These results give some promising results. It should be noted however that, due to the lack of some simulation and experimental data, the calculated energy was done without taking into consideration other parameters (such as the ball/ball and ball/chamber interactions, impacts with the sonotrode per second …etc.).

The chemical analysis of the surfaces after SMAT revealed the presence of external elements issued from the different parts of the experimental setup. Titanium, Aluminium and Vanadium were found at the surface of the AISI 316L treated samples as the result of a transfer from the sonotrode, which is made of the Ti-6Al-4V alloy. Another contamination by Chromium was depicted. Its concentration reached about 25 wt. % (the initial material containing about 17 wt. %). This contamination was suggested to originate from the D2 die steel from which the chamber was made of. This alloy contains large Chromium carbides (M7C3 type), very rich in Chromium, which may have been extracted by the balls and deposited on the samples surface. Some additional experiments should be undertaken to confirm this finding and its interpretation. In a more general manner, in addition to take care of the atmospheric environment to ovoid oxidation, it appears that SMAT should be carried out in a treatment device made of polymeric materials to avoid significant contamination.

The surface contamination affects the surface properties (as was discussed in this manuscript) and the analysis of the surface must take this into account. For example, the X-Ray Diffraction analysis of the SMAT-ed AISI 660 steel has revealed that the level of background (because of florescence) of the XRD traces was influenced by the extent of the SMAT induced contamination. The amount of contamination, essentially by Titanium, was depicted because the chromium radiation induced fluorescence of the Titanium. As its content increased, the background level increased simultaneously. The XRD analysis technique could thus be an interesting tool in the contamination analysis of complex shape parts, or as a non-destructive characterisation method (contrarily to the GD-OES).

Concerning the Duplex treatments analysis given in Chapter 4, the results showed that the surface hardness was significantly enhanced after SMAT+nitriding. The increase is about 350 % and 200 % in comparison with the initial and nitrided samples, respectively. This increase did not correspond to the simple cumulative effect of the SMAT + nitriding treatments. More complex interactions are generated where the plastic deformation state could be a key point of this enhancement. It was suggested that this hardness increase was also due to the formation of TiN or TiAl nitrides. An hypothesis that must be experimentally verified in the future.

Despite this important increase in hardness, it was also observed that the activation by SMAT does not directly lead to an enhancement of the nitrogen diffusion and an associated increase in thickness. In this respect, our results are not consistent with the results from the literature, even the most recent ones. Indeed, while non-continuous and thinner nitrided layer were formed on the surface of the SMAT-ed AISI 316L because of the contamination (see previous section) that could break the nitrogen diffusion. Our results also show that, even after removing these elements by electrolytic polishing, the nitriding treatment did not lead to the formation of a thicker layer. The latter thickness remained inferior to a nitrided initial material. Our results therefore suggest that the contamination is the only fact responsible for the limitation of the nitrogen diffusion within the surface of the AISI 316L. The formed microstructure and compressive plastic deformation state imparted by the SMAT may have an influence.

Further investigations were then carried out using other surface activators, to avoid the contamination and introduce a different plastic deformation state. Using the Cold Rolling (CR) as surface activator, interesting results were obtained. Actually, when reduction rate increased, the diffusion increases too, and the thickness of the formed nitrided layer is multiplied by 2 ($\sim$ 4 μm) in comparison with the initial material (about 2 μm) when a reduction ratio of 75 % was used. The surface hardness of the CR+nitrided samples was also increased to reach about 740 HV, almost 4 times the initial material hardness. It was also noticed that this hardness level is quite similar to the one obtained on SMAT+nitrided sample. After the CR, no contamination occurred on the surface and the assumption that the hardness increase was due to the precipitation of nitrides is then not valid. Also, as it is clear that cold rolling introduces a high amount of dislocations but does not result in the formation of a nanostructured layer, the idea that the enhanced diffusion is associated solely to a reduction of the grain size after SMAT can be ruled out. The mechanisms responsible of this enhancement could be the plastic deformation state of the surface, and also the stress state after the SMAT and CR. On-going investigations, not detailed in the present thesis, are carried out to understand the effect of the stress state on the surface hardness modifications.

The last technique used for the surface activation was the High Current Pulsed Electron Beam (HCPEB), in order to avoid the contact with the treated surfaces, and also it can be used for the treatment of complex samples shapes. Two grades of the AISI 316L were treated: the AISI 316LM conventional grade, and AISI 316LS, richer in Sulphide to change the surface morphology after the HCPEB treatment (higher density of craters). For the AISI 316LM, it has been shown that an increase of the nitrided layer thickness occurred when under low energy of electron beam, and remained stable under high energy. However, for the second grade (AISI 316LS), an enhancement of the nitrogen diffusion was observed only when a low energy of the electron beam is used, while under higher energy, the nitrided layer thickness as quite similar to the initial nitrided material. These first results showed that the HCPEB -under some specific experimental conditions-could be efficient for increasing both the nitrided layer thickness and the surface hardness of the AISI 316L. It should also be noted that the hardness obtained on the HCPEB and the HCPEB –N treated samples was significantly lower than in for the SMAT-ed and cold rolled samples. This could be due to the low plastic deformation imparted to the material after the HCPEB and the HCPEB-N treatments.

Despite all the analyses carried out in the present work, the effectiveness of the surface activation by surface treatments techniques remains complex to explain. The application of the Hertz theory allowed to get a good estimation of the SMAT effect on microstructure, and particularly the evolution of the formed layers thicknesses. However, complementary information, issued from the simulations works for example, can help to estimate more precisely the imparted energy to the surface during the treatment. A combined experimental-simulation work could lead to the estimation of the balls impacts number with the treated surface, and the material properties (hardness, strength ...etc.) as function of the SMAT parameters. Refinement of the suggested model in the present work could then be carried out.

Always concerning the SMAT, it could be interesting to do treatments in a chamber in polymer (instead of die steel used in the present study). This will allow to avoid the surface contamination (no need of surface 'cleaning'), and the obtained hardness after the SMAT+nitriding treatment will remain very high. Actually, even if the nitrogen diffusion was not enhanced, the hardness reached very high level. However, the surface polishing to remove the contaminated layer has led to a significant increase of the surface hardness. The use of a chamber in polymer could have an important effect on the surface hardness.

Finally, as only the hardness was investigated as a mechanical property, it could be interesting to study the effect of the SMAT on the lifetime of the treated materials. Mechanical tests

such tensile, fatigue or wear resistance tests could be carried out. Corrosion tests in different fields and under different temperatures could also be done to characterize the physical and chemical properties of the SMAT-ed surfaces.

Finally, the experimental results obtained showed that the plastic deformation state was different after the different surface activation techniques. Thus, the plastic deformation state should be studied more in details to understand the direct effect on nitrogen diffusion. Materials of different Stack Fault Energies (SFEs) should be subjected to surface activation prior to nitriding. This will activate different plastic deformation mechanisms and would help to better understand the nitrogen incorporation within different deformed surfaces.